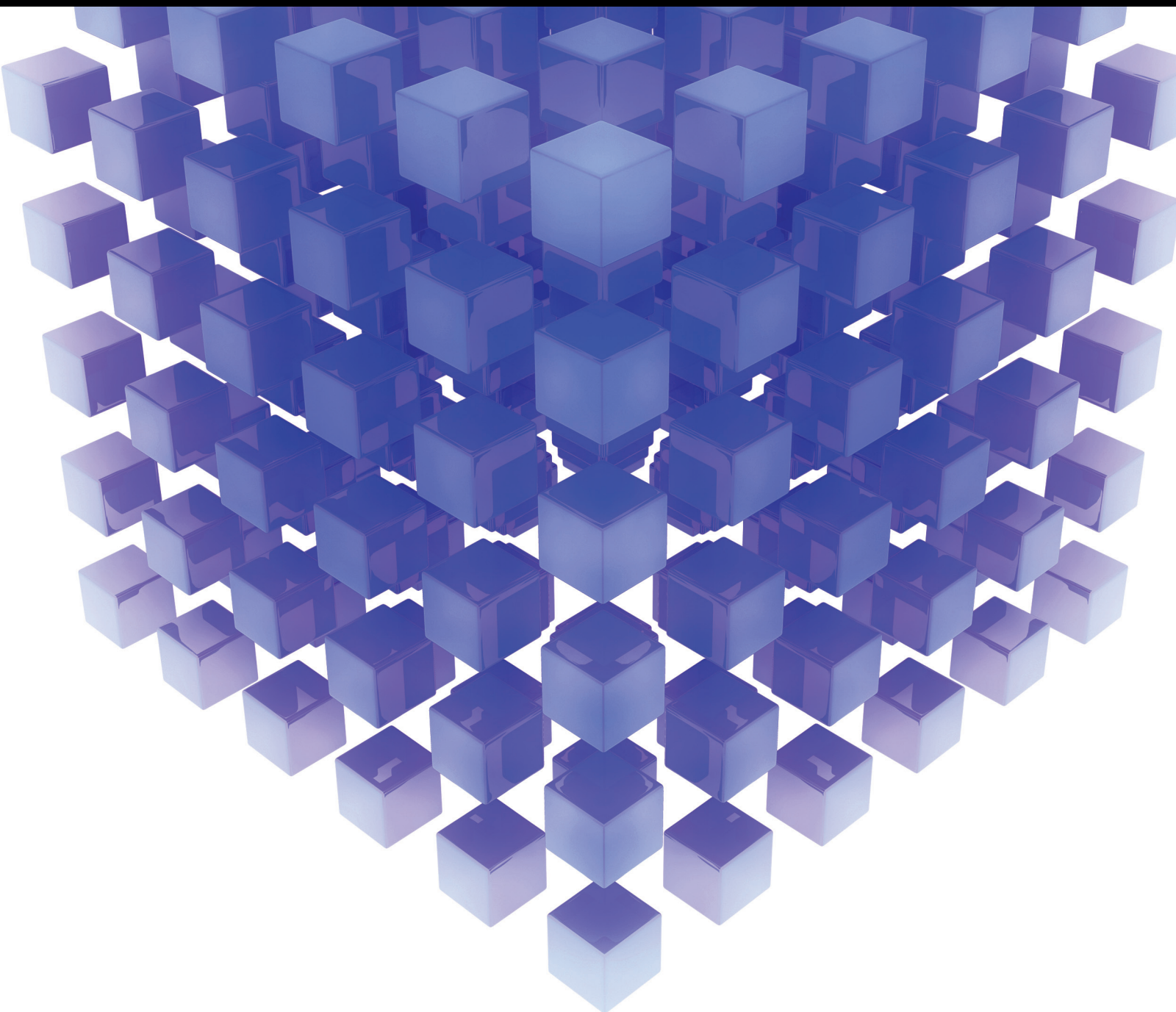


STRUCTURAL DAMAGE Modelling AND ASSESSMENT

GUEST Editors: ANAXAGORAS ELENAS, YURI PETRYNA, AND NAWAWI CHOUW



Structural Damage Modelling and Assessment

Structural Damage Modelling and Assessment

Guest Editors: Anaxagoras Elenas, Yuri Petryna,
and Nawawi Chouw



Copyright © 2014 Hindawi Publishing Corporation. All rights reserved.

This is a special issue published in "Mathematical Problems in Engineering." All articles are open access articles distributed under the Creative Commons Attribution License, which permits unrestricted use, distribution, and reproduction in any medium, provided the original work is properly cited.

Editorial Board

Mohamed Abd El Aziz, Egypt	Alex Elías-Zúñiga, Mexico	Stefano Lenci, Italy
Eihab M. Abdel-Rahman, Canada	Anders Eriksson, Sweden	Roman Lewandowski, Poland
Rashid K. Abu Al-Rub, USA	Vedat S. Erturk, Turkey	Shihua Li, China
Sarp Adali, South Africa	Moez Feki, Tunisia	Ming Li, China
Salvatore Alfonzetti, Italy	Ricardo Femat, Mexico	S. Li, Canada
Igor Andrianov, Germany	Roberto Fontes Valente, Portugal	Jian Li, China
Sebastian Anita, Romania	Claudio Fuerte-Esquivel, Mexico	Teh-Lu Liao, Taiwan
W. Assawinchaichote, Thailand	Zoran Gajic, USA	Panos Liatsis, UK
Er-wei Bai, USA	Ugo Galvanetto, Italy	Kim Meow Liew, Hong Kong
Ezzat G. Bakhoum, USA	Xin-Lin Gao, USA	Yi-Kuei Lin, Taiwan
José Manoel Balthazar, Brazil	Furong Gao, Hong Kong	Shueei M. Lin, Taiwan
Rasajit Kumar Bera, India	Behrouz Gatmiri, Iran	Jui-Sheng Lin, Taiwan
Jonathan N. Blakely, USA	Oleg V. Gendelman, Israel	Wanquan Liu, Australia
Stefano Boccaletti, Spain	Paulo Batista Gonçalves, Brazil	Bin Liu, Australia
Stephane P. A. Bordas, USA	Oded Gottlieb, Israel	Yuji Liu, China
Daniela Boso, Italy	Fabrizio Greco, Italy	Paolo Lonetti, Italy
M. Boutayeb, France	Quang Phuc Ha, Australia	Vassilios C. Loukopoulos, Greece
Michael J. Brennan, UK	Tony Sheu Wen Hann, Taiwan	Chien-Yu Lu, Taiwan
Salvatore Caddemi, Italy	Thomas Hanne, Switzerland	Junguo Lu, China
Piermarco Cannarsa, Italy	Katica R. Hedrih, Serbia	Alexei Mailybaev, Brazil
Jose E. Capilla, Spain	M. I. Herreros, Spain	Manoranjan K. Maiti, India
Carlo Cattani, Italy	Wei-Chiang Hong, Taiwan	Oluwole Daniel Makinde, South Africa
Marcelo Cavalcanti, Brazil	Jaromir Horacek, Czech Republic	Rafael Martínez-Guerra, Mexico
Diego J. Celentano, Chile	Gordon Huang, Canada	Driss Mehdi, France
Mohammed Chadli, France	Huabing Huang, China	Roderick Melnik, Canada
Arindam Chakraborty, USA	Chuangxia Huang, China	Xinzhu Meng, China
Yong-Kui Chang, China	Yi Feng Hung, Taiwan	Jose Merodio, Spain
Michael J. Chappell, UK	Hai-Feng Huo, China	Yuri Vladimirovich Mikhlin, Ukraine
Kui Fu Chen, China	Asier Ibeas, Spain	Gradimir Milovanović, Serbia
Kue-Hong Chen, Taiwan	Anuar Ishak, Malaysia	Ebrahim Momoniat, South Africa
Xinkai Chen, Japan	Reza Jazar, Australia	Trung Nguyen Thoi, Vietnam
Jyh-Horng Chou, Taiwan	Zhijian Ji, China	Hung Nguyen-Xuan, Vietnam
Slim Choura, Tunisia	Jun Jiang, China	Ben T. Nohara, Japan
Cesar Cruz-Hernandez, Mexico	J. J. Judice, Portugal	Sotiris K. Ntouyas, Greece
Erik Cuevas, Mexico	Tadeusz Kaczorek, Poland	Claudio Padra, Argentina
Swagatam Das, India	Tamas Kalmar-Nagy, USA	Bijaya Ketan Panigrahi, India
Filippo de Monte, Italy	Tomasz Kapitaniak, Poland	Francesco Pellicano, Italy
Yannis Dimakopoulos, Greece	Hamid R. Karimi, Norway	Matjaž Perc, Slovenia
Baocang Ding, China	Metin O. Kaya, Turkey	Vu Ngoc Phat, Vietnam
Joao B. R. Do Val, Brazil	Farzad Khani, Iran	Maria do Rosário Pinho, Portugal
Daoyi Dong, Australia	Ren-Jieh Kuo, Taiwan	Seppo Pohjolainen, Finland
B. Dubey, India	Jurgen Kurths, Germany	Stanislav Potapenko, Canada
Horst Ecker, Austria	Claude Lamarque, France	Sergio Preidikman, USA
M. Onder Efe, Turkey	Usik Lee, Korea	Carsten Proppe, Germany
Elmetwally Elabbasy, Egypt	Marek Lefik, Poland	Hector Puebla, Mexico

Justo Puerto, Spain	Grigori M. Sisoev, UK	Youqing Wang, China
Dane Quinn, USA	Christos H. Skiadas, Greece	Gerhard-Wilhelm Weber, Turkey
Kumbakonam Rajagopal, USA	Davide Spinello, Canada	Jeroen Witteveen, The Netherlands
Gianluca Ranzi, Australia	Sri Sridharan, USA	Kwok-Wo Wong, Hong Kong
Sivaguru Ravindran, USA	Hari M. Srivastava, Canada	Ligang Wu, China
G. Rega, Italy	Rolf Stenberg, Finland	Zhengguang Wu, China
Pedro Ribeiro, Portugal	Changyin Sun, China	Gongnan Xie, China
J. Rodellar, Spain	Xi-Ming Sun, China	Wang Xing-yuan, China
Rosana Rodriguez-Lopez, Spain	Jitao Sun, China	Xi Frank Xu, China
Alejandro J. Rodriguez-Luis, Spain	Andrzej Swierniak, Poland	Xuping Xu, USA
Carla Roque, Portugal	Yang Tang, Germany	Jun-Juh Yan, Taiwan
Rubén Ruiz García, Spain	Allen Tannenbaum, USA	Xing-Gang Yan, UK
Manouchehr Salehi, Iran	Cristian Toma, Romania	Suh-Yuh Yang, Taiwan
Miguel A. F. Sanjuán, Spain	Gerard Olivar Tost, Colombia	Mahmoud T. Yassen, Egypt
Ilmar Ferreira Santos, Denmark	Irina N. Trendafilova, UK	Mohammad I. Younis, USA
Nickolas S. Sapidis, Greece	Alberto Trevisani, Italy	Bo Yu, China
Evangelos J. Sapountzakis, Greece	Jung-Fa Tsai, Taiwan	Huang Yuan, Germany
Bozidar Sarler, Slovenia	Kuppalapalle Vajravelu, USA	S.P. Yung, Hong Kong
Andrey V. Savkin, Australia	Victoria Vampa, Argentina	Ion Zaballa, Spain
Massimo Scialia, Italy	Josep Vehi, Spain	Ashraf M. Zenkour, Saudi Arabia
Mohamed A. Seddeek, Egypt	Stefano Vidoli, Italy	Jianming Zhan, China
Leonid Shaikhet, Ukraine	Yijing Wang, China	Yingwei Zhang, China
Cheng Shao, China	Cheng C. Wang, Taiwan	Xu Zhang, China
Bo Shen, Germany	Dan Wang, China	Lu Zhen, China
Jian-Jun Shu, Singapore	Xiaojun Wang, China	Liancun Zheng, China
Zhan Shu, UK	Qing-Wen Wang, China	Jian Guo Zhou, UK
Dan Simon, USA	Yongqi Wang, Germany	Zexuan Zhu, China
Luciano Simoni, Italy	Moran Wang, China	Mustapha Zidi, France

Contents

Structural Damage Modelling and Assessment, Anaxagoras Elenas, Yuri Petryna, and Nawawi Chouw
Volume 2014, Article ID 532345, 2 pages

Fuzzy Neural Network-Based Damage Assessment of Bridge under Temperature Effect, Yubo Jiao, Hanbing Liu, Yongchun Cheng, Xianqiang Wang, Yafeng Gong, and Gang Song
Volume 2014, Article ID 418040, 9 pages

Seismic-Parameter-Based Statistical Procedures for the Approximate Assessment of Structural Damage, A. Elenas
Volume 2014, Article ID 916820, 22 pages

Quasistatic Seismic Damage Indicators for RC Structures from Dissipating Energies in Tangential Subspaces, Wilfried B. Krätzig and Yuri S. Petryna
Volume 2014, Article ID 615792, 11 pages

Structural Health Monitoring Based on Combined Structural Global and Local Frequencies, Jilin Hou, Łukasz Jankowski, and Jinping Ou
Volume 2014, Article ID 405784, 13 pages

A GIS-Enabled Approach for Assessing Damage Potential of Levee Systems Based on Underlying Geology and River Morphology, Mustafa Saadi and Adda Athanasopoulos-Zekkos
Volume 2013, Article ID 936468, 20 pages

The Influence of Infill Wall Topology and Seismic Characteristics on the Response and Damage Distribution in Frame Structures, Nikos Nanos and David Begg
Volume 2013, Article ID 506319, 12 pages

Simultaneous Identification of Moving Vehicles and Bridge Damages Considering Road Rough Surface, Qingxia Zhang, Łukasz Jankowski, and Zhongdong Duan
Volume 2013, Article ID 963424, 12 pages

Factor of Safety Reduction Factors for Accounting for Progressive Failure for Earthen Levees with Underlying Thin Layers of Sensitive Soils, Adam J. Lobbestael, Adda Athanasopoulos-Zekkos, and Josh Colley
Volume 2013, Article ID 893602, 13 pages

Qualitative Behaviour of Elastic-Plastic Solutions for a Class of Damage Mechanics Models Near Bimaterial Interfaces: A Simple Analytical Example, Sergei Alexandrov and Yusof Mustafa
Volume 2013, Article ID 197632, 5 pages

Earthquake Damage Assessment for RC Structures Based on Fuzzy Sets, Haoxiang He, Maolin Cong, and Yongwei Lv
Volume 2013, Article ID 254865, 11 pages

An Exact Approach for Structural Damage Assessment, Q. W. Yang
Volume 2013, Article ID 230957, 7 pages

Study of the Residual Strength of an RC Shear Wall with Fractal Crack Taking into Account Interlocking Interface Phenomena, O. Panagouli and K. Iordanidou
Volume 2013, Article ID 101484, 14 pages

Editorial

Structural Damage Modelling and Assessment

Anaxagoras Elenas,¹ Yuri Petryna,² and Nawawi Chouw³

¹ Department of Civil Engineering, Democritus University of Thrace, 67100 Xanthi, Greece

² Department of Civil Engineering, Technical University Berlin, 13355 Berlin, Germany

³ Department of Civil and Environmental Engineering, The University of Auckland, New Zealand

Correspondence should be addressed to Anaxagoras Elenas; elenas@civil.duth.gr

Received 17 March 2014; Accepted 17 March 2014; Published 3 April 2014

Copyright © 2014 Anaxagoras Elenas et al. This is an open access article distributed under the Creative Commons Attribution License, which permits unrestricted use, distribution, and reproduction in any medium, provided the original work is properly cited.

A lot of research work has been done during the last decades, focusing on the structural damage modelling and assessment. This rapidly growing scientific field forms a basis for efficient structural design, health monitoring, and lifetime management. The computer-based modelling and assessment make a quantification of the structural damage evolution possible. It is an important tool for prediction or explanation of damage in a large variety of civil engineering structures. In this context, the structures can be real, planned, or experimental specimens. Several new damage simulation and evaluation approaches, including analytical, numerical, and intelligent procedures, have been considered in the present special issue.

A. Elenas presents two statistical methods for the approximate evaluation of the postseismic damage status of buildings based on twenty intensity parameters of seismic excitations. The first is multilinear regression analysis, and the second is discriminant analysis. The overall damage index of Park and Ang, the maximum interstory drift ratio, and the maximum softening of DiPasquale and Cakmak are used to describe the structural damage status.

W. B. Krätzig and Y. S. Petryna apply recent research on structural damage description to earthquake-resistant design concepts. They define damage indicators, which are able to quantify the arising structural damage. Such damage measures are based on dissipated energies of virtual mode shapes/modal forces which can be derived from the tangential stiffness matrix in the framework of nonlinear finite element analysis. The paper bridges a gap to the quasistatic seismic safety concepts of most design codes. The developed concept is checked by reanalyses of two experimentally investigated reinforced concrete frames.

J. Hou et al. present a parameter estimation method for structural health monitoring based on the combined measured global frequencies and local frequencies of the structure. Initially, an experiment provides low-order modes which can reflect the global information of the structure. Then, a mass is added to the structural member to increase the local dynamic characteristic and to make the member have the local primary frequency, which belongs to structural local frequency and is sensitive to local parameters. Finally, the parameters of the structure can be optimized accurately using the combined structural global frequencies and structural local frequencies.

M. Saadi and A. Athanasopoulos-Zekkos present a GIS enabled approach for assessing damage potential of levees systems. Spatial variability of soil properties is correlated with regional variables such as distance from the nearest river segment, river meandering sinuosity index, and surface geology. A geostatistical ordinary Kriging approach is used for developing these correlations. Soil strength parameters of identified levee stratigraphy layers were statistically analyzed using a geostatistical ordinary Kriging approach and correlated with preselected regional variables. Excessive underseepage and loss of freeboard due to soil liquefaction are evaluated as the two damage indices for earthen levees.

N. Nanos and D. Begg investigate the influence of alternative infill wall topologies in terms of a frame structure's seismic behavior and damage distribution characteristics. Their work was carried out with utilizing nonlinear dynamic analyses combined with a set of spectrum compatible artificial accelerograms for all individual cases to obtain the relevant structural response. Structural damage results were

quantified by the global structure damage index of Park and Ang and the maximum interstory drift ratio.

Q. Zhang et al. present an effective procedure for a simultaneous identification of moving vehicles and structural damage based on a virtual distortion method. The vehicle parameters and the structural damage are treated as optimization variables. Using a moving dynamic influence matrix the response of the damaged system to given optimization variables could be computed quickly without the need of a numerical simulation and the repeated assembly of the time-variant system parameter matrix at each time step.

A. J. Lobbestael et al. investigate the effects of progressive failure on flood embankments with underlying thin layers of soft and sensitive soils. A parametric analysis is conducted to investigate the effect of thin layers of soft sensitive soils on the stability of flood embankments. A flood embankment is modeled by the limit equilibrium method and the finite element method. The foundation profile is altered to determine the extent to which varying soft and sensitive soils affect the stability of the embankment, with respect to progressive failure.

S. Alexandrov and Y. Mustafa present an exact analytic solution for a class of elastic-plastic models with damage evolution. Special attention is devoted to the qualitative behavior of the solution in the vicinity of the bimaterial interface.

H. He et al. present a global damage index based on multiple linear force-deformation curves in pushover analysis to evaluate the damage of reinforced concrete structures. Multiple damage indices about displacement and energy for performance-based design are considered. The relation of multiple damage indices and the fuzzy damage set is presented by a comprehensive fuzzy evaluation. Thus, a method is proposed for performance-based multiple fuzzy seismic damage assessment of reinforced concrete frame structures.

Q. W. Yang proposes an exact flexibility perturbation technique for damage identification in statically determinate structures, which is based on matrix spectral decomposition and minimum-rank update theory. The procedure considered can reveal a reliable extent of damage by a simple computation without any higher-order approximation or iteration, regardless of whether the damage is small or large.

O. Panagouli and K. Iordanidou examine the postcracking strength of a reinforced concrete shear wall by taking into account the complex geometry of the crack and the mixed friction-plastification mechanisms that develop in the vicinity of the crack. Because of the significance of the crack geometry, a multiresolution analysis based on fractal geometry is performed, taking into account the size of the aggregates of concrete. The constitutive materials are assumed to have elastic-plastic behavior.

Y. Jiao et al. present an effective strategy for eliminating temperature effects in damage identification of bridges. Thereby the authors use adaptive neurofuzzy inference system (ANFIS) that combines the advantages of neural networks and fuzzy inference system used as damage identification algorithm.

By compiling these papers, the editors hope that the readers will benefit from the latest development in the field of structural damage modelling and assessment of civil engineering structures.

*Anaxagoras Elenas
Yuri Petryna
Nawawi Chouw*

Research Article

Fuzzy Neural Network-Based Damage Assessment of Bridge under Temperature Effect

Yubo Jiao, Hanbing Liu, Yongchun Cheng, Xianqiang Wang, Yafeng Gong, and Gang Song

College of Transportation, Jilin University, No. 5988 Renmin Street, Changchun 130025, China

Correspondence should be addressed to Yubo Jiao; jiaoyubo86@163.com

Received 24 July 2013; Revised 16 December 2013; Accepted 30 December 2013; Published 5 March 2014

Academic Editor: Yuri Petryna

Copyright © 2014 Yubo Jiao et al. This is an open access article distributed under the Creative Commons Attribution License, which permits unrestricted use, distribution, and reproduction in any medium, provided the original work is properly cited.

Vibration-based method has been widely applied for damage identification of bridge. Natural frequency, mode shape, and their derivatives are sensitive parameters to damage. However, these parameters can be affected not only by the health of structure, but also by the changing temperature. It is essential to eliminate the influence of temperature in practice. Therefore, a fuzzy neural network-based damage assessment method is proposed in this paper. Uniform load surface curvature is used as damage indicator. Elasticity modulus of concrete is assumed to be temperature dependent in the numerical simulation of bridge model. Through selecting temperature and uniform load surface curvature as input variables of fuzzy neural network, the algorithm can distinguish the damage from temperature effect. Comparative analysis between fuzzy neural network and BP network illustrates the superiority of the proposed method.

1. Introduction

Bridge structure is playing significant role in modern transport system and economic development. With the rapid growth of traffic volume, the loads carried by bridges increase dramatically. External environment also exacerbates the deterioration of materials. Damage inevitably occurs in structures under the coupling effect of load and environment, which will lead to the deficiency of carrying capacity [1, 2]. Therefore, it is necessary to identify the structural damage and strengthen the bridge. The research on appropriate damage identification methods has received extensive attention [3, 4].

Vibration tests have been widely performed in bridge health monitoring. The dynamic characteristics such as eigenfrequencies, modal shapes, and damping ratios of structure contain effective information on bridge health status [5]. Vibration-based damage identification methods are proved feasible in laboratory and field testing. The theoretical background is that damage will modify the stiffness and mass of structure and then alter the modal data. Conversely, modal parameters can be regarded as damage indicators of structure [6]. However, these indicators are sensitive to not only

damage, but also environmental conditions such as humidity, wind, and, most important, temperature [7, 8]. Wahab and de Roeck [9] conducted dynamic tests for a prestressed concrete bridge in spring and in winter and observed a change of 4%~5% in natural frequencies. Farrar et al. [10] found that the first eigenfrequency of Alamosa Canyon Bridge varies by approximately 5% during a 24 h time period. Zhou et al. [11] obtained 770 h modal frequencies and temperature data from the instrumented cable-stayed Ting Kau Bridge in Hongkong; the environmental variation accounts for changes in modal frequencies of 0.005 Hz and 0.018 Hz in absolute sense and 1.505% to 6.689% in relative sense for the first eight modes. Moser and Moaveni [12] presented results from a continuous monitoring system installed on Dowling Hall Footbridge. Significant variability in the identified natural frequencies is observed; these changes in natural frequencies are strongly correlated with temperature. Therefore, temperature effect must be effectively considered in practical application of damage identification.

Some researches have been conducted to solve this problem in recent years. One of the methods is to search the correlation between eigenfrequencies and corresponding

temperatures [13–15]. Peeters and Roeck [13] adopted a Black-box model to describe the variations of eigenfrequencies as a function of temperature. Damage can be detected if eigenfrequencies of the new data exceed certain confidence intervals of the model. Sohn et al. [14] presented a linear adaptive model to discriminate the changes of natural frequencies due to temperature changes from those caused by structural damage or other environmental effects. Peeters et al. [15] used the ARX models to simulate the eigenfrequencies. If a new measured eigenfrequency lies outside the estimated confidence intervals, it is likely that the bridge is damaged. Z24 Bridge verified its feasibility. However, this kind of method possesses several drawbacks [16, 17]. Firstly, the optimal locations of temperature sensors may be difficult to determine. Secondly, the definition of environmental variables which affect the structural features is difficult. Moreover, it would be difficult for sensors to monitor environmental variables over a long time. Another group of methods can minimize the environmental effect without measuring temperatures. Yan et al. [16] proposed a principal-component-analysis- (PCA-) based method to distinguish between changes of modal data due to environmental variation and structural damage under linear or weakly nonlinear cases. In a companion paper [18], they conducted a further extension of the proposed method to handle nonlinear cases, which may be encountered in some complex structures. Sohn et al. [7] developed a novel detection technique which can take into account the environmental conditions of system in order to minimize false positive indications. Autoassociative neural networks are employed to discriminate system changes of interest such as structural damage from other variations. As pointed out by Meruane and Heylen [19], these methods cannot identify the damage location and severity. They proposed a damage detection method which is able to deal with temperature variations. The objective function correlates mode shapes and natural frequencies, and a parallel genetic algorithm handles the inverse problem.

In this paper, a fuzzy neural network-based damage assessment method which can eliminate the temperature effect is proposed. Adaptive network-based fuzzy inference system (ANFIS) is a fuzzy inference system implemented in the framework of adaptive networks, which avoids the complexity and difficulty of traditional neural networks. Meanwhile, it can also overcome the shortcoming of poor learning ability for traditional fuzzy inference system [20]. Uniform load surface (ULS) is a derivative from modal flexibility, which is found to have much less truncation effect and is least sensitive to experimental error [21]. Therefore, ULS parameter is selected as damage indicator. Pham [22] pointed out that the changes of ambient temperature mainly affect the elastic modulus of the construction material and therefore the stiffness of the entire bridge. Shoukry et al. [23] obtained the relationship between temperature and elastic modulus of concrete. The numerical model of structure assumes that the elastic modulus of the materials is temperature dependent. Through considering temperature and ULS parameter in the calculating process of ANFIS, it can distinguish the damage from temperature effect. In order to verify its superiority,

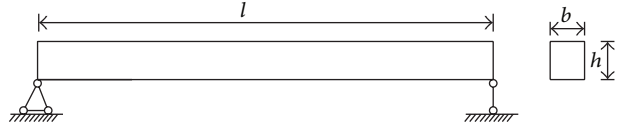


FIGURE 1: Diagram of simply supported Euler-Bernoulli beam.

comparative analysis between fuzzy neural network and BP network is conducted.

2. Theoretical Background

2.1. Dynamics Background under Temperature Effect. According to existing research results, temperature alters the modal parameters through a complicated way. On one hand, temperature effect will affect mechanical properties of materials. On the other hand, the geometry is sensitive to temperature, which will change constraint conditions. A simply supported Euler-Bernoulli beam with uniform section shown in Figure 1 is considered for modal analysis under temperature effect.

It is assumed that mass and constraint conditions remain unchanged and temperature only affects the geometry and mechanical properties. The undamped flexural vibration frequency of order n for beam structure can be calculated by [24–27]

$$f_n = \frac{n^2 \pi h}{2l^2} \sqrt{\frac{E}{12\rho}}, \quad (1)$$

where l and h are the length and height of beam, respectively. ρ is material density and E is elastic modulus.

According to variational principles [28], it can be obtained that

$$\begin{aligned} \delta f_n = & (\delta h) \frac{n^2 \pi}{2l^2} \sqrt{\frac{E}{12\rho}} + (-2l^{-3} \cdot \delta l) \frac{n^2 \pi h}{2} \sqrt{\frac{E}{12\rho}} \\ & + \left(\frac{1}{2} E^{-1/2} \cdot \delta E \right) \frac{n^2 \pi h}{2l^2} \sqrt{\frac{1}{12\rho}} \\ & + \left(-\frac{1}{2} \rho^{-3/2} \cdot \delta \rho \right) \frac{n^2 \pi h}{2l^2} \sqrt{\frac{E}{12}}, \end{aligned} \quad (2)$$

where δ represents an increment in the corresponding parameters.

Therefore, it can be furtherly derived that

$$\begin{aligned} \frac{\delta f_n}{f_n} &= \frac{\delta f_n}{((n^2 \pi h / 2l^2) \sqrt{E / 12\rho})} \\ &= \frac{\delta h}{h} - 2 \frac{\delta l}{l} + \frac{1}{2} \frac{\delta E}{E} - \frac{1}{2} \frac{\delta \rho}{\rho}. \end{aligned} \quad (3)$$

TABLE 1: Temperature-elastic modulus data obtained by Shoukry et al. [23].

Temperature (°C)	-20	-10	0	10	20
Elastic modulus ($\times 10^{10}$ Pa)	2.937	2.855	2.744	2.703	2.523

Assuming that the thermal coefficient of linear expansion of the material is θ_t and the temperature coefficient of modulus is θ_E , it can be obtained that

$$\begin{aligned} \frac{\delta h}{h} &= \theta_t \delta t, & \frac{\delta l}{l} &= \theta_t \delta t, \\ \frac{\delta \rho}{\rho} &= -3\theta_t \delta t, & \frac{\delta E}{E} &= \theta_E \delta t. \end{aligned} \quad (4)$$

Here we assume that the variation of modulus with temperature is linear for small changes in temperature. Consider the following:

$$\frac{\delta f_n}{f_n} = \frac{1}{2} (\theta_t + \theta_E) \delta t. \quad (5)$$

It can be seen from (5) that $\theta_t \approx 1.0 \times 10^{-5}/^\circ\text{C}$ and $\theta_E \approx -4.5 \times 10^{-3}/^\circ\text{C}$ for concrete under 100°C , $\theta_E \gg \theta_t$ [25]. Therefore, modulus of concrete is the main factor altering the modal frequency.

In above calculation, constraint condition is not considered. The axial force exerted on both ends of the beam is

$$F = \frac{1}{2} \mu mg, \quad (6)$$

where μ is the friction coefficient and mg is weight of the beam.

According to modal analysis, natural frequency of beam under axial force can be calculated by

$$f'_n = f_n \sqrt{1 + \frac{Fl^2}{n^2 \pi^2 EI}}, \quad (7)$$

where I is moment of inertia. Assuming that $\mu = 0.5$, (7) can be transformed into

$$f'_n = \omega_n \sqrt{1 + \frac{mgl^2}{4n^2 \pi^2 EI}} = f_n \sqrt{1 + \frac{1}{n^2} \cdot \frac{mgl^2}{4\pi^2 EI}}, \quad (8)$$

where $mgl^2 \ll 4\pi^2 EI$, $\sqrt{1 + (1/n^2) \cdot (mgl^2/4\pi^2 EI)} \approx 1$, so constraint condition has little influence on modal frequency.

Through above theoretical analysis, we can obtain that temperature effect alters modal frequency mainly by changing the elastic modulus of concrete. Shoukry et al. [23] got the relationship between temperature and modulus by laboratory tests which are listed in Table 1. Based on the research results, an ANFIS-based temperature effect elimination method is proposed.

2.2. Adaptive Network-Based Fuzzy Inference System (ANFIS). Taking the fuzzy inference system with two inputs (x, y) and one output, for example, the if-then rules are listed as follows [20].

Rule 1: if x is A_1 and y is B_1 , then $f_1 = p_1 \cdot x + q_1 \cdot y + r_1$.

Rule 2: if x is A_2 and y is B_2 , then $f_2 = p_2 \cdot x + q_2 \cdot y + r_2$, where x, y are input variables for nodes, symbols A_1, A_2, B_1 , and B_2 are linguistic expressions, f_1 and f_2 are output variables and $p_1, q_1, r_1, p_2, q_2, r_2$ are parameters.

The fuzzy inference mechanism of Sugeno model is shown in Figure 2, and the equivalent structure for ANFIS is shown in Figure 3. The same membership functions are adopted, and the output for i th node at l th layer is represented by $O_{l,i}$.

Layer 1: every node i in this layer has a corresponding node function.

$$\begin{aligned} O_{1,i} &= \mu_{A_i}(x), \quad i = 1, 2, \\ O_{1,i} &= \mu_{B_{i-2}}(y), \quad i = 3, 4, \end{aligned} \quad (9)$$

where symbols A, B are linguistic expressions (such as “small” or “large”). $O_{1,i}$ is membership degree for fuzzy set $A = (A_1, A_2, B_1, B_2)$; it specifies the degree to which the given inputs x and y satisfy the quantifier A . $\mu(x)$ is membership function which can be Bell, Sigmoid, or other related functions.

Layer 2: nodes in this layer are all fixed nodes represented by Π , and the output is the product of all inputs. Consider the following:

$$O_{2,i} = \omega_{A_i}(x) \mu_{B_i}(y), \quad i = 1, 2. \quad (10)$$

Output of each node represents the incentive intensity for one rule. Generally, the node function can be T -Norms operators.

Layer 3: nodes in this layer are all fixed nodes represented by N . The i th node is used for getting the normalized incentive intensity. Consider the following:

$$O_{3,i} = \bar{\omega} = \frac{\omega_i}{\omega_1 + \omega_2}, \quad i = 1, 2. \quad (11)$$

Layer 4: nodes in this layer are adaptive nodes with corresponding function. Consider the following:

$$O_{4,i} = \bar{\omega} \times f_i = \bar{\omega} \times (p_i x + q_i y + r_i), \quad i = 1, 2, \quad (12)$$

where $\bar{\omega}$ are normalized incentive intensity calculated by (11) and $\{p_i, q_i, r_i\}$ are parameters.

Layer 5: this layer is with only one node and labeled by Σ , which is used to calculate the transferred message and acts as the overall output.

$$\text{Overall output} = O_{5,i} = \sum \bar{\omega}_i \times f_i = \frac{\sum_i \bar{\omega}_i \times f_i}{\sum_i \bar{\omega}_i}. \quad (13)$$

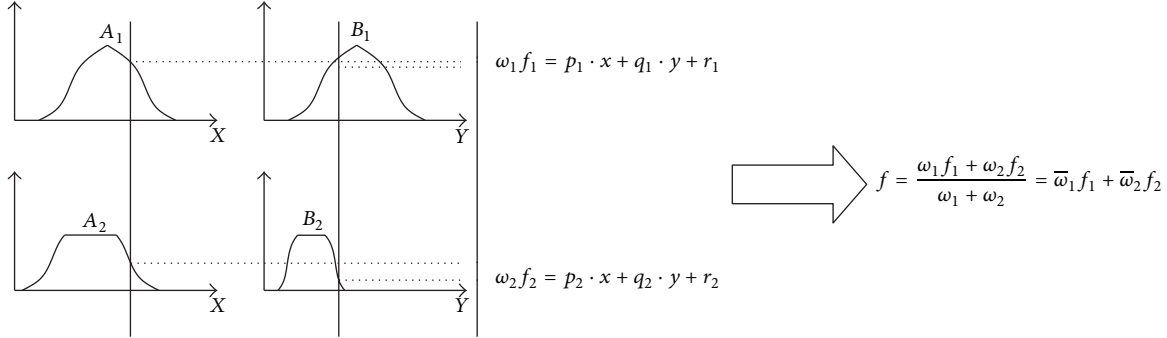


FIGURE 2: One-order Sugeno model with two rules and inputs.

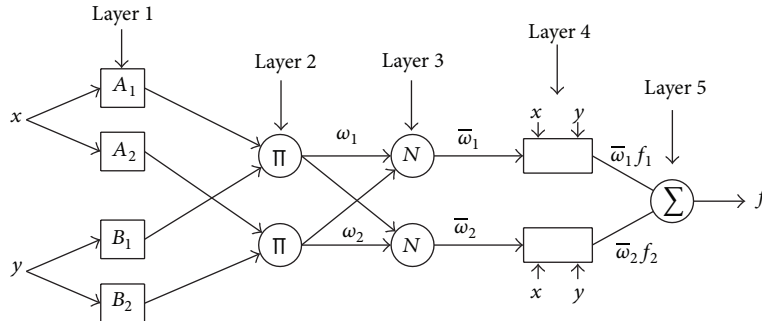


FIGURE 3: Basic structure of ANFIS.

2.3. Uniform Load Surface (ULS). The modal flexibility matrix can be calculated by (14) based on natural frequencies and mode shapes [21]. Consider the following:

$$f_{i,j} = \sum_{k=1}^m \frac{\phi^k(i)\phi^k(j)}{\omega_k^2}, \quad (14)$$

where ϕ is mass normalized mode shape vector, ω is natural frequency, k is the order of modal data, i and j are node numbers, m is the totally orders needed for calculation of modal flexibility matrix. It can be seen from (14) that the modal contribution to flexibility matrix decreases rapidly as the frequencies increase, so the flexibility matrix converges rapidly as the number of contributing lower modes increases. It reveals that an approximation of flexibility matrix can be obtained through several lower modes.

The deflection vector $\{\bar{f}\}$ under uniform load which is called the uniform load surface [27] can be calculated by

$$\{\bar{f}\} = \begin{bmatrix} f_{11} & f_{12} & \dots & f_{1n} \\ f_{21} & f_{22} & \dots & f_{2n} \\ \vdots & \vdots & \ddots & \vdots \\ f_{n1} & f_{n2} & \dots & f_{nn} \end{bmatrix} \begin{Bmatrix} 1 \\ 1 \\ \vdots \\ 1 \end{Bmatrix}, \quad (15)$$

where

$$\begin{aligned} \bar{f}(i) &= \sum_{j=1}^n f_{i,j} = \sum_{j=1}^n \left(\sum_{k=1}^m \frac{\phi^k(i)\phi^k(j)}{\omega_k^2} \right) \\ &= \sum_{k=1}^m \frac{\phi^k(i) \sum_{j=1}^n \phi^k(j)}{\omega_k^2}. \end{aligned} \quad (16)$$

Uniform load surface curvature (ULSC) can be obtained by the second order differential of $\{\bar{f}\}$, as shown in the following equation:

$$\text{ULSC} = \frac{\bar{f}(i+1) + \bar{f}(i-1) - 2 \times \bar{f}(i)}{l^2}, \quad (17)$$

where l is the element length.

The uniform load surface curvature difference (ULSCD) can be calculated by

$$\text{ULSCD} = \text{ULSC}^d - \text{ULSC}^u, \quad (18)$$

where ULSC^u , ULSC^d are the uniform load surface curvatures before and after damage, respectively.

Numerical simulation is conducted for a simply supported beam with rectangular cross-section in order to verify the effectiveness of ULS parameters. The length (L) is 9.0 m; the width (B) and height (H) of cross-section are 0.6 m and 1.0 m, respectively. The material is concrete with the compressive strength of 30 MPa and density of 2500 kg/m³. Finite element model is constructed by ANSYS; it includes 15 elements and 16 nodes with element length of 0.6 m (Figure 4).

The damage severity of structure is represented by reduction in the element stiffness and it can be defined by

$$D = \frac{(E^u - E^d)}{E^u}, \quad (19)$$

where D represents the damage severity of elements, E is Young's modulus of the bridge material, and the superscripts

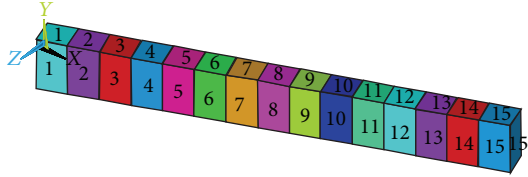


FIGURE 4: Finite element simulation for simply supported bridge with uniform section.

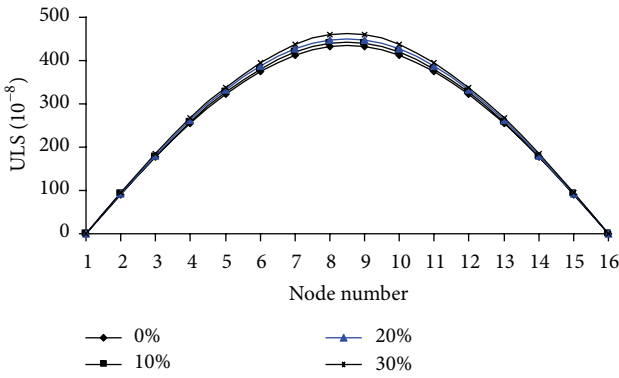


FIGURE 5: Relationship between ULS index and damage severity.

u and d represent undamaged and damaged elements, respectively.

Taking the damage identification of element 8 with damage severity of 0%, 10%, 20%, and 30% at temperature 30°C, for example, the ULS, ULSC, and ULSCD parameters can be calculated by (15)~(18); they are shown in Figures 5, 6, and 7.

As can be seen from Figures 5~7, ULS parameter can be used to identify the damage occurrence, while ULSC and ULSCD can localize the damage, and ULSCD possesses better effect.

3. Numerical Simulation for Damage Identification Based on ANFIS

3.1. Damage Identification Process and Characteristic Parameters. The specific calculation process for ANFIS-based damage identification is shown in Figure 8.

The normalized temperature and ULSCD parameters are selected as input variables of ANFIS, while damage severity of element is output one. Consider the following:

$$\text{Input} = \{\bar{T}, \overline{\text{ULSCD}}_1, \overline{\text{ULSCD}}_2, \dots, \overline{\text{ULSCD}}_n\}, \quad (20)$$

where $\overline{\text{ULSCD}}_i$ is normalized ULSCD vector and \bar{T} is normalized temperature vector.

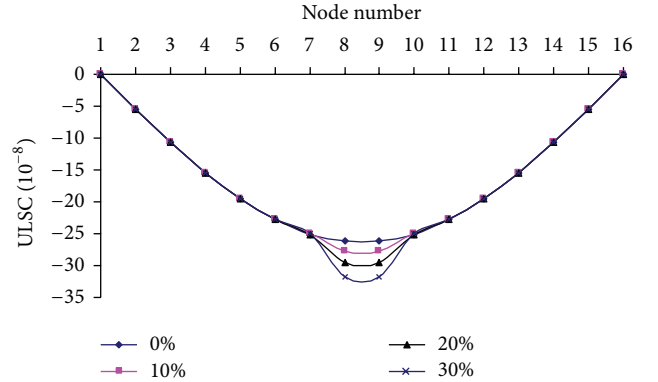


FIGURE 6: Relationship between ULSC and damage severity.

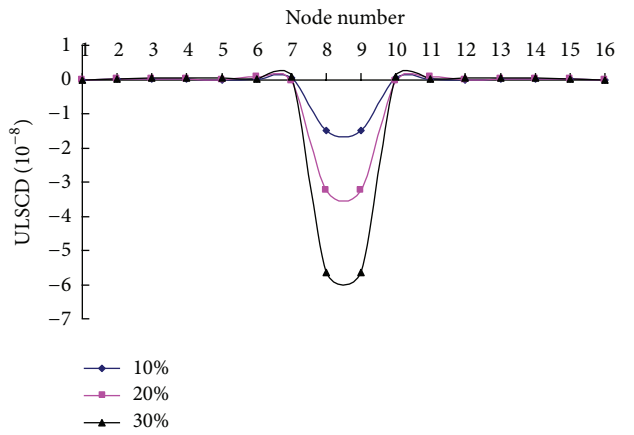


FIGURE 7: Relationship between ULSCD and damage severity.

Taking the damage identification of element 8, for example, its input variable can be represented by

$$\text{Input} = \{\bar{T}, \overline{\text{ULSCD}}_8\}. \quad (21)$$

Membership function for input variable is Gauss type; ANFIS can be initialized by fuzzy-C clustering. The ANFIS structure used in this paper is shown in Figure 9.

3.2. ANFIS-Based Damage Assessment under Temperature Effect. In order to determine the parameters of ANFIS, certain numbers of training samples are needed to realize the adjustment and optimization. 15 samples listed in Table 2 are selected for training and forming the ANFIS structure.

A hybrid learning algorithm based on back propagation and least squares is used for training, which can adjust the premise and conclusion parameters and produce if-then rule base automatically.

ANFIS can achieve adaptive adjustment of membership functions. The same initial function is adopted for input and output variables; it is shown in Figure 10.

The membership functions for input variables (\bar{T} and $\overline{\text{ULSCD}}_8$) after training are shown in Figures 11 and 12.

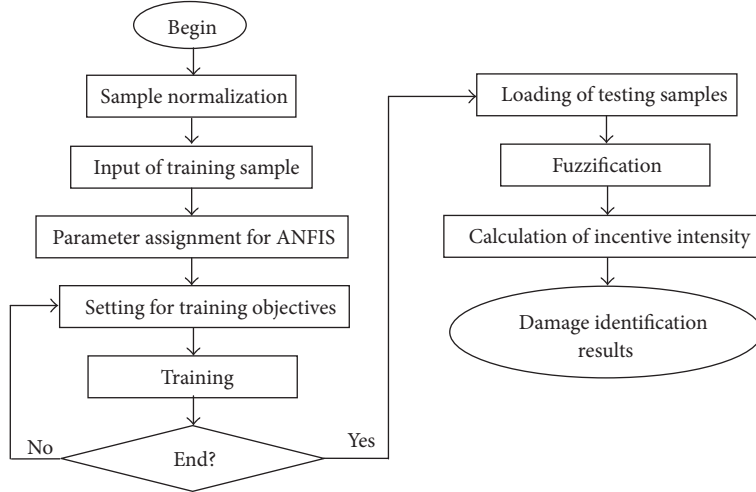


FIGURE 8: Damage identification process of ANFIS.

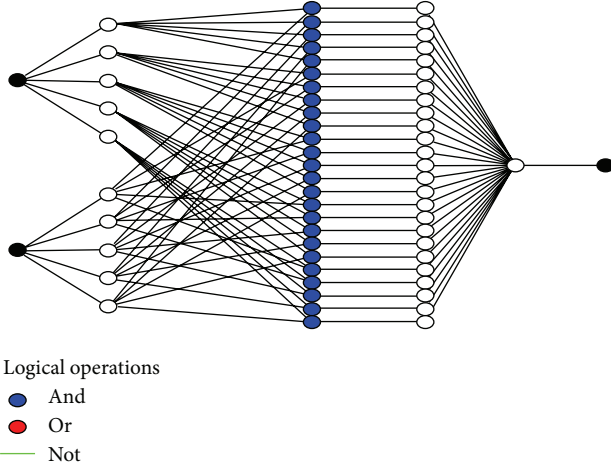


FIGURE 9: Structure for damage identification of ANFIS.

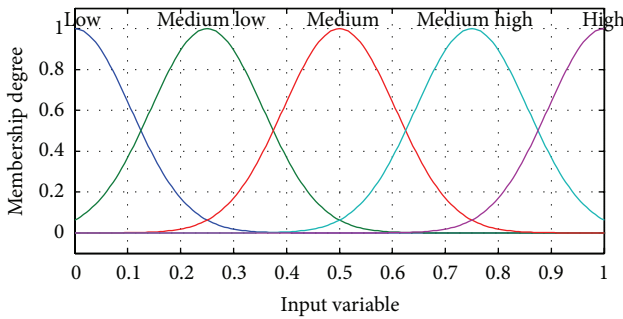


FIGURE 10: Membership function of input variables before training.

Test samples are constructed to verify the feasibility of ANFIS. The test samples and corresponding identification results are listed in Table 3.

As can be seen from Table 3, the proposed method in this paper can effectively identify the damage condition of bridge.

TABLE 2: Cases for training.

Temperature (°C)	Damage severity	ULSCD ₈ (10 ⁻⁸)	Damage condition
-20	10%	-1.3097	Slight damage
	20%	-2.8716	Moderate damage
	30%	-4.9760	Severe damage
-10	10%	-1.3488	Slight damage
	20%	-2.9618	Moderate damage
	30%	-5.1336	Severe damage
0	10%	-1.4048	Slight damage
	20%	-3.0803	Moderate damage
	30%	-5.3394	Severe damage
10	10%	-1.4256	Slight damage
	20%	-3.1265	Moderate damage
	30%	-5.4208	Severe damage
20	10%	-1.5260	Slight damage
	20%	-3.3502	Moderate damage
	30%	-5.8044	Severe damage

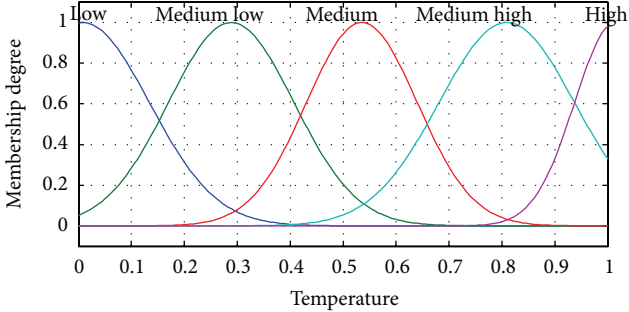
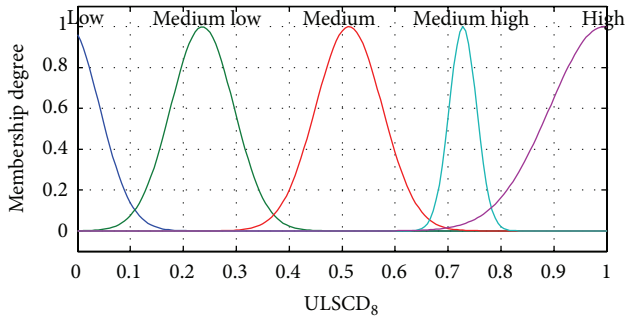
It reveals that ANFIS can realize the adaptive identification and possesses favorable accuracy.

4. Comparative Analysis between ANFIS and BP Networks

4.1. Damage Identification Based on BP Networks under Temperature Effect. Changes of frequencies are used as damage identification parameters; it can be calculated by

$$\Delta\omega_i = \omega^u - \omega^d, \quad (22)$$

where ω^u and ω^d are natural frequencies before and after damage, respectively.

FIGURE 11: Membership function of \bar{T} after training.FIGURE 12: Membership function of $\bar{\text{ULSCD}}_8$ after training.

The input variable for BP neural networks is shown in the following equation:

$$\text{Input} = \{T, \Delta\omega_1, \Delta\omega_2, \Delta\omega_3, \Delta\omega_4\}. \quad (23)$$

Under the temperatures -20°C , -10°C , 0°C , 10°C , and 20°C , damage severity of 5%, 10%, 15%, and 20% for each element of 4, 6, and 8 is selected as training samples, while 7%, 12%, and 18% are test samples. The identification results are listed in Table 4.

The maximum relative error for BP neural networks-based damage assessment is 5.17%; the identification results are satisfactory.

4.2. Comparison of Identification Accuracy between ANFIS and BP. Comparative analysis is conducted in order to compare the superiority between BP-frequency and ANFIS-ULS-based methods. A similarity calculation formula is constructed to conduct evaluation considering the dimension difference between two methods. Consider the following:

$$d(R^E, R^A) = \sqrt{\frac{\sum_{i=1}^n [(R_i^E - R_i^A)/R_i^E]^2}{n}}, \quad (24)$$

where R^E and R^A are the expected and actual outputs of damage identification, respectively. $d(R^E, R^A)$ represents the distance between R^E and R^A . The bigger the $d(R^E, R^A)$ is, the lower the relevance between R^E and R^A is. n is the number of test samples.

According to (24) and Tables 3 and 4, the similarities are calculated for the identification results of BP and ANFIS.

TABLE 3: Cases for testing and identification results of ANFIS.

Temperature ($^{\circ}\text{C}$)	Damage severity	$\text{ULSCD}_8 (10^{-8})$	Expected outputs	Actual results
-20	12%	-1.61	1	1.03
-10	18%	-2.63	2	1.95
0	8%	-1.09	1	0.98
10	27%	-4.70	3	3.04
20	23%	-4.06	2	2.05
-8	10%	-1.41	1	1.05
16	19%	-3.10	2	1.97

TABLE 4: Damage severity identification based on frequency and neural network.

Damaged elements	Damage severity (%)	Temperature ($^{\circ}\text{C}$)	Identification results (%)	Relative error (%)
4	7	10	7.11	1.57
		20	6.79	3.00
	12	10	12.21	1.75
		20	12.32	2.67
	18	10	18.32	1.78
		20	17.68	1.78
	7	10	7.31	4.43
		20	7.24	3.43
6	12	10	11.56	3.67
		20	11.58	3.50
	18	10	17.28	4.00
		20	18.26	1.44
	8	10	7.18	2.57
		20	7.23	3.29
		12	11.69	2.58
		20	12.62	5.17
	18	10	18.55	3.06
		20	18.82	4.56

$d(R^E, R^A)_{\text{BP}} = 0.032$, $d(R^E, R^A)_{\text{ANFIS}} = 0.028$, and $d(R^E, R^A)_{\text{ANFIS}} < d(R^E, R^A)_{\text{BP}}$. Therefore, the identification results of ANFIS are more relevant to the expected results. It reveals that ANFIS possesses more favorable accuracy.

5. Conclusions

Temperature effect can cause abnormal changes of modal parameters, which will lead to incorrect damage identification results. This paper presents an effective strategy for eliminating temperature effect in damage identification of bridge. ANFIS combines the advantages of neural networks and fuzzy inference system, which is used as damage identification algorithm. ULS, ULSC, and ULSCD are proved to localize damage locations accurately; ULSCD possesses more favorable effect. Therefore, temperature and ULSCD are treated as input variables of ANFIS for the damage assessment. In numerical simulation, elastic modulus of concrete

is assumed to be temperature dependent; 15 samples are used for training and constructing ANFIS structure. Numerical simulation results reveal that the proposed method can effectively identify the damage condition of test samples. Comparative analysis is conducted for comparing the superiority between BP and ANFIS. A similarity calculation formula is constructed for evaluation, and the comparative analysis reveals that ANFIS results are more relevant to actual situation. It means that the proposed method in this paper possesses more favorable accuracy than BP network.

Considering the complexity of damage identification of bridge under temperature effect, the damage identification with more samples and damaged elements should be conducted in the future.

Conflict of Interests

The authors declare that there is no conflict of interests regarding the publication of this paper.

Acknowledgments

The authors express their appreciation for the financial support of National Natural Science Foundation of China under Grant nos. 51378236 and 51278222 and “985 Project” of Jilin University.

References

- [1] K. Dems and Z. Mróz, “Damage identification using modal, static and thermographic analysis with additional control parameters,” *Computers & Structures*, vol. 88, no. 21–22, pp. 1254–1264, 2010.
- [2] A. D. Orcesi and D. M. Frangopol, “Optimization of bridge maintenance strategies based on structural health monitoring information,” *Structural Safety*, vol. 33, no. 1, pp. 26–41, 2011.
- [3] J. M. Ko and Y. Q. Ni, “Technology developments in structural health monitoring of large-scale bridges,” *Engineering Structures*, vol. 27, no. 12, pp. 1715–1725, 2005.
- [4] L. A. Overby and M. D. Todd, “Effects of noise on transfer entropy estimation for damage detection,” *Mechanical Systems and Signal Processing*, vol. 23, no. 7, pp. 2178–2191, 2009.
- [5] K. Zhang, H. Li, Z. D. Duan, and S. S. Law, “A probabilistic damage identification approach for structures with uncertainties under unknown input,” *Mechanical Systems and Signal Processing*, vol. 25, no. 4, pp. 1126–1145, 2011.
- [6] H. P. Chen, “Application of regularization methods to damage detection in large scale plane frame structures using incomplete noisy modal data,” *Engineering Structures*, vol. 30, no. 11, pp. 3219–3227, 2008.
- [7] H. Sohn, K. Worden, and C. F. Farrar, “Novelty detection under changing environmental conditions,” in *Smart Structures and Materials 2001: Smart Systems for Bridges, Structures, and Highways*, vol. 4330 of *Proceedings of SPIE*, pp. 108–118, Newport Beach, Calif, USA, March 2001.
- [8] Y. Q. Ni, X. G. Hua, K. Q. Fan, and J. M. Ko, “Correlating modal properties with temperature using long-term monitoring data and support vector machine technique,” *Engineering Structures*, vol. 27, no. 12, pp. 1762–1773, 2005.
- [9] M. A. Wahab and G. de Roeck, “Effect of temperature on dynamic system parameters of a highway bridge,” *Structural Engineering International*, vol. 7, no. 4, pp. 266–270, 1997.
- [10] C. Farrar, S. Doebling, P. Cornwell, and E. Straser, “Variability of modal parameters measured on the Alamosa Canyon Bridge,” in *International Society for Optical Engineering*, vol. 3089 of *Proceedings of SPIE*, pp. 257–263, Orlando, Fla, USA, February 1997.
- [11] H. F. Zhou, Y. Q. Ni, and J. M. Ko, “Constructing input to neural networks for modeling temperature-caused modal variability: mean temperatures, effective temperatures, and principal components of temperatures,” *Engineering Structures*, vol. 32, no. 6, pp. 1747–1759, 2010.
- [12] P. Moser and B. Moaveni, “Environmental effects on the identified natural frequencies of the Dowling Hall Footbridge,” *Mechanical Systems and Signal Processing*, vol. 25, no. 7, pp. 2336–2357, 2011.
- [13] B. Peeters and G. D. Roeck, “One-year monitoring of the Z24-Bridge: environmental effects versus damage events,” *Earthquake Engineering & Structural Dynamics*, vol. 30, no. 2, pp. 149–171, 2001.
- [14] H. Sohn, M. Dzwonczyk, E. G. Straser, A. S. Kiremidjian, K. Law, and T. Meng, “An experimental study of temperature effect on modal parameters of the Alamosa Canyon Bridge,” *Earthquake Engineering & Structural Dynamics*, vol. 28, no. 7–8, pp. 879–897, 1999.
- [15] B. Peeters, J. Maeck, and G. D. Roeck, “Vibration-based damage detection in civil engineering: excitation sources and temperature effects,” *Smart Materials and Structures*, vol. 10, no. 3, pp. 518–527, 2001.
- [16] A. Yan, G. Kerschen, P. D. Boe, and J. Golinval, “Structural damage diagnosis under varying environmental conditions—part I: a linear analysis,” *Mechanical Systems and Signal Processing*, vol. 19, no. 4, pp. 847–864, 2005.
- [17] J. Kullaa, “Elimination of environmental influences from damage-sensitive features in a structural health monitoring system,” in *Structural Health Monitoring—The Demands and Challenges*, pp. 742–749, CRC Press, Palo Alto, Calif, USA, 2001.
- [18] A. M. Yan, G. Kerschen, P. D. Boe, and J.-C. Golinval, “Structural damage diagnosis under varying environmental conditions—part II: local PCA for non-linear cases,” *Mechanical Systems and Signal Processing*, vol. 19, no. 4, pp. 865–880, 2005.
- [19] V. Meruane and W. Heylen, “Structural damage assessment under varying temperature conditions,” *Structural Health Monitoring*, vol. 11, no. 3, pp. 345–357, 2012.
- [20] R. Singh, A. Kainthola, and T. N. Singh, “Estimation of elastic constant of rocks using an ANFIS approach,” *Applied Soft Computing*, vol. 12, no. 1, pp. 40–45, 2012.
- [21] Z. Zhang and A. E. Aktan, “Application of modal flexibility and its derivatives in structural identification,” *Research in Nondestructive Evaluation*, vol. 10, no. 1, pp. 43–61, 1998.
- [22] T. Pham, *The influence of thermal effects on structural health monitoring of Attridge Drive Overpass [M.S. thesis]*, Department of Civil Engineering, University of Saskatchewan, Saskatchewan, Canada, 2009.
- [23] S. N. Shoukry, G. W. William, B. Downie, and M. Y. Riad, “Effect of moisture and temperature on the mechanical properties of concrete,” *Construction and Building Materials*, vol. 25, no. 2, pp. 688–696, 2011.
- [24] R. W. Clough and J. Penzien, *Dynamics of Structure*, McGraw-Hill, New York, NY, USA, 2nd edition, 1993.

- [25] Y. Xia, H. Hao, G. Zanardo, and A. Deeks, “Long term vibration monitoring of an RC slab: temperature and humidity effect,” *Engineering Structures*, vol. 28, no. 3, pp. 441–452, 2006.
- [26] R. D. Adams, P. Cawley, C. J. Pye, and B. J. Stone, “A vibration technique for nondestructively assessing the integrity of structures,” *Journal of Mechanical Engineering Science*, vol. 20, no. 2, pp. 93–100, 1978.
- [27] R. D. Blevins, *Formulas for Natural Frequency and Mode Shape*, Van Nostrand Reinhold, New York, NY, USA, 1979.
- [28] C. Lanczos, *The Variational Principles of Mechanics*, Dover, New York, NY, USA, 4th edition, 1986.

Research Article

Seismic-Parameter-Based Statistical Procedures for the Approximate Assessment of Structural Damage

A. Elenas

Department of Civil Engineering, Institute of Structural Mechanics and Earthquake Engineering, Democritus University of Thrace, Vas. Sofias 12, 67100 Xanthi, Greece

Correspondence should be addressed to A. Elenas; elenas@civil.duth.gr

Received 9 August 2013; Revised 2 January 2014; Accepted 6 January 2014; Published 23 February 2014

Academic Editor: Yuri Petryna

Copyright © 2014 A. Elenas. This is an open access article distributed under the Creative Commons Attribution License, which permits unrestricted use, distribution, and reproduction in any medium, provided the original work is properly cited.

This study describes two statistical methodologies to estimate the postseismic damage status of structures based on seismic parameters as novel combined procedures in earthquake engineering. Thus, a multilinear regression analysis and discriminant analysis are utilized considering twenty seismic parameters. Overall damage indices describe the postseismic damage status. Nonlinear dynamic analyses furnish the damage indices, which are considered as exact indices and references for the subsequent study. The aim is to approximate the postseismic damage indices or the damage grade of buildings using statistical methods, thus avoiding complex nonlinear dynamic analyses. The multilinear regression procedure evaluates the damage indices explicitly, and the discriminant analysis furnishes the damage grade of the structures. The proposed methods are applied to a frame structure. A set of 400 natural accelerograms is used for the training phase of the models. The quality of the models is tested initially by the same set of natural accelerograms and then by a blind prediction using a second set of synthetic accelerograms. The results of both proposed methods have shown a correct classification percentage ranging from 87.75% to 97.50% and from 70% to 90% for the sets of the natural and synthetic accelerograms, respectively.

1. Introduction

Several seismic parameters have been presented in the literature during the last several decades. These parameters can be used to express the intensity of the seismic excitations and to simplify their description. Postseismic field observations and numerical investigations have indicated the interdependency between the seismic parameters and damage status of buildings after earthquakes [1, 2]. The latter can be expressed by proper damage indices, whereas the interdependency between the considered quantities can be quantified numerically by appropriate correlation coefficients.

This paper expands on the above, providing alternative statistical procedures for the approximate assessment of the structural Postseismic damage grade. Thus, the first step in the proposed new methodology is to choose a set of seismic parameters that represents the properties of the accelerograms. Next, the intensity parameters chosen in the first step are evaluated for a set of natural or artificial accelerograms. The damage indices for all considered accelerograms are

subsequently calculated for the building of interest. Statistical analyses are applied to the resulting data from the previous steps to extract a statistical model for the prediction of the Postseismic damage status of structures. Finally, the new methodology is verified by a blind prediction.

As mentioned previously, the proposed statistical methods are used to estimate the Postseismic structural damage status. Approximation methods are well known and broadly used in earthquake engineering. The evaluation of the fundamental period of a building from its geometric dimensions is such an approximation provided by several antiseismic codes. Thus, the fundamental period can be approximated using a simple formula depending on the type of structure (e.g., steel, reinforced concrete, masonry, frame, or wall) and the geometric dimensions of the examined building instead of needing to solve a complicated eigenvalue problem that depends on mass and stiffness matrices.

The proposed methodologies can be used, for instance, by public authorities for a quick and accurate estimation of the Postseismic damage status or for estimating damage

scenarios for specific buildings. The proposed techniques are simpler to apply than the more complicated and time-consuming nonlinear dynamic analyses. The novel application of the proposed statistical procedures in the specific field of earthquake engineering is also feasible for nonspecialists, in contrast to nonlinear dynamic analyses, which can only be performed by expert engineers.

2. Seismic Intensity Parameters

In general, the intensity parameters can be classified into peak, spectral, and energy parameters. Twenty parameters have been selected to represent the seismic excitation. They have been chosen from all three seismic parameter categories. The following seismic parameters are considered: peak ground acceleration (PGA); peak ground velocity (PGV); the ratio PGA/PGV; Arias' intensity (I_0); root mean square acceleration (RMS_a); the strong motion duration of Trifunac/Brady ($T_{0.90}$); seismic power ($P_{0.90}$); the spectral intensities of Housner (SI_H), Kappos (SI_K), and Martinez-Rueda (SI_{MR}); effective peak acceleration (EPA); maximum effective peak acceleration (EPA_{max}); seismic energy input (E_{inp}); cumulative absolute velocity (CAV); the seismic damage potential of Araya/Saragoni (DP_{A/S}); central period (CP); spectral acceleration (SA); spectral velocity (SV); spectral displacement (SD); and the intensity of Fajfar/Vidic/Fischinger ($I_{F/V/F}$). Table 1 provides an overview of the used parameters and the literature references.

The Arias intensity [3] is a measure of the total energy content of seismic excitation and is defined by the following relation:

$$I_0 = \frac{\pi}{2g} \int_0^{t_e} (\ddot{x})^2 dt. \quad (1)$$

Here, I_0 is the Arias intensity, t_e is the total seismic duration, and \ddot{x} is the seismic ground acceleration.

The root mean square acceleration RMS_a [4] is a measure of the mean energy content calculated by the following relation:

$$RMS_a = \sqrt{\frac{1}{t_e} \int_0^{t_e} (\ddot{x})^2 dt}. \quad (2)$$

The Husid diagram [5] is the time history of the seismic energy content scaled to the total energy content. It is defined by the following relation:

$$H(t) = \frac{\int_0^t (\ddot{x})^2 dt}{\int_0^{t_e} (\ddot{x})^2 dt}, \quad (3)$$

where $H(t)$ is the Husid diagram as a function of time t .

The strong motion duration of Trifunac/Brady is defined as the time elapsed between 5% and 95% of the Husid diagram [6] and is defined by the following relation:

$$T_{0.90} = T_{0.95} - T_{0.05}, \quad (4)$$

where $T_{0.90}$ is the strong motion duration and $T_{0.95}$ and $T_{0.05}$ are the time elapsed at 95% and 5% of the Husid diagram, respectively.

TABLE 1: Seismic parameters.

Number	Seismic parameters	Reference
1	PGA	[4]
2	PGV	[4]
3	PGA/PGV	[4]
4	I_0	[3]
5	RMS _a	[4]
6	$T_{0.90}$	[6]
7	$P_{0.90}$	[7]
8	SI _H	[8]
9	SI _K	[9]
10	SI _{MR}	[10]
11	EPA	[11]
12	EPA _{max}	[11]
13	E_{inp}	[13]
14	CAV	[1]
15	DP _{A/S}	[14]
16	CP	[15]
17	SD	[17]
18	SV	[17]
19	SA	[17]
20	$I_{F/V/F}$	[18]

The power $P_{0.90}$ [7] is a measure of the energy content per time unit of the seismic excitation and is defined by the following relation:

$$P_{0.90} = \frac{H_{0.95} - H_{0.05}}{T_{0.90}}. \quad (5)$$

Here, $P_{0.90}$ is the power of the seismic excitation, $H_{0.95}$ and $H_{0.05}$ the nonnormalized energy level, at 95% and 5% of the Husid diagram, respectively, and $T_{0.90}$ is the strong motion duration of Trifunac/Brady.

According to Housner [8], the spectrum intensity is given by the relation

$$SI_H = \int_{0.1}^{2.5} PSV(T, \xi = 2\%) dT, \quad (6)$$

where PSV is the pseudovelocity curve, T is the natural period of a single-degree-of-freedom (SDOF) system, and ξ is the damping coefficient. In the present work, the integral in (6) is evaluated for a damping ratio equal to 2% of the critical damping, as recommended by Housner when he introduced this quantity [8]. However, it is now generally accepted that the Housner spectral intensity is valid for any level of damping (e.g., 5% of critical damping) [7].

In the definition of the spectrum intensity after Kappos [9]:

$$SI_K = \int_{T_n-t_1}^{T_n+t_2} PSV(T, \xi) dT, \quad (7)$$

the integration limits are dependent on the fundamental period of the structure T_n and the period intervals t_1 and t_2 . Kappos suggested $t_1 = t_2 = 0.2T_n$.

Martinez-Rueda [10] introduced a spectral intensity definition accounting for the dynamic properties of the structure which is defined as

$$\text{SI}_{\text{MR}} = \frac{1}{T_h - T_y} \int_{T_y}^{T_h} \text{PSV}(T, \xi) dT, \quad (8)$$

where T_h the hardening period and T_y is the yield period, which are computed using the tangent stiffness of the hardening branch and using the tangent stiffness after the appearance of the first plastic hinge of the idealized lateral response of the structure, respectively. The required idealized lateral response of the structure for the evaluation of T_h and T_y has been performed by a nonlinear pushover analysis as suggested by Martinez-Rueda [10].

The effective peak acceleration (EPA) [11, 12] is the average of the spectral ordinates of the elastic acceleration response spectrum (for 5% critical damping) in the period interval [0.1 s, 0.5 s], divided by a standard value 2.5. It is defined by the following relation:

$$\text{EPA} = \frac{\overline{\text{SA}}_{0.1s \div 0.5s}(\xi = 0.05)}{2.5}. \quad (9)$$

The maximum EPA (EPA_{\max}) is a variation of the EPA definition. Here, the period interval is not constant (as in the previous case from 0.1 to 0.5 s) but is a sliding window of 0.4 s, which sweeps the entire elastic acceleration response spectrum for 5% critical damping and provides the maximum of all possible EPA values calculated in this manner.

The input seismic energy [13] is defined by the following relation:

$$E_{\text{inp}} = m \int_0^{t_e} (\ddot{u} + \ddot{x}) \dot{x} dt. \quad (10)$$

Here, E_{inp} is the input seismic energy of a SDOF system, t_e is the total seismic duration, m is the mass, u is the displacement of the system relative to the ground, and x is the ground displacement.

The cumulative absolute velocity (CAV) [1] is defined as the area under the absolute accelerogram:

$$\text{CAV} = \int_0^{t_e} |\ddot{x}| dt. \quad (11)$$

Araya and Saragoni [14] introduced the destructiveness potential ($\text{DP}_{\text{A/S}}$) of a seismic excitation, defined as

$$\text{DP}_{\text{A/S}} = \frac{I_0}{\nu_0^2}, \quad (12)$$

where I_0 is the Arias intensity and ν_0 is the intensity of the seismic acceleration zero-crossings. ν_0 is defined as the number of intersections of the acceleration ordinates with the time axis (points with zero acceleration) per time unit in a seismic acceleration time-history (accelerogram).

The central period (CP) is the reciprocal value of the number of positive zero-crossings (points where the sign of the considered function changes from negative to positive) of the seismic acceleration per time unit [15]. The

CP is a frequency content indicator and not an authentic seismic intensity parameter. However, this parameter has been used to characterize the seismic damage potential of seismic excitations (together with the term PGA/PGV and the strong motion duration of Trifunac/Brady $T_{0.90}$) [16]. For this reason, the CP has been included in the set of the seismic intensity parameters used in the present study.

The response spectra describe the maximum response of a SDOF system to a particular input motion as a function of the natural period (or natural frequency) and the damping ratio of the SDOF system [17]. For each ground motion measurement there are displacement (SD), velocity (SV), and acceleration (SA) response spectra, respectively.

Finally, the seismic intensity of Fajfar/Vidic/Fischinger [18] is defined as

$$I_{\text{F/V/F}} = \nu_{\max}(T_{0.90})^{0.25}, \quad (13)$$

where ν_{\max} is the peak ground velocity (PGV) of the ground motion and $T_{0.90}$ is the strong motion duration of Trifunac/Brady.

3. Seismic Acceleration Time Histories

The expected damage potential of a seismic excitation on a particular structure is the prime consideration for the selection of the accelerograms for the presented methodology. Seismic excitations that generate a wide spectrum of damage, from negligible to severe, are considered for statistical reasons. Thus, the present investigation utilized 400 worldwide natural acceleration records with strong seismic activity. Table 2 provides data for all the utilized seismic events (event name, country, date, record station, component, and PGA). Figure 1 is a scatter plot of standard (Richter) magnitude versus epicentral distance of all utilised seismic excitations. Furthermore, Tables 3 and 4 provide the number of accelerograms used per country and per PGA range. All of the above-mentioned seismic acceleration time histories have been investigated by a computer-supported evaluation of their seismic parameters, as presented in the previous section and in Table 1.

The number of the used accelerograms is essential for the accuracy of the statistical models. In addition, the utilized accelerograms must generate a whole spectrum of damage (low, medium, large, and total) for statistical completeness. However, regional (locally possible) seismic records do not exist in sufficient quantity for most of the seismically active areas. Therefore, a set of worldwide natural acceleration records has been utilized for the present study. Alternatively, artificial accelerograms compatible with the design spectrum, combined with a scaling procedure (to generate a whole spectrum of damage), could be employed. In that case, the variability of the frequency content is limited.

4. Damage Indices

Among the many structural response parameters, attention is focused on those that can best describe seismic damage. The attention is focused on overall structural damage indices

TABLE 2: Data for the utilized seismic events.

Number	Seismic event	Country	Date	Station	Component	PGA (g)	Magnitude	Epicentral distance (km)
1	Long Beach	USA	10/3/1933	No. 288	S08W	0.131	6.4	38.1
2	Long Beach	USA	10/3/1933	No. 288	N82W	0.152	6.4	38.1
3	Long Beach	USA	10/3/1933	No. 131	NS	0.193	6.4	19.2
4	Long Beach	USA	10/3/1933	No. 331	EW	0.156	6.4	19.2
5	Long Beach	USA	10/3/1933	No. 136	N39E	0.100	6.4	45.2
6	Long Beach	USA	10/3/1933	No. 136	N51W	0.064	6.4	45.2
7	Lower California	USA	30/12/1934	No. 117	S00W	0.157	6.5	65.6
8	Lower California	USA	30/12/1934	No. 117	S90W	0.179	6.5	65.6
9	Helena Montana	USA	3/10/1935	No. 323	S00W	0.144	6.2	6.3
10	Helena Montana	USA	3/10/1935	No. 323	S90W	0.143	6.2	6.3
11	Imperial Valley	USA	18/5/1940	No. 117a	S00E	0.341	6.9	16.9
12	Imperial Valley	USA	18/5/1940	No. 117b	S00E	0.342	6.9	16.9
13	Imperial Valley	USA	18/5/1940	No. 117a	S90W	0.210	6.9	16.9
14	Imperial Valley	USA	18/5/1940	No. 117b	S90W	0.210	6.9	16.9
15	Santa Barbara	USA	30/6/1941	No. 283	N45E	0.234	5.5	14.9
16	Santa Barbara	USA	30/6/1941	No. 283	S45E	0.172	5.5	14.9
17	Northern California	USA	9/3/1949	No. 28	N89W	0.194	5.2	19.9
18	Puget Sound	USA	13/4/1949	Olympia	N176E	0.161	7.1	26.4
19	Puget Sound	USA	13/4/1949	Olympia	N266E	0.274	7.1	26.4
20	Western Washington	USA	13/4/1949	No. 325	N04W	0.162	7.1	17.0
21	Western Washington	USA	13/4/1949	No. 325	N86E	0.275	7.1	17.0
22	Kern County	USA	21/7/1952	No. 283	S48E	0.129	7.5	87.7
23	Kern County	USA	21/8/1952	No. 1095	N21E	0.152	7.5	46.4
24	Kern County	USA	21/8/1952	No. 1095	S69E	0.176	7.5	46.4
25	Eureka	USA	21/12/1954	89509	349	0.165	6.6	23.5
26	Eureka	USA	21/12/1954	89509	79	0.253	6.6	23.5
27	Eureka	USA	21/12/1954	No. 1022	79	0.149	6.6	35.0
28	Eureka	USA	21/12/1954	No. 1022	N46W	0.189	6.6	35.0
29	Eureka	USA	21/12/1954	No. 1023	N44E	0.156	6.6	39.7
30	Eureka	USA	21/12/1954	No. 1023	N46W	0.197	6.6	39.7
31	Southern California	USA	18/3/1957	No. 272	NS	0.163	4.7	6.3
32	Southern California	USA	18/3/1957	No. 272	EW	0.086	4.7	6.3
33	Hollister	USA	8/4/1961	No. 028	N89W	0.176	5.6	22.2
34	Hollister	USA	8/4/1961	No. 028	N89W	0.169	5.6	22.2
35	Hokkaido	Japan	23/4/1962	Kushiro Met.	EW	0.281	7.0	75.0
36	Hokkaido	Japan	23/4/1962	Kushiro Met.	NS	0.517	7.0	75.0
37	Niigata	Japan	16/6/1964	Niigata	NS	0.129	7.5	59.0
38	Niigata	Japan	16/6/1964	Niigata	EW	0.171	7.5	59.0
39	Ibaraki	Japan	14/11/1964	Atom. En. Res	NS	0.260	5.1	8.0
40	Suruga Bay	Japan	20/4/1965	Shimizu	EW	0.153	6.1	30.0
41	Puget Sound	USA	29/4/1965	Olympia	N176E	0.134	6.5	63.0
42	Puget Sound	USA	29/4/1965	Olympia	N266E	0.195	6.5	63.0
43	Puget Sound	USA	29/4/1965	No. 325	S04E	0.134	6.5	61.0
44	Puget Sound	USA	29/4/1965	No. 325	S86E	0.194	6.5	61.0
45	Etorofu	Japan	5/4/1966	Hoshina-A	EW	0.500	5.4	4.0
46	Parkfield California	USA	27/6/1966	No. 013	N65E	0.480	5.6	3.5
47	Parkfield California	USA	27/6/1966	No. 014	N05W	0.348	5.6	3.5
48	Parkfield California	USA	27/6/1966	No. 014	N85E	0.426	5.6	7.1

TABLE 2: Continued.

Number	Seismic event	Country	Date	Station	Component	PGA (g)	Magnitude	Epicentral distance (km)
49	Parkfield California	USA	27/6/1966	No. 015	N50E	0.233	5.6	7.1
50	Parkfield California	USA	27/6/1966	No. 015	N40W	0.270	5.6	11.2
51	Parkfield California	USA	27/6/1966	No. 097	N65W	0.264	5.6	11.2
52	Parkfield California	USA	27/6/1966	No. 097	S25W	0.341	5.6	12.0
53	Parkfield California	USA	27/6/1966	No. 014	N05W	0.348	5.6	12.0
54	Parkfield California	USA	27/6/1966	No. 014	N85E	0.426	5.6	14.0
55	Ariake	Japan	12/11/1966	Ariake	N40E	0.129	5.5	19.0
56	Ibaraki	Japan	19/11/1967	Atom. En. Res	NS	0.464	6.0	50.0
57	Ibaraki	Japan	19/11/1967	Atom. En. Res	EW	0.350	6.0	50.0
58	Wakayama	Japan	30/3/1968	Wakayama Harbor	NS	0.293	5.0	5.0
59	Wakayama	Japan	30/3/1968	Wakayama Harbor	EW	0.442	5.0	5.0
60	Hyuganada	Japan	1/4/1968	New Ind. City	NS	0.288	7.5	60.0
61	Hyuganada	Japan	1/4/1968	New Ind. City	EW	0.351	7.5	60.0
62	Honshu	Japan	16/5/1968	Muroran Harbor	EW	0.155	8.2	290.0
63	Honshu	Japan	16/5/1968	Shin-Ishikari B.	L	0.182	8.2	319.0
64	Honshu	Japan	16/5/1968	Shin-Ishikari B.	T	0.194	8.2	319.0
65	Honshu	Japan	16/5/1968	Horoman Bridge	L	0.126	8.2	159.0
66	Honshu	Japan	16/5/1968	Miyako Harbor	NS	0.165	8.2	187.0
67	Honshu	Japan	16/5/1968	Miyako Harbor	EW	0.158	8.2	187.0
68	Honshu	Japan	16/5/1968	Aomori Harbor	NS	0.227	8.2	243.0
69	Honshu	Japan	16/5/1968	Aomori Harbor	EW	0.197	8.2	243.0
70	Honshu	Japan	16/5/1968	Hachinohe Harbor	NS	0.312	8.2	187.0
71	Honshu	Japan	16/5/1968	Hachinohe Harbor	EW	0.206	8.2	187.0
72	Honshu	Japan	16/5/1968	Miyako Harbor	NS	0.155	8.2	226.0
73	Honshu	Japan	16/5/1968	Miyako Harbor	EW	0.124	8.2	226.0
74	Aomori Prefecture	Japan	23/5/1968	Miyako Harbor	NS	0.133	6.3	78.0
75	Aomori Prefecture	Japan	12/6/1968	Miyako Harbor	NS	0.190	7.2	81.0
76	Aomori Prefecture	Japan	12/6/1968	Miyako Harbor	EW	0.164	7.2	81.0
77	Saitama Prefecture	Japan	1/7/1968	Shinagawa	EW	0.127	6.1	58.0
78	Hokkaido	Japan	21/1/1970	Horoman Bridge	L	0.149	6.7	46.0
79	Hokkaido	Japan	21/1/1970	Horoman Bridge	T	0.215	6.7	46.0
80	Iwate Prefecture	Japan	1/4/1970	Miyako Harbor	NS	0.190	5.8	17.0
81	Iwate Prefecture	Japan	1/4/1970	Miyako Harbor	EW	0.162	5.8	17.0
82	Miyazaki Prefecture	Japan	26/7/1970	New Ind. City	EW	0.140	6.7	21.0
83	San Fernando	USA	9/2/1971	No. 279	S16E	1.148	6.6	6.7
84	San Fernando	USA	9/2/1971	No. 279	S74W	1.055	6.6	6.7
85	San Fernando	USA	9/2/1971	No. 151	N54W	0.123	6.6	41.5
86	San Fernando	USA	9/2/1971	No. 110	N21E	0.309	6.6	29.8
87	San Fernando	USA	9/2/1971	No. 110	N69W	0.265	6.6	29.8
88	San Fernando	USA	9/2/1971	No. 111	S00W	0.153	6.6	29.8
89	San Fernando	USA	9/2/1971	No. 135	S00W	0.167	6.6	34.8
90	San Fernando	USA	9/2/1971	No. 135	N90E	0.207	6.6	34.8
91	San Fernando	USA	9/2/1971	No. 217	S00W	0.147	6.6	38.6
92	San Fernando	USA	9/2/1971	No. 137	N50W	0.126	6.6	41.2
93	San Fernando	USA	9/2/1971	No. 137	S40W	0.169	6.6	41.2
94	San Fernando	USA	9/2/1971	No. 285	S51E	0.203	6.6	32.9
95	San Fernando	USA	9/2/1971	No. 285	S75W	0.174	6.6	32.9
96	San Fernando	USA	9/2/1971	No. 199	S00E	0.158	6.6	38.8

TABLE 2: Continued.

Number	Seismic event	Country	Date	Station	Component	PGA (g)	Magnitude	Epicentral distance (km)
97	San Fernando	USA	9/2/1971	No. 199	N90E	0.162	6.6	38.8
98	San Fernando	USA	9/2/1971	No. 122	S70E	0.266	6.6	31.0
99	San Fernando	USA	9/2/1971	No. 122	S20W	0.209	6.6	31.0
100	San Fernando	USA	9/2/1971	No. 166	S53E	0.236	6.6	41.2
101	San Fernando	USA	9/2/1971	No. 166	S37W	0.192	6.6	41.2
102	San Fernando	USA	9/2/1971	No. 416	EW	0.162	6.6	36.6
103	San Fernando	USA	9/2/1971	No. 148	N37E	0.196	6.6	39.9
104	San Fernando	USA	9/2/1971	No. 148	S53E	0.188	6.6	39.9
105	San Fernando	USA	9/2/1971	No. 160	N30W	0.242	6.6	40.9
106	San Fernando	USA	9/2/1971	No. 160	S60W	0.221	6.6	40.9
107	San Fernando	USA	9/2/1971	No. 211	NS	0.154	6.6	38.8
108	San Fernando	USA	9/2/1971	No. 211	EW	0.130	6.6	38.8
109	San Fernando	USA	9/2/1971	No. 266	S90W	0.189	6.6	34.9
110	San Fernando	USA	9/2/1971	No. 264	NOOE	0.198	6.6	38.1
111	San Fernando	USA	9/2/1971	No. 264	N90E	0.182	6.6	38.1
112	San Fernando	USA	9/2/1971	No. 267	S82E	0.208	6.6	30.7
113	San Fernando	USA	9/2/1971	No. 267	S08W	0.139	6.6	30.7
114	San Fernando	USA	9/2/1971	No. 466	N11E	0.220	6.6	28.3
115	San Fernando	USA	9/2/1971	No. 466	N79W	0.146	6.6	28.3
116	San Fernando	USA	9/2/1971	No. 461	S81E	0.140	6.6	27.6
117	San Fernando	USA	9/2/1971	No. 461	S09W	0.129	6.6	27.6
118	San Fernando	USA	9/2/1971	No. 126	S69E	0.168	6.6	27.6
119	San Fernando	USA	9/2/1971	No. 126	S21W	0.144	6.6	27.6
120	San Fernando	USA	9/2/1971	No. 128	N21E	0.346	6.6	23.9
121	San Fernando	USA	9/2/1971	No. 128	N69W	0.277	6.6	23.9
122	San Fernando	USA	9/2/1971	No. 220	N00E	0.164	6.6	29.1
123	San Fernando	USA	9/2/1971	No. 220	S90W	0.148	6.6	29.1
124	San Fernando	USA	9/2/1971	No. 226	S89W	0.154	6.6	34.8
125	San Fernando	USA	9/2/1971	No. 226	S01E	0.156	6.6	34.8
126	San Fernando	USA	9/2/1971	No. 279	S74W	1.055	6.6	6.7
127	San Fernando	USA	9/2/1971	No. 128	N69W	0.278	6.6	23.9
128	Adak	USA	2/5/1971	Adak	N090E	0.204	7.1	78.9
129	Adak	USA	2/5/1971	Adak	N090E	0.205	7.1	78.9
130	Santiago	Chile	9/7/1971	Santiago Univ.	N10W	0.156	7.5	117.0
131	Chiba	Japan	11/10/1971	Kashima Harbor	EW	0.169	5.2	12.0
132	Kushiro	Japan	11/10/1971	Kushiro	NS	0.143	5.8	33.0
133	Central California	USA	4/9/1972	USGS 1211	N61E	0.471	4.8	9.8
134	Central California	USA	4/9/1972	USGS 1211	N29W	0.516	4.8	9.8
135	Central North Island	New Zealand	5/1/1973	ATENE C	N40E	0.143	6.7	67.0
136	Central North Island	New Zealand	5/1/1973	ATENE C	N50W	0.153	6.7	67.0
137	Nemuro	Japan	17/6/1973	Kushiro	NS	0.201	7.4	112.0
138	Nemuro	Japan	17/6/1973	Kushiro	EW	0.127	7.4	112.0
139	Lefkada	Greece	4/11/1973	Lefkada	L	0.041	5.0	19.0
140	Lefkada	Greece	4/11/1973	Lefkada	T	0.074	5.0	19.0
141	Lefkada	Greece	4/11/1973	Lefkada	L	0.515	5.8	20.0
142	Lefkada	Greece	4/11/1973	Lefkada	T	0.258	5.8	20.0
143	Hollister	USA	28/11/1974	Gilroy Array	S67W	0.135	5.2	12.0
144	Hollister	USA	28/11/1974	Hollister	N87W	0.163	5.2	9.8

TABLE 2: Continued.

Number	Seismic event	Country	Date	Station	Component	PGA (g)	Magnitude	Epicentral distance (km)
145	Cape Mendocino	USA	12/1/1975	Petrolia	N75E	0.180	5.2	19.0
146	Oita Prefecture	Japan	21/4/1975	Beppu Harbor	EW	0.138	6.4	41.0
147	Cape Mendocino	USA	6/5/1975	Shelter Cove	N70E	0.168	5.3	63.0
148	Humboldt County	USA	7/6/1975	Petrolia	S60E	0.199	5.2	31.0
149	Humboldt County	USA	7/6/1975	Petrolia	N75E	0.158	5.2	31.0
150	Whittier Narrows	USA	7/6/1975	Petrolia	N15W	0.128	5.2	31.0
151	Oroville	USA	6/8/1975	USGS 0001	N90E	0.292	4.7	7.6
152	Oroville	USA	6/8/1975	USGS 0001	N00E	0.620	4.7	7.6
153	Oroville	USA	11/8/1975	USGS 0001	S55E	0.389	4.4	1.0
154	Oroville	USA	11/8/1975	USGS 0001	N35E	0.284	4.4	1.0
155	Denizli	Turkey	19/8/1976	Denizli Met.	NS	0.344	4.4	1.0
156	Vrancea	Romania	4/3/1977	Bucharest	EW	0.175	7.4	170.0
157	Vrancea	Romania	4/3/1977	Bucharest	SN	0.202	7.4	170.0
158	Vrancea	Romania	4/3/1977	Bucharest	NS	0.194	7.4	165.0
159	Vrancea	Romania	4/3/1977	Bucharest	EW	0.163	7.4	165.0
160	Izmir	Turkey	16/12/1977	Izmir	NS	0.409	5.3	6.0
161	Izmir	Turkey	16/12/1977	Izmir	EW	0.136	5.3	6.0
162	Miyagi Prefecture	Japan	12/6/1978	Ofunato Harbor	N41E	0.207	7.4	116.0
163	Miyagi Prefecture	Japan	12/6/1978	Ofunato Harbor	E41S	0.222	7.4	116.0
164	Miyagi Prefecture	Japan	12/6/1978	Siogama Harbor	NS	0.314	7.4	120.0
165	Miyagi Prefecture	Japan	12/6/1978	Siogama Harbor	EW	0.288	7.4	120.0
166	Dursunbey	Turkey	18/7/1979	Dursunbey	NS	0.234	5.2	10.0
167	Dursunbey	Turkey	18/7/1979	Dursunbey	EW	0.309	5.2	10.0
168	Coyote Lake	USA	6/8/1979	USGS 1409	S40E	0.251	5.9	14.4
169	Coyote Lake	USA	6/8/1979	USGS 1409	N50E	0.188	5.9	14.4
170	Coyote Lake	USA	6/8/1979	USGS 1413	N40W	0.299	5.9	10.3
171	Coyote Lake	USA	6/8/1979	USGS 1413	S50W	0.408	5.9	10.3
172	Imperial Valley	USA	15/10/1979	El Centro	230	0.367	6.6	27.6
173	Imperial Valley	USA	15/10/1979	El Centro	140	0.517	6.6	27.6
174	Imperial Valley	USA	15/10/1979	El Centro	230	0.349	6.6	18.5
175	Imperial Valley	USA	15/10/1979	El Centro	140	0.483	6.6	18.5
176	Imperial Valley	USA	15/10/1979	El Centro	230	0.405	6.6	33.9
177	Imperial Valley	USA	15/10/1979	El Centro	140	0.309	6.6	33.9
178	Imperial Valley	USA	15/10/1979	El Centro	140	0.138	6.6	27.8
179	Imperial Valley	USA	15/10/1979	El Centro	140	0.151	6.6	27.8
180	Imperial Valley	USA	15/10/1979	El Centro	230	0.162	6.6	27.6
181	Imperial Valley	USA	15/10/1979	El Centro	140	0.229	6.6	27.6
182	Imperial Valley	USA	15/10/1979	El Centro	230	0.275	6.6	27.3
183	Imperial Valley	USA	15/10/1979	El Centro	140	0.221	6.6	27.3
184	Imperial Valley	USA	15/10/1979	El Centro	230	0.147	6.6	36.3
185	Imperial Valley	USA	15/10/1979	El Centro	140	0.130	6.6	36.3
186	Imperial Valley	USA	15/10/1979	El Centro	360	0.137	6.6	33.9
187	Imperial Valley	USA	15/10/1979	El Centro	270	0.145	6.6	33.9
188	Imperial Valley	USA	15/10/1979	USGS 5058	S50W	0.362	6.6	27.9
189	Imperial Valley	USA	15/10/1979	USGS 5058	S40E	0.352	6.6	27.9
190	Imperial Valley	USA	15/10/1979	USGS 5115	S50W	0.365	6.6	31.5
191	Imperial Valley	USA	15/10/1979	USGS 5115	S40E	0.309	6.6	31.5
192	Imperial Valley	USA	15/10/1979	USGA 5028	S50W	0.450	6.6	27.1

TABLE 2: Continued.

Number	Seismic event	Country	Date	Station	Component	PGA (g)	Magnitude	Epicentral distance (km)
193	Imperial Valley	USA	15/10/1979	USGA 5028	S40E	0.331	6.6	27.1
194	Imperial Valley	USA	15/10/1979	USGA 0942	S50W	0.429	6.6	27.1
195	Imperial Valley	USA	15/10/1979	USGA 0942	S40E	0.332	6.6	27.1
196	Imperial Valley	USA	15/10/1979	USGS 5054	S50W	0.762	6.6	6.7
197	Imperial Valley	USA	15/10/1979	USGS 5054	S40E	0.584	6.6	6.7
198	Imperial Valley	USA	15/10/1979	USGS 0958	S50W	0.438	6.6	27.2
199	Imperial Valley	USA	15/10/1979	USGS 0958	S40E	0.599	6.6	27.2
200	Imperial Valley	USA	15/10/1979	USGS 0952	S50W	0.360	6.6	27.6
201	Imperial Valley	USA	15/10/1979	USGS 0952	S40E	0.539	6.6	27.6
202	Imperial Valley	USA	15/10/1979	USGS 5165	NS	0.473	6.6	26.3
203	Imperial Valley	USA	15/10/1979	USGS 5165	EW	0.339	6.6	26.3
204	Imperial Valley	USA	15/10/1979	USGS 0955	S50W	0.349	6.6	27.2
205	Imperial Valley	USA	15/10/1979	USGS 0955	S40E	0.480	6.6	27.2
206	Livermore	USA	24/1/1980	CDMG 0364	EW	0.031	5.9	24.4
207	Livermore	USA	24/1/1980	CDMG 0364	NS	0.027	5.9	24.4
208	Mammoth Lakes	USA	27/5/1980	SER no. 3679	S34E	0.337	6.2	17.3
209	Mammoth Lakes	USA	27/5/1980	SER no. 3679	N56E	0.138	6.2	17.3
210	Mammoth Lakes	USA	27/5/1980	SER no. 1480	NS	0.389	6.2	19.8
211	Mammoth Lakes	USA	27/5/1980	SER no. 1480	EW	0.344	6.2	19.8
212	Mammoth Lakes	USA	27/5/1980	SER no. 3754	S15E	0.631	6.2	14.8
213	Mammoth Lakes	USA	27/5/1980	SER no. 3754	N75E	0.452	6.2	14.8
214	Korinthos	Greece	24/2/1981	Athens	L	0.221	6.7	69.0
215	Korinthos	Greece	24/2/1981	Korinthos	L	0.233	6.7	31.0
216	Korinthos	Greece	24/2/1981	Korinthos	T	0.299	6.7	31.0
217	Korinthos	Greece	24/2/1981	Xylokastro	L	0.289	6.7	35.0
218	Korinthos	Greece	24/2/1981	Xylokastro	T	0.114	6.7	35.0
219	Korinthos	Greece	25/2/1981	Athens	T	0.095	6.7	69.0
220	Korinthos	Greece	25/2/1981	Korinthos	L	0.117	6.7	33.0
221	Korinthos	Greece	25/2/1981	Korinthos	T	0.121	6.7	33.0
222	Lefkada	Greece	10/3/1981	Lefkada	L	0.057	5.8	53.0
223	Lefkada	Greece	10/3/1981	Lefkada	T	0.097	5.8	53.0
224	Lefkada	Greece	10/3/1981	Preveza	L	0.141	5.8	39.0
225	Lefkada	Greece	10/3/1981	Preveza	T	0.137	5.8	39.0
226	Lefkada	Greece	10/4/1981	Lefkada	L	0.023	4.7	34.0
227	Lefkada	Greece	10/4/1981	Lefkada	T	0.036	4.7	34.0
228	Westmoreland	USA	26/4/1981	WEST 2588	EW	0.354	5.6	11.2
229	Westmoreland	USA	26/4/1981	WEST 2588	NS	0.435	5.6	11.2
230	Lefkada	Greece	25/5/1981	Lefkada	L	0.057	4.7	25.0
231	Lefkada	Greece	25/5/1981	Lefkada	T	0.032	4.7	25.0
232	Lefkada	Greece	27/5/1981	Lefkada	L	0.117	5.5	3.0
233	Lefkada	Greece	27/5/1981	Lefkada	T	0.093	5.5	3.0
234	Ionian	Greece	17/1/1983	Argostoli	NS	0.162	7.2	28.7
235	Ionian	Greece	17/1/1983	Argostoli	WE	0.139	7.2	28.7
236	Heraklio	Greece	19/3/1983	Heraklio	T	0.170	5.7	38.0
237	Ionian	Greece	23/3/1983	Argostoli	NS	0.177	5.9	29.0
238	Ionian	Greece	23/3/1983	Argostoli	WE	0.234	5.9	29.0
239	Ionian	Greece	24/3/1983	Argostoli	NS	0.242	5.5	14.7

TABLE 2: Continued.

Number	Seismic event	Country	Date	Station	Component	PGA (g)	Magnitude	Epicentral distance (km)
240	Ionian	Greece	24/3/1983	Argostoli	WE	0.299	5.5	14.7
241	Coalinga	USA	2/5/1983	Coalinga	360	0.595	6.5	28.1
242	Coalinga	USA	2/5/1983	Coalinga	270	0.549	6.5	28.1
243	Coalinga	USA	2/5/1983	Coalinga	360	0.264	6.5	40.6
244	Coalinga	USA	2/5/1983	Coalinga	270	0.371	6.5	40.6
245	Coalinga	USA	2/5/1983	Coalinga	360	0.189	6.5	36.4
246	Coalinga	USA	2/5/1983	Coalinga	270	0.212	6.5	36.4
247	Horasan	Turkey	30/10/1983	Horasan	NS	0.149	6.9	30.0
248	Heraklio	Greece	1/3/1984	Heraklio	L	0.106	4.7	30.0
249	Heraklio	Greece	1/3/1984	Heraklio	T	0.197	4.7	30.0
250	Morgan Hill	USA	24/4/1984	Anderson Dam	340	0.283	6.2	15.0
251	Morgan Hill	USA	24/4/1984	Anderson Dam	250	0.416	6.2	15.0
252	Morgan Hill	USA	24/4/1984	Gilroy Array	0	0.183	6.2	38.0
253	Morgan Hill	USA	24/4/1984	Gilroy Array	0	0.215	6.2	38.1
254	Morgan Hill	USA	24/4/1984	Gilroy Array	90	0.280	6.2	38.1
255	Morgan Hill	USA	24/4/1984	Gilroy Array	270	0.217	6.2	37.9
256	Morgan Hill	USA	24/4/1984	Gilroy Array	360	0.328	6.2	37.9
257	Morgan Hill	USA	24/4/1984	No. 47380	90	0.210	6.2	38.8
258	Morgan Hill	USA	24/4/1984	No. 47380	0	0.154	6.2	38.8
259	Valparaiso	Chile	3/3/1985	Lolleo	100	0.187	7.8	120.0
260	Valparaiso	Chile	3/3/1985	Lolleo	10	0.182	7.8	120.0
261	Valparaiso	Chile	3/3/1985	Lolleo	100	0.437	7.8	120.0
262	Valparaiso	Chile	3/3/1985	Lolleo	10	0.698	7.8	120.0
263	Valparaiso	Chile	3/3/1985	Vina del Mar	290	0.233	7.8	43.0
264	Valparaiso	Chile	3/3/1985	Vina del Mar	200	0.356	7.8	43.0
265	Valparaiso	Chile	3/3/1985	Valparaiso	50	0.292	7.8	36.0
266	Valparaiso	Chile	3/3/1985	Valparaiso	140	0.163	7.8	36.0
267	Valparaiso	Chile	3/3/1985	Santiago	L	0.124	7.8	130.0
268	Valparaiso	Chile	8/4/1985	Lolleo	100	0.167	7.5	120.0
269	Valparaiso	Chile	8/4/1985	Lolleo	10	0.200	7.5	120.0
270	Michoacan	Mexico	19/9/1985	SCT1	N90W	0.168	8.1	400.0
271	Michoacan	Mexico	19/9/1985	La Union	N00E	0.163	8.1	107.0
272	Michoacan	Mexico	19/9/1985	Michoacan	N90W	0.162	8.1	111.0
273	Michoacan	Mexico	19/9/1985	La Union	N90E	0.147	8.1	107.0
274	Michoacan	Mexico	19/9/1985	Caleta de Campo	N00E	0.139	8.1	21.0
275	Michoacan	Mexico	19/9/1985	Caleta de Campo	N90E	0.138	8.1	21.0
276	Michoacan	Mexico	19/9/1985	La Villita	N00E	0.121	8.1	65.0
277	Michoacan	Mexico	21/9/1985	Michoacan	S00E	0.156	7.5	91.0
278	Michoacan	Mexico	21/9/1985	Michoacan	N90W	0.140	7.5	91.0
279	Michoacan	Mexico	21/9/1985	Papatoa	S00E	0.252	7.5	130.0
280	Nahanni	Canada	9/11/1985	Slide Mountain	330	0.374	5.0	5.8
281	Nahanni	Canada	9/11/1985	Slide Mountain	240	0.451	5.0	5.8
282	Nahanni	Canada	23/12/1985	Iverson	10	1.080	6.9	8.0
283	Nahanni	Canada	23/12/1985	Iverson	280	1.319	6.9	8.0
284	Nahanni	Canada	23/12/1985	Iverson	10	0.224	6.9	8.0
285	Nahanni	Canada	23/12/1985	Slide Mountain	330	0.386	6.9	15.0
286	Nahanni	Canada	23/12/1985	Slide Mountain	240	0.534	6.9	15.0
287	Nahanni	Canada	23/12/1985	Nahanni	360	0.190	6.9	23.8

TABLE 2: Continued.

Number	Seismic event	Country	Date	Station	Component	PGA (g)	Magnitude	Epicentral distance (km)
288	Nahanni	Canada	23/12/1985	Nahanni	270	0.192	6.9	23.8
289	Kalamata	Greece	13/9/1986	Kalamata	L	0.217	6.0	10.0
290	Kalamata	Greece	13/9/1986	Kalamata	T	0.291	6.0	10.0
291	Kalamata	Greece	15/9/1986	Kalamata	L	0.328	4.1	7.0
292	Kalamata	Greece	15/9/1986	Kalamata	T	0.161	4.1	7.0
293	San Salvador	San Salvador	10/10/1986	No. 90005	270	0.524	5.4	5.7
294	San Salvador	San Salvador	10/10/1986	No. 90005	180	0.391	5.4	5.7
295	San Salvador	San Salvador	10/10/1986	No. 90018	0	0.214	5.4	6.2
296	San Salvador	San Salvador	10/10/1986	No. 90018	270	0.296	5.4	6.2
297	San Salvador	San Salvador	10/10/1986	No. 90006	180	0.412	5.4	4.3
298	San Salvador	San Salvador	10/10/1986	No. 90006	90	0.681	5.4	4.3
299	San Salvador	San Salvador	10/10/1986	No. 90014	90	0.339	5.4	4.5
300	San Salvador	San Salvador	10/10/1986	No. 90014	0	0.421	5.4	4.5
301	Strazhitsa	Bulgaria	7/12/1986	V. Tarnovo	L	0.067	5.7	225.0
302	Strazhitsa	Bulgaria	7/12/1986	V. Tarnovo	T	0.074	5.7	225.0
303	Whittier Narrows	USA	1/10/1987	No. 24157	90	0.149	6.1	27.0
304	Whittier Narrows	USA	1/10/1987	No. 24157	0	0.139	6.1	27.0
305	Whittier Narrows	USA	1/10/1987	Tarzana	90	0.527	6.1	43.3
306	Whittier Narrows	USA	1/10/1987	Tarzana	360	0.397	6.1	43.3
307	Whittier Narrows	USA	1/10/1987	Hollywood	0	0.201	6.1	25.2
308	Whittier Narrows	USA	1/10/1987	Inglewood	90	0.219	6.1	25.8
309	Whittier Narrows	USA	1/10/1987	Inglewood	0	0.246	6.1	25.8
310	Whittier Narrows	USA	1/10/1987	Long Beach	90	0.233	6.1	27.4
311	Whittier Narrows	USA	1/10/1987	Long Beach	0	0.144	6.1	27.4
312	Whittier Narrows	USA	1/10/1987	Alhambra	90	0.284	6.1	6.8
313	Whittier Narrows	USA	1/10/1987	Alhambra	360	0.250	6.1	6.8
314	Whittier Narrows	USA	1/10/1987	Whittier	180	0.382	6.1	15.6
315	Whittier Narrows	USA	1/10/1987	Whittier	90	0.607	6.1	15.6
316	Whittier Narrows	USA	1/10/1987	Vernon	7	0.267	6.1	15.7
317	Whittier Narrows	USA	1/10/1987	Vernon	277	0.240	6.1	15.7
318	Whittier Narrows	USA	1/10/1987	Norwalk	360	0.201	6.1	21.9
319	Whittier Narrows	USA	1/10/1987	Norwalk	360	0.235	6.1	21.9
320	Rhodos	Greece	5/10/1987	Rhodos	L	0.056	5.6	27.0
321	Rhodos	Greece	5/10/1987	Rhodos	T	0.052	5.6	27.0
322	Superstition Hills	USA	24/11/1987	Wildlife Liq.	360	0.131	6.6	30.0
323	Superstition Hills	USA	24/11/1987	Wildlife Liq.	90	0.129	6.6	30.0
324	Lefkada	Greece	24/4/1988	Lefkada	L	0.114	5.0	33.0
325	Lefkada	Greece	24/4/1988	Lefkada	T	0.208	5.0	33.0
326	Valsamata	Greece	18/5/1988	Valsamata	L	0.165	5.8	23.0
327	Valsamata	Greece	18/5/1988	Valsamata	T	0.174	5.8	23.0
328	Valsamata	Greece	22/5/1988	Valsamata	L	0.053	5.5	21.0
329	Valsamata	Greece	22/5/1988	Valsamata	T	0.079	5.5	21.0
330	Kyllini	Greece	16/10/1988	Zakynthos	NS	0.125	6.0	36.0
331	Kyllini	Greece	16/10/1988	Zakynthos	WE	0.167	6.0	36.0
332	Vartholomio	Greece	19/10/1988	Vartholomio	L	0.047	4.4	19.0
333	Vartholomio	Greece	19/10/1988	Vartholomio	T	0.035	4.4	19.0
334	Vartholomio	Greece	31/10/1988	Vartholomio	L	0.062	4.8	17.0
335	Vartholomio	Greece	31/10/1988	Vartholomio	T	0.035	4.8	17.0

TABLE 2: Continued.

Number	Seismic event	Country	Date	Station	Component	PGA (g)	Magnitude	Epicentral distance (km)
336	Nafpaktos	Greece	22/12/1988	Nafpaktos	L	0.112	5.0	10.0
337	Nafpaktos	Greece	22/12/1988	Nafpaktos	T	0.103	5.0	10.0
338	Loma Prieta	USA	17/10/1989	Anderson Dam	340	0.239	7.0	96.7
339	Loma Prieta	USA	17/10/1989	Anderson Dam	250	0.239	7.0	96.7
340	Loma Prieta	USA	17/10/1989	Hollister	255	0.281	7.0	48.1
341	Loma Prieta	USA	17/10/1989	Hollister	165	0.276	7.0	48.1
342	Loma Prieta	USA	17/10/1989	Palo Alto Hospital	302	0.341	7.0	46.3
343	Loma Prieta	USA	17/10/1989	Palo Alto Hospital	212	0.378	7.0	46.3
344	Loma Prieta	USA	17/10/1989	Hollister	180	0.217	7.0	45.0
345	Loma Prieta	USA	17/10/1989	Hollister	90	0.252	7.0	45.0
346	Loma Prieta	USA	17/10/1989	Stanford	360	0.255	7.0	51.5
347	Loma Prieta	USA	17/10/1989	Stanford	90	0.215	7.0	51.5
348	Loma Prieta	USA	17/10/1989	Calaveras	180	0.142	7.0	46.5
349	Loma Prieta	USA	17/10/1989	Calaveras	90	0.191	7.0	46.5
350	Loma Prieta	USA	17/10/1989	Apeel Array	133	0.223	7.0	64.1
351	Loma Prieta	USA	17/10/1989	Apeel Array	43	0.272	7.0	64.1
352	Loma Prieta	USA	17/10/1989	Emeryville	350	0.210	7.0	96.7
353	Loma Prieta	USA	17/10/1989	Emeryville	260	0.255	7.0	96.7
354	Loma Prieta	USA	17/10/1989	Anderson Dam	333	0.239	7.0	96.7
355	Loma Prieta	USA	17/10/1989	Anderson Dam	243	0.245	7.0	96.7
356	Loma Prieta	USA	17/10/1989	Emeryville	350	0.210	7.0	96.7
357	Loma Prieta	USA	17/10/1989	Emeryville	260	0.255	7.0	96.7
358	Loma Prieta	USA	17/10/1989	Emeryville	260	0.209	7.0	96.7
359	Loma Prieta	USA	17/10/1989	Emeryville	350	0.182	7.0	96.7
360	Loma Prieta	USA	17/10/1989	San Francisco	95	0.220	7.0	96.7
361	Aigio	Greece	17/5/1990	Aigio	T	0.203	5.0	20.0
362	Erzincan	Turkey	13/3/1992	Erzincan	NS	0.392	6.9	6.0
363	Erzincan	Turkey	13/3/1992	Erzincan	EW	0.492	6.9	6.0
364	Northridge	USA	17/1/1994	Los Angeles	166	0.257	6.4	13.7
365	Northridge	USA	17/1/1994	Los Angeles	76	0.462	6.4	13.7
366	Northridge	USA	17/1/1994	Los Angeles	348	0.133	6.4	31.0
367	Northridge	USA	17/1/1994	Los Angeles	258	0.147	6.4	31.0
368	Northridge	USA	17/1/1994	Canoga Park	90	0.334	6.4	6.0
369	Northridge	USA	17/1/1994	Los Angeles	360	0.260	6.4	42.2
370	Northridge	USA	17/1/1994	Los Angeles	270	0.154	6.4	42.2
371	Northridge	USA	17/1/1994	Malibu Canyon	360	0.173	6.4	14.9
372	Northridge	USA	17/1/1994	Malibu Canyon	270	0.161	6.4	14.9
373	Northridge	USA	17/1/1994	Littlerock	300	0.120	6.4	61.3
374	Northridge	USA	17/1/1994	Topanga	360	0.326	6.4	6.0
375	Northridge	USA	17/1/1994	Topanga	270	0.194	6.4	6.0
376	Northridge	USA	17/1/1994	Los Angeles	360	0.164	6.4	31.2
377	Northridge	USA	17/1/1994	Los Angeles	270	0.291	6.4	31.2
378	Northridge	USA	17/1/1994	Los Angeles	325	0.383	6.4	19.1
379	Northridge	USA	17/1/1994	Los Angeles	235	0.298	6.4	19.1
380	Northridge	USA	17/1/1994	Los Angeles	325	0.247	6.4	28.7
381	Northridge	USA	17/1/1994	Jensen	22	0.388	6.4	12.2
382	Northridge	USA	17/1/1994	Jensen	292	0.621	6.4	12.2
383	Northridge	USA	17/1/1994	USC no. 0003	S00E	0.444	6.4	2.2

TABLE 2: Continued.

Number	Seismic event	Country	Date	Station	Component	PGA (g)	Magnitude	Epicentral distance (km)
384	Northridge	USA	17/1/1994	USC no. 0006	N90E	0.430	6.4	11.1
385	Northridge	USA	17/1/1994	USC no. 0009	S90W	0.248	6.4	12.0
386	Northridge	USA	17/1/1994	USC no. 0013	N09E	0.434	6.4	12.7
387	Northridge	USA	17/1/1994	USC no. 0014	S55E	0.434	6.4	15.5
388	Northridge	USA	17/1/1994	USC no. 0016	N90E	0.257	6.4	16.5
389	Northridge	USA	17/1/1994	USC no. 0021	N00W	0.409	6.4	26.5
390	Northridge	USA	17/1/1994	USC no. 0053	S16W	0.381	6.4	6.0
391	Northridge	USA	17/1/1994	USC no. 0054	S65W	0.324	6.4	25.2
392	Northridge	USA	17/1/1994	USC no. 0055	N90E	0.503	6.4	13.0
393	Northridge	USA	17/1/1994	USC no. 0056	N46E	0.411	6.4	21.5
394	Northridge	USA	17/1/1994	USC no. 0057	N00W	0.389	6.4	25.6
395	Northridge	USA	17/1/1994	USC no. 0091	S70E	0.420	6.4	24.9
396	Northridge	USA	17/1/1994	USC no. 0095	N90W	0.186	6.4	42.9
397	Lefkada	Greece	25/2/1994	Lefkada	L	0.171	5.8	16.0
398	Lefkada	Greece	25/2/1994	Lefkada	T	0.197	5.8	16.0
399	Kobe	Japan	17/1/1995	Kobe	EW	0.619	6.9	1.0
400	Kobe	Japan	17/1/1995	Kobe	NS	0.821	6.9	1.0

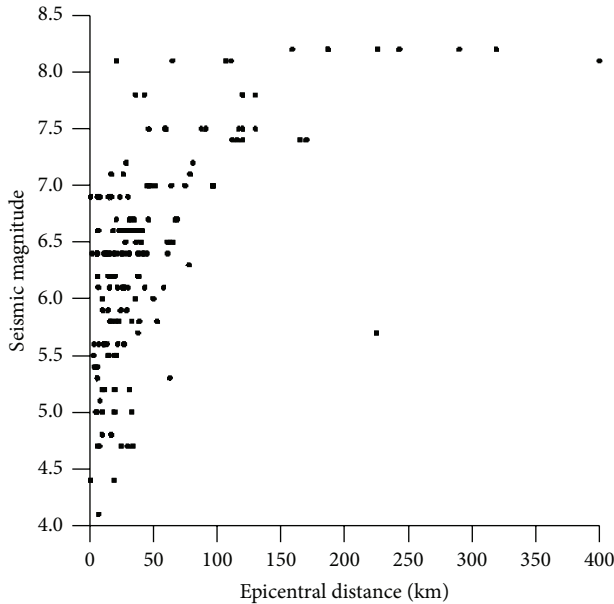


FIGURE 1: Plot of standard seismic magnitudes versus epicentral distances.

(OSDI_s) because these parameters summarily lump all existing damage in columns and beams into a single value, which can then be easily interrelated with the single-value seismic parameters. For this purpose, the modified overall damage index of Park and Ang [19, 20] is used in the present study. In this model, the global damage is obtained as a weighted average of the local damage at the ends of each element, with the dissipated energy as the weighting function. The local damage index according to Park and Ang must be calculated using the following equation:

$$\text{DI}_{\text{P/A,Local}} = \frac{\theta_m - \theta_r}{\theta_u - \theta_r} + \frac{\beta}{M_y \theta_u} E_T, \quad (14)$$

TABLE 3: Number of accelerograms employed per country.

Country	Number of accelerograms
Bulgaria	2
Canada	9
Chile	12
Greece	54
Japan	46
Mexico	10
New Zealand	2
Romania	4
San Salvador	6
Turkey	8
USA	247

TABLE 4: Number of accelerograms employed per PGA range.

PGA range (g)	Number of accelerograms
0.01–0.1	23
0.1–0.2	165
0.2–0.3	103
0.3–0.4	50
0.4–0.5	32
0.5–0.6	13
0.6–0.7	7
>0.7	7

where θ_m is the maximum rotation during the load history, θ_u is the ultimate rotation capacity of the section, θ_r is the recoverable rotation at unloading, β is a constant parameter (0.1–0.15 for nominal strength deterioration [21]), M_y is the yield moment of the section, and E_T is the dissipated hysteretic energy.

In this study, the numerical value of parameter β in (14) is equal to 0.1. This value corresponds to nominal strength

TABLE 5: Damage classification limits.

	Low	Medium	Large	Total
OSDI of Park and Ang ($DI_{P/A,Global}$) and of DiPasquale and Cakmak (δ_M)	≤ 0.3	$0.3 < OSDI \leq 0.6$	$0.6 < OSDI \leq 0.8$	> 0.8
MISDR (%)	≤ 0.5	$0.5 < MISDR \leq 1.5$	$1.5 < MISDR \leq 2.5$	> 2.5

degradation [21]. However, the numerical value of β can vary in the range between 0 (no strength degradation) and 0.4 (severe deterioration) [21]. A low β value corresponds to well-detailed reinforced concrete or steel members [22]. In contrast, a high β value corresponds to poorly detailed reinforced concrete members or to unreinforced masonry [20].

The OSDI of Park and Ang is defined by the following equation:

$$DI_{P/A,Global} = \frac{\sum_{i=1}^n DI_{P/A,Local} E_i}{\sum_{i=1}^n E_i}, \quad (15)$$

where E_i is the energy dissipated at location i and n is the number of locations at which the local damage is computed.

The maximum interstory drift ratio (MISDR) has been selected as a second OSDI. It is defined as the maximum interstory drift (u_{max}) normalized by the story height (h), as given by the relation

$$MISDR = \frac{|u|_{max}}{h} 100 [\%]. \quad (16)$$

The maximum softening index of DiPasquale and Cakmak [23] has been selected as a third OSDI, which is based on the vibration parameters of the structure. It is given by the following expression:

$$\delta_M = 1 - \frac{T_0}{T_{max}}, \quad (17)$$

where δ_M is the maximum softening, T_0 is the fundamental period, and T_{max} is the maximum natural period of the examined structure during the excitation. For the evaluation of T_{max} the instantaneous natural period is required to be evaluated, which is accompanied by the actual time-dependent (instantaneous) tangent stiffness matrix. The latter varies with time due to nonlinear phenomena. The natural period computed for each time step of a nonlinear dynamic analysis presents high variability. The duration of these maximum values is very short, and therefore, their influence in the natural period of an equivalent linear system is not significant. Thus, a more meaningful indication of the change in the natural period can be obtained by observing a moving average of the instantaneous natural period using a sliding time window for the smoothness of the time-fundamental period curve [23, 24]. The time-fundamental period curve can be evaluated by a nonlinear dynamic procedure that calculates the fundamental period of the structure by considering the stiffness degradation in every time step. T_0 is the initial, fundamental

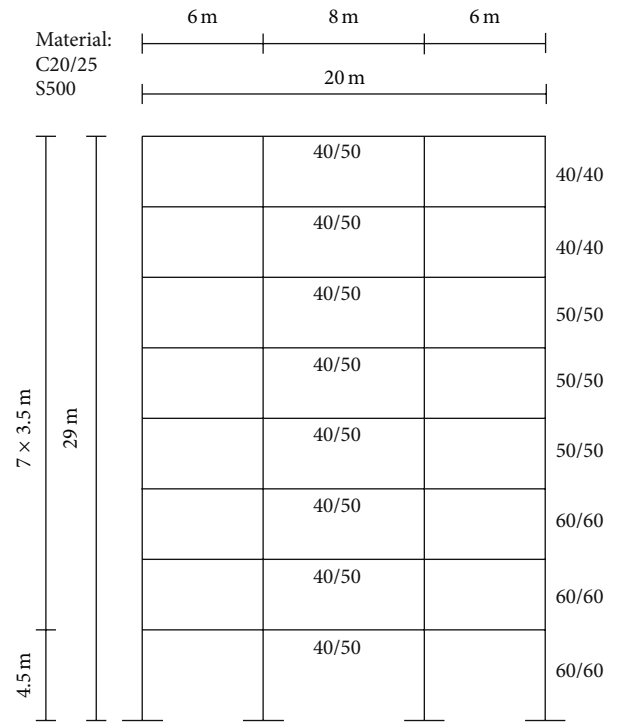


FIGURE 2: Examined reinforced concrete frame structure.

period of the structure that corresponds to the initial stiffness of the structure.

Table 5 presents the range limits of the four damage classes using the different damage indices [25]. The four levels (low, medium, large, and total) correspond to undamaged or minor damage, repairable damage, irreparable damage, and partial or total collapse of the structure.

5. Application

The proposed procedures have been applied to a reinforced concrete structure, shown in Figure 2, and designed in agreement with the rules of the recent Eurocodes for structural concrete and aseismic structures, EC2 and EC8 [26, 27]. The fundamental period of the frame was 1.20 s. The following loads have been considered: self-weight, seismic loads, snow, wind, and live loads. The cross-sections of the beams are treated as T-beams with a 40 cm width, 20 cm plate thickness, 50 cm total beam height, and 1.45 m effective plate width. The distances between each frame of the structure have been chosen to be 6 m. According to the EC8 Eurocode, the structure shown in Figure 2 is considered an “importance

class II, ductility class M" structure with category B subsoil. The ordinate of the used elastic response spectrum of EC8 was 0.24 g.

After designing and detailing the reinforced concrete frame structure, nonlinear dynamic analyses were carried out to evaluate the structural seismic response. For this purpose, the computer program IDARC [21] has been used. The hysteretic behavior of the beams and columns has been specified at both ends of each member using a three-parameter Park model [21]. This hysteretic model incorporates stiffness degradation, strength deterioration, nonsymmetric response, slip-lock, and a trilinear monotonic envelope. The parameter values that specify the above degrading parameters have been chosen from the cyclic force-deformation characteristics from experimental results of the typical components of the studied structure [20]. Thus, nominal parameters for stiffness degradation and strength deterioration have been chosen. In contrast, no pinching has been considered. Realistic hysteretic material models result in realistic proposed statistical models. On the other hand, simplified assumptions for the hysteretic material models, like ignoring the pinching effect (default option in the utilized computer program IDARC [21]), do not affect on principle the value of the proposed statistical models that are in any case procedures for the approximate assessment of structural damage. Of the several response parameters, the focus is on the OSDIs. Consequently, the OSDIs of Park and Ang and of DiPasquale and Cakmak (maximum softening index) and the MISDR have been calculated for all of the accelerograms corresponding to the excitations given in Table 2, which were used as the seismic input for the nonlinear dynamic analyses. For the evaluation of the global damage index of DiPasquale and Cakmak according to (17), a sliding time window of 2.5 s is used to smooth the time-fundamental period curve. This window size is between 2 and 5.5 times the fundamental period T_0 of the examined structure ($T_0 = 1.20$ s), as suggested by Rodriguez-Gómez/Cakmak [24]. The maximum value of the smoothed time-fundamental period curve is the maximum natural period of the examined structure during each seismic excitation considered (T_{\max} in (17)). Finally, the hardening period T_h and yield period T_y needed for the assessment of the SI_{MR} in (8) are evaluated by a nonlinear pushover analysis, as described in Section 2. Their numerical values are $T_y = 1.2$ s and $T_h = 1.5$ s.

6. Multilinear Regression Analysis

In general, a multilinear regression analysis [28] is used to express a dependent variable (y) by (n)-independent variables (x_i , with $i = 1, \dots, n$) and a constant value (a) minimizing the error term (e), as shown by the relation

$$y = a + b_1x_1 + b_2x_2 + \dots + b_nx_n + e. \quad (18)$$

In the present study, the dependent variable (y) represents each used OSDI (of Park and Ang, of DiPasquale and Cakmak (maximum softening index), and the MISDR), and the independent variables (x_i) are the twenty seismic parameters ($n = 20$) shown in Table 1.

TABLE 6: Multilinear regression model for the OSDI of Park and Ang.

Parameter	Estimate	Lower limit	Upper limit
Constant	-0.032	-0.063	-0.001
PGA	0.370	0.234	0.507
PGV	0.084	-0.030	0.199
PGA/PGV	0.005	-0.004	0.014
I_0	0.007	0.004	0.009
RMS _a	-0.074	-0.156	0.008
$T_{0.90}$	0.0004	-0.001	0.001
$P_{0.90}$	-0.004	-0.015	0.006
SI _H	0.036	-0.004	0.077
SI _K	-0.014	-0.127	0.099
SI _{MR}	-0.379	-0.543	-0.215
EPA	-0.385	-0.652	-0.118
EPA _{max}	0.076	0.004	0.148
E_{inp}	0.037	0.013	0.061
CAV	-0.020	-0.052	0.011
DP _{A/S}	-0.202	-0.437	0.032
CP	0.038	-0.022	0.098
SD	-0.110	-0.428	0.207
SV	0.167	0.074	0.260
SA	0.031	-0.092	0.154
$I_{F/V/F}$	0.017	-0.018	0.051

The analyses have been carried out using the statistical software STATGRAPHICS [29]. The regression results for the OSDIs after Park and Ang, for the MISDR, and for the maximum softening index after DiPasquale and Cakmak are given in Tables 6–9 and will be presented in detail subsequently. Thus, the result for the OSDI after Park and Ang is given in Table 6. The equation of the fitted multilinear model is

$$\begin{aligned} DI_{P/A, \text{Global}} = & -0.032 + 0.370\text{PGA} + 0.084\text{PGV} \\ & + \frac{0.005\text{PGA}}{\text{PGV}} + 0.007\text{Arias} \\ & - 0.074\text{RMS}_a - 0.0004T_{0.90} - 0.004P_{0.90} \\ & + 0.036\text{SI}_H - 0.014\text{SI}_K - 0.379\text{SI}_{MR} \\ & - 0.385\text{EPA} + 0.076\text{EPA}_{\text{max}} + 0.037E_{\text{inp}} \\ & - 0.020\text{CAV} - 0.202\text{DP}_{A/S} + 0.038\text{CP} \\ & - 0.110\text{SD} + 0.167\text{SV} + 0.031\text{SA} \\ & + 0.017I_{F/V/F}. \end{aligned} \quad (19a)$$

$R^2 = 0.859$, which indicates that the model as fitted explains 85.9% of the variability in the Park and Ang OSDI.

TABLE 7: Multilinear regression model for the OSDI of Park and Ang without the constant term.

Parameter	Estimate	Lower Limit	Upper Limit
PGA	0.324	0.195	0.454
PGV	0.072	-0.042	0.186
PGA/PGV	-0.001	-0.008	0.005
I_0	0.007	0.005	0.009
RMS _a	-0.095	-0.175	-0.016
$T_{0.90}$	-0.001	-0.002	0.000
$P_{0.90}$	-0.003	-0.014	0.007
SI _H	0.028	-0.012	0.068
SI _K	-0.010	-0.123	0.104
SI _{MR}	-0.337	-0.496	-0.178
EPA	-0.370	-0.637	-0.102
EPA _{max}	0.076	0.003	0.148
E_{inp}	0.043	0.019	0.067
CAV	-0.020	-0.052	0.012
DP _{A/S}	-0.202	-0.437	0.034
CP	0.008	-0.044	0.060
SD	-0.086	-0.403	0.232
SV	0.154	0.062	0.247
SA	0.045	-0.077	0.168
$I_{F/V/F}$	0.016	-0.018	0.051

In addition, Table 6 presents the 95% confidence intervals for the coefficients in the multilinear model. Each variable coefficient in (19a) and in Table 6, or generally in (18), is interpreted as the change in the response based on a one-unit change in the corresponding explanatory variable keeping all other variables fixed. This interpretation is fictitious because it is not possible in a seismic accelerogram to change only one of the seismic parameters. Furthermore, in some explanatory variables (seismic parameters), a one-unit change can be easily observed (such as the SMD after Trifunac/Brady), whereas such a change cannot be easily observed in others (such as the SD). In addition, the comparison between coefficients of different explanatory variables is not possible because they are assigned quantities having different dimensions and units [30]. Finally, the constant term ("a" in (18) and "-0.032" in (19a)) has a physical meaning only in the case in which all of the explanatory variables x_i can simultaneously have zero values. Otherwise, as in the present study in which the seismic parameters with zero values are out of the observed value range, the constant term is an extrapolated value without a physical meaning. However, Table 7 presents the coefficients and their 95% confidence intervals for the multilinear regression model of the OSDI after Park and Ang, without the constant term ($R^2 = 0.900218$). As indicated by R^2 , both models (with and without the constant term) explain a high percentage of the variance (85.9% and 90%, resp.) in the dependent variable.

Similarly, Table 8 presents the multilinear model for the MISDR ($R^2 = 0.799279$) and Table 9 presents the model for the OSDI (maximum softening index) after DiPasquale and Cakmak ($R^2 = 0.763627$), along with their 95% confidence

TABLE 8: Multilinear regression model for the MISDR.

Parameter	Estimate	Lower limit	Upper limit
Constant	-0.072	-0.290	0.147
PGA	2.331	1.380	3.281
PGV	0.359	-0.438	1.156
PGA/PGV	0.046	-0.017	0.109
I_0	0.043	0.028	0.058
RMS _a	-0.322	-0.893	0.249
$T_{0.90}$	0.003	-0.004	0.010
$P_{0.90}$	-0.019	-0.089	0.052
SI _H	0.410	0.129	0.691
SI _K	-0.520	-1.308	0.268
SI _{MR}	-2.726	-3.864	-1.587
EPA	-0.873	-2.731	0.985
EPA _{max}	0.019	-0.483	0.522
E_{inp}	-0.048	-0.216	0.120
CAV	-0.397	-0.619	-0.175
DP _{A/S}	1.475	-0.155	3.104
CP	-0.167	-0.583	0.250
SD	-2.292	-4.501	-0.084
SV	1.802	1.155	2.449
SA	0.236	-0.619	1.090
$I_{F/V/F}$	0.024	-0.217	0.264

intervals. The fitted multilinear models for these global structural damage indices are provided by

$$\begin{aligned}
 DI_{P/A,\text{Global}} = & -0.072 + 2.331\text{PGA} + 0.359\text{PGV} \\
 & + \frac{0.046\text{PGA}}{\text{PGV}} + 0.043\text{Arias} \\
 & - 0.322\text{RMS}_a + 0.003T_{0.90} - 0.019P_{0.90} \\
 & + 0.410\text{SI}_H - 0.520\text{SI}_K - 2.726\text{SI}_{MR} \\
 & - 0.873\text{EPA} + 0.019\text{EPA}_{max} - 0.048E_{inp} \\
 & - 0.397\text{CAV} - 1.475\text{DP}_{A/S} - 0.167\text{CP} \\
 & - 2.292\text{SD} + 1.802\text{SV} + 0.236\text{SA} \\
 & + 0.024I_{F/V/F},
 \end{aligned} \tag{19b}$$

$$\begin{aligned}
 DI_{P/A,\text{Global}} = & -0.090 + 0.293\text{PGA} + 0.094\text{PGV} \\
 & + \frac{0.017\text{PGA}}{\text{PGV}} + 0.001\text{Arias} \\
 & - 0.035\text{RMS}_a + 0.0002T_{0.90} - 0.005P_{0.90} \\
 & + 0.019\text{SI}_H + 0.237\text{SI}_K - 0.178\text{SI}_{MR} \\
 & - 0.288\text{EPA} + 0.027\text{EPA}_{max} + 0.081E_{inp} \\
 & - 0.032\text{CAV} - 0.656\text{DP}_{A/S} + 0.097\text{CP} \\
 & + 0.648\text{SD} - 0.079\text{SV} - 0.040\text{SA} \\
 & + 0.011I_{F/V/F}.
 \end{aligned} \tag{19c}$$

TABLE 9: Multilinear regression model for the OSDI of DiPasquale and Cakmak.

Parameter	Estimate	Lower limit	Upper limit
Constant	-0.090	-0.130	-0.050
PGA	0.293	0.119	0.466
PGV	0.094	-0.052	0.239
PGA/PGV	0.017	0.005	0.028
I_0	0.001	-0.002	0.004
RMS _a	-0.035	-0.140	0.069
$T_{0.90}$	0.0002	-0.001	0.001
$P_{0.90}$	-0.005	-0.018	0.008
SI _H	0.019	-0.032	0.071
SI _K	0.237	0.093	0.380
SI _{MR}	-0.178	-0.386	0.030
EPA	-0.288	-0.627	0.052
EPA _{max}	0.027	-0.065	0.118
E_{inp}	0.081	0.050	0.112
CAV	-0.032	-0.072	0.009
DP _{A/S}	-0.656	-0.953	-0.358
CP	0.097	0.021	0.173
SD	0.648	0.245	1.052
SV	-0.079	-0.197	0.039
SA	-0.040	-0.196	0.116
$I_{F/V/F}$	0.011	-0.032	0.055

The models, represented by the regression equations, are strictly valid only within the range of the data (in the present study these data are the values of the seismic parameters employed) used to develop these regression equations (training phase). Trying to predict the outcome outside the range of the data can be seriously misleading and is not advised.

The initial set of explanatory variables (see (19a), (19b), and (19c)) contains a relative large number of seismic intensity parameters. Thus, in the present study twenty seismic intensity quantities have been used (Table 1) to avoid an a priori omission of important, independent (explanatory) seismic parameters. A regression model with only a few explanatory variables (e.g., two to three accidentally selected parameters) runs the risk of becoming an unreliable or invalid regression model. However, a statistically systematic reduction of the initial regression model is possible. This reduction has been realized in the present study by a stepwise backward elimination procedure combined with an elimination criterion.

Thus, the multilinear regression model, which contains the twenty examined seismic parameters (Model 1), can be simplified to consider fewer parameters without losing significant model quality. This simplification is realized by successive elimination of the independent variables with a P value greater than or equal to 0.05 (elimination criterion) because that term is not statistically significant at the 95% or higher confidence level. This lack of significance is explained by the strong correlation between several seismic parameters.

The P value is the smallest level of significance that would lead to rejection of the null hypothesis H_0 with the given data.

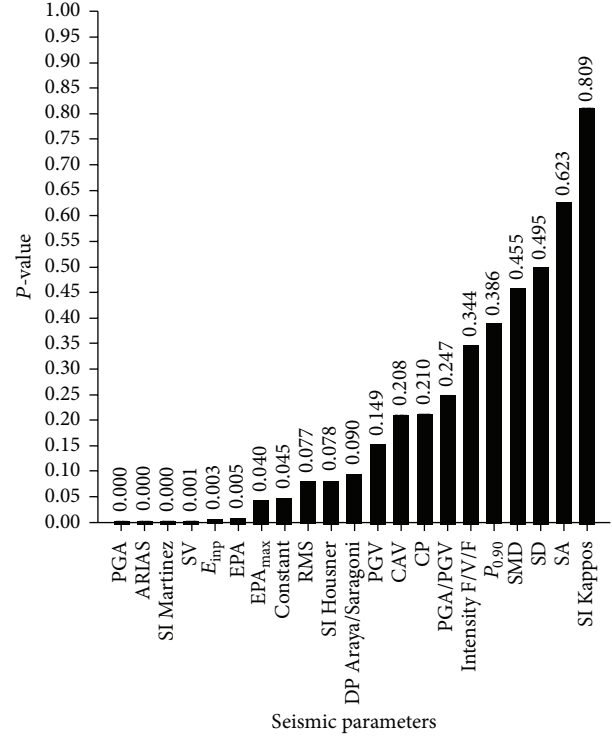


FIGURE 3: P values in ascending order for all of the terms of regression equation (19a).

In the case of multilinear regression analysis, the null hypothesis (H_0) and alternative hypothesis (H_a) are $H_0 : b_i = 0$ and $H_a : b_i \neq 0$, where b_i are the coefficients of the explanatory variables in (18) [30]. Thus, the importance to keep a seismic intensity parameter in the regression model is determined by the previously described explicit statistical procedure.

As an example, Figure 3 presents the P values for all of the terms of regression equation (19a) (Table 6) in ascending order. The SI after Kappos parameter has the maximum P value (0.809) which is greater than 0.05. Therefore, this specific parameter can be eliminated from the considered model. Subsequently, a new regression equation is evaluated without the Kappos SI parameter in its explanatory variables, and the corresponding P values are different from those of the initial equation (19a) (with all of the seismic parameters considered initially). In the new regression equation the explanatory variable (seismic parameter), with the maximum P value greater than 0.05, will be eliminated. This elimination procedure is repeatedly applied until all of the P values of the explanatory variables remain less than 0.05. Applying the described procedure to (19a), the sequence of the eliminated parameters is SI after Kappos, SA, SD, SMD, $I_{F/V/F}$, $P_{0.90}$, CP, DP_{A/S}, and PGA/PGV. The result of this procedure is the reduced regression model shown in Table 10. It is not recommended to eliminate all of the explanatory variables that have a P value greater than 0.05 in Figure 3 at once from the regression model in (19a) because the P values are different in the case of stepwise elimination of explanatory variables and in the case of their at-once elimination.

TABLE 10: Reduced multilinear regression model for the OSDI of Park and Ang.

Parameter	Estimate	Lower limit	Upper limit
Constant	-0.015	-0.031	0.001
PGA	0.367	0.235	0.500
PGV	0.111	0.017	0.206
I_0	0.007	0.005	0.009
RMS _a	-0.082	-0.149	-0.014
SI _H	0.037	0.003	0.072
SI _{MR}	-0.354	-0.496	-0.212
EPA	-0.430	-0.683	-0.176
EPA _{max}	0.086	0.016	0.157
E_{inp}	0.023	0.012	0.035
CAV	-0.028	-0.046	-0.009
SV	0.166	0.120	0.213

TABLE 11: Reduced multilinear regression model for the MISDR.

Parameter	Estimate	Lower limit	Upper limit
Constant	0.003	-0.104	0.110
PGA	2.217	1.309	3.126
I_0	0.039	0.029	0.050
SI _H	0.190	0.041	0.339
SI _{MR}	-2.542	-3.393	-1.691
CAV	-0.353	-0.475	-0.231
DP _{A/S}	0.974	0.281	1.668
SD	-2.431	-4.541	-0.320
SV	1.836	1.413	2.259

Thus, in accordance with the proposed stepwise elimination procedure with a P value greater than 0.05 criterion, Tables 10, 11, and 12 show the reduced multilinear models (Model 2) for the OSDI of Park and Ang ($R^2 = 0.856131$), the MISDR ($R^2 = 0.795159$), and the OSDI (maximum softening index) of DiPasquale and Cakmak ($R^2 = 0.757862$) with their respective 95% confidence intervals.

The independent variables in the reduced regression model are selected by the proposed statistical procedure primarily to predict the damage indicator and not to explain it physically. Therefore, it is not unexpected that different seismic parameters are used for the adequate prediction of different damage indices (Tables 10–12).

The multilinear regression is a robust procedure, even for the case in which two or more explanatory variables are linearly dependent or highly correlated. Perfect multicollinearity occurs when two or more explanatory variables in the multilinear regression are linearly dependent. This multicollinearity type is rare. Imperfect multicollinearity occurs when two or more regressors are highly correlated. Perfect and imperfect multicollinearity does not affect the overall predictive power or reliability of the regression model. However, multicollinearity does reduce the effectiveness of a regression analysis if its primary purpose is to determine the specific effects of the various independent variables. The goal of the present study is to predict the dependent

TABLE 12: Reduced multilinear regression model for the OSDI of DiPasquale and Cakmak.

Parameter	Estimate	Lower limit	Upper limit
Constant	-0.092	-0.126	-0.059
PGA	0.289	0.131	0.448
PGA/PGV	0.015	0.005	0.024
SI _K	0.191	0.073	0.310
SI _{MR}	-0.243	-0.398	-0.087
E_{inp}	0.085	0.063	0.107
CAV	-0.021	-0.038	-0.005
DP _{A/S}	-0.743	-0.995	-0.491
CP	0.121	0.051	0.190
SD	0.468	0.144	0.793

variable (damage indices) from a set of independent variables (seismic intensity parameters); therefore, multicollinearity does not affect the quality of the proposed multilinear regression model. Nevertheless, the proposed stepwise backward elimination procedure reduces the number of independent variables and consequently provides models with less multicollinearity. An a priori omission of several independent variables includes the risk of becoming an untrustworthy model.

7. Testing the Multilinear Regression Model

To verify the quality of the full (Model 1) and the reduced (Model 2) regression models, in general, it is sufficient that the validation data set is a fraction of the training data set. In the present study, the validation data consists of 410 accelerograms, separated into two sets. The first one is identical to the 400 accelerograms used for the training phase of the regression model, as shown in Table 2. The second set is from an entirely different set of 10 artificial accelerograms. In their original form, the latter are compatible with the design spectrum employed. Thus, set 1 is used as internal and set 2 as external validation set. This is common validation procedure in statistical analyses. Two utilized artificial accelerograms are presented in Figure 4. Because the examined frame structure is designed using the same spectrum to which the artificial accelerograms are compatible, the expected damage grade will be low. However, the proposed statistical models must also be verified for medium, large, and total damage grades. Therefore, some of the artificial accelerograms have been scaled (the ordinates of the considered seismic accelerogram have been multiplied by a factor with a value greater than one) to achieve medium, large, and total damage grades. Thus, some of these accelerograms have been scaled to produce medium, large, and total structural damages for each of the examined damage indicators. The program SIMQKE [31] has been utilized to create the aforementioned artificial accelerograms. The method used by the program for the artificial seismic accelerogram generation is the superposition of sinusoids having random phase angles and amplitudes derived from a stationary power spectral density function of the motion. The produced signals

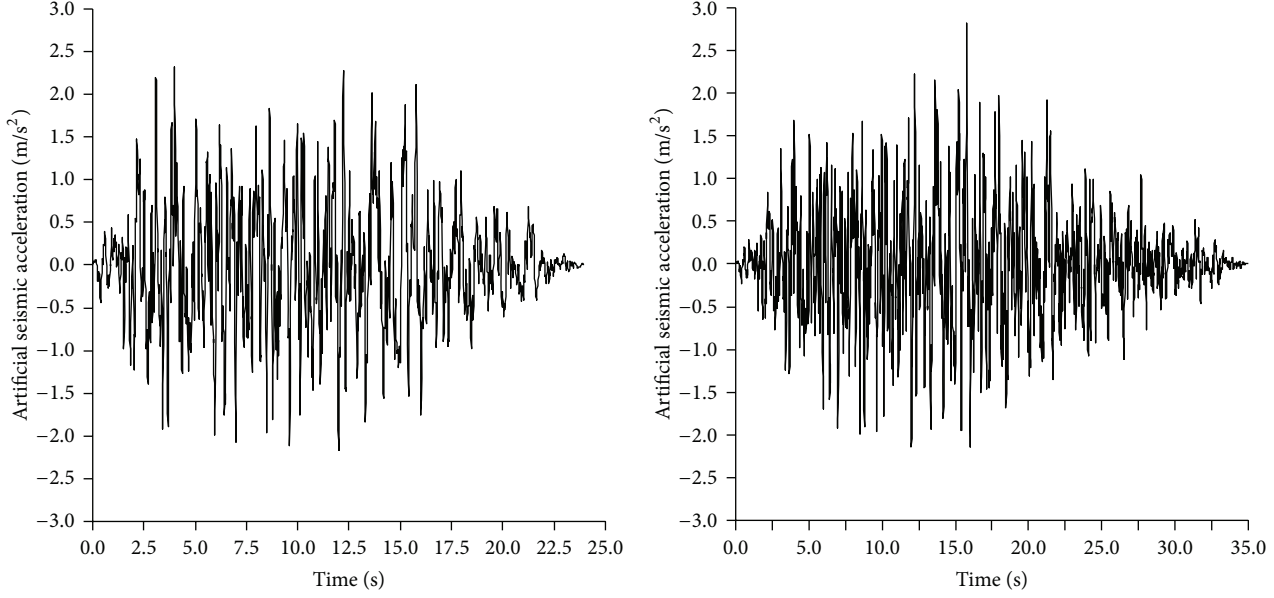


FIGURE 4: Two utilized artificial accelerograms.

TABLE 13: Damage prediction results for the regression models.

Regression	OSDI	Correctly predicted damage values	
		Set 1	
		400 accelerograms	10 accelerograms
Model 1	$\text{DI}_{\text{P/A,Global}}$	386 (96.50%)	9 (90%)
	MISDR	390 (97.50%)	8 (80%)
	δ_M	379 (94.75%)	8 (80%)
Model 2	$\text{DI}_{\text{P/A,Global}}$	385 (96.25%)	9 (90%)
	MISDR	388 (97.00%)	8 (80%)
	δ_M	380 (95.00%)	7 (70%)

are then enveloped in a trapezoidal shape to simulate the nonstationary characteristics of the ground motion [31]. The following input data are required for the generation of the artificial accelerograms: peak ground acceleration (PGA), total duration (TD), duration of the ascending and the descending parts of the trapezoidal envelope, and design spectrum with which the artificial accelerograms must be compatible. Another option is to use natural accelerograms instead of the artificial accelerograms to verify the proposed models. Scaling an accelerogram to a greater PGA value is a simple procedure to produce accelerograms with more energy content and damage potential. The seismic intensity parameters have been evaluated also for all the utilized scaled accelerograms because they change with the scaling process.

Table 13 presents the prediction results of all of the examined damage indicators. In this context, correct prediction means that the evaluated damage index lies within the 95% confidence interval of the multilinear regression model, as provided in Tables 6–12. Thus, the results of Model 1 display correct predictions, from 94.75% to 97.50% and from 80% to 90% for acceleration sets 1 and 2, respectively. In addition,

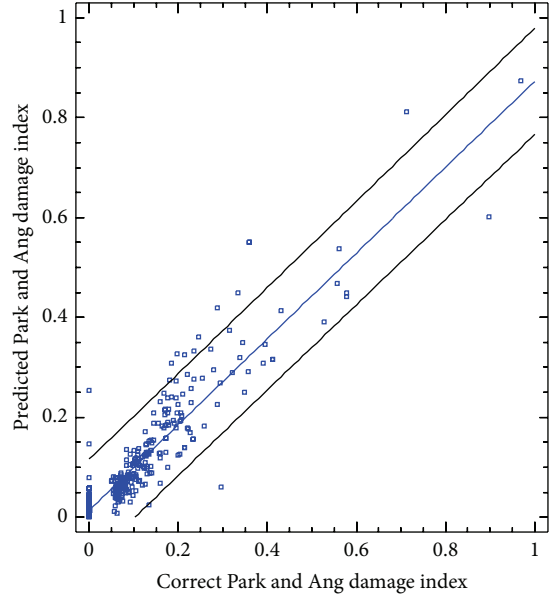


FIGURE 5: Regression line and the 95% confidence interval of the correct versus predicted Park and Ang OSDI values.

Figure 5 shows the regression line and the 95% confidence interval of the correct versus predicted Park and Ang OSDI values. In this case the coefficient of determination $R^2 = 85.9\%$. This indicates that the model as fitted explains 85.9% of the variability in Park and Ang damage index. Furthermore, the percentages of correct prediction for Model 2 are from 95% to 97% and from 70% to 90% for acceleration sets 1 and 2, respectively. Model 2, with its reduced number of seismic parameters in the regression model, is not of poorer quality than Model 1, and the results of acceleration set

TABLE 14: Correlation coefficients between correct and predicted OSDI values based on regression analyses.

Regression	OSDI	Correlation coefficients			
		Set 1		Set 2	
		400 accelerograms		10 accelerograms	
Model 1	Pearson correlation	Spearman rank correlation	Pearson correlation	Spearman rank correlation	
	DI _{P/A,Global}	0.927	0.912	0.975	0.953
	MISDR	0.894	0.921	0.979	0.958
Model 2	δ _M	0.874	0.841	0.962	0.833
	DI _{P/A,Global}	0.925	0.913	0.977	0.953
	MISDR	0.892	0.933	0.982	0.967
	δ _M	0.871	0.846	0.982	0.827

2 are satisfactory, particularly for the OSDI of Park and Ang and the MISDR. Finally, Table 14 shows the Pearson and the Spearman rank correlation coefficients between the correct and predicted values of all examined OSDIs based on regression analyses. The numerical results show a high correlation in all cases.

8. Discriminant Analysis

In the case for which it is sufficient to know the Postseismic damage grade as provided in Table 5 (low, medium, large, and total), then a statistical discriminant analysis can be performed. The purpose of discriminant analysis is to classify objects into one or more possible groups based on a set of features that describe the objects [32]. In general, we assign an object to one of a number of predetermined groups based on observations made about the object. The discriminant analysis creates an equation which will minimize the possibility of misclassifying cases into their respective groups or categories.

The principle is to find the discriminant functions for each group. The element to be classified belongs to the group with the greatest value of the discriminant functions. In the present study, four groups and twenty independent parameters are used. Thus, the discriminant functions are given by the relations

$$\begin{aligned} F_1 &= a_{0,1} + a_{1,1}X_{1,1} + a_{2,1}X_{2,1} + \cdots + a_{20,1}X_{20,1}, \\ F_2 &= a_{0,2} + a_{1,2}X_{1,2} + a_{2,2}X_{2,2} + \cdots + a_{20,2}X_{20,2}, \\ F_3 &= a_{0,3} + a_{1,3}X_{1,3} + a_{2,3}X_{2,3} + \cdots + a_{20,3}X_{20,3}, \\ F_4 &= a_{0,4} + a_{1,4}X_{1,4} + a_{2,4}X_{2,4} + \cdots + a_{20,4}X_{20,4}, \end{aligned} \quad (20)$$

where F_i are the discriminant functions, $a_{j,i}$ are parameters to be specified, and $X_{j,i}$ are known quantities. Here, $i = 4$ (four damage grade groups) and $j = 20$ (twenty seismic parameters). The discriminant analysis has a direct analytical solution and therefore, calculations are very fast. The produced models are concise and easily programmed. On the other hand, the discriminant analysis is sensitive to outliers.

9. Testing the Discriminant Analysis Model

To verify the quality of the discriminate analysis, the same two sets of accelerograms from the regression analysis have

TABLE 15: Damage prediction results for the discriminant analysis.

OSDI	Correctly predicted damage grade	
	Set 1	
	400 accelerograms	10 accelerograms
DI _{P/A,Global}	390 (97.50%)	7 (70%)
MISDR	351 (87.75%)	8 (80%)
δ _M	374 (93.50%)	9 (90%)

been used. Table 15 presents the prediction results of all of the examined damage indicators. In this context, correct prediction means that the damage grade estimate by the discriminant analysis agrees with the corresponding evaluation of the nonlinear dynamic analysis. The results display correct predictions from 87.75% to 97.50% and from 70% to 90% for acceleration sets 1 and 2, respectively. Figure 6 shows the correct versus predicted damage grade based on the Park and Ang OSDI values. The points out of the diagonal line show the incorrect classified cases. Thus, 9 cases have been classified in damage group 2 (medium damage) instead of the correct damage group 1 (low damage) and 1 case has been classified in damage group 2 (medium damage) instead of the correct damage group 4 (total damage). The points in the diagonal line show the correct classified cases (390 cases, 97.5%). The corresponding discriminating functions have been evaluated with P values less than 0.05 and are statistically significant at the 95.0% confidence level. Thus, all points in Figure 6 are inside the 95.0% confidence interval.

10. Remarks on the Proposed Statistical Procedures

The proposed regression models (Tables 6–12) and discriminant analysis model are clearly tailored to the examined reinforced concrete frame structure. For another structure, the nonlinear dynamic analyses should be repeated to determine the coefficients in the regression models (Tables 6–9) and in the discriminant analysis model. Although the proposed procedures are applied to a two-dimensional reinforced concrete frame as an example, they could be applied to any two-dimensional frame and expanded to three-dimensional frames for other building materials (e.g., steel, masonry, timber) or to other building types (e.g., bridges, shell structures).

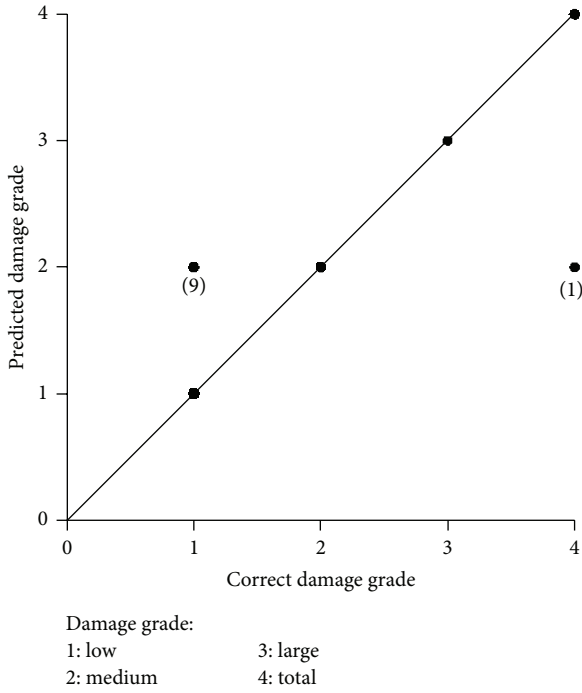


FIGURE 6: Discriminant analysis results. Correct versus predicted damage grade based on the Park and Ang OSDI values.

Furthermore, the set of twenty seismic intensity parameters considered here could be extended with additional quantities or partially or totally replaced by other parameters. However, the proposed procedure remains the same regardless of the structure examined and seismic intensity parameters employed. Thus, in the first step, a set of seismic intensity parameters is evaluated for a set of accelerograms. Then, nonlinear dynamic analyses furnish the damage indices of the considered structure. In the final step, the coefficients of the proposed statistical models (multivariate regression and discriminant analysis) are determined.

The proposed procedures are simple and accurate tools for the estimation of the damage index of a building by a multivariate regression analysis and of its Postseismic damage grade by discriminant analysis. These multivariate statistical techniques do not replace the exact nonlinear dynamic analyses, which are necessary to determine the coefficients of the statistical models, but they do serve as a simple utility for the Postseismic damage status estimation of a specific building based on seismic intensity parameters. Evaluation of the coefficients in statistical models, in which nonlinear dynamic analyses are obligatory, must be performed by professional engineers. If the models have been defined, then they may feasibly be applied by nonspecialists. The presumption is that the seismic parameters employed are known or estimated. The nonlinear analyses and determination of the proposed statistical models are complicated and time-consuming numerical procedures that must be performed by professional engineers (e.g., this can be realized in connection with the design procedure of a considered new building and the evaluated statistical models can be announced to the

building owner and the housing authority). The statistical models are determined by the evaluation of the coefficients in (18) and (20) for the regression and discriminant models, respectively. These statistical models can be easily and quickly applied once they are resolved. They could also be used by nonspecialists under the assumption that the seismic intensity parameters for an actual seismic event are provided by the responsible authorities (e.g., seismological institutes). The proposed methods convert the complicated dynamic nonlinear models to black boxes that take the ground motion information and predict the Postseismic damage levels. Thus, as mentioned in the introduction section, the proposed procedures can be applied to damage scenarios of important buildings (e.g., hospitals, schools, bridges, silos, and hangars) by public authorities. The proposed statistical models are faster and easier to use than the nonlinear dynamic analyses. Epigrammatic, nonlinear dynamic analyses can be utilized only by specialists, while on the other hand, the proposed statistical models can be utilized also by nonspecialists. Thus, nonspecialists can approximately evaluate the Postseismic damage status of buildings, ignoring the exact damage values provided by nonlinear dynamic analysis. The exact damage value needs not to be known once the statistical models are resolved. Furthermore, the proposed methods can handle probable uncertainties in the seismic ground motion and variability in structural or material properties by parametric analyses or by their combination with fuzzy logic procedures (fuzzy regression analysis). Finally, the proposed method can also be applied to a group of buildings. In that case, the damage parameters must be appropriately tailored to describe the Postseismic damage status and the proposed statistical procedures can be applied once on the group and not repeatedly on separate buildings. A proper damage status description could be a financial damage index [25].

Alternative procedures for seismic damage potential classification are presented in the literature and are based on intelligent techniques. Thus, fuzzy logic, artificial neural network, neurofuzzy and adaptive neurofuzzy inference systems, and support vector machines techniques have been used for seismic damage potential classification. The efficiency of the intelligent techniques was expressed by the correct classification rates of a set of accelerograms that were not used during the training process. The intelligent techniques provided a correct classification rate between 71% and 97.5%. The results depend on the used procedure, the overall structural damage indices (MISDR or $DI_{P/A,Global}$), and the number of training samples [33]. The intelligent techniques in comparison with the proposed statistical procedures have no significant better correct classification rates and are not appropriate to be used by nonspecialists.

11. Conclusions

Two statistical methods have been presented for the evaluation of the Postseismic damage status of buildings based on the parameters of the seismic excitation. The first is multilinear regression analysis, and the second is discriminant analysis. Twenty seismic parameters have been extracted from the accelerograms employed. The overall damage index

of Park and Ang, the MISDR, and the maximum softening of DiPasquale and Cakmak have been used to describe the damage status of the structures. The multilinear regression has been used for the explicit evaluation of the damage indices. In contrast, the discriminant analysis furnished the Postseismic damage grade of the structures. These statistical procedures, combined with seismic intensity parameters, are novel methodologies in earthquake engineering and advantageous for the estimation of the damage indices and damage grades of buildings after severe seismic excitations.

The proposed statistical methods have been applied to an eight-story reinforced concrete frame structure designed in accordance with the rules of the EC2 and EC8 Eurocodes for reinforced concrete and antiseismic structures, respectively. A set of 400 natural accelerograms has been applied for the training phase of the models. In addition to the first set, a second set of synthetic accelerograms has been used to verify the statistical methods. The numerical results have shown that 94.75–97.50% and 70–90% of the first and second sets of accelerograms, respectively, were correctly classified in accordance with their damage potential for the examined structure within the confidence interval provided by the regression analysis. In addition, the regression model with a reduced number of considered seismic parameters is not of poorer quality than the model that takes all twenty seismic parameters into account. In contrast, the damage grades for 87.75–97.50% and 70–90% of the first and second sets of accelerograms, respectively, were correctly predicted by the discriminant analysis. Thus, these results led to the conclusion that the multilinear regression analysis and discriminant analysis are useful tools for the prediction of the Postseismic damage status when the seismic parameters are known. Finally, based on the regression and the discriminant analysis results of the 10 examined artificial accelerograms (set 2 in Tables 13 and 14), it can be suggested to use the Park and Ang OSDI and the maximum softening index of DiPasquale and Cakmak as appropriate Postseismic damage value and damage grade estimators of a building, respectively.

Conflict of Interests

The author declares that there is no conflict of interests regarding the publication of this paper.

References

- [1] L. Cabañas, B. Benito, and M. Herráiz, “An approach to the measurement of the potential structural damage of earthquake ground motions,” *Earthquake Engineering and Structural Dynamics*, vol. 26, no. 1, pp. 79–92, 1997.
- [2] A. Elenas and K. Meskouris, “Correlation study between seismic acceleration parameters and damage indices of structures,” *Engineering Structures*, vol. 23, no. 6, pp. 698–704, 2001.
- [3] A. Arias, “A measure of earthquake intensity,” in *Seismic Design for Nuclear Power Plants*, R. J. Hansen, Ed., pp. 438–483, MIT Press, Cambridge, Mass, USA, 1970.
- [4] K. Meskouris, *Structural Dynamics: Models, Methods, Examples*, Ernst & Sohn, Berlin, Germany, 2000.
- [5] R. L. Husid, “Analisis de terremotos: analisis general,” *Revista del IDEM*, vol. 8, no. 1, pp. 21–42, 1969.
- [6] M. D. Trifunac and A. G. Brady, “A study on the duration of strong earthquake ground motion,” *Bulletin of the Seismological Society of America*, vol. 65, no. 3, pp. 581–626, 1975.
- [7] P. C. Jennings, “Engineering seismology,” in *Earthquakes: Observation, Theory and Interpretation*, H. Kanamori and E. Boschi, Eds., pp. 138–173, Italian Physical Society, Varenna, Italy, 1982.
- [8] G. W. Housner, “Spectrum intensities of strong motion earthquakes,” in *Proceedings of the Symposium on Earthquake and Blast Effects on Structures*, pp. 20–36, EERI, Oakland, Calif, USA, 1952.
- [9] A. J. Kappos, “Sensitivity of calculated inelastic seismic response to input motion characteristics,” in *Proceedings of the 4th U.S. National Conference on Earthquake Engineering*, pp. 25–34, EERI, Oakland, Calif, USA, 1990.
- [10] J. E. Martinez-Rueda, “Scaling procedure for natural accelerograms based on a system of spectrum intensity scales,” *Earthquake Spectra*, vol. 14, no. 1, pp. 135–152, 1998.
- [11] *Tentative Provisions for the Development of Seismic Regulations for Buildings*, ATC 3-06 Publication, US Government Printing Office, Washington, DC, USA, 1978.
- [12] D. Lungu, A. Aldea, A. Zaicenco, and T. Cornea, “PSHA and GIS technology-tools for seismic hazard macrozonation in Eastern Europe,” in *Proceedings of the 11th European Conference on Earthquake Engineering*, Balkema, Rotterdam, The Netherlands, 1998, CD-ROM.
- [13] C.-M. Uang and V. V. Bertero, “Evaluation of seismic energy in structures,” *Earthquake Engineering & Structural Dynamics*, vol. 19, no. 1, pp. 77–90, 1990.
- [14] R. Araya and G. R. Saragoni, “Earthquake accelerogram destructiveness potential factor,” in *Proceedings of the 8th World Conference on Earthquake Engineering*, pp. 835–842, EERI, El Cerrito, Calif, USA, 1984.
- [15] E. H. Vanmarcke and S. S. P. Lai, “Strong-motion duration and RMS amplitude of earthquake records,” *Bulletin of the Seismological Society of America*, vol. 70, no. 4, pp. 1293–1307, 1980.
- [16] K. Meskouris, W. B. Krätzig, and U. Hanskötter, “Nonlinear computer simulations of seismically excited wall-stiffened reinforced concrete buildings,” in *Proceedings of the 2nd International Conference on Structural Dynamics (EURODYN '93)*, pp. 49–54, Balkema, Lisse, The Netherlands, 1993.
- [17] A. K. Chopra, *Dynamics of Structures*, Prentice-Hall, Englewood Cliffs, NJ, USA, 1995.
- [18] P. Fajfar, T. Vidic, and M. Fischinger, “A measure of earthquake motion capacity to damage medium-period structures,” *Soil Dynamics and Earthquake Engineering*, vol. 9, no. 5, pp. 236–242, 1990.
- [19] Y.-J. Park and A. H.-S. Ang, “Mechanistic seismic damage model for reinforced concrete,” *Journal of Structural Engineering*, vol. 111, no. 4, pp. 722–739, 1985.
- [20] Y. J. Park, A. H.-S. Ang, and Y. K. Wen, “Damage-limiting aseismic design of buildings,” *Earthquake Spectra*, vol. 3, no. 1, pp. 1–26, 1987.
- [21] A. M. Reinhorn, H. Roh, M. Sivaselvan et al., “IDARC2D version 7.0: a program for the inelastic damage analysis of structures,” Tech. Rep. MCEER-09-0006, MCEER, State University of New York at Buffalo, New York, NY, USA, 2009.
- [22] Y. H. Chai, M. J. N. Priestley, and F. Seible, “Analytical model for steel-jacketed RC circular bridge columns,” *Journal of Structural Engineering*, vol. 120, no. 8, pp. 2358–2376, 1994.

- [23] E. DiPasquale and A. S. Cakmak, "Detection and assessment of seismic structural damage," Tech. Rep. NCEER-87-0015, NCEER, State University of New York at Buffalo, New York, NY, USA, 1987.
- [24] S. Rodriguez-Gómez and A. S. Cakmak, "Evaluation of seismic damage indices for reinforced concrete structures," Tech. Rep. NCEER-90-0022, NCEER, State University of New York at Buffalo, New York, NY, USA, 1990.
- [25] S. K. V. Gunturi and H. C. Shah, "Building specific damage estimation," in *Proceedings of the 10th World Conference on Earthquake Engineering*, pp. 6001–6006, Balkema, Rotterdam, The Netherlands, 1992.
- [26] EC2, *Eurocode 2: Design of Concrete Structures—Part 1: General Rules and Rules for Buildings*, European Committee for Standardisation, Brussels, Belgium, 2000.
- [27] EC8, *Eurocode 8: Design of Structures for Earthquake Resistance—Part 1: General Rules, Seismic Actions, and Rules for Buildings*, European Committee for Standardisation, Brussels, Belgium, 2004.
- [28] D. C. Montgomery and G. C. Runger, *Applied Statistics and Probability for Engineers*, John Wiley & Sons, New York, NY, USA, 2003.
- [29] Statpoint Technologies Inc., *STATGRAPHICS Centurion XV User Manual*, StatPoint, Herndon, Va, USA, 2005.
- [30] W. Navidi, *Statistics for Engineers and Scientists*, McGraw-Hill, New York, NY, USA, 2011.
- [31] D. Gasparini and E. H. Vanmarcke, *SIMQKE—A Program for Artificial Motion Generation, User's Manual and Documentation*, Publication no. R76-4, Civil Engineering Department, Massachusetts Institute of Technology, Cambridge, Mass, USA, 1976.
- [32] S. Sharma, *Applied Multivariate Techniques*, John Wiley & Sons, New York, NY, USA, 1996.
- [33] A. Elenas, "Alternative intelligent techniques for seismic damage classification of buildings based on seismic intensity parameters," in *Proceedings of the 2nd International Conference on Soft Computing Technology in Civil, Structural and Environmental Engineering*, pp. 17–39, Civil-Comp Press, Crete, Greece, 2011.

Research Article

Quasistatic Seismic Damage Indicators for RC Structures from Dissipating Energies in Tangential Subspaces

Wilfried B. Krätsig^{1,2} and Yuri S. Petryna³

¹ Institute for Statics & Dynamics, Ruhr-University Bochum, 44780 Bochum, Germany

² Kraetzig & Partners Engineering Consultants, Buscheyplatz 9-13, 44801 Bochum, Germany

³ Technical University of Berlin, Gustav-Meyer-Allee 25, 13355 Berlin, Germany

Correspondence should be addressed to Yuri S. Petryna; yuriy.petryna@tu-berlin.de

Received 4 September 2013; Accepted 29 September 2013; Published 12 January 2014

Academic Editor: Anaxagoras Elenas

Copyright © 2014 W. B. Krätsig and Y. S. Petryna. This is an open access article distributed under the Creative Commons Attribution License, which permits unrestricted use, distribution, and reproduction in any medium, provided the original work is properly cited.

This paper applies recent research on structural damage description to earthquake-resistant design concepts. Based on the primary design aim of life safety, this work adopts the necessity of additional protection aims for property, installation, and equipment. This requires the definition of damage indicators, which are able to quantify the arising structural damage. As in present design, it applies nonlinear quasistatic (pushover) concepts due to code provisions as simplified dynamic design tools. Substituting so nonlinear time-history analyses, seismic low-cycle fatigue of RC structures is approximated in similar manner. The treatment will be embedded into a finite element environment, and the tangential stiffness matrix \mathbf{K}_T in tangential subspaces then is identified as the most general entry for structural damage information. Its spectra of eigenvalues λ_i or natural frequencies ω_i of the structure serve to derive damage indicators D_i , applicable to quasistatic evaluation of seismic damage. Because $\det \mathbf{K}_T = 0$ denotes structural failure, such damage indicators range from virgin situation $D_i = 0$ to failure $D_i = 1$ and thus correspond with FEMA proposals on performance-based seismic design. Finally, the developed concept is checked by reanalyses of two experimentally investigated RC frames.

1. Introduction

The remarkable reduction of life losses in seismic events over the last 75 years is clearly a merit of the enormous increase in research on structural seismic safety. Consequently, due to improvements of earthquake-resistant design concepts and of modern seismic codes, for example, EC 8 [1], earthquakes with thousands of fatalities until far into the 20th century demand nowadays only few ones. But while in several strong earthquakes (San Fernando 1971, Imperial Valley 1979, Loma Prieta 1989, Northridge 1994, Tohoku 2011) life losses remained limited, material losses raised dramatically with each event. This trend cries for new seismic design concepts beyond life protection, namely, a better control of earthquake damage along the structures' paths to seismic failure. This requires a more intensive emphasis on structural seismic damage, which by experience correlates with material losses from installations and equipment.

Structural safety concepts compare actions S on a particular structure with its resistance R , generally for code-prescribed limit states. Structural failure is then defined as

$$\text{failure} = \{f\} := \{R \leq S\}. \quad (1)$$

Code standards transform (1) into limit state conditions $g(\mathbf{X})$ for state vectors \mathbf{X} , the latter as functions of the design variables \mathbf{X}_d :

$$g(\mathbf{X}) = (\gamma_R)^{-1} R(\mathbf{X}) - \gamma_S \times S(\mathbf{X}) \leq 0 \quad \text{for failure}, \\ > 0 \quad \text{for survival}, \quad (2)$$

in which the partial safety factors γ_S of the actions S and γ_R of the resistance R are due to national code regulations. Obviously, (2) formulates structural safety by virtue of force variables at failure point, a customary manner in structural engineering.

Such design concepts are also code prescribed in case of seismic failure. But the explained extension of seismic design aims requires a turn towards structural damage, wherein the seismic damage formation—not force resistance R —has to be prosecuted, until limited by final damage bounds. Consequently, such more advanced protection aims like reduction of material losses must be combined with the basic safety objective of human life protection, which can be done within techniques of performance-based seismic design [2].

Codified seismic design concepts [1] are generally based on (linear elastic) response spectra. Codes favor the use of quasistatic analyses instead of full time histories, corresponding well with quasistatic constitutive laws [3] from monotonic material tests. If linear elastic structural models are applied, the evaluation of damage is impossible, since design formats (2) are tailored towards force-limitations [4]. It is a usual design practice. Inclusion of damage always requires consideration of material nonlinearity. The simplest quasistatic seismic simulation technique then uses nonlinear pushover analyses.

On the other hand, seismic loading creates low-cycle fatigue processes in the materials involved, which after 20 to 1000 sufficiently intensive load cycles will lead to seismic failure. Those damage paths to failure can be marked by damage indicators [5], generally in dynamic settings. But in structural earthquake-resistant design practice, time-history computations—especially with time-dependent material laws—are very rare. So this paper addresses the question whether realistic estimates for such time-dependent structural damage evolutions can be approximated by nonlinear quasistatic damage evaluation.

To approach these aims, the paper will be based on damage-controlled limit states as proposed in performance-based seismic engineering concepts [2]. It then depicts pushover analyses, followed by description and time-invariant approximation of low-cycle (RC) fatigue processes, justifying a quasistatic treatment. The work will close with necessary steps for quasistatic seismic damage evaluation, followed by two applications.

2. Extended Seismic Protection Based on Damage Indicators

Losses in strong seismic events, human as well as material ones, depend on the seismically dismissed energy, the area's population density, the degree of economic development, and the level of earthquake-resistant safety provisions. Buildings have been primarily designed for protection of human lives, but we will also be aware of material losses. As a consequence of this, not only one seismic event (of 475 years of return period) should be considered, but also the building's functionality has to be differentiated.

Figure 1 elucidates this idea in the well-known concept of the Federal Emergency Management Agency (FEMA) [2] and of the Structural Engineers Association of California (SEAOC) [6]. Such performance-based seismic design concept centers the attention towards the quantification of seismic damage in the design, assuming the latter to be correlated

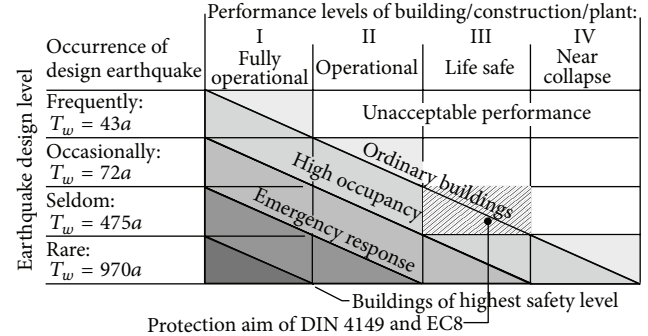


FIGURE 1: Recommended performance objectives for buildings [2].

TABLE 1: Limit states and damage levels according to FEMA 273.

	Structural limit states	Damage levels	Damage indices
ND	No damage, virgin structure	0	0.00
IO	Immediate occupancy	I	0.05
ID	Incipient damage		0.10
LS	Life safety threatens	II	0.20/0.25
CP	Collapse prevention	III	0.40/0.50
IC	Incipient collapse	IV	>0.90

with material losses of installation and equipment. This basic assumption of seismic damage correlation avoids modeling of each installation/equipment element as attached structural component in the computational model, but it remains an empirical working hypothesis requiring the determination of the generated seismic structural damage.

Figure 1 proposes in this sense different protection aims of buildings in the columns, and seismic events of increasing intensities in the rows, measured in return periods T_w [1]. In the diagonal, classes of structures are distinguished with different design damages/vulnerabilities for various seismic events. Table 1 explains the damage states in more detail, introducing damage levels as follows [2].

- (i) Level 0: no damage, virgin structure.
- (ii) Level I: very limited structural damage, no risk of life-threatening injury.
- (iii) Level II: significant damage, low risk of life-threatening injury.
- (iv) Level III: substantial damage, significant risk of injury from falling hazards.
- (v) Level IV: collapse is imminent, highest risk of life to occupants.

FEMA documents, for example, [2, 6], order numerical values to these damage levels; they also propose a normalization from 0.00 (virgin) to 1.00 (seismic failure). But the interesting fact is that no advice is given by FEMA, which of the existing damage indicators is preferred.

In the literature there exist a great variety of damage indices, as can be seen from the survey in [5]. Most indicators describe damage in local cross-sections; thus they are unsuited for damage description of complete structures.

But most important: All indices are rather empirical, and none of them has a sound foundation from mathematics or structural mechanics, as we see on the hybrid PARK-ANG index [7], which combines dissipated energies with inelastic story drifts:

$$D = \frac{\delta_m}{\delta_f} + \beta \frac{E_r}{F_y \delta_f}. \quad (3)$$

Herein δ_m (δ_f) denotes the maximum occurring (bearable) structural displacement. E_r is the total dissipated energy, F_y the structural yield resistance, and β a parameter to be determined by tests [7]. The combination of dissipated energies and story drifts in (3) is really too empirical to be applied in a theoretical sound earthquake-resistant design concepts.

In Section 6 we will derive a set of damage indices D_i , $i = 1, \dots, n$, from inherent mechanical properties of a particular structure's path to seismic failure. These parameters will have the following main properties serving as an optimal basis for earthquake-resistant designs.

- (i) They will be related to the entire structure.
- (ii) They will describe the seismic low-cycle process with a sufficient accuracy from the mechanical viewpoint.
- (iii) They will be based on mechanics, for example, the structural state variables of the seismic process.
- (iv) They will range from 0.00 (undamaged virgin state) to 1.00 (failure).

The authors have certain experiences with indices D_i for damage problems other than seismic ones. They have found that values around 0.6 separate economically structural repairs from reconstruction. This holds especially for RC structures, on which we will now concentrate.

3. Quasistatic Nonlinear Simulation

For application in present anti-seismic design concepts, the further treatment will be quasistatic. Then for monotonic deformation processes of materially nonlinear responding structures, tangential subspace simulations up to failure are well-established tools in present engineering. Because of material degradation of the structural resistance R during earthquakes, seismic damage simulations are nonlinear processes. To derive their governing response equations we imbed the treatment for arbitrary structures into a FE-environment, in which the nodal degrees of freedom are arranged in the m -dimensional vector field

$$\mathbf{V} = \{V_1 \ V_2 \ \dots \ V_i \ \dots \ V_m\}, \quad (4)$$

and the nodal forces, in dual order to \mathbf{V} , in

$$\mathbf{P} = \{P_1 \ P_2 \ \dots \ P_i \ \dots \ P_m\}. \quad (5)$$

In this frame the structural response is governed by the following nonlinear stiffness equation, with \mathbf{G} as the vector functional of the structural resistance R :

$$\mathbf{G}(\mathbf{V}, \mathbf{d}) = \mathbf{P}. \quad (6)$$

This m -dimensional set of nonlinear algebraic equations describes equilibrium/compatibility in terms of the internal resistance \mathbf{G} —with inelastic deformation (\mathbf{V}) and damaging (\mathbf{d}) material model properties—due to an external force process \mathbf{P} . All nonlinear structural properties, anchored generally in the constitutive laws on Gauss point level (see Figure 2), are assumed to be fixed in required quality in \mathbf{G} .

To derive the basis for incremental-iterative solution strategies from (6), we decompose the external nodal kinematics \mathbf{V} and loads \mathbf{P} of a certain structural state into variables $\bar{\mathbf{V}}$, $\bar{\mathbf{P}}$ of a known fundamental state and their unknown increments $\delta\mathbf{V}$, $\delta\mathbf{P}$, reaching from fundamental to neighboring position:

$$\mathbf{V} = \bar{\mathbf{V}} + \delta\mathbf{V}, \quad \mathbf{P} = \bar{\mathbf{P}} + \delta\mathbf{P}. \quad (7)$$

Assuming now all increments as infinitesimally small variations, we gain from the first variation of (6) with respect to the fundamental state $\bar{\mathbf{V}}$, $\bar{\mathbf{P}}$ the m -dimensional set of algebraic equation for the increments $\delta\mathbf{V}$, $\delta\mathbf{P}$; namely,

$$\left. \frac{\partial \mathbf{G}}{\partial \mathbf{V}} \right|_{\bar{\mathbf{V}}} \cdot \delta\mathbf{V} = \delta\mathbf{P}. \quad (8)$$

Substituting herein for the load variation $\delta\mathbf{P} = \mathbf{P} - \bar{\mathbf{P}}$, then for $\bar{\mathbf{P}}$ the left-hand side of the original stiffness relation (6), we receive the tangential stiffness equation, which forms the basis of finally applied iterative solution techniques:

$$\mathbf{K}_T(\bar{\mathbf{V}}, \bar{\mathbf{d}}) \cdot \delta\mathbf{V} = \delta\mathbf{P} = \mathbf{P} - \mathbf{F}_I(\bar{\mathbf{V}}, \bar{\mathbf{d}}), \quad (9)$$

with the vector $\delta\mathbf{V}$ of the increments of the global degrees of freedom, and

$$\mathbf{K}_T = \left. \frac{\partial \mathbf{G}}{\partial \mathbf{V}} \right|_{\bar{\mathbf{V}}} \quad \text{the tangential stiffness matrix}, \quad (10)$$

$$\mathbf{F}_I = \mathbf{G}(\bar{\mathbf{V}}, \bar{\mathbf{d}}) \quad \text{the internal equilibrium force vector.} \quad (11)$$

Since \mathbf{K}_T and \mathbf{F}_I depend on the reached deformation $\bar{\mathbf{V}}$, the tangential stiffness equation requires iterative solution techniques for the increments $\delta\mathbf{V}$. In (9), \mathbf{P} represents the total applied load at a certain solution point, and \mathbf{d} stands for the structural damage, later on detected as function of \mathbf{K}_T .

Materially nonlinear structural analyses, here applied as pushover analyses, can be carried out on rather different levels of mechanical exactness and complexity: beams with plastic hinges, with or without stiffness iterations, are the least complex alternative; nonlinear multilevel (multiscale) simulations form the other extreme [8]. Thus different model complexity may influence the simulation accuracy of (9) and so the later seismic damage detection.

In order to detail (macroscopic) materially nonlinear structural FE simulations [8], we return to a multilevel (multi-scale) simulation concept as the most complex analysis scheme and distinguish the following four simulation levels due to Figure 2.

- (i) The first one is the structural level, on which all variables of the tangential stiffness relation (9) are defined.

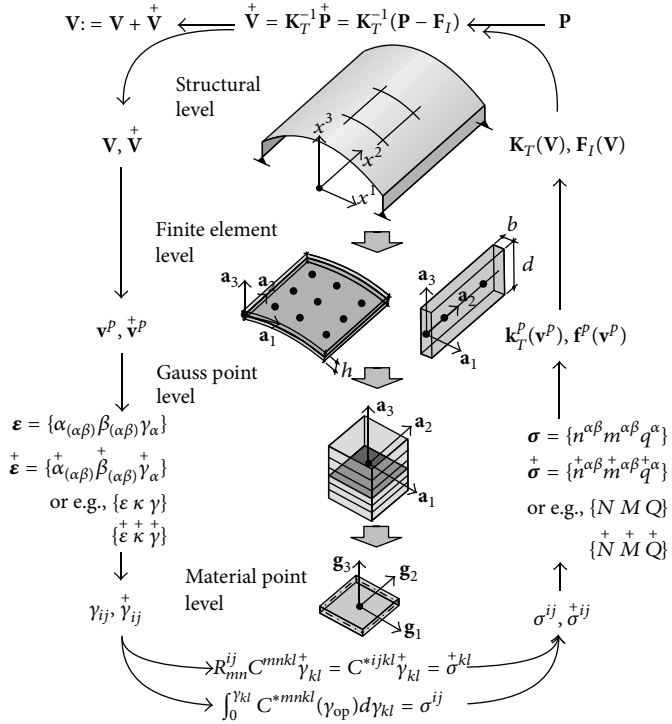


FIGURE 2: Variables and analysis scheme of multilevel simulation technique.

- (ii) The second one is the level of classical FEs (beams, plates, and shells), connected with the previous one by kinematic relations in the nodal points.
- (iii) In the third level, with regard to materially nonlinear actions and damage phenomena, the applied FEs—see Figure 2—are equipped in their GAUSS points with a layered structure, such that each FE-GAUX point consists of a chain of integration subpoints, one in each layer.
- (iv) Finally, at these subpoints on material level, the constitutive relations including their nonlinear properties and failure bounds are defined.

The material point level is generally the lowest macroscopic simulation level in design practice. It collects all material information usually in a 3D ($x^i : x^1, x^2, x^3$) or 2D ($x^\alpha : x^1, x^2$) simulation space. Here suitable constitutive laws of the material components have to be activated [9], for incorporation in K_T and F_I . Applying beam, plate, or shell elements, engineering simplifications for constitutive laws and failure conditions are often in favor, particularly for design purposes (see Section 8).

4. Nonlinear Pushover Analyses

We now return to seismic problems, that means to problems of nonlinear dynamics, if the structure's path until seismic

failure will be investigated. Instead of attempting to solve the original nonlinear equation of motion

$$\mathbf{M} \cdot \ddot{\mathbf{V}} + \mathbf{G}(\dot{\mathbf{V}}, \mathbf{V}, \mathbf{d}) = \mathbf{P}(t), \quad (12)$$

we concentrate for a short moment on the tangential subspace to $\{\dot{\mathbf{V}}, \dot{\mathbf{V}}, \mathbf{V}, \mathbf{P}\}$ and thus on the incremental tangential equation of motion:

$$\mathbf{M} \cdot \delta \ddot{\mathbf{V}} + \mathbf{C}_T \cdot \delta \dot{\mathbf{V}} + \mathbf{K}_T \cdot \delta \mathbf{V} = \mathbf{P}(t) - \mathbf{F}_I(t). \quad (13)$$

The derivation of (13) from the original nonlinear equation of motion (12) can be found in detail in [10]. In (13), the vectors $\{\delta \dot{\mathbf{V}}, \delta \dot{\mathbf{V}}, \delta \mathbf{V}\}$ represent increments of the nodal equivalents, namely, accelerations, velocities, and deformation degrees of freedom. As a nonlinear differential equation in time t , (13) would require time-history solution for an (spectrum-compatible) acceleration functions $a(t)$, with stiffness iterations in each time step.

In the present structural design practice, such complex nonlinear time-history verifications are completely unusual. National seismic codes generally require linear dynamic analyses, if time-history simulations are selected; mostly linear quasistatic formats are applied. Pushover analyses serve since 30 years as approximate quasistatic but nonlinear substitution.

Pushover analyses [4, 11] are based on standardized design spectra of the respective site [12], generally prescribed in the respective code, and on dynamic structural properties, namely, mode shapes as well as natural frequencies of

the undamaged structure. A pushover analysis consists of the following essential steps [13].

- (i) We select a (code-given) design spectrum of seismic accelerations for the building site.
- (ii) The considered structure is represented by a suitable FE discretization, and all (nonlinear) material properties on suitable structural levels (Figure 2) are specified.
- (iii) Execution of an eigenvalue analysis of the undamaged linear-elastic structural model to receive critical natural frequencies (or periods) and corresponding mode shapes. From them follow the modal participation factors, which form the seismic load bases for each mode shape in each structural point.
- (iv) With all these information the design spectrum delivers maximum seismic modal excitation loads and maximum modal pseudodeformations.
- (v) Both groups of variables are then united by modal superposition, if different mode shapes participate in the seismic response.
- (vi) These superposed seismic nodal loads are applied in incremental manner on the structure for a quasistatic nonlinear simulation process, the pushover analysis. It stops after all seismic loads are applied, the structural model fails, or the deformation limit has been reached. The gained stress resultants then are the basis of the seismic design, as detailed in [12, 14].

In summary, pushover verifications are nonlinear quasistatic approximations of a highly nonlinear dynamic loading process. So one can never expect exact correspondence of their solutions compared to those ones of nonlinear time-history analyses. But from comparable simulations in the literature it seems to hold true that pushover analyses deliver mostly some upper bounds of the internal forces, not far away from physical reality. In engineering design practice these strong deficiencies of pushover concepts, mainly the incognizance of the true alternating seismic actions towards failure [11], and the ignorance of the structural stiffness weakening are allowed, if nonlinearity will be taken into account in a simple manner.

All values of dynamic structural stiffness used in this approximate analysis stem from the undamaged (virgin) structure. The fact that they will decrease during the seismic damage process and may finally end up with those ones of the deadly injured structure may confirm the suspicion that the pushover concept delivers upper bounds of the design variables, since generally inelastic mechanisms reduce the design forces [4, 15].

In spite of all these deficiencies, pushover analyses will be considered as the background of this present work for time-independent seismic damage evaluation and to estimate seismic vulnerabilities of structures under design. Before detailing this we will now have a look into low-cycle fatigue processes to also find for them a quasistatic approximation.

5. Quasistatic Damage Approximation of Low-Cycle Fatigue

Seismic failure of RC structures or their components follows a low-cycle fatigue process, in which after 20–100 stress-strain alternations of sufficient intensity cross-sections will fail. In modern research, such fatigue processes are treated as complex phenomena on mesoscale with detailed description of crack-formation, crack-closing, bond-slip, and internal stress redistribution. In the design of structures, empirical macroscopic models for low-cycle fatigue failure are applied; the most modern ones are based on dissipated energies, whereby close correspondence to monotonic failure of RC specimen is aspired [16, 17].

Some energetic contribution has been modeled also in the second contribution of the PARK-ANG indicator (3), in an extremely simplified and unsatisfying manner. Accepting the properties of damage indices from Section 2, a much better damage description is the D_Q -index introduced in [17]. This indicator consists solely of dissipated energies of cyclic deformations, up to failure. D_Q has a sound theoretical (macroscopic) basis and has been tested extensively in large-scale experiments [17] on beams, columns, and beam-column connections. Bending as well as normal and shear force failure has been considered. For cyclic failure on one side of a particular cross-section, the D_Q -index distinguishes primary half cycles (energies of new deformation amplitudes) and secondary half cycles (energies of redeformation amplitudes) of the cyclic damage process, a distinction discovered by [18]. For all further D_Q -details the reader is referred to [5, 17].

In the following, we present a brief explanation for a cross-section with double reinforcement under cyclic bending. In the moment-curvature ($M-\kappa$) plane, as explained in Figure 3, two damage contributions D_Q^+ for positive deformation and D_Q^- for negative deformation are defined as

$$D_Q^+ = \frac{E_P^+ + E_S^+}{E_M^+ + E_S^+}, \quad D_Q^- = \frac{E_P^- + E_S^-}{E_M^- + E_S^-}, \quad (14)$$

with E_P^+ as complete dissipated energies of all primary half cycles, E_S^+ as complete dissipated energies of all secondary half cycles, and E_M^+ as dissipated failure energy for monotonic deformation, all for positive deformation. The minus sign in (14) holds for negative deformation (reverse deformation cycles). From these constituents, the final D_Q -indicator is defined as follows:

$$D_Q = D_Q^+ + D_Q^- + D_Q^+ * D_Q^-. \quad (15)$$

This indicator can be formed successively during numerical time-step integration or from recorded dynamic test data. As observed from (14) and (15), D_Q is scaled such that the virgin situation starts with $D_Q = 0$, and failure is designated for $D_Q = 1$. Figures 4 and 5 demonstrate these properties by a recalculation of an elderly beam experiment from Berkeley [5].

In quasistatic approximations, for example, pushover analyses, all time-history integrations have to be avoided. So

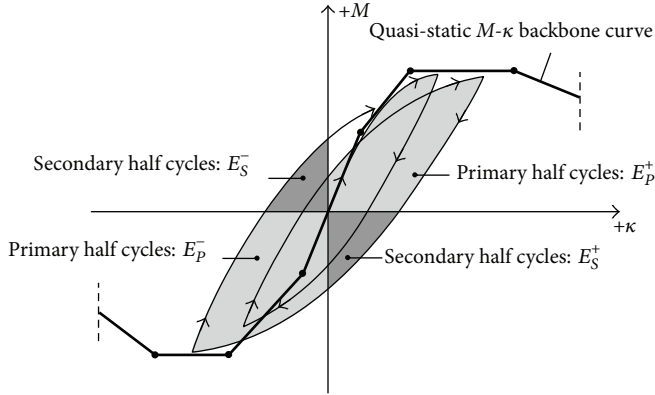


FIGURE 3: Cyclic deformation and dissipated energies.

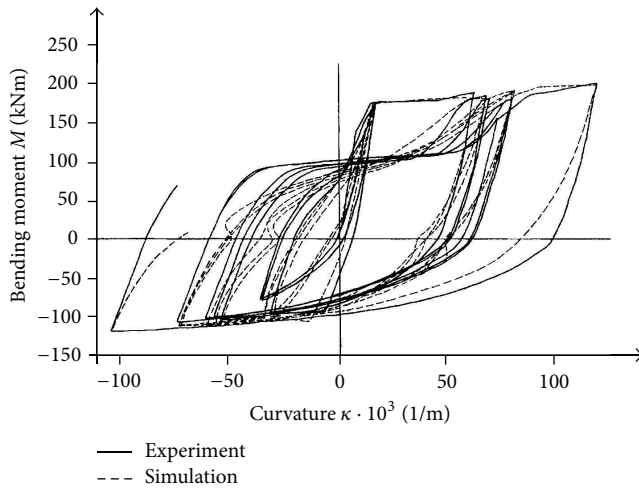


FIGURE 4: Moment-curvature relation of a cyclically loaded test beam.

energy? For proof, we transform one of the parameters from (14) into an infinite TAYLOR-series:

$$D_Q^+ = \frac{E_P^+}{E_M^+} + \frac{E_S^+}{E_M^+} \left(1 - \frac{E_P^+}{E_M^+} \right) - \left(\frac{E_S^+}{E_M^+} \right)^2 \left(1 - \frac{E_P^+}{E_M^+} \right)^2 + \dots \quad (16)$$

We observe thereby that the normalized monotonic energies E_P^+/E_M^+ , determinable just from quasistatic analyses, form the first and dominant terms in D_Q^+ , respectively. All the following energy contributions in (16) obviously can be considered as correction terms of higher order.

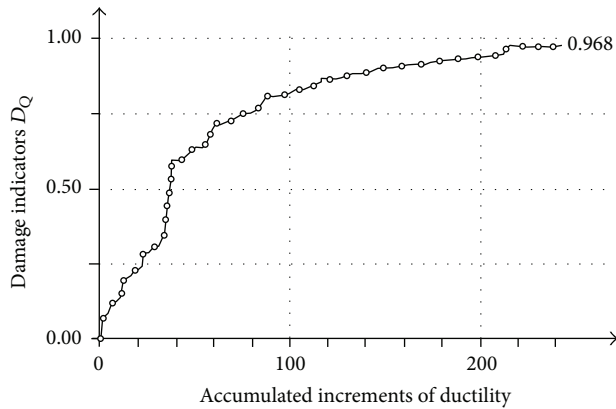
We now transform this recognition to complete structures. For design purposes, we are primarily interested in the maximum seismic damage. The upper limit $D_Q^+ = 1$ of (16) is formed for $E_P^+ \Rightarrow E_M^+$, so a quasistatic failure analysis seems well applicable to determine the upper limits of contributing sectional damage. Consequently, estimation of structural damage from pushover concepts can be transferred as an upper limit estimate to the entire structures.

6. Time-Invariant Approximation of Seismic Damage

During a seismic event of sufficient intensity, RC structures will be weakened by inelastic actions and eventually fail. This degradation process can be monitored as a successive stiffness reduction of the structural resistance R , reflected in the vector functional \mathbf{G} (6). Since structural damage \mathbf{d} depends also on the forming inelastic deformation, the tangential stiffness matrix \mathbf{K}_T (10) is considered as the most suitable entry for damage description [19, 20].

The damage measures, later defined in (18), had been derived mainly for deterioration and life-duration problems of structures, in which the time scale is enlarged compared to physical time t , such that quasistatic treatment is justified. Using time-independent pushover analyses as approximation of nonlinear structural seismic processes, time is completely deleted, such that quasistatic damage description is the only alternative.

How is \mathbf{K}_T connected with structural softening and failure? Figure 6 repeats the basic fact that for integer structures

FIGURE 5: D_Q -damage evolution corresponding to Figure 4.

still for one single cross-section we set up the question if D_Q can be approximated by a monotonic deformation process, only using the backbone curve and its monotonic failure

Definition: structural integrity is defined by stable equilibrium paths (for simplicity, structural instabilities are excluded)

$$[\mathbf{K}_T] \cdot [\dot{\mathbf{V}}] = [\mathbf{P}] - [\mathbf{F}_i] \longrightarrow [\dot{\mathbf{V}}] = [\mathbf{K}_T^{-1}] \cdot ([\mathbf{P}] - [\mathbf{F}_i])$$

Prerequisites for structural integrity:

\mathbf{K}_T : nonsingular $\det \mathbf{K}_T \neq 0$

positive definite $\dot{\mathbf{V}}^T \cdot \mathbf{K}_T \cdot \dot{\mathbf{V}} > 0$

all eigenvalues $\lambda_i > 0, 1 \leq i \leq m$

FIGURE 6: Conditions for structural integrity.

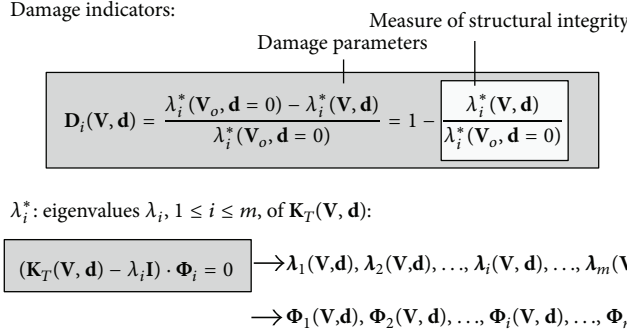


FIGURE 7: Definition of damage indicators.

\mathbf{K}_T is regular and positive definite; thus all its (hypothetically) transformed main diagonal elements are positive. In case of structural failure, \mathbf{K}_T gets singular, $\det \mathbf{K}_T = 0$ and thus at least one main diagonal stiffness element vanishes. So \mathbf{K}_T accompanies all quasistatic structural responses, also time-independently approximated seismic ones, from structural birth until final failure [9, 19–21].

Since \mathbf{K}_T (generally) is quadratic and symmetric, it can be transformed into a diagonal form, with the eigenvalues $\lambda_i, i = 1, 2, \dots, m$, as principal stiffness elements

$$\bar{\mathbf{K}}_T = \text{diag}\{\lambda_1 \ \lambda_2 \ \dots \ \lambda_i \ \dots \ \lambda_m\}. \quad (17)$$

The diagonal matrix (17) can be used to form sets of damage indicators $D_i, i = 1, 2, \dots, m$, as repeated in detail in Figure 7:

$$D_i = \frac{\lambda_i(\mathbf{V}_0, \mathbf{d} = 0) - \lambda_i(\mathbf{V}, \mathbf{d})}{\lambda_i(\mathbf{V}_0, \mathbf{d} = 0)} = 1 - \frac{\lambda_i(\mathbf{V}, \mathbf{d})}{\lambda_i(\mathbf{V}_0, \mathbf{d} = 0)}. \quad (18)$$

From this definition we observe that the elements of D_i take values between $D_i = 0$ for the undamaged state and $D_i = 1$ for the failure state. Obviously, these damage indicators are able to denote properly all additional limit states from Table 1. Further, they have been gained as inherent structural mechanics properties of a considered structure, controlled by its nonlinear quasistatic seismic response path. Obviously, the D_i have a much more sound foundation than all other damage indicators, also that PARK-ANG index (3).

As explained in Figure 7, damage indicators (18) are defined by using the eigenvalues of \mathbf{K}_T as state variables of a certain deformed structural situation. For evaluation, in each damage state these eigenvalues have to be solved from the eigenvalue problem

$$[\mathbf{K}_T(\mathbf{V}, \mathbf{d}) - \Lambda] \cdot \Phi_\lambda = \mathbf{0}. \quad (19)$$

Herein, Λ forms a $(m * m)$ diagonal matrix of all eigenvalues λ_i , the actual principal stiffness elements of the structure. Φ_λ assembles the rows of eigenvectors (eigenmode shapes) of \mathbf{K}_T . If we remember orthogonality of Φ_λ , we find from (19) by left multiplication with Φ_λ^T

$$\Phi_\lambda^T \Phi_\lambda = \mathbf{I} \implies \Lambda = \bar{\mathbf{K}}_T = \Phi_\lambda^T \mathbf{K}_T(\mathbf{V}, \mathbf{d}) \Phi_\lambda, \quad (20)$$

that the matrix Λ describes physically an energy. Because \mathbf{K}_T is defined in the tangential subspace of the increments $\{\delta \mathbf{V}, \delta \mathbf{P}\}$, Λ can be interpreted as virtually dissipated energy at the point of \mathbf{K}_T .

Classical nonlinear structural dynamics offers a highly efficient extension of (17), (19) for practical damage detection, in numerical simulation as well as in physical testing. Therefore we superpose upon an actual nonlinearly deformed, quasistatic state of response $(\mathbf{P}, \mathbf{V}, \mathbf{d})$ of the considered structure an infinite set of infinitesimally small harmonic vibrations

$$\delta \mathbf{P} = \mathbf{0}: (\mathbf{K}_T - \omega_i^2 \mathbf{M}) \cdot \delta \mathbf{V} = \mathbf{0}, \quad i = 1, \dots, m. \quad (21)$$

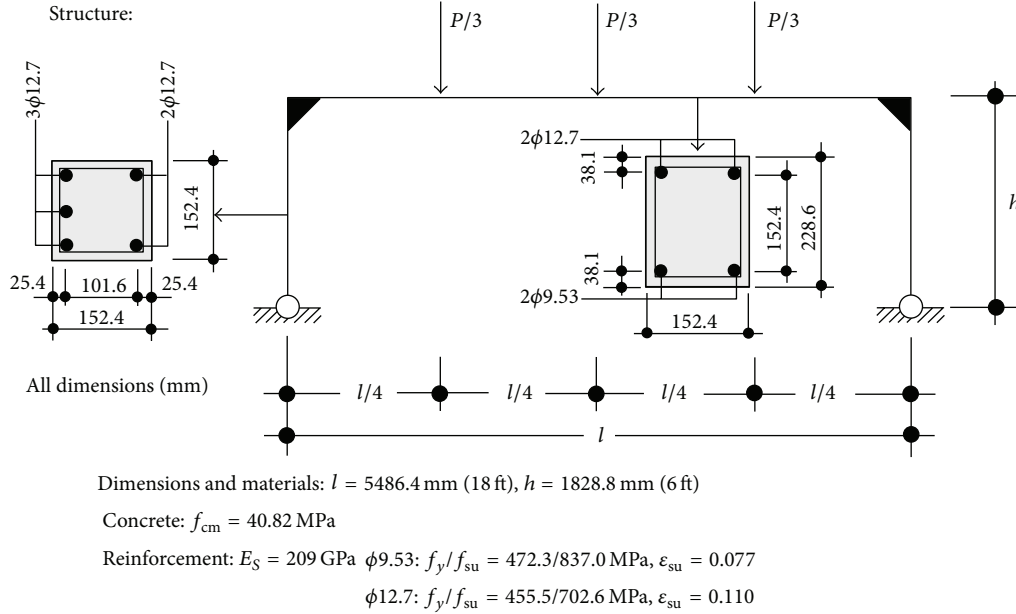


FIGURE 8: Dimensions and material specifications of RC test frame.

Studying the (squared) frequency spectrum ω_i^2 as a solution of the eigenvalue problem (21), the latter delivers for zeros of \mathbf{K}_T the statement $\omega_i^2 = 0$, identical with the quasistatic failure condition $\det \mathbf{K}_T = 0$. So for \mathbf{M} distributed evenly over the structure, eigenfrequencies ω_i are likewise well suited as the eigenvalues λ_i in (17) for damage detection:

$$[\mathbf{K}_T(\mathbf{V}, \mathbf{d}) - \Omega \mathbf{M}] \cdot \Phi_\omega = \mathbf{0}. \quad (22)$$

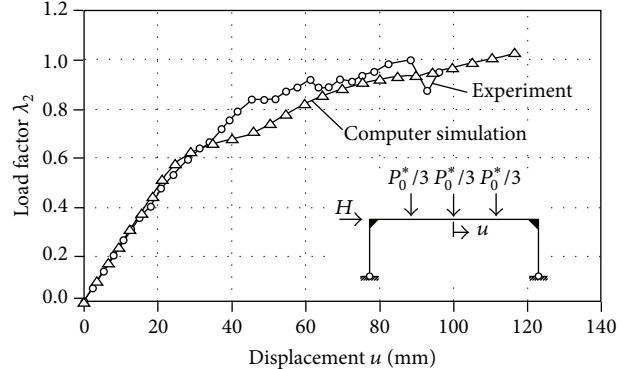
Herein Ω forms a $(m * m)$ diagonal matrix with the (squared) frequency spectrum ω_i^2 on its main diagonal. The $(m * m)$ square matrix Φ_ω collects the rows of all m vibration mode shapes. From (21) we derive by left-hand multiplication with Φ_ω^T

$$\Phi_\omega^T \mathbf{M} \Phi_\omega = \mathbf{I} \implies \Omega = \text{diag}\{\omega_i^2\} = \Phi_\omega^T \mathbf{K}_T(\mathbf{V}, \mathbf{d}) \Phi_\omega, \quad (23)$$

interpreting ω_i^2 as virtually dissipating energies of the modal forces ($\mathbf{K}_T \Phi_\omega$) along the virtual vibration mode shapes Φ_ω^T . An analogous energy interpretation has just been drawn from (20). The use of eigenfrequencies ω_i for evaluation of damage indicators compared to eigenvalues λ_i is advantageous, because of generally less problems in setting up (22) compared to (19). This substitution holds true, because both matrices Λ and Ω can be related to each other by:

$$\Lambda = \Phi_\omega^T \mathbf{M} \Phi_\lambda \Omega \Phi_\lambda^{-1} \Phi_\omega. \quad (24)$$

In the literature, also more complex functions of the eigenvalues λ_i are recommended for formation of damage indicators [6] due to the definition on top of Figure 7.

FIGURE 9: Load-deflection diagram for horizontal loading H .

7. Example 1: Damage Formation in RC Test Frame

We now demonstrate the application of the derived damage concept by hand of a RC test frame, the testing of which had been published in detail 40 years ago [22]. The test frame as well as all necessary geometrical and material data of this experiment is reprinted in Figure 8.

The 2-hinge test frame carries three equal loads $P/3$ in the quarter-points of the girder, and one horizontal load H on the girder due to Figure 9. For an anti-seismic design, the evaluation of H from a seismic design spectrum due to the steps in Chapter 4 is straight forward. In one of the experiments [22], the test frame first was predamaged by a total vertical loading up to $P_0^* = 26.5 \text{ kN}$. Maintaining this load then the horizontal (pushover) load H as sketched in Figure 9 has been applied and increased until failure of the structure at $H = 14.2 \text{ kN}$.

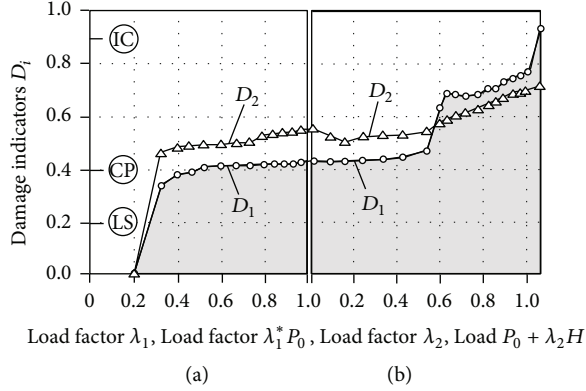


FIGURE 10: Damage indicators for vertical (a) load and additional horizontal (b) load H .

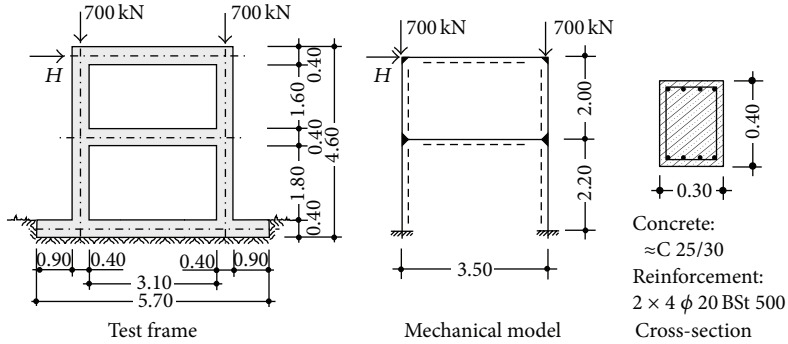


FIGURE 11: 2-story RC test frame.

The load-deformation diagram $P(V, d)$ of the second loading phase, the application of the horizontal force, in Figure 9 plots H against the horizontal girder displacement u . Therein both the experimentally monitored and the computed deformations are plotted, the latter evaluated by the described multilevel-simulation concept in a complicated nonlinear analysis. Both curves show sufficient correspondence for encouragement of the damage simulation.

Those results are depicted in Figure 10 for both damage variables D_1 , D_2 , based on the eigenvalues λ_1 , λ_2 . The computed damage variables D_1 , D_2 are plotted there in the left part of the Figure as functions of the vertical loading, then in the right part as functions of the horizontal (pushover) load H . Details of the complicated nonlinear load-deformation process can be observed much clearer by hand of the damage evolution on this latter Figure. Obviously, D_1 describes the structure's path to final failure, although its effect under vertical loading is less than D_2 . At the point of the extreme load H , structural equilibrium could be iterated for the last time, terminating the final damage evolution in Figure 10(b) somewhere between 0.90 and 1.00, close to the theoretical unit value.

8. Example 2: Damage Formation of a 2-Story RC Frame

A 2-story RC frame will serve as second example, the testing of which had been described in [23]. Figure 11 depicts all

necessary dimensions, with equal cross-sections of both beams and columns. In this example, the frame model applied in the nonlinear simulation is a simple beam/column structure. The concrete strength corresponds to C25/30, and the reinforcement, 4 bars of 20 mm diameter on each side, has the European steel quality BSt 500.

To demonstrate the general applicability of the derived damage concept, this example will use an extremely simple, straightforward design analysis, without any sophisticated nonlinear simulation techniques. It will again show only the nonlinear pushover analysis and omit any seismic evaluation of the applied horizontal load H . The analysis is carried out as in simple design practice by the use of a linear elastic frame program and successive load application on the structure. At each structural position reaching the yield moment of the beam model, a plastic hinge is introduced, and the further analysis is carried out with this reduced redundant structure. The stiffness reductions of the progressively cracking RC members, on their way to reinforcement yielding, are considered by iterations. As a foundation of this modeling, Figure 12 shows the $M-\kappa$ diagrams, purely based on the (monotonic) prescriptions in [3].

The gained load-displacement curve is compared in Figure 13 with the global backbone curve of the cyclic swell test [23] demonstrating excellent agreement. The damage evolution on Figure 14 uses eigenfrequencies, evaluated for each different structural systems of each load step. Because

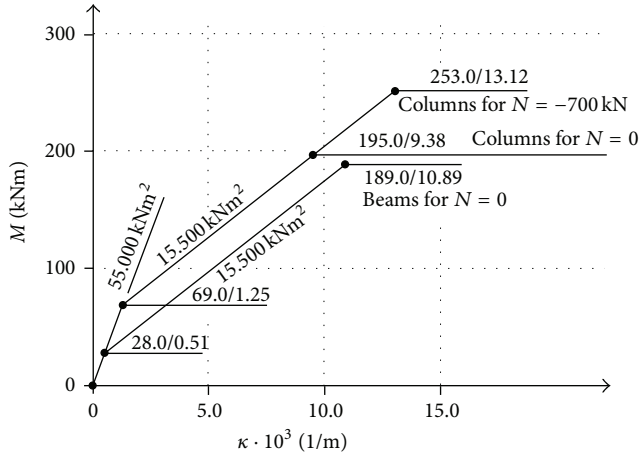


FIGURE 12: M - κ diagrams for all sections of the test frame.

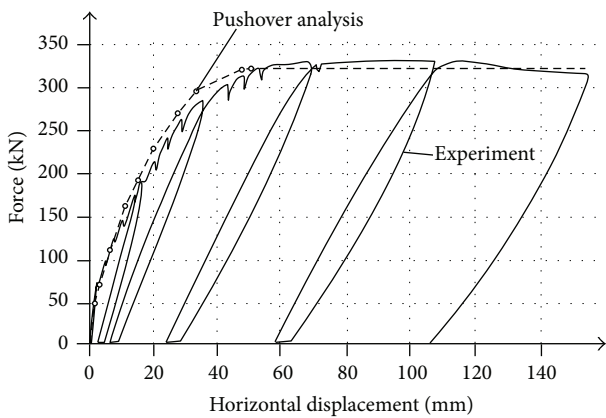


FIGURE 13: Load-deflection diagram of test frame under horizontal load H .

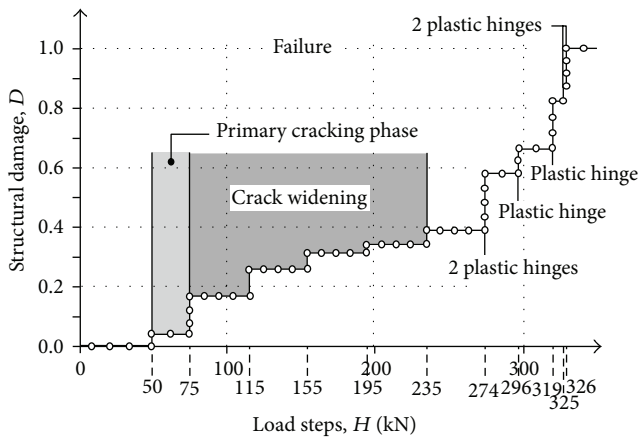


FIGURE 14: Damage indicators (eigenfrequencies) of test frame under load H .

of the applied plastic hinge model, the analysis is straightforward by standard software. Looking at Figure 14, we can clearly distinguish the brief uncracked phase with $D \equiv 0$ from the further primary cracking and crack-widening phases. Close to failure at $D = 1$, we observe the expected

rapidly successive formation of plastic hinges, transforming the originally resistant structure into a kinematic chain.

9. Summary

In the center of present seismic design codes stands the safe protection of human lives, but with growing building investments, installation, and equipment also viewpoints of property protection increase. As proposed by FEMA Standards [2], such extension requires the prosecution of a structure's damage path by damage indicators, which are able to scale the arising structural damage.

The present manuscript derives such a damage indicator, based on dissipated energies of virtual mode shapes/modal forces, and is connected to the structural response by the tangential stiffness matrix K_T during the nonlinear solution process. Thereby it adopts the quasistatic seismic safety concepts of most design codes and proposes for damage evaluation the seismic load-path evolution of the tangential stiffness K_T as well known from pushover analyses. Using the evolution of its eigenvalues or natural frequencies, the paper derives damage indicators, which fulfill all requirements from [2] and are—as accompanying data fields of design analyses—relatively easy to determine. The present examples should be further extended, for instance, to new structural types, in order to get more general experience with the applicability of the proposed damage measures.

Seismic damage is known as a low-cycle fatigue process, which is approximated in this manuscript in a quasistatic manner. Similar damage indicators have been successfully applied to the analysis of longtime structural deterioration [9, 19] and also to high-cycle fatigue structural phenomena [24].

Conflict of Interests

The authors declare that there is no conflict of interests regarding the publication of this paper.

References

- [1] EC 8, *Design Provisions for Earthquake Resistance of Structures*, CEN European Committee for Standardization, Brussels, Belgium, 1994.
- [2] Federal Emergency Management Agency, “Guidelines for the seismic rehabilitation of buildings,” FEMA 273, Federal Emergency Management Agency, Washington DC, USA, 1997.
- [3] EC 2, *Design of Concrete Structures, Part 1: General Rules and Rules for Buildings*, CEN European Committee for Standardization, Brussels, Belgium, 1991.
- [4] A. J. Kappos and G. Panagopoulos, “Performance-based seismic design of 3D RC buildings using inelastic static and dynamic analysis procedures,” *ISET Journal of Earthquake Technology*, vol. 41, pp. 141–158, 2004.
- [5] W. B. Krätsig and K. Meskouris, “Assessment of seismic structural vulnerability as a low-cycle fatigue process,” in *Proceedings of the 11th European Conference on Earthquake Engineering*, P. Bischi et al., Ed., pp. 161–178, A.A. Balkema, Rotterdam, The Netherlands, 1999.

- [6] SEAOC, “Vision 2000—performance based seismic design of buildings,” Committee Report, Structural Engineers Association of California, Sacramento, Calif, USA, 1995.
- [7] Y. Park and A. H.-S. Ang, “Mechanistic seismic damage model for reinforced concrete,” *Journal of Structural Engineering*, vol. 111, no. 4, pp. 722–739, 1985.
- [8] W. B. Krätsig, “Multi-level modeling technique for elasto-plastic structural responses,” in *Proceedings of the 5th International Conference Computational Plasticity*, D. R. J. Owen et al., Ed., vol. 1, pp. 457–468, CIMNE, Barcelona, Spain, 1997.
- [9] W. B. Krätsig and Y. S. Petryna, “Structural damage and life-time estimates by nonlinear FE simulation,” *Engineering Structures*, vol. 27, no. 12, pp. 1726–1740, 2005.
- [10] W. B. Krätsig, “Damage indicators for estimates of seismic vulnerability,” in *Innovations in Computational Structures Technologies*, B. H. V. Topping et al., Ed., pp. 111–132, Saxe-Coburg Publications, Stirlingshire, UK, 2006.
- [11] H. Krawinkler and G. D. P. K. Seneviratna, “Pros and cons of a pushover analysis of seismic performance evaluation,” *Engineering Structures*, vol. 20, no. 4–6, pp. 452–464, 1998.
- [12] B. Gupta and S. K. Kunzath, “Adaptive spectra-based pushover procedure for seismic evaluation of structures,” *Earthquake Spectra*, vol. 16, no. 2, pp. 367–392, 2000.
- [13] V. Kilar and P. Fajfar, “Simplified push-over analysis of building structures,” in *Proceedings of the 11th World Conference on Earthquake Engineering*, pp. 59–66, Acapulco, Mexico, 1996.
- [14] A. K. Chopra, *Dynamics of Structures, Theory and Applications to Earthquake Engineering*, Prentice Hall, Upper Saddle River, NJ, USA, 2001.
- [15] L. Petti, L. Marino, M. De Iuliis, and G. Giannatasio, “The role of modeling in the push-over analysis of existing framed structures,” in *Proceedings of the (COMPDYN '07)*, M. Papadrakakis et al., Ed., Civil Engineering Software, Rethymno, Greece, June 2007.
- [16] E. DiPasquale and A. S. Cakmak, “Detection and assessment of seismic structural damage,” National Center for Research on Earthquake Engineering Research, Technical Report NCEER-87-0015, State University of New York, Buffalo, NY, USA, 1987.
- [17] I. F. Meyer, W. B. Krätsig, and F. Stangenberg, “Damage prediction in reinforced concrete frames under seismic action,” *EEE-European Earthquake Engineering*, vol. 3, pp. 9–15, 1988.
- [18] A. Ötes, “Zur werkstoffgerechten Berechnung der Erdbebenbeanspruchung in Stahlbetontragwerken,” Tech. Rep. 25, Institute f. Reinforced Concrete, TH Darmstadt, 1985.
- [19] W. B. Krätsig and Y. S. Petryna, “Fundamental tools for structural damage indication and lifetime management,” in *Proceedings of the 2nd International Conference on Lifetime-Oriented Design Concepts (ICLODC '04)*, F. Stangenberg et al., Ed., SFB 398, Ruhr-University, Bochum, Germany, 2004.
- [20] Y. S. Petryna, “Structural degradation, reliability and lifetime simulations of civil engineering structures,” in *Proceedings of the 9th International Conference on Structural Safety and Reliability (ICOSSAR'05)*, Rome, Italy, G. Augusti, G. I. Schueller, and M. Ciampoli, Eds., Millpress, Rotterdam, The Netherlands, 2005.
- [21] Y. S. Petryna and W. B. Krätsig, “Compliance-based structural damage measure and its sensitivity to uncertainties,” *Computers and Structures*, vol. 83, no. 14, pp. 1113–1133, 2005.
- [22] G. C. Ernst, G. M. Smith, A. R. Riveland, and D. N. Pierce, “Basic reinforced concrete frame performance under vertical and horizontal loads,” *American Concrete Institute Journal*, vol. 70, no. 4, pp. 261–269, 1973.
- [23] F. J. Vecchio and M. B. Emara, “Shear deformations in reinforced concrete frames,” *ACI Structural Journal*, vol. 89, no. 1, pp. 46–56, 1992.
- [24] Y. S. Petryna, D. Pfanner, F. Stangenberg, and W. B. Krätsig, “Reliability of reinforced concrete structures under fatigue,” *Reliability Engineering and System Safety*, vol. 77, no. 3, pp. 253–261, 2002.

Research Article

Structural Health Monitoring Based on Combined Structural Global and Local Frequencies

Jilin Hou,¹ Łukasz Jankowski,² and Jinping Ou^{1,3}

¹ School of Civil Engineering, Dalian University of Technology, Dalian 116024, China

² Institute of Fundamental Technological Research, Polish Academy of Sciences, 02-106 Warsaw, Poland

³ School of Civil Engineering, Harbin Institute of Technology, Harbin 150090, China

Correspondence should be addressed to Jilin Hou; hou.jilin@hotmail.com

Received 9 August 2013; Accepted 5 December 2013; Published 9 January 2014

Academic Editor: Yuri Petryna

Copyright © 2014 Jilin Hou et al. This is an open access article distributed under the Creative Commons Attribution License, which permits unrestricted use, distribution, and reproduction in any medium, provided the original work is properly cited.

This paper presents a parameter estimation method for Structural Health Monitoring based on the combined measured structural global frequencies and structural local frequencies. First, the global test is experimented to obtain the low order modes which can reflect the global information of the structure. Secondly, the mass is added on the member of structure to increase the local dynamic characteristic and to make the member have local primary frequency, which belongs to structural local frequency and is sensitive to local parameters. Then the parameters of the structure can be optimized accurately using the combined structural global frequencies and structural local frequencies. The effectiveness and accuracy of the proposed method are verified by the experiment of a space truss.

1. Introduction

Structural Health Monitoring (SHM) [1] is a hot research in civil engineering. Structural parameter estimation, such as model updating and damage identification [2, 3], is an important theoretical base for providing reliable model, structural damage detection, forecasting, and its safety assessment.

In SHM, many researches have investigated parameter estimation like model updating, damage detection and localization, and so forth. The structural parameters are usually optimized using natural frequency and mode shape [4], flexibility matrix [5], responses in time-domain or frequency-domain [6], and so forth. Among the dynamic information, natural frequency reflects the most basic dynamic performance of the structure, and it can be identified easily, accurately, robustly, and reliably. So the methods based on mode are widely used for parameters estimation. In 2000, Yun and Bahng [7] monitor the local stiffness modifications using natural frequencies and mode shapes. In 2007, Jaishi and Ren [8] update the parameters of the finite element model based on eigenvalue and strain energy residuals. In 2011, An and Ou [9] detect local damages of a truss structure using local mode.

Usually, the identified low order natural frequencies are not enough for estimating the structural parameters in civil engineering. Aiming at solving this problem, adding mass on structure is an effective way to increase dynamic information. In 1992, Nalitolela et al. [10] add mass or stiffness on the structure for model updating, where the mode of the perturbed structures is used. In 1993, Nalitolela et al. [11] further improve their method by adding imaged stiffness on the beam. In 2001, Cha and Pillis [12] use the orthogonal conditions of the system's eigenvalue problem for identifying damage by adding known masses on the structure. In 2011 Dinh et al. [13] use the state-space transformation of the system's eigenvalue problem to improve the method.

However, with structures in civil engineering being more and more huge and complexity, the accurate parameter estimation of structure has becoming more and more difficult, which requires the proper dynamic measurements, as well as the efficient exploitation of the measurements. Therefore, this paper combined both the structural global frequencies and structural local frequencies for parameter estimation, and the method of adding mass is employed to make the local structure have Local Primary Frequency (LPF) [14],



FIGURE 1: A truss experimental model.

which not only increases the useful measured information but also improves its sensitivity to the local parameters. The experiment of a space truss is performed for the verification of the proposed method.

2. SHM by Combined Global and Local Mode

Structures in civil engineering are large scale, complex, and insensitive to the damage, and hence the accurate estimation of their structural parameters requires the utilization of a great quantity of their dynamic information. Modal information including frequency and vibration mode is most commonly used in Structural Health Monitoring (SHM). In this paper, structural global frequencies are used together with local frequencies to estimate physical parameters of the structures.

2.1. Structural Global Frequency. Generally, structural global modes reflect the overall dynamic characteristics of the structure, and thereby they have certain relation with physical quantities related to the integrity, such as the elastic modulus and the density. For global modes, usually only low-order modes can be obtained in practice from the global measurements. However low-order modes are usually insensitive to the variation of structural local parameters. For instance, the first-order mode of a large-scale structure generally changes little due to the cause that only one structural element is damaged.

In civil engineering area, the modes of the large-scale structures are often identified by the methods like Eigensystem Realization Algorithm (ERA), Stochastic Subspace Identification method (SSI), and so on, using the free responses or random responses. Then the parameter estimation is performed based on the identified modes. At present, these methods based on identified modes [1–4, 8, 9] have been intensively investigated and so they are not introduced in detail here.

2.2. Structural Local Frequency. As well known, structural local frequency is a type of mode that can reflect local dynamic characteristics of the local structure and is sensitive

to the variation of local parameters. Generally speaking, structural local frequency refers to a high-order structural mode. Compared with the obtained structural global frequency, structural local mode mainly displays local dynamic characteristics of the structure. Thus, using local structural frequency, the structural local parameters can be evaluated more accurately.

First, Local Primary Frequency (LPF) is illustrated in the following subsection, which refers to one natural frequency corresponding to the vibration of the local structure under certain excitations.

2.2.1. Local Primary Frequency (LPF). The acceleration frequency response of the structure $H(\omega)$ can be expressed as

$$H(\omega) = \sum_{r=1}^n \frac{(j\omega)^2 C \varphi_r \varphi_r^T B}{\omega_r^2 - \omega^2 + j2\zeta_r \omega_r \omega}, \quad (1)$$

where j is imaginary unit, ζ_r is the r th damping ratio, ω_r is the r th natural frequency, φ_r is the r th normalized mode shape, B is load position matrix, and C is observation matrix.

Substitute $\omega = \omega_r$ into (1); then the corresponding frequency response $H(\omega_r)$ has the approximate expression as follows:

$$H(\omega_r) \approx \frac{jC\varphi_r \varphi_r^T B}{2\zeta_r}. \quad (2)$$

It can be seen from (2) that, apart from the modal parameters of the structure, the measured response of the structure mainly depends on the excitation and the sensor positions. Therefore, to obtain the structural local frequencies of the structure, the sensors and excitation are required to be placed locally.

Usually, more than one natural frequency is likely to be excited even under local excitation. Among these natural frequencies, there are not only structural local frequencies, but the frequencies which represent the structural global information are also included. In practice, it is difficult to accurately separate high-sensitivity local frequencies from these frequencies. In this way, Local Primary Frequency (LPF) is defined: under local excitation, if the structure mainly vibrates in local positions with one main natural frequency, then the natural frequency is defined as LPF. The LPF is highly sensitive to the corresponding local parameters, which is a crucial factor in the proposed method of the structural parameter estimation. Obtainment of LPF is analyzed in Section 2.2.3, and before that the related sensitivity analysis is discussed.

2.2.2. Sensitivity Analysis. Let a linear structure have n degrees of freedom (Dofs), and denote by K_0 and M_0 , respectively, the stiffness matrix and mass matrix of the theoretical FEM model structure. Assume the structure has m parameters to be estimated, which are only related to the stiffness. The parameter modification coefficients are denoted by $\mu_1, \mu_2, \dots, \mu_n$, which are, respectively, the ratio of the actual modified stiffness matrix K_i^d to the stiffness matrix

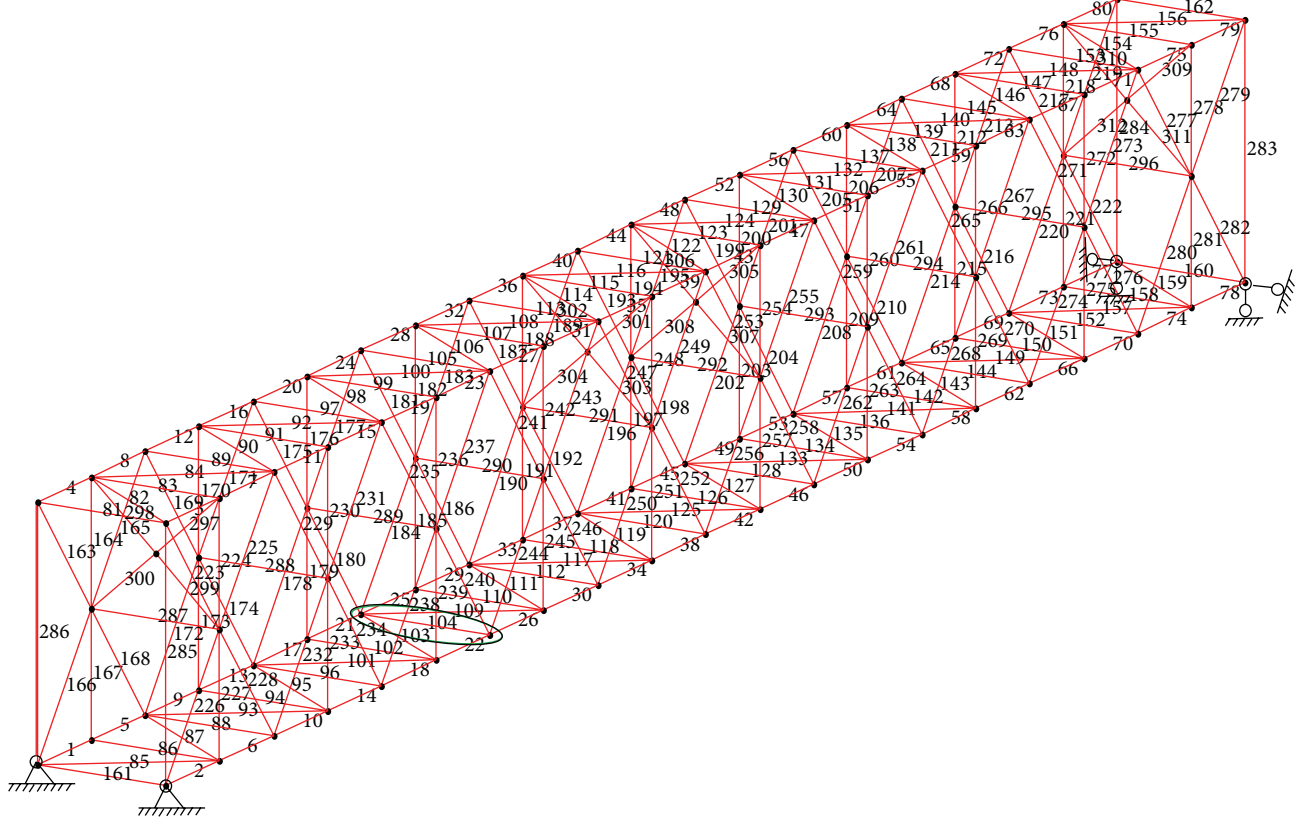


FIGURE 2: The element numbers of truss model.

of theoretical FEM model K_i . The stiffness matrix of real structure K is expressed as

$$K^d = \sum \mu_i K_i, \quad K_i = N_i^T K_{i,s} N_i, \quad (3)$$

where K_i is the i th extended substructure stiffness matrix of theoretical FEM model, $K_{i,s}$ is the corresponding substructure matrix in local coordinate system, N_i is the localization matrix linking the global Dofs to the i th local substructural Dofs.

Via the relation of the natural frequency to the substructure stiffness matrix, the sensitivity of the r th natural frequency ω_r to the i th parameter modification coefficient μ_i can be stated as

$$\frac{\partial \omega_r}{\partial \mu_i} = \frac{\varphi_r^T K_i \varphi_r}{2\omega_r} = \frac{\varphi_{r,i}^T K_{i,s} \varphi_{r,i}}{2\omega_r}, \quad (4)$$

where $\varphi_{r,i} = N_i \varphi_r$ is the r th mass-normalized mode shape related to the i th parameter. Then, the sum of the relative sensitivity of all the parameters can be computed as follows [15]

$$\sum_i \frac{1}{\omega_r} \frac{\partial \omega_r}{\partial \mu_i} = \sum_i \frac{\varphi_{r,i}^T K_{i,s} \varphi_{r,i}}{2\omega_r^2} = \frac{1}{2}. \quad (5)$$

2.2.3. Adding Masses and LPF. Generally, the response of local substructure doesn't have LPF. Hence, masses are added

artificially on local structure to cause the local structure have a LPF and make it mainly vibrate at the LPF. As a part of the local structure, the added mass can increase the vibration energy of the local structure and restrain the vibration energy dispersion from local structure to global structure. As a result, the local structure may vibrate with one natural frequency, that is, the defined Local Primary Frequency.

Comparing (2) and (4), it can be seen that the expression of the frequency response is similar on the structure to the expression of the relative sensitivity. Therefore, it can be inferred that there is a certain correlation between the amplitude of the frequency response and the sensitivity: the larger the amplitude is, the higher the corresponding sensitivity may be. That is because, under local excitation, the structural frequency response shows the maximum amplitude at the position of the caused LPF. Moreover, this indicates that LPF is more sensitive to local parameters than other natural frequencies.

In addition, as shown in (5), the sum of the relative sensitivity of a natural frequency to all parameters is a constant value of 0.5. Hence, if the relative sensitivity of LPF according to the concerned local parameter is higher, then the LPF will have lower sensitivity to other parameters. Therefore, the accuracy of the parameter estimation can be improved using LPF to optimization.

2.3. The Objective Function. The modification of the concerned parameters is taken as the optimization variables,

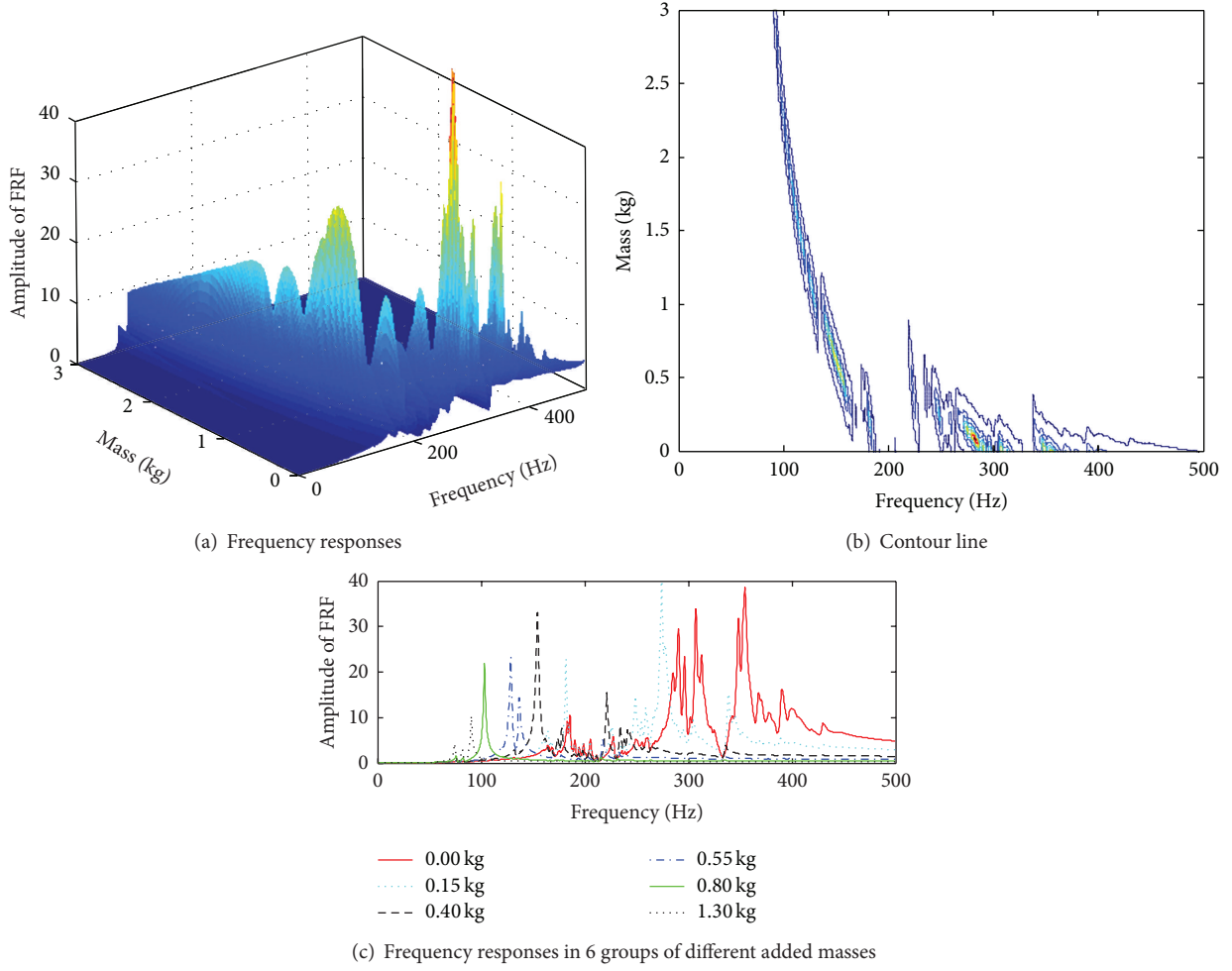


FIGURE 3: The out-plane frequency responses of the truss after adding masses.

and the objective function $f(\mu)$ is built via combining the information of both global structural frequencies and LPF:

$$f(\mu) = \sum_i \left\| \frac{\omega_{g,i}(\mu) - \bar{\omega}_{g,i}}{\bar{\omega}_{g,i}} \right\| + \sum_j \left\| \frac{\omega_{s,j}(\mu) - \bar{\omega}_{s,j}}{\bar{\omega}_{s,j}} \right\|, \quad (6)$$

where μ is the variable to be identified; $\bar{\omega}_{g,i}$ is the identified i th low-order natural frequency of the global structure, while $\omega_{g,i}(\mu)$ is the corresponding frequency of the theoretical FEM model; $\bar{\omega}_{s,j}$ is the measured LPF of the j th local parameter, while $\omega_{s,j}(\mu)$ is the corresponding LPF of the theoretical FEM model.

3. Truss Experiment

An experiment of a space truss model is performed here to introduce and test the proposed method by combining the global and local frequency.

3.1. Truss Model. A supported steel 20-span space truss is shown in Figure 1. It is 8 m long with the height of 0.9 m, width of 0.56 m, and consists of 312 members and 108 nodes.

TABLE 1: Three types of members in truss structure.

Types	Member A	Member B	Member C
Number	80	198	34
Tubes			
Outside diameter (mm)	30	20	14
Thick (mm)	8	3	3
Bolt			
Types	M20	M16	M10
Length (mm)	100	90	60

Young's modulus is 2.06 Gpa, and the density is 7850 Kg/m³. The members, steel tubes, are connected by bolted spherical joints (bottom right in Figure 1). The members are classified into three types according to their radius, which are listed in Table 1.

The theoretical Finite Element (FE) model is built, where each member is defined as an element. Then the FE model has 312 elements with 108 nodes and 638 degrees of freedom. Figure 2 shows the element numbers of the truss model. The element cross-sections and initial moments are calculated

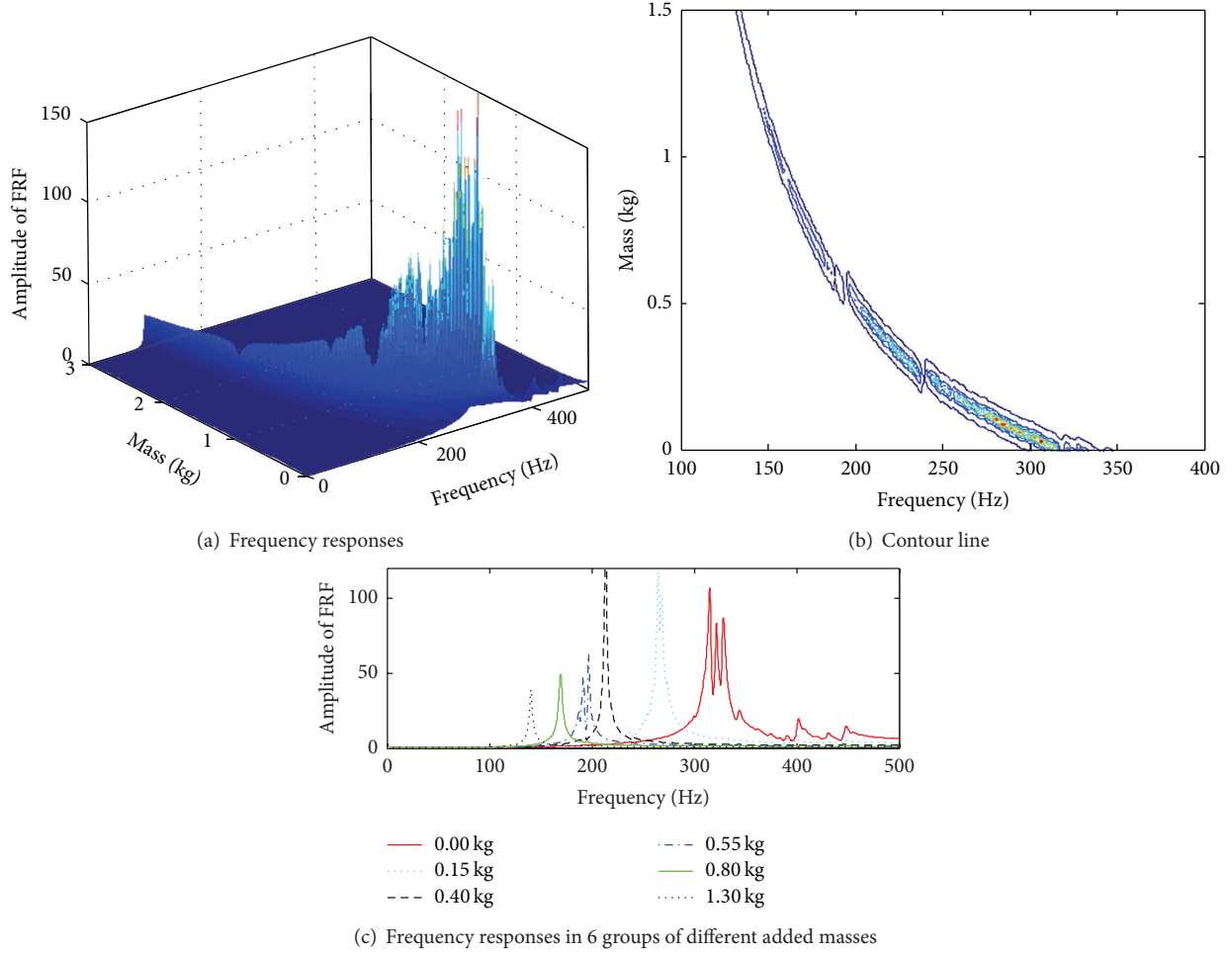


FIGURE 4: The in-plane frequency response after adding masses.

from the geometric dimensioning according to the steel tube. The nodes are rigid. The weight of the spherical joints and bolts is considered by certain mass points located on the nodes. Each mass point has the value of 2.83 kg.

3.2. Numerical Analysis of LPF. In order to investigate the influence of the added mass on LPF, the bottom element number 104 of the FE model is taken as an example, marked by a black circle in Figure 2, and the analysis is performed numerically. The mass is added in the middle of member number 104 and the impulse excitation is also applied in the middle of the member. After the mass addition, the in-plane frequency response of the member and the out-plane frequency response are compared, respectively (here, the in-plane refers to the one corresponding to the outer contour of the truss). Figures 3 and 4, respectively, show the corresponding in-plane and out-plane frequency responses in 6 groups of different added masses (mass = 0.00, 0.15, 0.40, 0.55, 0.80, and 1.30 kg). Figures 3 and 4 both provide similar phenomenon. The increase in mass causes the peaks of the frequency response change from multifrequencies into a single frequency (the caused LPF). But with the increase in

mass, the value of LPF is reduced. When the value of LPF reduction reaches a certain degree, the frequency response will appear multipeaks. Then if the added mass value is continuing to increase, the peaks of frequency response return to a single peak again. The comparison between Figures 3 and 4 indicates that, under the same additional mass, the in-plane LPF is larger than the out-plane LPF. The member section is a circle and member stiffness is identical in all directions, and further the whole truss owns larger in-plane stiffness at boundary of the member; therefore, with the same additional mass value, the in-plane local characteristics of the member are more significant. Hence, the in-plane response of the member is used for the estimation in the test of experiment.

For each in-plane frequency response shown in Figure 4(c), the sensitivity analysis of the natural frequencies corresponding to the peaks is computed, respectively, which are shown in Figure 5. When no mass is added, the frequency response in Figure 3(c) shows three peaks at the respective frequency of 315.4 Hz, 321.9 Hz, and 328.0 Hz. The relative sensitivities of the corresponding three natural frequencies are illustrated in Figure 5(a): around 0.08, 0.06, and 0.05, respectively. It shows that the three relative sensitivities are far larger than the sensitivities of the rest 311 members.

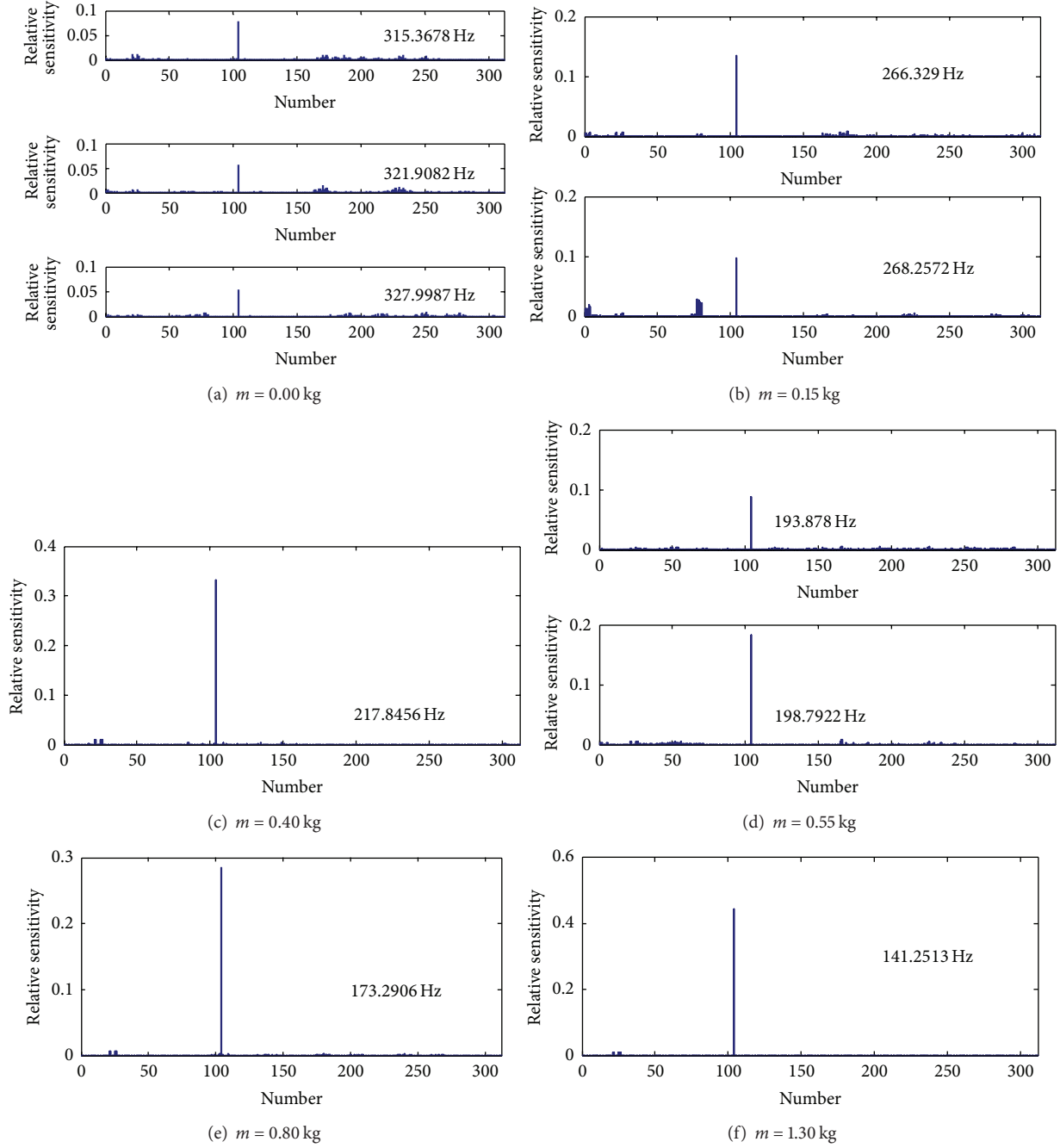


FIGURE 5: The relative sensitivities of the excited frequencies in 6 cases of adding mass.

Equation (5) shows that the sum of all the relative sensitivities is 0.5, so it can be inferred that the influence of the number 104 member on the three order frequencies only accounts for $0.08/0.5 = 16\%$, $0.06/0.5 = 12\%$, and $0.05/0.5 = 10\%$, respectively. When the added mass is 0.15 kg, the two natural frequencies corresponding to the peaks of the frequency response have the relative sensitivities of 0.13 and 0.11, respectively, as exhibited in Figure 5(b). When the added mass is 0.40 kg, there is only one peak and the relative sensitivity of the corresponding natural frequency is 0.33, as shown in Figure 5(c). Apparently, the more the peaks of the excited

response, the lower the sensitivity of the corresponding natural frequency. When the added mass is 0.55 kg, due to the change of modal order, the frequency response shows two peaks and the relative sensitivities of the corresponding frequencies are decreased to 0.1 and 0.18, respectively, as shown in Figure 5(d). As the mass keeps on increasing, the frequency response changes from multiple peaks to a single peak and the corresponding sensitivities show a significant increase. When the mass is 0.8 and 1.3 kg, the sensitivities of the corresponding frequencies are, respectively, 0.28 and 0.43, as displayed in Figures 5(e) and 5(f).

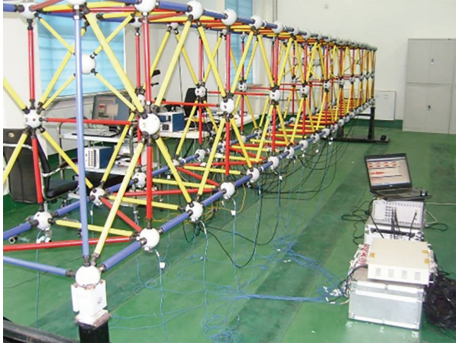


FIGURE 6: Accelerations placement.

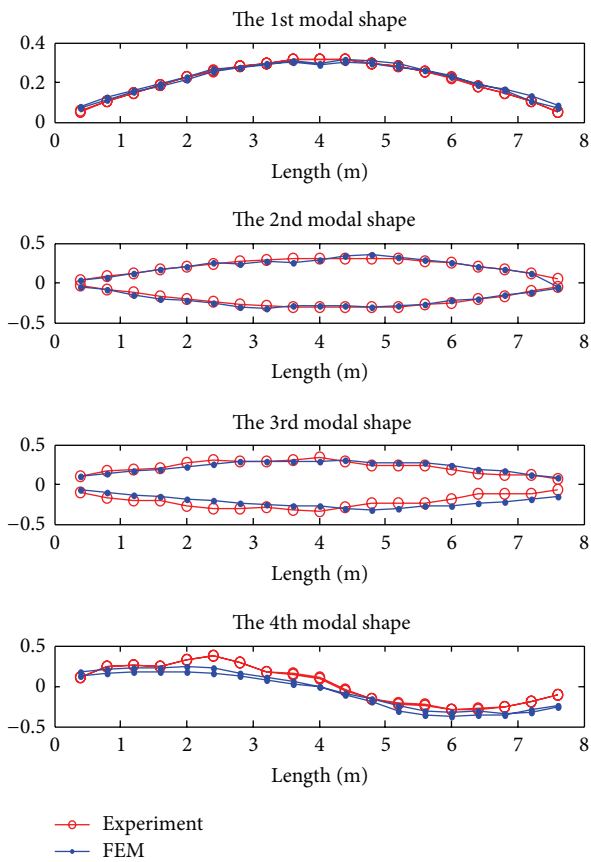


FIGURE 7: The comparison of modes of global structure.

The above numerical analysis among the relation of the adding mass, LPF, and the sensitivity provides the evidence for the following experiment performance.

3.3. Model Updating of the Space Truss Experimentally

3.3.1. Modal Test of the Global Truss. Accelerometers are located on the bottom nodes of the truss, shown in Figure 6. Ambient excitation is applied on the structure, and the modal shapes and frequencies are identified via the caused random responses, shown in Figure 7 and Table 2. Figure 7 and Table 2, respectively, compare the modal shapes and

TABLE 2: The errors of lower order natural frequencies of global structure.

Order	Experimental	Theoretical	Error
1	18.4	23.27	26.47%
2	27.6	34.41	24.67%
3	36.8	52.58	42.89%
4	53.3	76.97	44.41%

frequencies which are obtained from the experimental model and FEM model. Table 2 shows that the errors between them are rather obvious, around 30%, which indicates that the theoretical FEM model is quite coarse.

3.3.2. Local Dynamic Test. Since member B in Table 1 includes most of the members, the local dynamic test is performed on the group of member B, which are further classified into four kinds according to their lengths and positions (Figure 8). In order to increase the local dynamic characteristic, masses are added in the middle of the members. Due to that the weight of one accelerometer and its connector is 340 g, so in the experiment the accelerometer also can play the role of additional mass, and the value of added mass is adjusted by the number of the located accelerometers. For long member, its local stiffness is relatively small, and one additional mass is enough; that is, one accelerometer is located. For short member, its local stiffness is big, and more masses (accelerometers) are needed. The location of the accelerometers or additional masses is shown in Figure 9.

Members-IV is first taken as an example to illustrate and experimentally verify that local characteristic can be increased via adding mass on the corresponding member. Three cases are discussed; that is, two, three, and four masses (accelerometers) are, respectively, added on middle of the number 251 member. In each case, a hammer excitation is applied on the middle of the member, and the corresponding responses of accelerometers are measured; then the spectral analysis is performed. The obtained power spectra in the three cases are shown in Figure 10. The bigger the additional mass value is, the more obvious the caused local characteristic will be. In the cases of two or three additional masses, the power spectra of the global structure have multiple peaks. So it is hard to judge which natural frequencies belong to the local structure and which frequencies reflect the characteristic of the global structure; that is to say, the local characteristic is not obvious. While in the case of four additional masses the power spectra only have one peak, it shows that the energy of the local excitation is mostly absorbed by the additional masses. In this case, the excited vibration mainly reflects the distortion of the local member, so the frequency corresponding to the peak in the power spectra is the LPF of the local member.

In order to compare the measured LPF and that of the theoretical model, 58 members are picked up to test, which are, respectively, 14 members from Members-I, 16 members from Members-II, 20 members from Members-III, and 8 members from Members-IV. The accelerometers (masses) are located on these members, respectively, according to Figure 9,

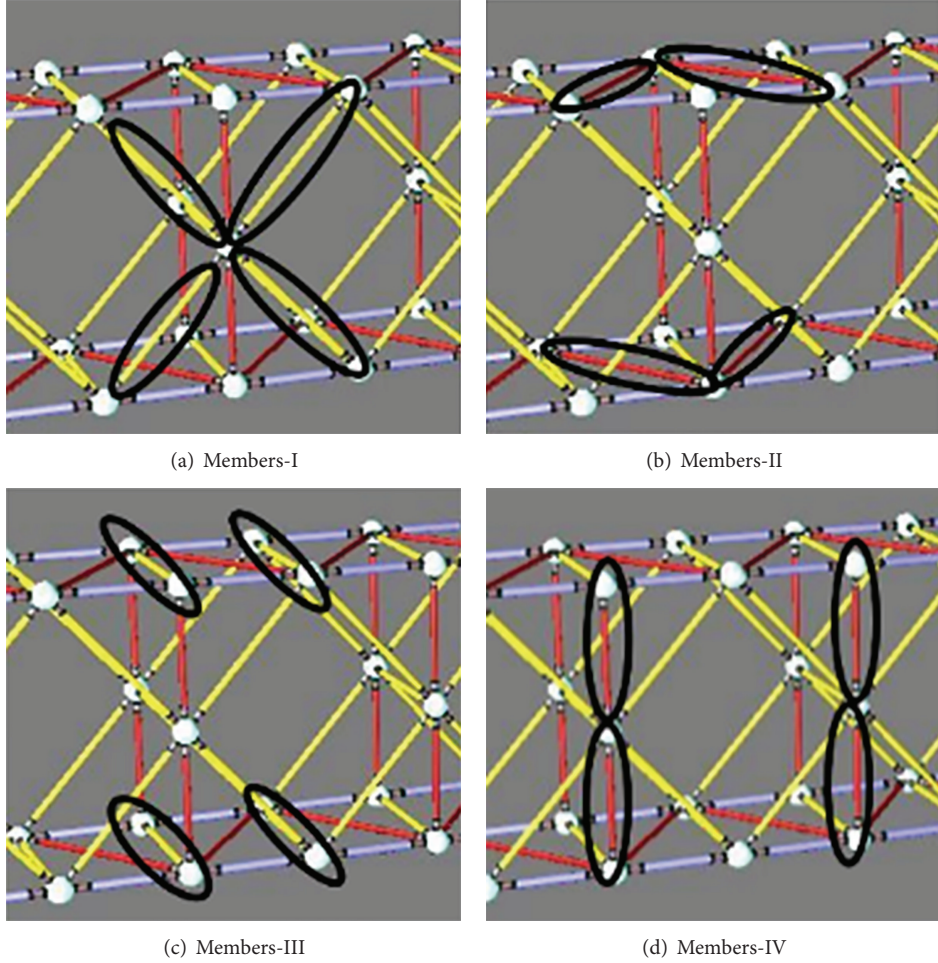


FIGURE 8: Four kinds of elements.

TABLE 3: The errors of local primary frequencies of 4 kinds of elements.

Types	Identified (Hz)	Theoretical (Hz)	Error
Members-I	138.67	151.24	9.06%
Members-II	140.63	155.57	10.62%
Members-III	166.02	176.28	6.18%
Members-IV	164.06	186.52	13.69%

and the respective hammer excitation is applied in the middle. The identified LPFs are shown in Figure 11. Take Members-I as an example; the 14 members show nearly identical LPF; see Figure 11(a). The main reason is summarized as follows: these members have the same material and geometric parameters in the global structure. For these members, each member and its surrounding nodes are connected in a similar way; also, the connection way between one member and other members is similar. Restraining stiffness of the global structure on the two ends of the member is also very approximate to each other and the local excitation was in the same position and direction for the 14 members. Furthermore, the local characteristics of the members are

amplified by the added masses. Therefore, with all the similar or identical conditions mentioned above, the LPFs of the members are similar to each other, although the members are at different positions in the global structure.

Table 3 compares the measured LPF and that of the theoretical FE model, where one member is chosen from each kind of members, respectively. It shows that the identified value from the experiment has obvious deviation from the theoretical value, which indicates that the theoretical model has significant error compared to the actual structure.

3.3.3. The Selection of Updating Parameters. In practice, actual Young's modulus of the steel, physical dimension, and the density have little error from the theoretical values. Then in this truss model, the factor of the errors of FEM model is mainly due to the node model, and so the parameters of node model are estimated in the model updating.

First the fine model of the bolted spherical joint, bolt, and the steel pipe are built considering their actual way of connection, shown in Figure 12. The local reinforcement of the spherical joint ($r = 4\text{ cm}$) to the ends of the tube is considered by a reinforcement parameter k which is the ratio of the spherical joint stiffness to the pipe stiffness,

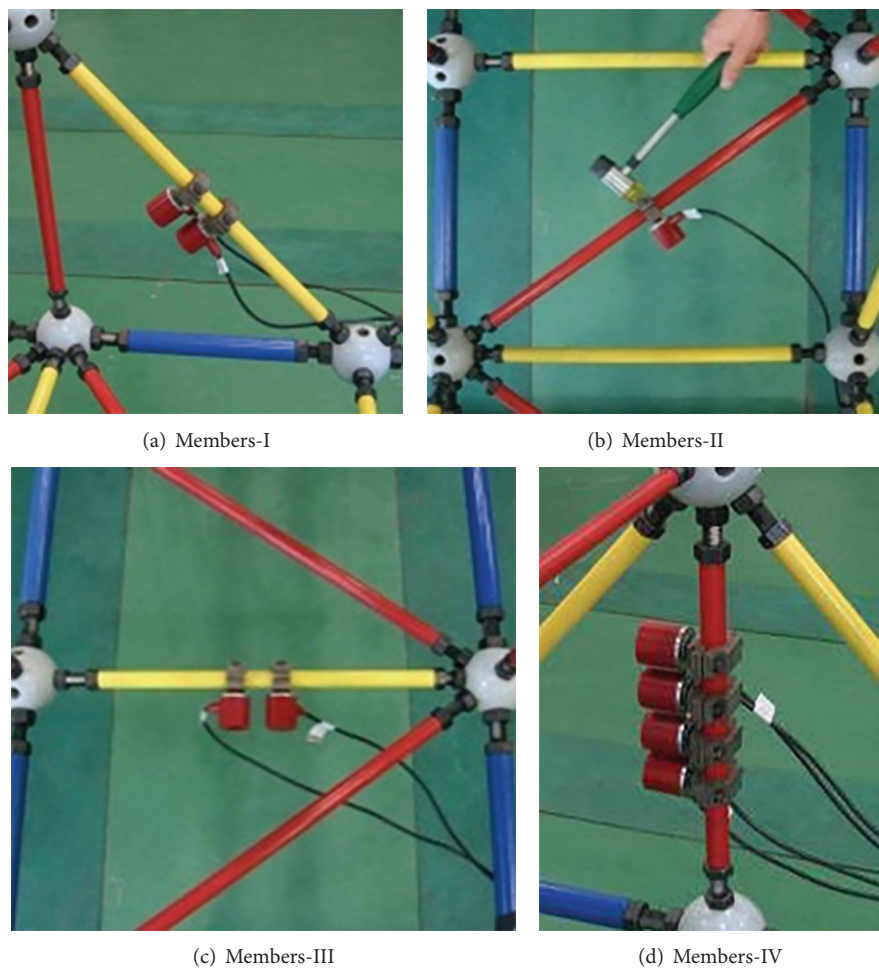


FIGURE 9: The placements of additional masses.

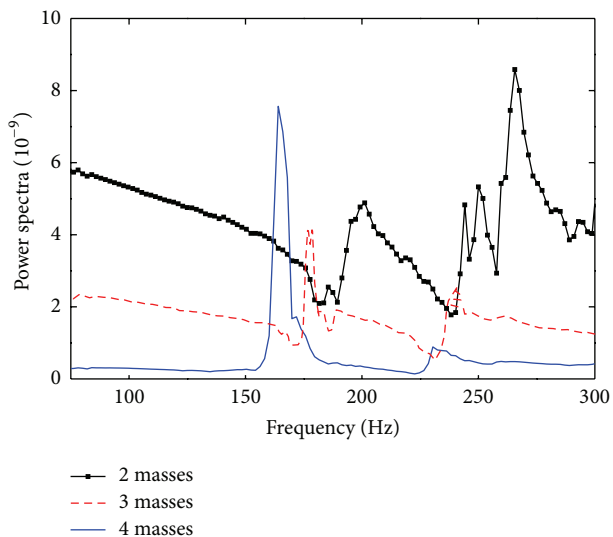


FIGURE 10: The power spectra.

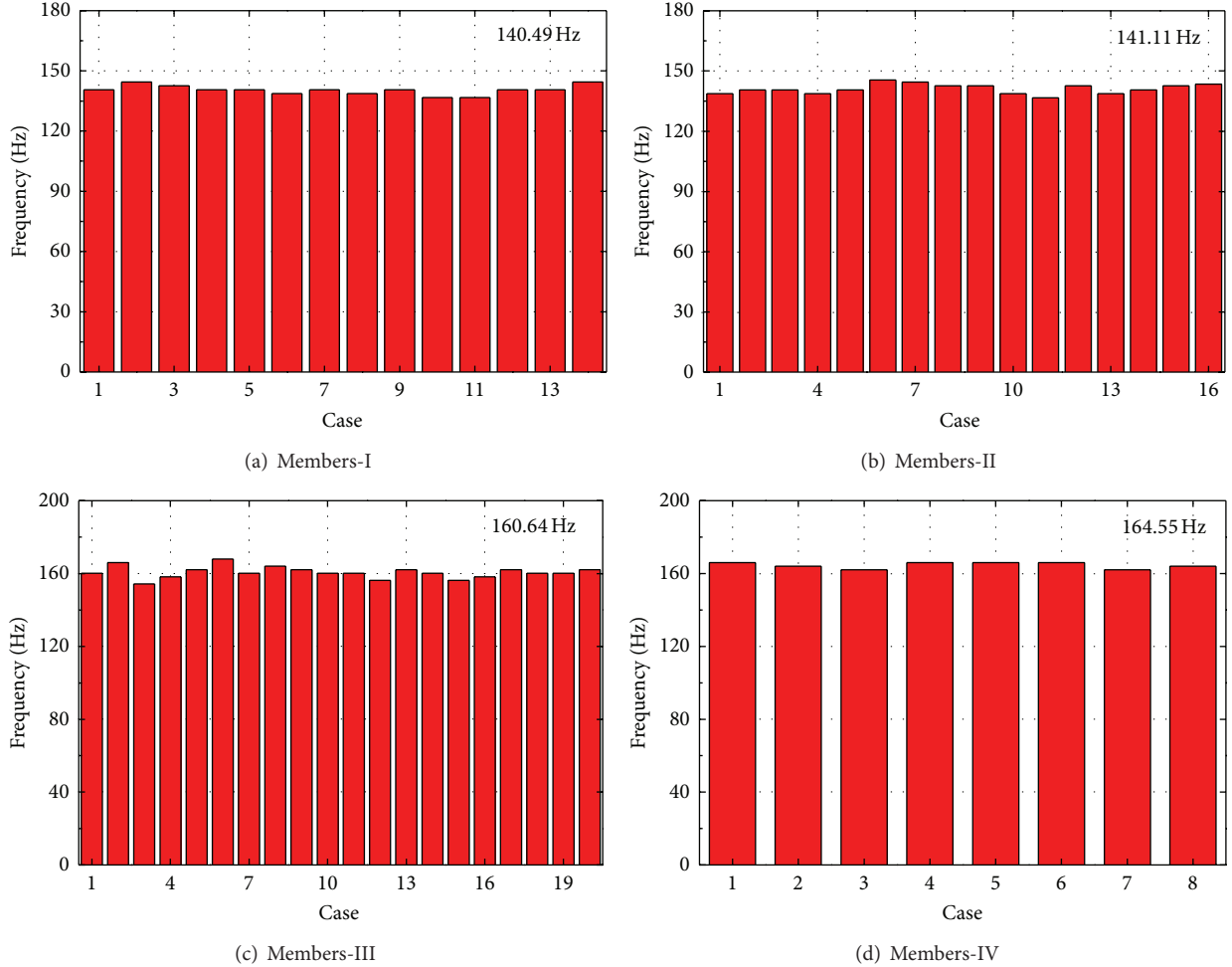


FIGURE 11: The identified local primary frequencies.

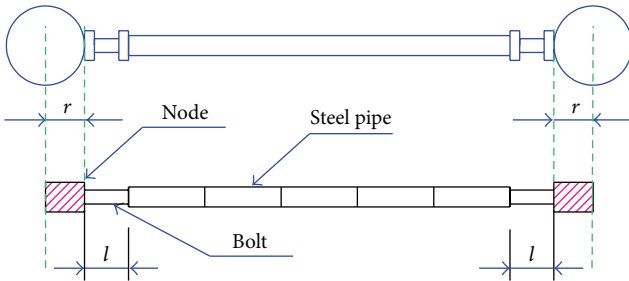


FIGURE 12: Fine modeling of the element.

and the definite value of k needs to be optimized. In addition, the local weakening caused by bolt is considered. Denote by l the weakening length, and l needs to be optimized. The stiffness in the weakening range takes the value of the bolt. In addition, there are some screw holes in the spherical joint which connect with bolts and nuts, so it is hard to determine the joint weight accurately, which needs to be updated. Above all, reinforcement parameter k , weakening length l , and the joint weight m are taken as the model updating parameters.

According to the model in Figure 12, a member is divided into 9 elements including 2 spherical joint elements, 2 bolt

elements, and 5 pipe elements. Then the whole FE model will have 2606 nodes with 2918 elements and 15614 degrees of freedom (Dofs). Certainly the FE model is complicated and the computational work will be very huge. Therefore, model reduction is used. For each member, the fine model has 9 elements and 60 Dofs. Through Guyan reduction, the 60 Dofs are condensed into 12 Dofs on the two ends of the member, and thus the dimensions for the condensed member stiffness and mass matrix are both 12. Then the condensed stiffness and mass matrix are used to assemble the parameter matrix of the whole FE model, except for the member with additional mass, that is, the member to be updated, of which its fine model with 60 Dofs is directly used without reduction. In this way, the consideration is balanced on the computational work, the relative accurate connection, and the accuracy of the local member analysis.

3.3.4. Model Updating. After building the fine FEM, the identified 4 modes (see Figure 7) and 58 LPFs (see Figure 11) are used to optimize the joint mass m , reinforcement parameter k_i , and weakening length l_i of the four kinds of members via the objective function (6). The optimized joint mass m equals 3.33 kg, and the optimized parameters k_i, l_i are shown

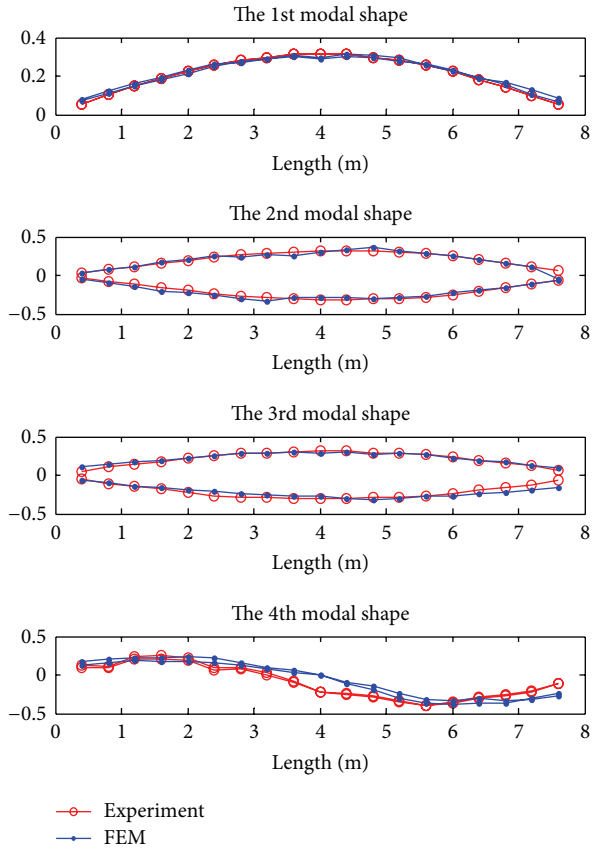


FIGURE 13: The comparison of modes of global structure.

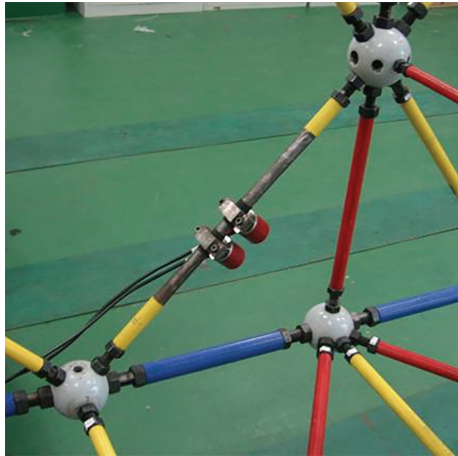


FIGURE 14: The damaged element.

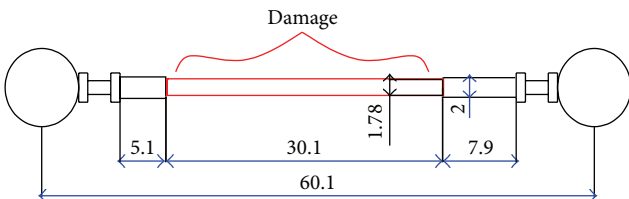


FIGURE 15: The actual damage of the damaged element (cm).

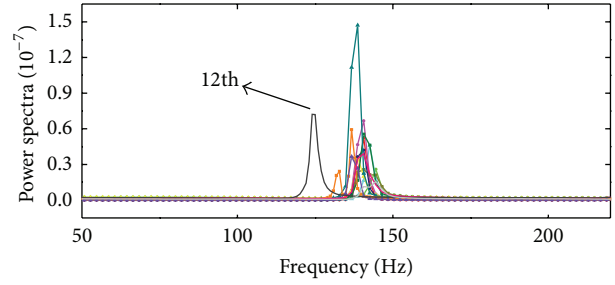


FIGURE 16: The power spectra of measured responses.

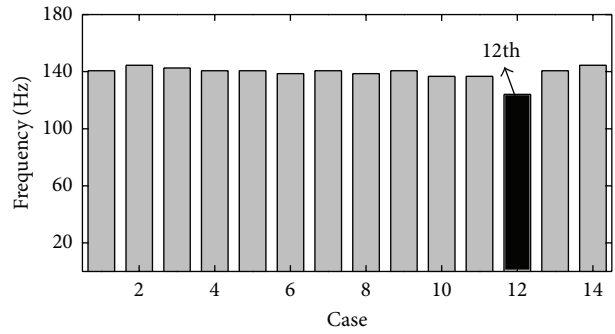


FIGURE 17: The local primary frequencies of the 14 elements.

TABLE 4: The model updating of the node parameters.

Type	l (cm)	k
Members-I	4.5	3.2
Members-II	2.9	4
Members-III	6.7	1.6
Members-IV	2.7	8

TABLE 5: The errors of lower order natural frequencies of global structure.

Order	Identified	Theoretical	Error
1	18.4	18.82	2.28%
2	27.6	27.25	-1.25%
3	36.8	38.63	4.97%
4	53.3	50.34	-5.55%

TABLE 6: The errors of local primary frequencies.

Types	Identified	Estimated	Error
Members-I	166.02	162.81	-1.93%
Members-II	140.63	138.99	-1.17%
Members-III	138.67	138.24	-0.31%
Members-IV	164.06	167.55	2.13%

in Table 4. Substitute the modified parameters into the FE model; the natural frequencies and modes of the FEM are computed and compared with the values identified from the measurements, respectively, shown in Table 5 and Figure 13. Table 6 lists some typical cases of the comparison of the LPFs between the identified values from the measurements and

the estimated values of the updated FE model. In all the comparisons, the biggest error is 5.55%, which shows that the updated FE model reflects the actual truss structure on both global dynamic behavior and local characteristic and the model is updated effectively and accurately.

3.4. Damage Identification. The type of Members-I is selected for introducing and verifying the method of damage identification using LPF. There are 14 members, and the 12th member is damaged (as shown in Figure 14). The damage dimensions of the 12th member are displayed in Figure 15, and the reduction of its flexural rigidity is 49%. So the actual damage extent of the member is 0.51, which is to be identified using LPF.

Two masses are placed in the middle of the member in the experiment; see Figure 14. The local dynamic test on Members-I, that is, 14 members, is performed, respectively. The power spectra of the response are illustrated in Figure 16 and the identified LPFs are shown in Figure 17. As can be seen from Figure 17, 13 undamaged members show similar LPF: 140.49 Hz on average, while the 12th member (the damaged one) shows slightly lower LPF: 124.02 Hz. This not only indirectly indicates that the 12th member is damaged, but also confirms that LPF is sensitive to the damage of the local member.

The damage extent of the 12th member is optimized using the updated FEM model. In the optimization, only one frequency (the LPF, 124.02 Hz) is used for optimizing objective function (6) with the assumption that all the rest parameters are undamaged. The optimization is performed quickly and accurately. The identified damage extent of 12th member is 0.577, which is approximate to the actual value 0.51.

4. Conclusion

This paper proposed a method for SHM using the combined structural global frequency and local frequency. An experiment of a space truss is conducted for verification of the proposed method. The obtained main conclusions are as follows.

- (1) Structural global frequencies reflect the global dynamic characteristics of the structure, but they are insensitive to local modification of large structure, while structural local frequencies reflect local dynamic characteristics of the structure and they are sensitive to the variation of local parameters. So, the combination of the two kinds of frequencies can improve the accuracy of parameters estimation in SHM.
- (2) In truss model, adding mass is an effective way to make the local structure have LPF, by which the local damage can be identified fast and accurately. The relation analysis among the adding masses, LPF, and the relative sensitivity is discussed as the evidence to obtain the LPF. However, when large value of additional mass is required, some challenges are encountered in actual operation and mass installation, which are subjects of an ongoing research.

Conflict of Interests

The authors declare that there is no conflict of interests regarding the publication of this paper.

Acknowledgments

The authors gratefully acknowledge the support of the Major State Basic Research Development Program of China (973 Program) (2013CB036305), of National Science Foundation of China (NSFC) (51108057, 51108066), of the Fundamental Research Funds for the Central Universities (China) (DUT13LK13), of Special Financial Grant from the China Postdoctoral Science Foundation (2012T50255), and of the Project of National Key Technology R&D Program (China) (2011BAK02B01, 2011BAK02B03, and 2006BAJ03B05). Financial support of the Polish National Science Centre Project “AIA” (DEC-2012/05/B/ST8/02971) and of Structural Funds in the Operational Programme-Innovative Economy (IE OP) financed from the European Regional Development Fund, Project “Modern material technologies in aerospace industry” (POIG.01.01.02-00-015/08), is gratefully acknowledged.

References

- [1] P. C. Chang, A. Flatau, and S. C. Liu, “Review paper: health monitoring of civil infrastructure,” *Structural Health Monitoring*, vol. 2, no. 3, pp. 257–267, 2003.
- [2] E. Figueiredo, G. Park, C. R. Farrar, K. Worden, and J. Figueiras, “Machine learning algorithms for damage detection under operational and environmental variability,” *Structural Health Monitoring*, vol. 10, no. 6, pp. 559–572, 2011.
- [3] W. Fan and P. Qiao, “Vibration-based damage identification methods: a review and comparative study,” *Structural Health Monitoring*, vol. 10, no. 1, pp. 83–111, 2011.
- [4] S. Hassiotis, “Identification of damage using natural frequencies and Markov parameters,” *Computers and Structures*, vol. 74, no. 3, pp. 365–373, 2000.
- [5] Z. Duan, G. Yan, J. Ou, and B. F. Spencer, “Damage localization in ambient vibration by constructing proportional flexibility matrix,” *Journal of Sound and Vibration*, vol. 284, no. 1-2, pp. 455–466, 2005.
- [6] R. M. Lin and D. J. Ewins, “Model updating using FRF data,” in *Proceedings of the 15th International Seminar on Modal Analysis*, pp. 141–162, Leuven, Belgium, 1990.
- [7] C.-B. Yun and E. Y. Bahng, “Substructural identification using neural networks,” *Computers and Structures*, vol. 77, no. 1, pp. 41–52, 2000.
- [8] B. Jaishi and W.-X. Ren, “Finite element model updating based on eigenvalue and strain energy residuals using multiobjective optimisation technique,” *Mechanical Systems and Signal Processing*, vol. 21, no. 5, pp. 2295–2317, 2007.
- [9] Y. An and J. Ou, “Experimental and numerical studies on model updating method of damage severity identification utilizing four cost functions,” *Structural Control and Health Monitoring*, vol. 20, no. 1, pp. 107–120, 2013.
- [10] N. G. Nalitolela, J. E. T. Penny, and M. I. Friswell, “Mass or stiffness addition technique for structural parameter updating,” *The International Journal of Analytical and Experimental Modal Analysis*, vol. 7, no. 3, pp. 157–168, 1992.

- [11] N. Nalitolela, J. E. T. Penny, and M. I. Friswell, "Updating model parameters by adding an imagined stiffness to the structure," *Mechanical Systems and Signal Processing*, vol. 7, no. 2, pp. 161–172, 1993.
- [12] P. D. Cha and L. G. de Pillis, "Model updating by adding known masses," *International Journal for Numerical Methods in Engineering*, vol. 50, no. 11, pp. 2547–2571, 2001.
- [13] H. M. Dinh, T. Nagayama, and Y. Fujino, "Structural parameter identification by use of additional known masses and its experimental application," *Structural Control and Health Monitoring*, vol. 19, no. 3, pp. 436–450, 2012.
- [14] J. L. Hou, L. Jankowski, and J. P. Ou, "Substructural damage identification using local primary frequency," in *Proceedings of the 11th International Symposium on Structural Engineering*, Guangzhou, China, December 2010.
- [15] J. L. Hou, L. Jankowski, and J. P. Ou, "Structural damage identification by adding virtual masses," *Structural and Multi-disciplinary Optimization*, vol. 48, pp. 59–72, 2013.

Research Article

A GIS-Enabled Approach for Assessing Damage Potential of Levee Systems Based on Underlying Geology and River Morphology

Mustafa Saadi and Adda Athanasopoulos-Zekkos

Civil and Environmental Engineering, University of Michigan, Ann Arbor, MI 48109, USA

Correspondence should be addressed to Adda Athanasopoulos-Zekkos; addazekk@umich.edu

Received 17 July 2013; Accepted 13 October 2013

Academic Editor: Anaxagoras Elenas

Copyright © 2013 M. Saadi and A. Athanasopoulos-Zekkos. This is an open access article distributed under the Creative Commons Attribution License, which permits unrestricted use, distribution, and reproduction in any medium, provided the original work is properly cited.

Flood protection levee systems are complex, interconnected systems, where failure at one location means failure of the entire system. Levees are formed through various geologic processes and human activities over time and information regarding soil properties is collected only at limited point locations and varies significantly both laterally and with depth. Prediction of levee performance in locations where no soil data is available becomes a limitation for system risk assessment studies. Geographic Information Systems (GIS) are particularly suitable for the complex and efficient management of spatial information, georeferencing capabilities, and geostatistical analysis. A GIS enabled approach for assessing damage potential of levees systems is presented. Spatial variability of soil properties is correlated with regional variables such as distance from nearest river segment, river meandering sinuosity index, and surface geology. A geostatistical ordinary kriging approach is used for developing these correlations. Soil strength parameters of identified levee stratigraphy layers were statistically analyzed using a geostatistical ordinary kriging approach and correlated with preselected regional variables. A levee system in Northern California is used as a pilot study for the proposed approach. Excessive underseepage and loss of freeboard due to soil liquefaction are evaluated as the two damage indices for earthen levees.

1. Introduction

Flood protection systems are important parts of the civil infrastructure of the United States. Recent natural disasters like Hurricane Katrina have provided warnings with regard to the need to maintain and upgrade the aging and deteriorating flood protection systems. Furthermore, the American Society of Civil Engineers (ASCE), in its most recently released Infrastructure Report Card [1], gave the country's infrastructure an overall average performance grade of D (poor) in a scale from A (exceptional) to F (failing). The newest infrastructure category, levees, received a D- (i.e., poor: the infrastructure is in poor to fair condition and mostly below standard, with many elements approaching the end of their service life. A large portion of the system exhibits significant deterioration. Condition and capacity are of significant concern with strong risk of failure). The Department of Water Resources (DWR) in California is currently helping in

leading the efforts for improving the nation's flood protection infrastructure by reevaluating the vulnerability of the flood protection systems in the San Joaquin and Sacramento River Valleys and in the Sacramento Delta region [2, 3].

The vast majority of US river cities, now growing at increasing rates, are protected from flooding by earthen levees. Present day earthen levees are at risk from many causes of failure (Figure 1) including seepage (both underseepage and throughseepage), erosion, and instability due to seismic loading. Seismic loading is a potentially grave hazard in many areas of the nation. Guidelines for a seismic element of levee design have never been implemented as a national standard practice, so there are many thousands of miles of seismically vulnerable levees throughout the nation (Figure 2).

Levee response and performance are dependent on the loading condition, as well as the levee geometry and the properties of the levee materials and the foundation soils. Due to the large physical extent of such systems along rivers

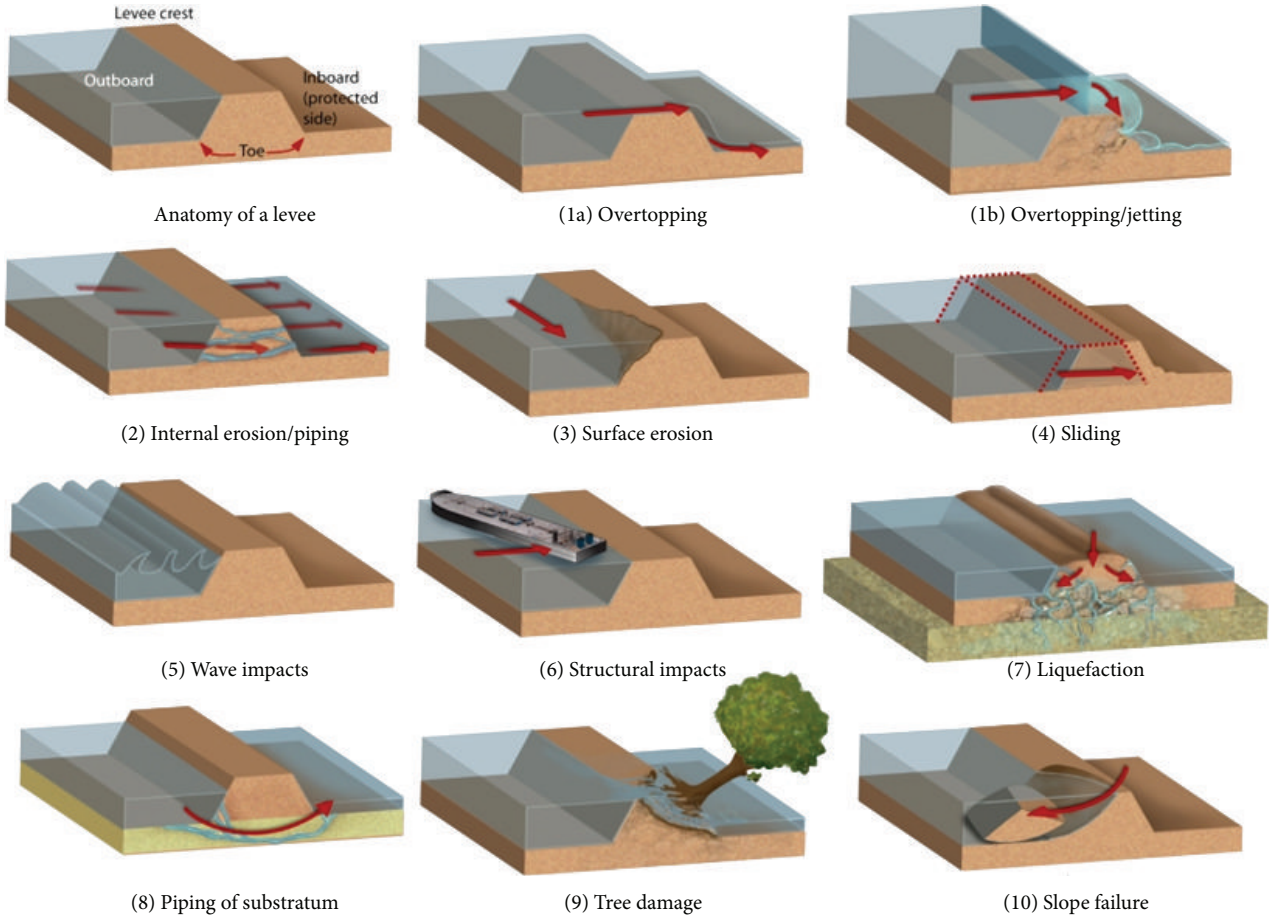


FIGURE 1: Basic levee failure mechanisms [7].

and canals and in the absence of as-built documentation, soil investigation data is at best available at scattered intervals along the levee length, carries a high level of uncertainty, and can be inconsistent, unreliable, or incomplete depending on when and by whom the investigation was carried out.

Earthen flood protection systems are complex, interconnected, adaptive engineered systems where failure at one location means failure of the system, and failure at different locations may result in flooding of different areas. The general risk assessment aspect of such engineered systems has recently become the topic of research efforts such as the Resilient and Sustainable Infrastructure Networks project [10]. However, even though levees stretch for long distances and are in part formed through various geologic processes and human activities over time, information regarding soil properties is collected only at a limited number of point locations and can vary significantly both laterally and with depth. Hence, this becomes a limitation in prediction of the performance of levees in locations where no soil data is available. Analyses with regard to levee vulnerability were performed to date only at locations with known soil properties [3, 11, 12]. A simplified procedure for the assessment of seismic vulnerability at a particular levee location with known soil properties has been proposed [13, 14] and is currently being adopted within the Urban Levee Project led

by URS Corp. for the Department of Water Resources in California and the under development USACE Guidelines for Seismic Evaluation of Levees, [15]. The spatial continuity of the results, however, is particularly critical in levee systems since failure of a levee at any location could result in the failure of the function of the overall flood protection system. The estimate of the earthen levee response in locations with no available soil data therefore becomes an issue of major concern. As such, it is critically important to develop an approach for assessing the risk of failure continuously along the length of levees. This paper presents an approach for a unified assessment of damage potential of earthen levee systems by developing a GIS-based computational platform that accounts for spatial variability of the soils and includes refined slope stability and liquefaction hazard assessment models, specifically tailored to earthen levees. The main assumptions for the study include a simplified soil characterization of the levee and foundation material, as well as a simplified determination of the probability of failure. Two damage indices were investigated: underseepage and soil liquefaction. Despite these assumptions and simplifications, the pilot study serves as an illustrative example of the application of the proposed methodology. The seismic hazard exposure of the flood protection system in California makes the area specifically appropriate for a pilot study for both

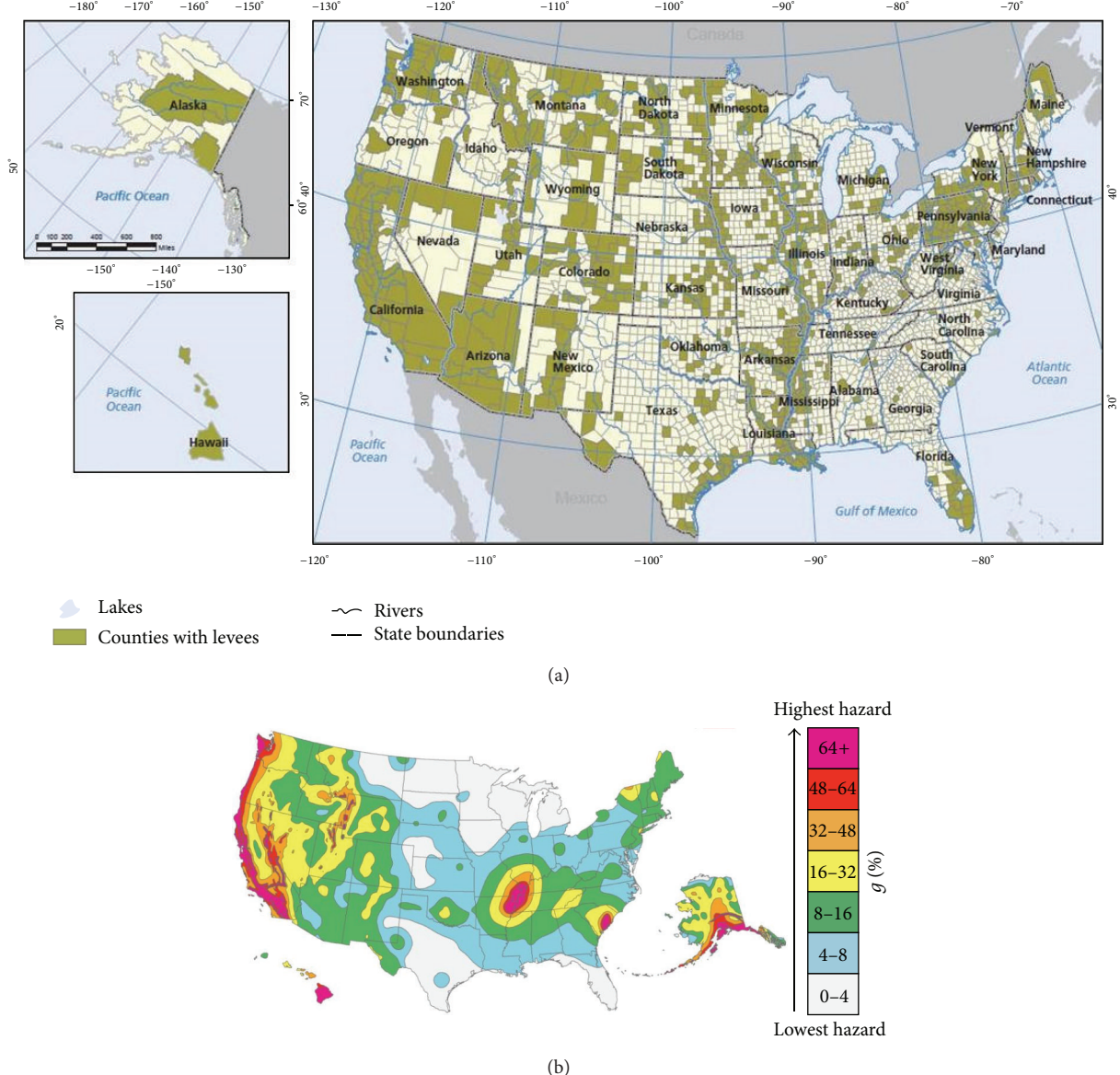


FIGURE 2: (a) Map of the United States counties that contain levees [8] and (b) National Seismic Hazard Map across the United States showing the levels of horizontal shaking that have a 2-in-100 chance of being exceeded in a 50-year period. Shaking is expressed as a percentage of g , the acceleration of a falling object due to gravity [9].

modes of failure. A representative region was chosen for the pilot study with a levee system surrounding and protecting a city in Northern California. The area is representative of the region which constitutes the greatest population density in Northern California and carries more than 25% of the nation's annualized risk [16].

2. Previous Work on Spatially Distributed Soil Properties

Soils and rocks in their natural state are among the most variable of all engineering materials. Quantitative measurements of soil properties in the early 1900s differentiated the new discipline of soil mechanics from the engineering of earth

works in the previous periods. However, these measurements revealed a great amount of variability in properties, not only from site to site and layer to layer but even within what seemed to be a homogenous material [22]. The variation in these parameters, due to inherent variations in composition and consistency during formation, is thus a three dimensional problem that involves the vertical stratification at any given point, as well as the planar deviations within a specific layer.

Ranges of data variation for soil property parameters have been reported by many researchers, especially starting in the 1960s [23–26]. Despite the work that has been done on this issue, it is not a closed matter, and more needs to be done, particularly on quantifying the level of additional effort required to improve existing characterization of a particular site [27].

TABLE 1: Coefficient of variation for common field measurements [4].

Test type	Property	Soil type	Mean	Units	COV (%)
CPT	q_T	Clay	0.5–2.5	MN/m ²	<20
	q_c	Clay	0.5–2	MN/m ²	20–40
	q_c	Sand	0.5–30	MN/m ²	20–60
VST	S_u	Clay	5–400	kN/m ²	10–40
SPT	N	Clay and sand	10–70	blows/ft	25–50
	A reading	Clay	100–450	kN/m ²	10–35
	A reading	Sand	60–1300	kN/m ²	20–50
	B reading	Clay	500–880	kN/m ²	10–35
DMT	B reading	Sand	350–2400	kN/m ²	20–50
	I_D	Sand	1–8		20–60
	K_D	Sand	2–30		20–60
	E_D	Sand	10–50	MN/m ²	15–65
	P_L	Clay	400–2800	kN/m ²	10–35
PMT	P_L	Sand	1600–3500	kN/m ²	20–50
	E_{PMT}	Sand	5–15	MN/m ²	15–65
	w_n	Clay and silt	13–100	%	8–30
	w_L	Clay and silt	30–90	%	6–30
	w_p	Clay and silt	15–15	%	6–30
Lab Index	PI	Clay and silt	10–40	%	— ^a
	LI	Clay and silt	10	%	— ^a
	γ, γ_D	Clay and silt	13–20	kN/m ³	<10
	D_r	Sand	30–70	%	10–40; 50–70 ^b

^aCOV = (3–1.2%)/mean; ^bthe first range of variables gives the total variability for the direct method of determination, and the second range of values gives the total variability for the indirect determination using SPT values.

One way to measure the variability of soil properties is similar to the work by Phoon and Kulhawy [4]. The extent, to which soil data might vary, is measured by the coefficients of variation (COV) for a variety of soil properties (Table 1). The COV is defined as the standard deviation divided by the mean. The range of values of the COV is large and is only reflective of conditions at a particular site. As such, there is a need for extending such measures of variability beyond site specific conditions and applying them to more general conditions of geological or geographical environments such as riverine or deltaic regions, as is the case in this study. Furthermore, although some of the general trends of variability in soil and rock can be anticipated, the uncertainty in practice can be larger than expected, with significant implications to geotechnical design and analysis [27].

In the absence of unlimited resources that would permit as many boreholes and tests as needed, geotechnical engineers find themselves most of the time having to deal with limited site investigation data. The traditional approach in dealing with limitation in design has been to use characteristic values of the soil properties combined with a factor of safety. However, for a particular soil layer, soil parameter data sampled at multiple locations on a site would likely plot in a bell-shaped curve. This variability, even in the smallest of sites, suggests that geotechnical engineering systems are amenable to a statistical approach, and most soil properties can be regarded as random variables conforming to the

“normal” or “Gaussian” theoretical distribution, thus established statistical methods based on the normal distribution may safely be applied in estimating design parameters [25, 28].

3. Field Data Collection and Processing

To achieve the main objective of this study, it was important to investigate and understand the spatial distribution of soil properties and levee characteristics in a selected geographical area. In this research the dependent variables were selected to be the soil type (e.g., sand, clay, and silt) and its associated properties (e.g., shear strength and unit weight). Independent variables (i.e., river sinuosity, surficial geology, and distance from river) were selected, based on theory and engineering judgment, to correlate with the dependent variables and then apply a geostatistical kriging approach to estimate the dependent variable’s spatial distribution. The underlying geology and river geomorphology in the study area have played an important role in identifying these variables in this research project. Geomorphology is by definition the study of landforms, such as naturally formed levees, and the history of formation and dynamic processes that shape them.

A pilot study area was selected so that the previously described variables and correlations could be studied and analyzed. The study area used for this research encompasses the levee system protecting Sacramento City as well as the Feather River, both situated at the northeastern limit of

TABLE 2: Data types and sources.

Data	Source
Surface soil data	Soil Survey Geographic Database (SSURGO)
Underlying geology features	United States Geological Survey (USGS)
Hydrological features and characteristics	National Hydrography Dataset (NHD)
Ground water table	National Water Information System (USGS)
Terrain elevation data	National Elevation Dataset (NED)
County limit, cities, and road networks	State, county, and city authorities
Population	US Census Bureau
Land cover	Multi-Resolution Land Characterization (MRLC)
Aerial maps	Bing maps, through the ArcGIS online Server
Levee geometry and soil properties	(i) Soil report for Sacramento City, US Army Corps of Engineers, 1987 (ii) Maps and borehole, URS Corporation and the California Department of Water Resources Urban Levee Evaluation Program, 2010

the San Joaquin-Sacramento delta region, where the levee material and cross sections can be considered typical of the area. A possible earthquake related levee system failure in Sacramento alone, as per one estimate, might put at risk more than 400,000 people and 170,000 structures and have a potential economic impact of \$7 to \$15 billion [29]. The study area is representative of the larger region constituting the greatest population density in Northern California and carrying more than 25% of the nation's annualized risk [16]. The specific areas used for data analysis and model development in this study were subsections of the larger SRFCP (Figure 3) grouped as follows:

- (1) city of Sacramento, comprising of West Sacramento region and American River,
- (2) Feather River, comprising of Feather River South and Reclamation District 784, City of Marysville, and Feather River North.

Data used for this study was collected from a number of sources (Table 2). Due to the spatial distribution of the data, the Geographic Information Systems (GIS) platform was used for reporting and analysing the data. Some of the spatial data was available from online databases such as the United States Geological Survey's Natural Map Viewer [30]. Other data was not available in GIS format, especially data related to geotechnical investigation and levee layouts, and had to be manually digitized.

The levee system is defined as the collection of earthen embankments with a corresponding delineated protected area. The levee system is divided for analysis purposes into segments called levee reaches. Levee reaches can be modeled based on the distribution of levee sections of similar embankment and foundation characteristics.

The underlying foundation geology below the river bed of the Sacramento River in California, according to Helley and Harwood [31], is detailed in Table 3. Manual tracing of the area limits was done using scanned hand-drawn USGS maps and GIS georeferencing and editing tools resulting in Figure 4.

A river's sinuosity is its tendency to meander back and forth across the floodplain over time, in what looks like an S-shaped pattern (Figure 5(a)). Mount [32] states that the scarcity of "perfectly straight" rivers in nature is widely believed to indicate that meandering is the more preferred state of single channel rivers. The development of sinuosity in a river takes place due to secondary flow (flow that moves downstream in a cylindrical spiral motion within the channel). The longitudinal bed profile of most rivers is divided into series of alternating high and low gradient segments. This results in the formation of riffles (high points on bed profile) and pools (deep water areas between riffles). In a low-sinuosity low-gradient channel, the overall stream power is usually low, the secondary flow minimal, and thus there is little erosion of the banks and the channel remains relatively static. However, when stream power is great enough, bank erosion will increase initiating the formation of meander bends. Increased meandering and outer bank erosion is matched by increased deposition of material on the opposite bank resulting in alternating point bars along the river length (Figure 5(b)). As a result of the above described process a "relatively straight" river section is expected to have less variability in the properties of the material deposited at its banks than a section that is "meandered."

The meander ratio, or sinuosity index, SI, is a means of quantifying how much a river or stream meanders. It measures the deviation of a river center path length from the shortest possible path and is a reflection of the channel length required to cover a given point-to-point straight line distance. SI is calculated as the length of the river channel center path divided by the straight line length of the valley containing the river. In straight streams, $SI = 1.0$, whereas a value of 4.0 is considered to be highly intricate meandering. For this study, and based on classifications by researchers in the field [5, 6] the scale shown in Table 4 was adopted.

In order to calculate SI, it is necessary first to define the length of "one meander wave," L , similar to the concept of the frequency of a sinusoid wave function (Figure 6). A number of authors [33, 34] refer back to the work by Leopold et al. [35] who found that meander wave length (L) varies from

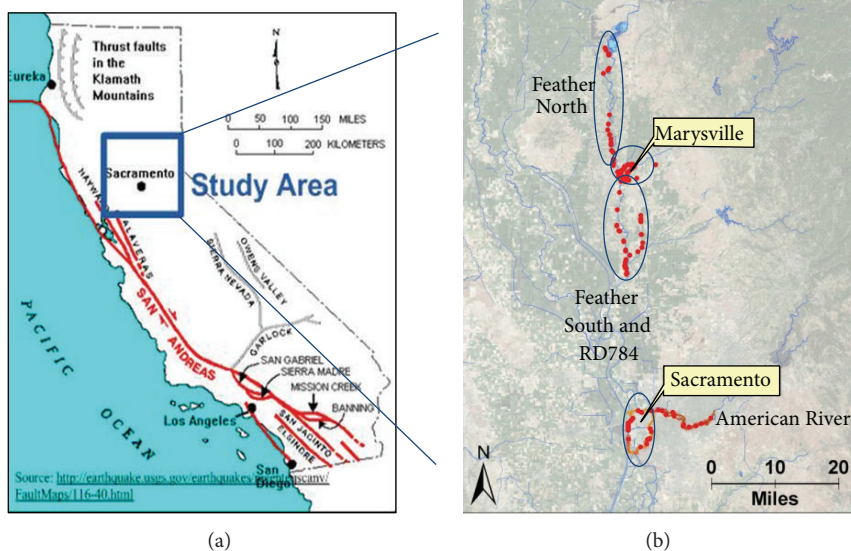


FIGURE 3: (a) Location of the study area in the state of California, with (b) close-up view and details of the locations of available geotechnical investigation boreholes around cities of Sacramento and Marysville.

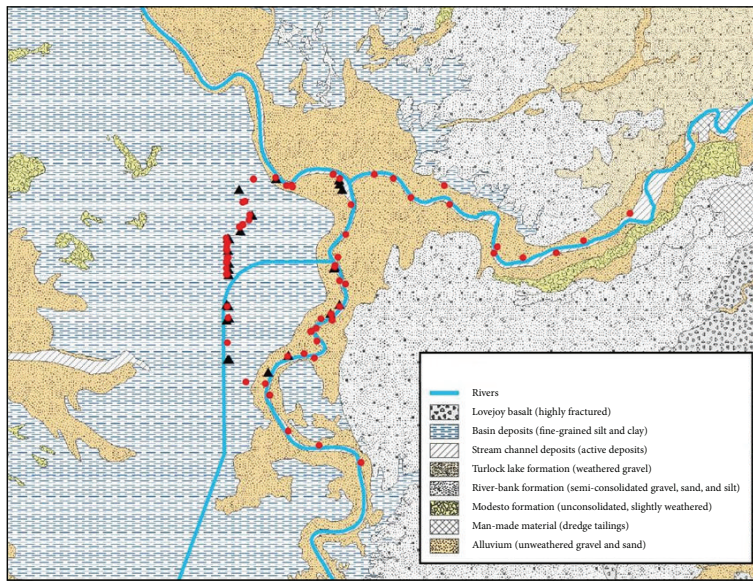


FIGURE 4: Underlying foundation geology regions drawn in ArcGIS reflecting the hand-drawn maps prepared by Helle and Harwood [31].

$L = 7.32w^{1.1}$ to $12.13w^{1.09}$ with the average being roughly equal to 10 times the river channel width " w ". No streams existing in nature owe all of their sinuosity to hydraulic factors, rather, almost all streams have some degree of both hydraulic and topographic sinuosity [6]. However, for simplicity, it is common to derive the SI based on concepts of hydraulics, which is what has been done in the present study.

A number of meander wave lengths, referred to as river segmentation levels, were applied at the study areas in order to come up with values of SI. The river features are divided into segments, each is equal to the segmentation levee of interest, and the calculated value of the sinuosity index is assigned to the individual segments (Figure 7). For the Sacramento City area, the river width varied from ~70 to

~210 m, with most river segments widths around the value of 150 m, giving a rough estimate of the expected meander length of 1,500 m. Using the above mentioned equations by Leopold et al. [35] the segmentation levels tried for Sacramento were 500 m, 1500 m, 1750 m, 2500 m, and 3500 m. For Feather River, the width varied from ~60 to ~150 m, with most river segments widths around the value of 100 m, giving a rough estimate of the expected meander length of 1,000 m. The segmentation levels tried in this area were 500 m, 1000 m, 1500 m, and 2500 m.

The issue of sinuosity is further complicated by having single versus multiple parallel river channels. Because of lateral migration of meandering streams, levees should be placed at a fair distance from migrating channels [33].

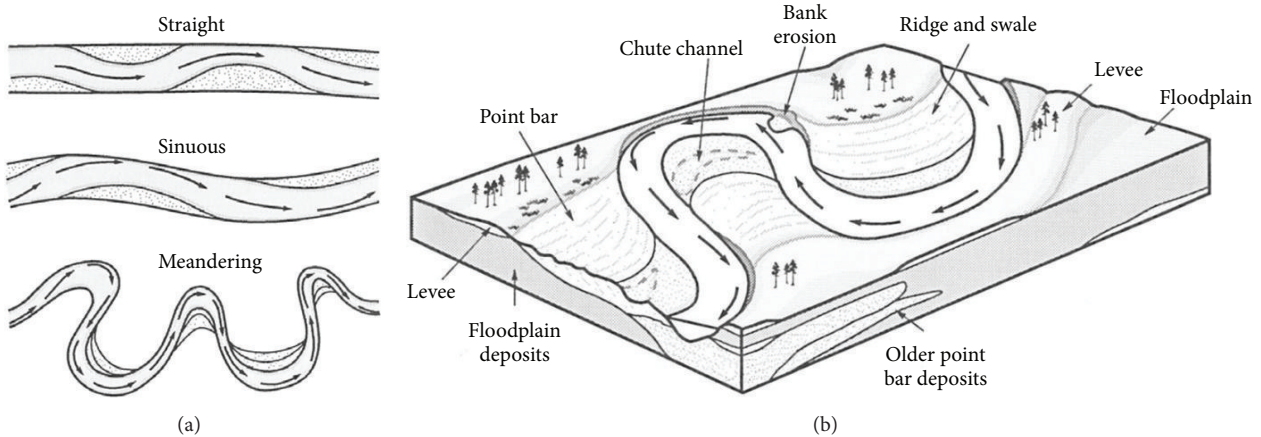


FIGURE 5: (a) Different levels of river meandering, with arrows indicating location of highest velocity flows and (b) major sedimentary features of a meandering single channel river, showing erosion and deposition process leading to formation of point bars [32].

TABLE 3: Underlying geology classification for the Sacramento River basin.

Deposit classification	Code	Short description	Geological epoch	Maximum thickness (m)
Alluvial deposits	Qa	Alluvium-unweathered gravel, sand, and silt	Holocene	10
Basin deposits	Qb	Basin deposits, undivided-Fine grained silt and clay	Holocene	60
Alluvial deposits	Qsc	Stream channel deposits of open, active stream channels (morphology constantly changing) Modesto formation—upper Member—unconsolidated, unweathered mix of gravel, sand, silt and clay	Holocene	25
Alluvial deposits	Qmu	Modesto formation—lower Member—unconsolidated, slightly weathered gravel, sand, silt, and clay	Pleistocene	120
Alluvial deposits	Qml	Riverbank formation—upper Member—unconsolidated alluvium composed of gravel, sand, and silt	Pleistocene	120
Alluvial deposits	Qru	Riverbank formation—lower Member—semiconsolidated gravel, sand, and silt	Pleistocene	120
Alluvial deposits	Qrl	Stream channel deposits of open, active stream channels (morphology constantly changing)	Pleistocene	120
Alluvial deposits	Qsc		Holocene	250

TABLE 4: Level of river meandering as a function of the sinuosity index, SI (after [5, 6]).

Sinuosity index, SI	Level of meandering
1.0-1.1	Straight
1.1-1.3	Sinuous
1.3-1.5	Slightly meandering
>1.5	Meandering

However, this is not always the case, especially in urban areas where insufficient space forces the building of levees at the edge of the stream. In the present study no multiple parallel

river channels were included. Thus it becomes important to determine the levee parts located in the highly meandered river sections in order to give them special attention in the analyses. Sacramento River is a meandering single-channel river that occupies one relatively stable main channel surrounded by an extensive floodplain. It is a prime example of meandering river, although channeling by public works projects has greatly altered the original pattern of such rivers [32].

The ground water table level in the study areas was determined because of its direct effect on the calculation of effective stress values in soil. The results of all calculated groundwater level, from data covering the period from 1983

TABLE 5: Calculated ground water table (GWT) levels (m) in the study area, mean sea level = 0 m.

Area	Elevation (m) from MSL		Relative depth (m)		
	Crest	Toe	GWT	GWT below crest	GWT below toe
Feather River North	30	25	15	15	10
Marysville	27	21	12	15	9
Feather River South and RD784	22	15	9	13	6
Sacramento City	12	6	0	12	6

TABLE 6: Summary of available geotechnical investigation borehole logs and cone penetration tests (CPTs) in the study areas.

Area	URS boreholes					URS Historical log	USACE Borehole	URS CPTs
	Borehole (B)	Hollow stem auger (A)	Hand auger (H)	Sonic core (S)	Piezometer (M)			
West Sacramento	26	—	—	—	4	9 ^a	34	25
American River	10	—	—	—	6	27 ^a	—	—
Marysville	49	—	—	4	16	—	—	—
RD784	21	—	—	2	—	—	—	—
Feather North	10	14	5	—	—	—	—	19
Feather South	14	10 ^b	6	—	—	—	—	74
Total	267							118

^aMany more available. These are a short list of historical boreholes used for this study.

^bOne borehole was “solid” and not “hollow” stem auger.

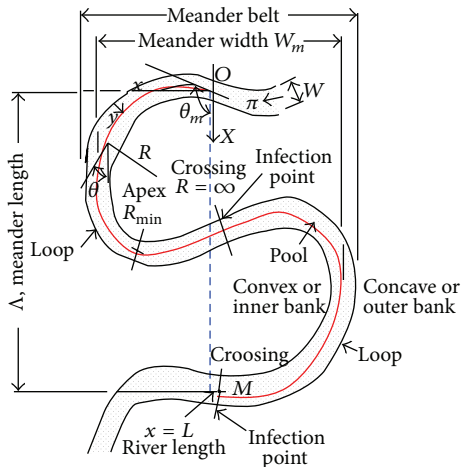


FIGURE 6: Characterization of a meandering river [33]. The sinuosity index is derived by dividing the river length (solid line), L , by the straight line valley length (dashed line).

to 2010 [36], are summarized in Table 5 and are in agreement with measurements available from the USACE report [17].

4. Geotechnical Investigation Data

As previously mentioned, geotechnical soil investigation data for the study area was collected from (1) URS corporation data from the California Urban Levee Evaluation Project [37] and (2) the USACE investigation report for Sacramento City [17]. Data from both sources included levee layout, levee geometry, boreholes logs, and field tests. The total number

of available logs, CPTs, and reported tests are summarized in Tables 6 and 7. All boreholes were digitized into a GIS format, and available test information was extracted for further analysis. Note that a large number of historical boreholes were reported in the URS dataset. No test results were available for these, and they were short-listed and only used in the process of identifying regional stratigraphy.

Laboratory test data reported in the URS database included Consolidated Undrained Strength (CU) and Vane Shear (VS) testing. However, the numerical values of these tests were not provided. Other lab test results included Water Content (WC), Liquid Limit (LL), Plasticity Index (PI), and Fines Content (%). CPT data was validated through close comparison to nearby borehole logs for soil layer delineation and soil classification. Subsequently, resulting common site specific CPT “signatures” (Figure 8) were developed for areas with no boreholes. CPT cone tip resistance was used to determine Undrained Shear Strength (S_u) of cohesive soils. The following empirical correlation [38] was used (1):

$$S_u = \frac{(q_t - \sigma_{vo})}{N_{kt}}, \quad (1)$$

where q_t is the corrected cone resistance, N_{kt} is an empirical cone factor, and σ_{vo} is the total in situ vertical stress.

The empirical parameter N_{kt} is site specific and can be back-calculated using available triaxial compression test results [17]. It is worth noting that for the same site, the value of N_{kt} varies depending on the type of laboratory test used to determine S_u [38]. Laboratory measured S_u values from USACE boreholes in West Sacramento were paired with corresponding nearby clay layers (at similar depth) from

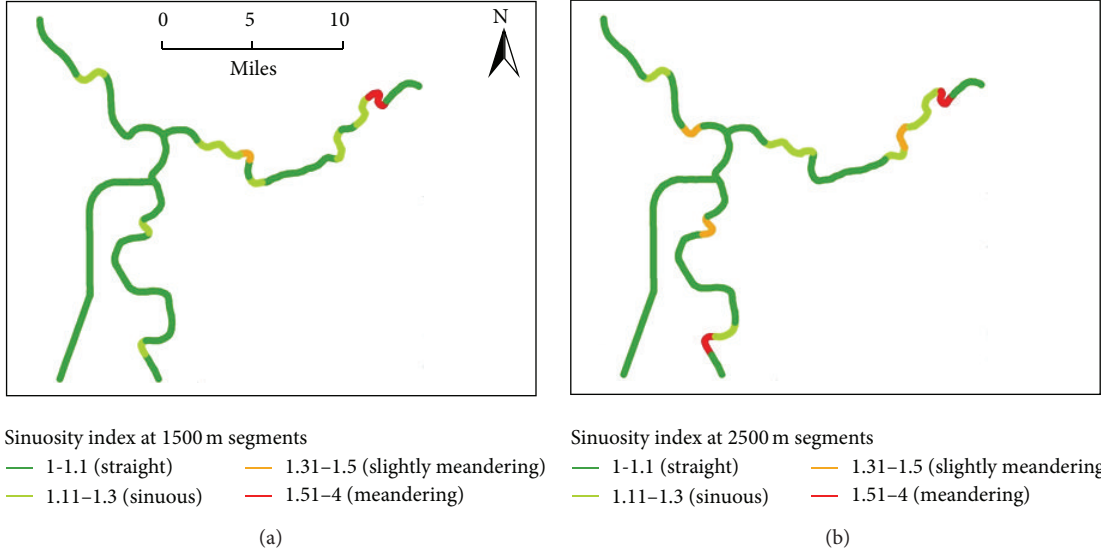


FIGURE 7: Comparison of sinuosity index outputs for different river segmentation levels at Sacramento City: (a) segmentation level of 1,500 m and (b) segmentation level of 2,500 m.

the URS CPTs. The back-calculated N_{kt} values had an average of 20.8 which is within, though at the high end of, ranges of N_{kt} values reported in the literature [38].

In order to derive friction angle, ϕ , values for cohesionless soils, Standard Penetration Test (SPT) values (N and N_{60}) had to be adjusted to $N_{1,60}$ using required correction factors and effective stress calculations made possible by the determined ground water table levels. A number of approaches were used for estimating friction angle, ϕ , values and are compared in Table 8. The friction angle in this study was derived from SPT using Kulhawy and Mayne [18] and from Cone Penetration Test (CPT) results using Robertson and Campanella [39]. Figure 8 shows a comparison of CPT data from this study with the soil classification chart proposed by Olsen and Mitchell [40].

5. Prediction of Regional Soil Stratigraphy

Prior to estimating the spatial variability of soil parameters, there is a need to estimate the soil stratigraphy in the area of study. Due to the increased uncertainties in derivation of strength parameters from in situ tests for silts, the focus was to determine the stratigraphy of sands and clays, since the derivation of strength parameters for those two categories of soils was possible given the available data. Therefore, a general category of “sand” was adopted for soils classified, according to the Unified Soil Classification System (USCS) [41], as poorly-graded sand (SP), well-graded sand (SW), poorly-graded sand with silt, that is, $5\% < \% \text{Fines} < 12\%$ (SP-SM), and well-graded sand with silt, that is, $5\% < \% \text{Fines} < 12\%$ (SW-SM). Similarly, a general category of “clay” was adopted for soils classified as fat clay (CH), lean clay (CL) and silty clay (CL-ML), according to USCS.

Furthermore, because of the geostatistical complexity of combining both the estimation of thickness variation of different layer types (qualitative parameter), with the estimation

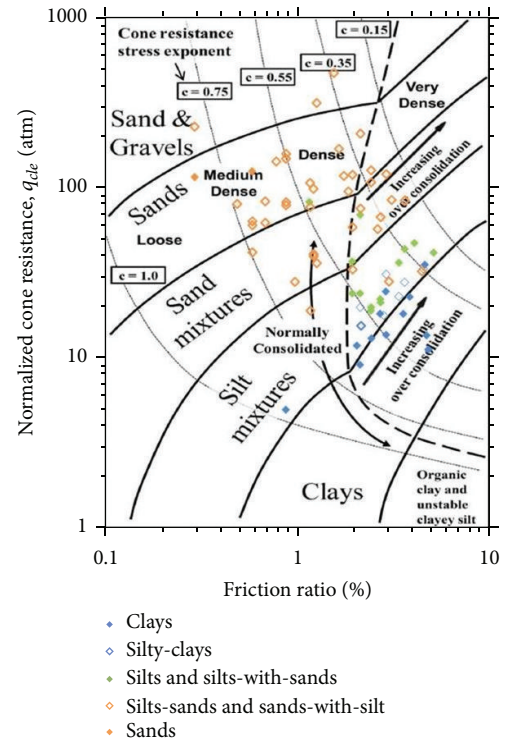


FIGURE 8: Example of collected CPT data from Sacramento City area plotted on the Olsen and Mitchell [40] soil classification chart.

of the soil parameter variability within each layer (quantitative parameter), and because the focus of this research was the study of soil properties variability, soil layers were assumed to exist at a constant thickness throughout the study areas. For each of the two study areas (Sacramento and Feather River) and based on the available borehole log classifications, plots were developed to help identify the stratigraphy of

the region. These plots do not include material identified as engineering fill within the levee, as the intent of the research is to study the spatial variation of naturally occurring soils. The plots also confirm that, within the area of study, the regional stratigraphy can be assumed to be uniform for the scope of this research. The layer delineation is determined based on the number of data points occurring with depth, in combination with the layer thickness for each data point in the respective borehole log. The “layer range” value for each identified layer represents the thickness of the band of soil where the identified layer was observed. The delineation of clay layers takes into account the corresponding delineation of the sand layers, and vice versa. As an example, Figure 9 shows the approach used for the delineation of layers in the Sacramento area based on available boreholes from USACE and URS datasets. The layers identified in Sacramento from Figure 9 are listed in Table 9. Similarly the resulting layer delineation for Feather River was performed using the URS boreholes, and the results are presented in Table 10. The number of layers observed was dependent on the limitation of depth of boreholes.

The following steps have been applied to all layers of both study areas. However, only figures relating to the identified “shallow clay layer in Sacramento” (the top layer in Figure 9) will be used as examples in the coming sections.

6. Prediction of Spatial Variability of Soil Parameters

6.1. Correlation of Soil Parameters with Regional Factors. For the delineated layers of clay and sand, the soil parameters that were studied were as follows: for sands, friction angle (ϕ) and fines content (%) and for clays, undrained shear strength (S_u), liquid limit (LL), plasticity index (PI), and ratio of water content to liquid limit (WC/LL).

The parameters were analyzed and correlations were developed, where applicable, with regional factors including distance to closest river, sinuosity of closest river segment, and underlying geology classification. The concept of “effective correlation distance” between the soil parameters and the factors was introduced, representing the distance beyond which no trend/correlation was observed or deemed physically significant. The “effective correlation distance” was determined from data in this study and could possibly change if additional data are provided in the future. Figure 10 is shown, as an example, for the shear strength parameter S_u of the Sacramento area shallow clay layer. As seen in the figure the S_u values increase with distance from the river up until 600 m but no specific trend is apparent for distances larger than 600 m. A possible explanation for this trend is that shallow clays close to the river have been deposited either more recently or have exhibited higher water tables and are therefore normally consolidated as opposed to shallow clays further away from the river where the water table may be lower allowing for overconsolidation of the clays and increase of S_u . Tables 11 and 12 show the established “effective correlation distance” and the “sinuosity index segmentation

level” for all seven layers. The latter is a reflection of the river meander length period.

Figure 11 summarizes the plots of the shallow clay layer parameters (S_u , LL, PI, and WC/LL) in Sacramento in relation to the distance from the centerline of closest river segment. A further analysis of the particular relation between S_u with geology (Figure 12) and sinuosity index (Figure 13) helps to establish preliminary relationships. For example, the latter figure implies that the value of S_u decreases with increased river sinuosity. The X-axis values in Figure 12, representing geology, are categorical values, thus no trend or fit can be deduced, but rather variability of S_u parameter with each particular geology type is established (Table 3).

6.2. Observations of Local versus Regional Effects. Clay in both shallow and deep layer and in both areas of study showed increasing trend of S_u with increasing distance from river (Figure 14). S_u values also increased with depth, which may be attributed to consolidation of the deeper layers over time.

As for relation of S_u to the different geological formations in the two study areas (Figure 15), a general observation is that clay S_u values in the areas of the Qa formation tend to have lower values than other areas. The Qa formation is defined as Alluvium-unweathered gravel, sand, and silt, as such clay is not the main component, which might provide an explanation for the lower values of S_u for clay in these areas, as compared to other formations.

Figure 16 shows the observed S_u relation to sinuosity index (SI). The higher number of data points at this low sinuosity level is due to the smaller number of river segments that are highly sinuous. An important observation across all areas of study and at shallow and deep clay layers is that S_u tends to decrease with increasing sinuosity of the closest river segment. A possible explanation of this phenomenon is that deposition of fine particles tends to be more uniform (leading to higher S_u values) if the river is less sinuous. Given the limited available data, however, it should be noted that more data points are needed to develop more robust correlations between SI and shear strength or soil type. Furthermore, due to the specific case study area that was used, the limited data was primarily available for SI values close to 1 (i.e., straight river sections). Note that the sinuosity is based on segmentation level of 1,750 m for Sacramento and 1,000 m for Feather River as discussed in Section 3.

6.3. Kriging Estimation Using Measured Parameter Values. The spatial variation of the soil strength parameters in the vicinity of levees was estimated by the ordinary kriging approach. The choice for ordinary kriging assumes that the local mean $m(u)$ is not necessarily closely related to the population (overall) mean and so only uses the samples (known values) in the local neighborhood of the estimate. The following steps demonstrate how to revise a spatially based kriging (solely based on distance between known points) into a revised kriged map that reflects correlation of soil parameters with regional factors in the riverine environment of the Sacramento River basin.

TABLE 7: Reported number of field and lab tests within the available geotechnical investigation boreholes and cone penetration tests (CPTs) in the study areas.

Area	SPT	URS boreholes and USACE								URS CPTs			
		MC ^a	CU ^b	VS ^b	WC	LL	PI	Fines	UU ^c	Rf ^d	qt ^d	fs ^d	u ₂ ^d
West Sacramento	648	46	11	2	173	166	166	298	30	25			
American River	133	4	—	—	35	13	12	56	—	—			
Marysville	651	19	15	—	39	35	35	90	—	—			
RD784	217	25	19	—	111	96	96	158	—	—			
Feather North	211	2	7	—	27	25	25	81	—	19			
Feather South	233	—	22	—	93	84	84	123	—	74			
Total	2093				478	419	418	806	30				

^aModified California test numbers to be converted to SPT equivalent.

^bNumerical results for Consolidated Undrained (CU) triaxial tests and Vane Shear (VS) tests were not provided.

^cUnconsolidated Undrained (UU) triaxial tests were only available from the USACE [17] data.

^dCPT logs represent continuous measurement of parameters.

TABLE 8: Relationship between $N_{1,60}$, density, and friction angle of sands.

$N_{1,60}$	Density	Friction angle, ϕ°			
		Kulhawy and Mayne [18]	Peck et al. [19]	Schmertmann [20]	Hatanaka and Uchida [21]
<5	Very loose	<31	<29	<28	<30
5–15	Loose	30–36	29–31	28–38	30–37
15–30	Medium	35–41	31–35	38–44	37–44
30–50	Dense	40–46	35–41	44–49	44–52
>50	Very dense	>42	>41	>49	>50

TABLE 9: Delineation of clay and sand layers in Sacramento area.

Location	Material	Depth	Depth order	Layer ref.	Absolute elevation (m) MSL = 0		
					From	To	Layer Range
Sacramento City	Clay	Shallow	1	1st clay	4	-4	8
	Sand	Shallow	2	1st sand	-2	-10	8
	Clay	Deep ^a	3	2nd clay	-11	-19	8
	Sand	Deep ^a	4	2nd sand	-18	-25	7

^aData available only from West Sacramento URS dataset.

TABLE 10: Delineation of clay and sand layers in Feather River area.

Location	Material	Depth	Depth order	Layer ref.	Absolute elevation (m) MSL = 0		
					From	To	Layer range
Feather South and RD784					17	10	7
Marysville	Clay	Shallow	1	1st clay	22	13	9
Feather North					25	17	8
Feather South and RD784					11	6	5
Marysville	Sand	Shallow	2	1st sand	15	8	7
Feather North					20	12	8
Feather South and RD784					7	0	7
Marysville	Clay	Deep	3	2nd clay	7	0	7
Feather North					12	6	6

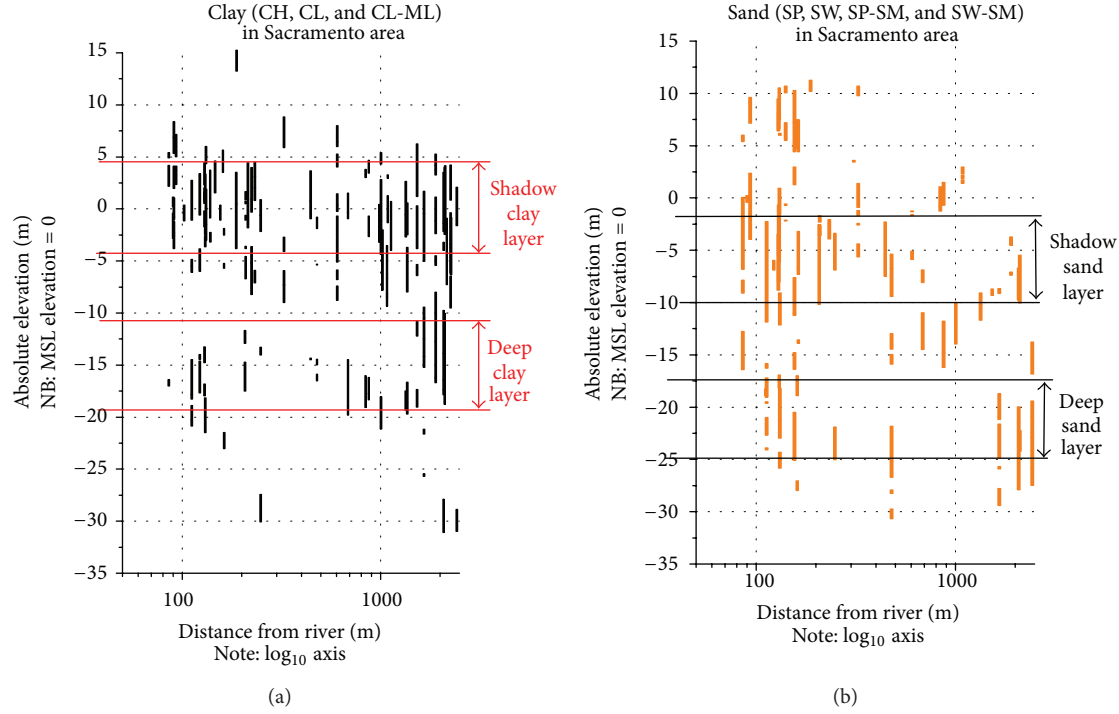
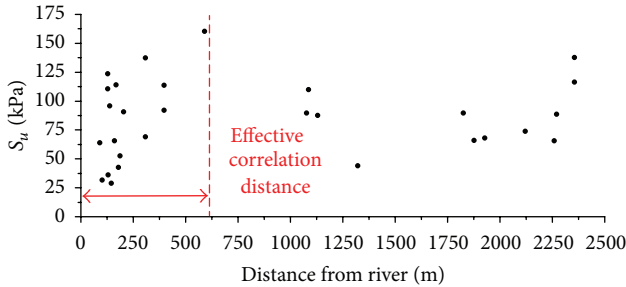


FIGURE 9: Process of layers delineation for clay and sand in Sacramento based on borehole log information.

TABLE 11: “Effective correlation distance” and “sinuosity index segmentation level” for soil layers in Sacramento area.

Location	Material	Depth	SI segmentation level (m)	Effective correlation distance (m)					
				ϕ	Fines	S_u	LL	PI	WC/LL
Sacramento City	Clay	Shallow	1750	—	—	600	600	600	1500
	Sand	Shallow	1750	450	450	—	—	—	—
	Clay	Deep	1750	—	—	n/a ^a	1500	1500	1500
	Sand	Deep	1750	450	450	—	—	—	—

^aOnly three data points, and all are at large distance from the river.

FIGURE 10: Example of determination of the “effective correlation distance” for the shear strength parameter, S_u , for the Sacramento area shallow clay layer.

Geostatistical analysis was performed using the ArcGIS Geostatistical Analyst software extension. Outputs of the geostatistical analysis of the known sampled data points include the empirical (or experimental) semivariogram, cross validation, and error plots, as well as information pertaining to the main variables of interest at this stage: nugget, range, and sill. A summary of the range, nugget, and partial sill

values from the semivariograms is presented in Table 13. The “correlation range” is the distance beyond which no spatial relation exists between points; that is, a known sampled points do not affect measurements at another point situated at this, or a larger, distance. The range value for clay is almost twice as large as the value for most sands. This is consistent with the observation that the effective correlation distance for clays was also larger than that of sand by a similar margin.

Kriging estimate maps were derived, with corresponding semivariograms, for all identified layers in the study areas. A sample map output of the kriging approach for the estimation of the shear strength S_u of the shallow foundation clay layer in Sacramento is shown in Figure 17, with shaded colour symbology representing variation of the estimated S_u values, classified as soft to medium clay ($S_u < 50$ kPa), stiff clay ($50 \text{ kPa} < S_u < 100$ kPa), very stiff clay ($100 \text{ kPa} < S_u < 150$ kPa), and hard clay ($S_u > 150$ kPa). The area between the dashed lines running parallel on both sides of the river represents the “effective correlation distance” between the soil parameter and the factors. The focus is to estimate the soil variability in within this distance from the river because (1)

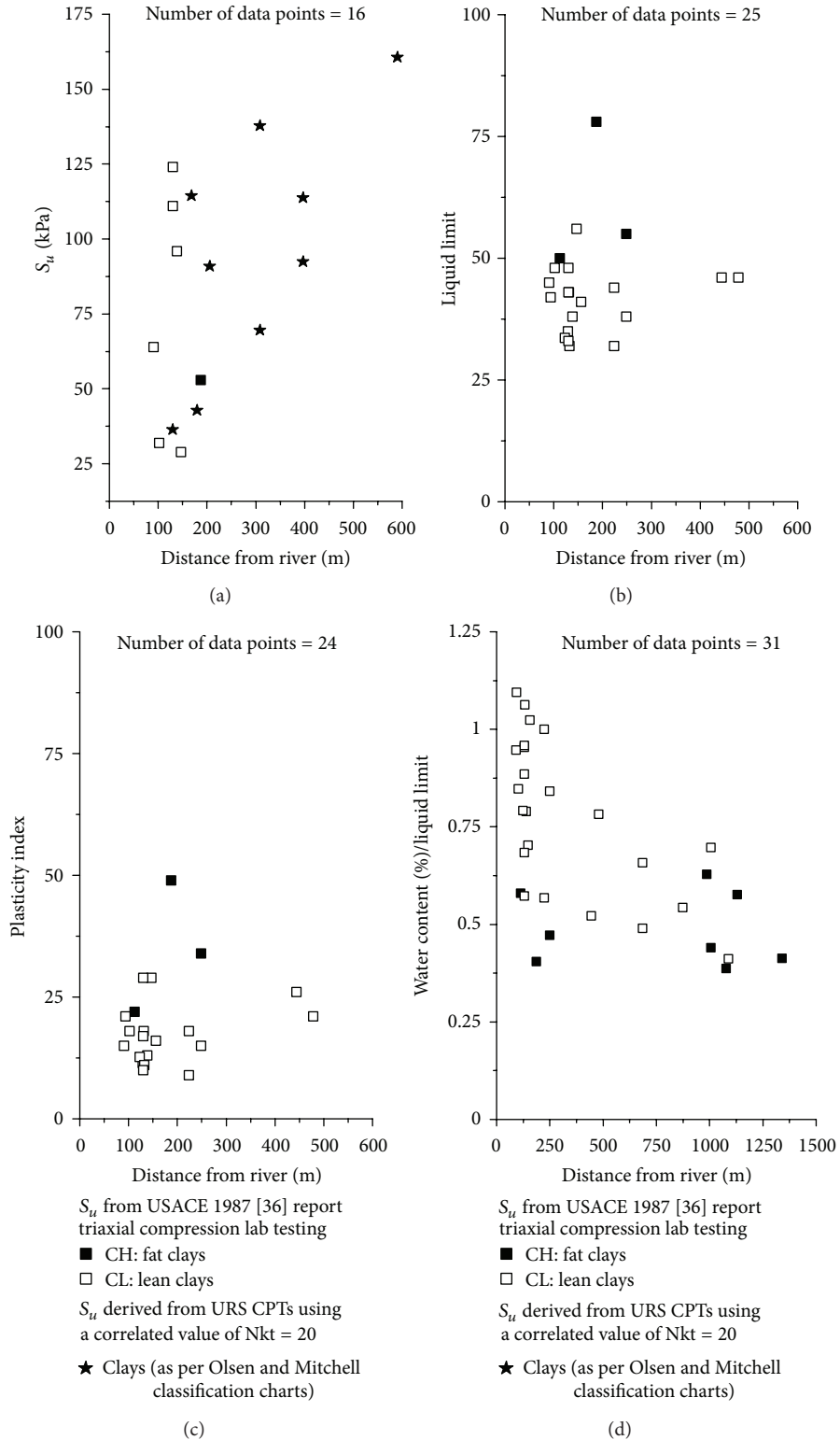


FIGURE 11: Relation of shallow clay soil parameters to distance from centerline of closest river segment in Sacramento.

TABLE 12: “Effective correlation distance” and “sinuosity index segmentation level” for soil layers in Feather River area.

Location	Material	Depth	SI segmentation level (m)	Effective correlation distance (m)				
				ϕ	Fines	S_u	LL	PI
Feather River	Clay	Shallow	1000	—	—	600	600	600
	Sand	Shallow	1000	450	450	—	—	—
	Clay	Deep	1000	—	—	600 ^a	600 ^a	600 ^a

^aData available only from Feather River South.

TABLE 13: Parameters from the ordinary kriging semivariograms of identified soil layers in the study areas.

Location	Depth	Material	Parameter	Unit	Correlation range (m)	Nugget ^a	Partial sill ^a
Sacramento City	Shallow	Clay	S_u	kPa	819	19.5	1730
	Shallow	Sand	ϕ	Degrees	400	0.3	3
	Deep	Clay	S_u	kPa	— ^b		
	Deep	Sand	ϕ	Degrees	177 ^c	1	17
Feather River	Shallow	Clay	S_u	kPa	— ^b		
	Shallow	Sand	ϕ	Degrees	407	1	11
	Deep	Clay	S_u	kPa	— ^b		

^aUnits of these elements is the “square of the corresponding parameter unit”.

^bNo kriging estimate could be done due to limited number of data points available for the S_u parameter of this layer.

^cThe low value of the range for the deep Sacramento River as compared to the other sand layers is due to limited number of data points at large distances for this particular layer.

TABLE 14: Simplified damage potential criteria used for underseepage and liquefaction.

Levee material	Clay	Sand	Clay	Sand
Foundation material	Clay	Clay	Sand	Sand
Underseepage	Of no concern	Of little concern	Of some concern	Of concern
Liquefaction	Of no concern	Of some concern	Of some concern	Of concern

correlation of soil strength parameters with regional factors has been established with this limitation and (2) this distance is far enough from the levee in a way that the soil parameter values beyond that will not affect the response of the levee fill.

6.4. Adjustment of Kriging Estimate Using Regional Correlations. A uniform grid of points was established within the effective correlation area from the river center. At these grid locations the estimated kriging S_u values were read and adjusted as needed to reflect the correlations with regional factors. A large grid size would not capture the correlations with the regional factors, nor will it capture the effect of spatial autocorrelation of individual soil parameters, and a confirmation of the most effective grid size requires field validation of the estimated parameters. Each location on the grid is assigned the attributes of (1) experimental kriging estimate value (Figure 17), (2) distance to closest segment of river, (3) geology layer, and (4) sinuosity of closest segment of river. These attributes are then used to represent the grid points on the plots of shear strength parameter S_u versus the corresponding factors.

Curve fits established between the soil strength parameters and the regional factors serve as a check to the ordinary kriging estimation method. Any grid location that exhibits values falling away from these established regional factor trends will have its S_u -kriging-estimate value revised in

order to fall within an acceptable confidence level, that is, a defined number of standard deviations, from the value at the best fit curve. Standard error/deviation can be defined for any distribution with finite first two moments, but it is most common to assume that the underlying distribution is normal. Once updates are made to all values that need adjustment, the kriging estimation map is recalculated, taking into account those updated values at the relevant grid point locations. The revised kriged map at the end of the modeling process is itself a continuous spatial distribution of the soil parameter estimates, and as such the value of the adjusted estimated parameter is read from any location within the effective correlation area on the map.

7. Response of Levee Segments

As previously mentioned, two critical failure modes of levee failure were considered in this study: failure due to excessive underseepage and failure due to liquefaction of the levee material or the foundation soils. Spatial joins were used to combine the levee and foundation material attributes (Figure 4). For simplicity at this stage of research, levee material was classified as a single layer (sand or clay) based on the major overall impression from soil investigation borehole data through the levee. The underlying geology map was used as the foundation layer and similarly classified in a rudimentary manner (sand or clay).

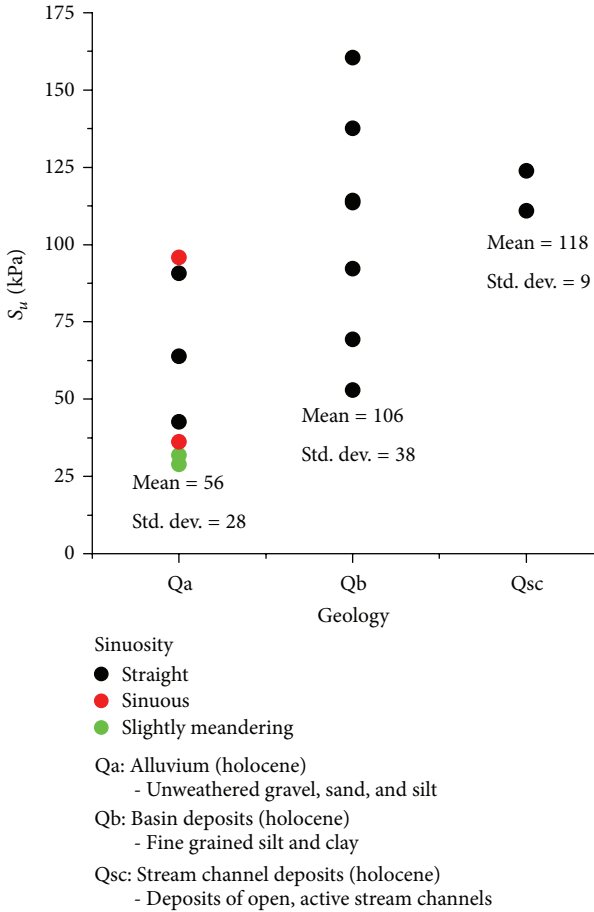


FIGURE 12: Relation of S_u (kPa) shallow clay soil parameter in Sacramento to geology, categorized as per sinuosity index.

Underseepage is one of the most common causes of levee failure that can occur either in the levee material or the underlying foundation. Sands, loose and dense, have a higher permeability than clays and thus are more prone to this particular mode of failure. Furthermore, deeper sand layer constituting the foundation under the levee will have a higher hydraulic gradient and thus will be more critical for underseepage than the case of sand in the levee itself. For seismic events, analysis for levee loss of freeboard due to soil liquefaction relies on preestablished typical levee cross-section analysis [13] by (1) characterizing the levee at each location as one of many typical levee cross-section profiles, (2) inputting the specific geometric characteristics and soil parameter values specific to the levee and foundation layers at that location, and (3) evaluating the distribution of the cyclic stress ratio (CSR), a measure for probability of triggering of liquefaction, for the levee cross sections.

A simplistic failure probability estimation criterion was used for this first-order analysis. Each soil layer combination, in this case the levee material and the foundation soil, is given a qualitative measure of failure potential due to either excessive underseepage or liquefaction. Results from the analyses are shown in Figure 19, and the criteria used in the initial analysis maps are summarized in Table 14.

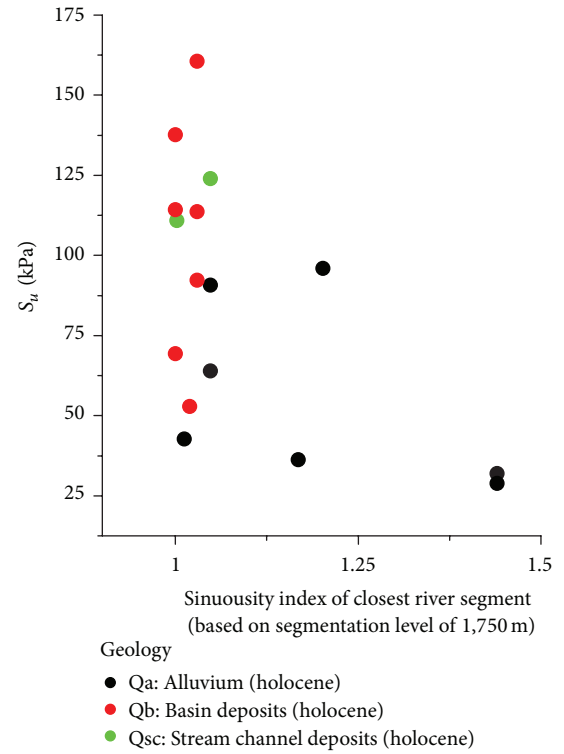


FIGURE 13: Relation of S_u (kPa) shallow clay soil parameter in Sacramento to sinuosity index, categorized as per regional geology.

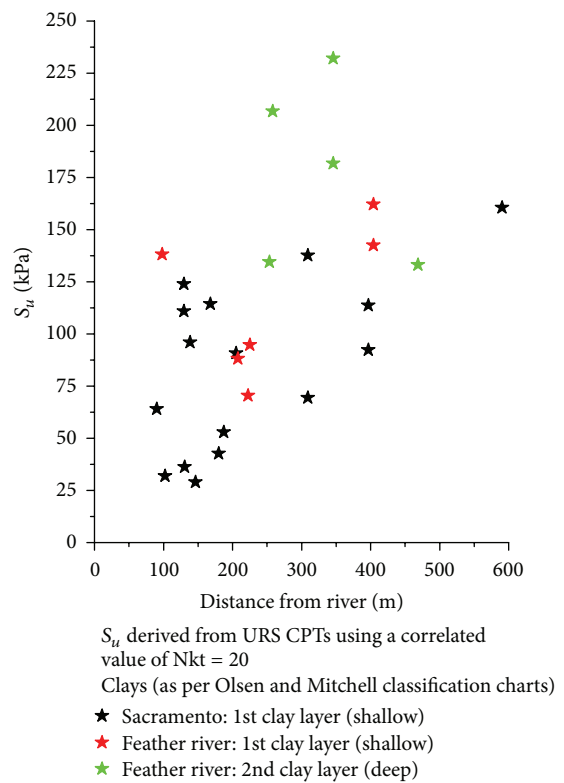


FIGURE 14: Relation of S_u (kPa) soil parameter to distance from centerline of closest river segment, in Sacramento and Feather River for both shallow and deep layers of clay.

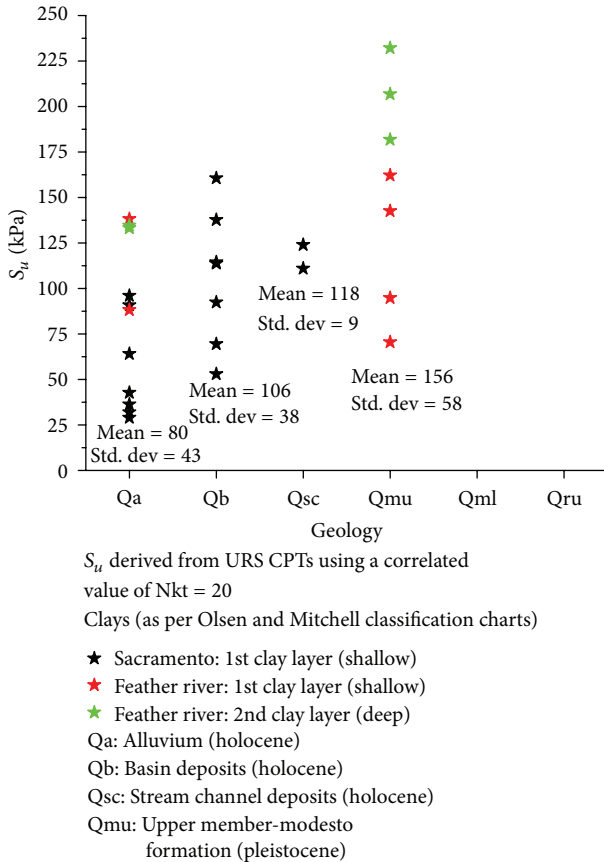


FIGURE 15: Relation of S_u (kPa) soil parameter to geology, in Sacramento and Feather River for both shallow and deep layers of clay.

8. Flood Scenarios, Damage Forecasting, and System Risk Assessment

The next step consisted of modelling the possible flood scenarios for all levee segments and then using a colour code for flooding of segments of either no, little, or more concern for failing due to both excessive underseepage and liquefaction. This was done using terrain slope and flow patterns obtained by analyzing a $10 \text{ m} \times 10 \text{ m}$ digital elevation model data. This was mainly achieved using the ArcGIS watershed tool, among others, in the model builder environment. This tool calculates all the area contributing flow to a particular point at a lower level. Since levees are at a higher level than the adjacent land and the objective is to get the area where water would flood (as opposed to water collecting downstream an area to a point), a digital elevation model was inverted, and the watershed tool was applied to it with water flowing towards the levee locations where failure would occur. The resulting flood scenarios for all levee segments, using the two considered methods of failure, were consistent with the landscape and terrain properties and are shown in Figure 20. Note that the presented flood model does not simulate the effect of water accumulation in the flooded areas, nor does it indicate where the water would ultimately go after a steady flow for a period of time. The model assumes that all the levee

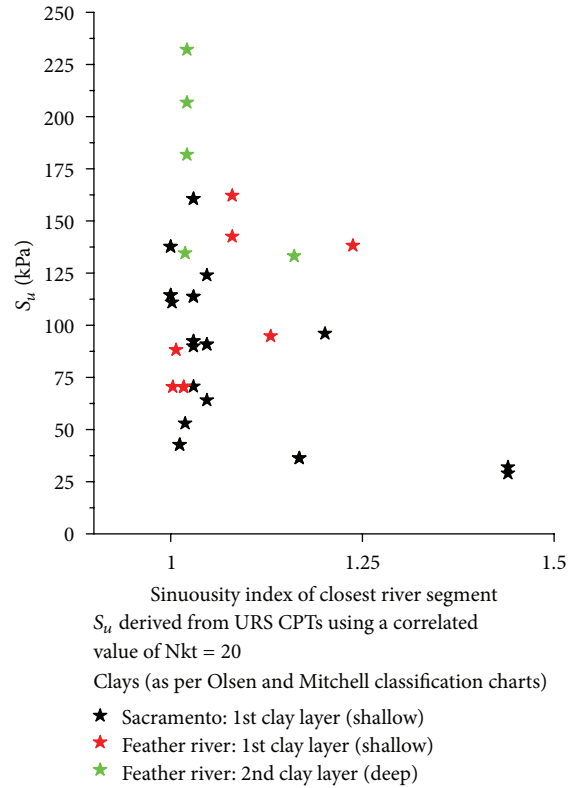


FIGURE 16: Relation of S_u (kPa) soil parameter to sinuosity index, in Sacramento and Feather River for both shallow and deep layers of clay.

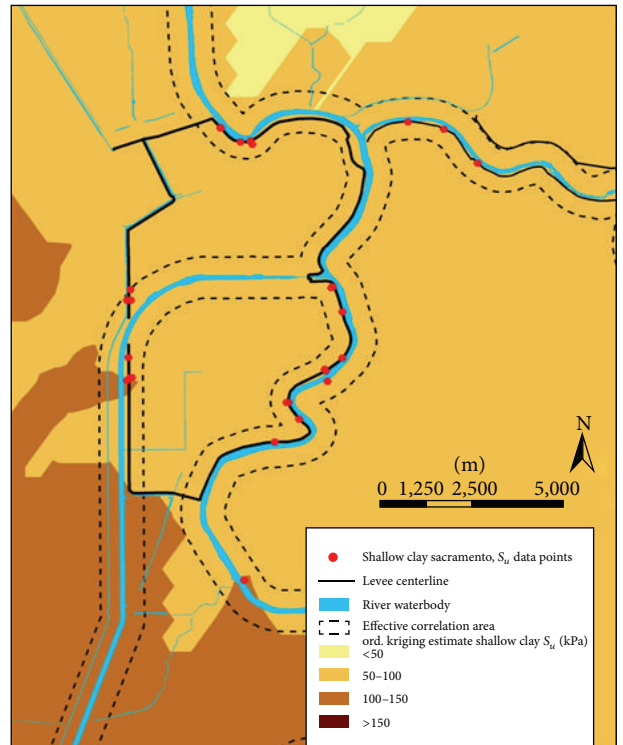


FIGURE 17: Sample output map of the ordinary kriging method applied for the S_u values in shallow clay layer of Sacramento.

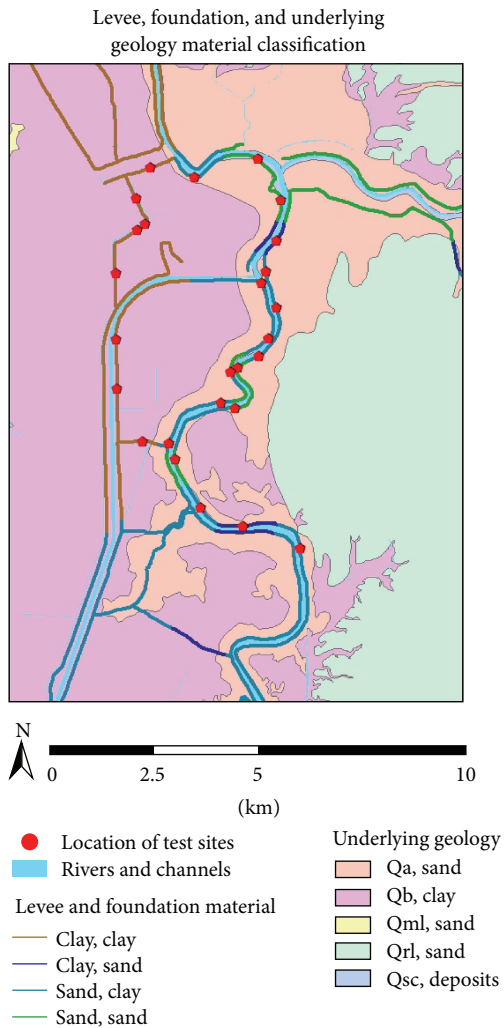


FIGURE 18: Levee and foundation material classification with underlying geology of the study area.

section that has failed is completely nonexistent physically, which is a worst case scenario; thus these calculations are conservative.

Flooded areas, as determined in the previous step, were combined and overlapped in the GIS platform with population data and presented in a 3D format using the ArcScene software. This step is performed to show the ease of visual representation and usefulness of the proposed work in helping decision makers and engineers to plan maintenance, repair, and emergency response operations. Finally, individual segment and overall levee system risk measures are assessed as a function of response analysis and resulting damage estimation by developing fragility curves for a range of ground motion intensities.

9. Conclusions

The proposed approach, even though simplified, offers a first-order estimate of the spatial vulnerability of a levee system and an efficient visualization of the results, thus enabling decision makers to quickly identify critical regions. This is

achieved by combining a geostatistical model of spatial soil variability with simplified approaches for estimating under-seepage and soil liquefaction levee vulnerability. Finally, GIS is used as the platform for manipulating and presenting information. A number of simplifications and assumptions have been made in order to complete the above analysis. This mainly involves the estimation of soil properties along the levee segments between the points with “known” properties and to a lesser extent the determination of the exact flooded areas (Figures 18 and 19). The soil properties’ variability issue needs to be addressed using a more detailed geostatistical spatial analysis approach in the future.

As a result of analyzing geotechnical investigation data in the area of study, the concept of “effective correlation distance” between the soil parameters and regional factors is introduced. This is a physical representation of the distance beyond which no trend/correlation was observed or deemed physically significant. For clay parameters this distance came out to be 600 m from either side of the river centerline. For sand parameters the distance was 450 m. Possible explanation of why sand distance is less than clay distance may be in the fact that sands settle closer to the levee in times of overtopping flooding due to larger heavier particle size as compared to silts and clays. Note that in Sacramento, the average river width is 150 m, and levees are typically around 100 m from the river centerline (i.e., on average 25 meters from river edge). Thus, for example, the limit of this effective correlation distance for clays is still 500 m away from the levees, which can be approximated as free-field conditions.

Another concept established is the “sinuosity index segmentation level.” This is a reflection of the river meander length period. Based on the available data, the ideal segmentation level was found to be close to 10 times the river channel width. Values imply that the Feather River (1,000 m segmentation) has a shorter meander length than the Sacramento River (1,750 m segmentation) that is, the Feather River meanders in shorter meander wave lengths than the Sacramento River.

The main finding of the soil variability model is the establishment of a number of correlations between soil strength parameters (friction angle, ϕ , for sands and shear strength, S_u , for clays) and a number of regional characteristics (underlying geology type, distance to river, and sinuosity of river). The correlations were studied for naturally occurring clay and sand typical foundation layers, located at both shallow and deep levels, in both regions of Sacramento and Feather Rivers.

The major findings from the development of the soil parameters estimation model, based on the above mentioned established correlations, are the following.

- (i) Clay in both shallow and deep layers and in both areas of study (Sacramento and Feather River) showed increasing trend of S_u with increasing distance from river (Figure 14). S_u values also increased with depth, which may be attributed to consolidation of the deeper layers over time.
- (ii) As for relation of S_u to the different geological formations in the two study areas (Figure 15), a general observation is that clay S_u values in the areas of the

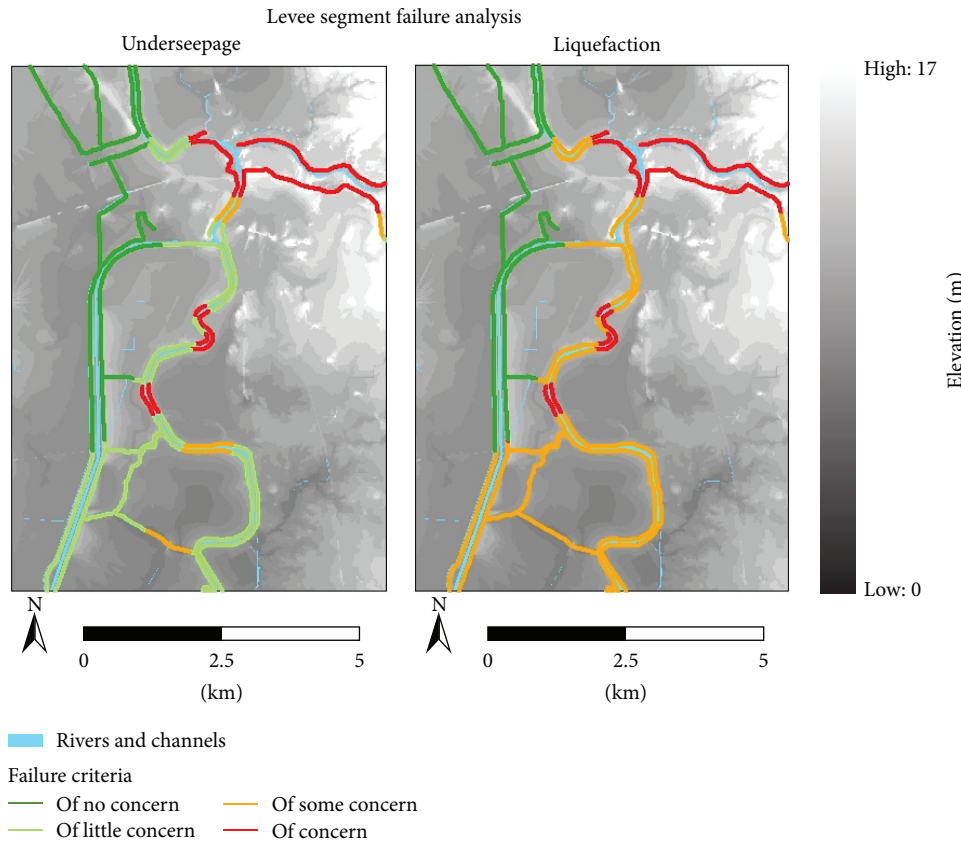


FIGURE 19: Results for failure analysis due to underseepage and liquefaction.

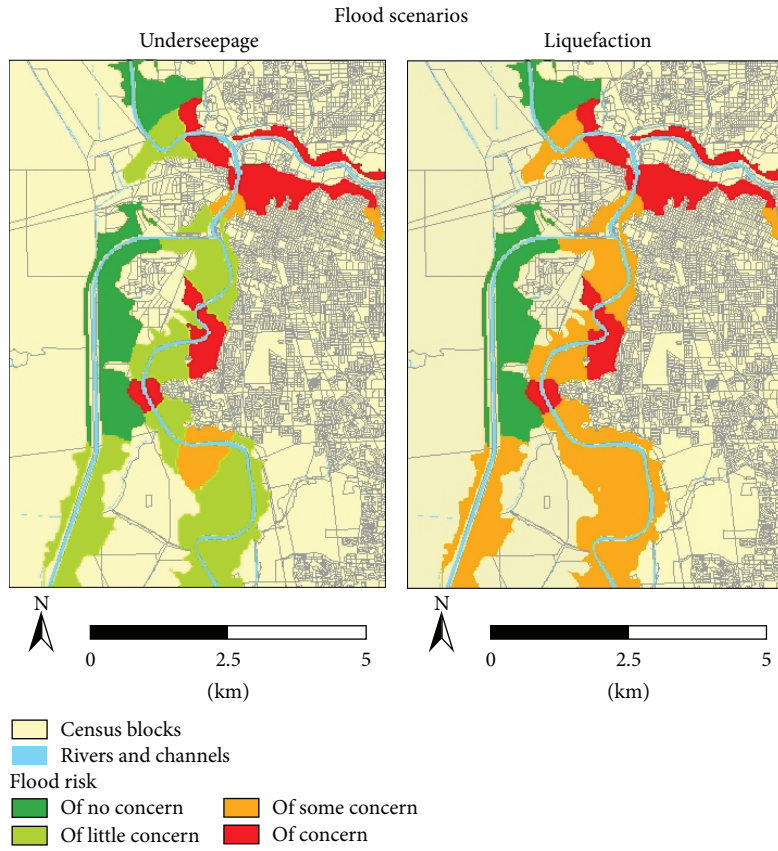


FIGURE 20: Flood scenarios from underseepage and liquefaction failures for all levee segments.

- Qa formation (defined as Alluvium—unweathered gravel, sand, and silt) tend to have lower values than other areas. The fact that clay is not the main component in this formation might provide an explanation for the lower values of S_u for any clay showing in these areas, as compared to other formations.
- (iii) For S_u relation to sinuosity index (Figure 16) there is a large scatter, at lower sinuosity levels. The higher number of data points at this low sinuosity level is due to the smaller number of river segments that are highly sinuous. An important observation across all areas of study and at all depths of layers is that S_u tends to decrease with increasing sinuosity of the closest river segment. However, more data points are needed to develop more robust correlations between SI and shear strength or soil type. Furthermore, due to the specific case study area that was used, the limited data used was primarily available for SI values close to 1 (i.e., straight river sections).
- Global observations that apply across the larger area of study included the increasing trend of shear strength, S_u , with increasing distance from the river and decreasing trend of S_u with increasing river sinuosity index levels. This study also presents a framework that can be used for future studies in the development of spatial correlations of soil properties.
- ## Acknowledgments
- The authors would like to thank Matt Hartigan, undergraduate student at the University of Michigan, who helped with the processing of some of the shear strength data as part of the Undergraduate Research Opportunities Program (UROP) at the University of Michigan. The authors are also grateful to the Rackham School of Graduate Studies for awarding Mustafa Saadi the Rackham Graduate Student Research Grant during his last year at the University of Michigan.
- ## References
- [1] ASCE, “Report Card for America’s Infrastructure,” 2013, <http://www.infrastructurereportcard.org/>.
 - [2] DWR, “California department of water resources,” 2011, <http://www.water.ca.gov/>.
 - [3] URS, “Technical memorandum—levee seismic vulnerability assessment methodology,” in *Urban Levee Geotechnical Evaluations Program*, 2008.
 - [4] K.-K. Phoon and F. H. Kulhawy, “On quantifying inherent soil variability, uncertainty in the geologic environment,” in *Proceedings of the Analysis and Computation Specialty Conference*, Madison, Wis, USA, 1996.
 - [5] N. D. Gordon, T. A. McMahon, B. L. Finlayson, C. J. Gippel, and R. J. Nathan, *Stream Hydrology*, John Wiley & Sons, New York, NY, USA, 2nd edition, 2004.
 - [6] J. E. Mueller, “An introduction to the hydraulic and topographic sinuosity indexes 1,” *Annals of the Association of American Geographers*, vol. 58, no. 2, pp. 371–385, 1968.
 - [7] Z. Deretsky, *Ten Ways a Levee Can Fail*, National Science Foundation, 2010.
 - [8] ASCE, *So You Live Behind a Levee?* American Society of Civil Engineers, 2010.
 - [9] USGS, “United States national seismic hazard maps,” 2008, <http://earthquake.usgs.gov/hazards/products/conterminous/2008/>.
 - [10] RESIN, “Resilient and sustainable infrastructure networks project (RESIN) at the University of California Berkeley,” 2011, <http://ccrm.berkeley.edu/resin/index.shtml>.
 - [11] DRMS, *Initial Technical Framework Paper: Levee Fragility, Delta Risk Management Strategy*, 2006.
 - [12] DRMS, *Initial Technical Framework Paper: Sacramento-San Joaquin Delta Risk Analysis (Approach and Basis of Analysis)*, Delta Risk Management Strategy, 2006.
 - [13] A. M. Athanasopoulos-Zekkos, *Select topics on the static and dynamic response and performance of earthen levees [Ph.D. thesis]*, Department of Civil and Environmental Engineering, University of California Berkeley, Berkeley, Calif, USA, 2008.
 - [14] A. Athanasopoulos-Zekkos and R. B. Seed, “Simplified methodology for consideration of 2D dynamic response of levees in liquefaction triggering evaluation,” *ASCE Journal of Geotechnical and Geoenvironmental Engineering*, vol. 139, no. 11, pp. 1911–1922, 2013.
 - [15] USACE, “Guidelines for the seismic evaluation of Levees,” ETL 1110-2-580, Department of the Army, Washington, DC, USA, 2013.
 - [16] FEMA, “FEMA-366: HAZUS-MH estimated annualized earthquake loss for the United States,” 2009, <http://www.fema.gov/library/viewRecord.do?id=3265>.
 - [17] USACE, *Levee Investigation, Reclamation District's 537 and 900 and Maintenance Areas 4 and 9, Sacramento River, Sacramento Bypass and Yolo Bypass, Yolo and Sacramento Counties, California*, Department of the Army, Office of the Chief of Engineers, U.S. Army Corps of Engineers, 1987.
 - [18] F. H. Kulhawy and P. W. Mayne, “Manual on estimating soil properties for foundation design,” Tech. Rep. EL-6800, Electric Power Research Institute, Palo Alto, Calif, USA, 1990.
 - [19] R. B. Peck, W. E. Hanson, and T. H. Thornburn, *Foundation Engineering*, Wiley & Sons, New York, NY, USA, 2nd edition, 1974.
 - [20] J. H. Schmertmann, “Measurement of in-situ shear strength,” in *Proceedings of the Conference on In Situ Measurement of Soil Properties*, vol. 2, pp. 57–138, American Society of Civil Engineers, Raleigh, NC, USA, 1975.
 - [21] M. Hatanaka and A. Uchida, “Empirical correlation between penetration resistance and internal friction angle of sandy soils,” *Soils and Foundations, Japanese Geotechnical Society*, vol. 36, no. 4, pp. 1–9, 1996.
 - [22] G. B. Baecher and J. T. Christian, “Spatial variability and geotechnical engineering,” in *Reliability Based Design in Geotechnical Engineering: Computations and Applications*, K.-K. Phoon, Ed., Taylor & Francis, 2008.
 - [23] S. Lacasse and F. Nadim, “Uncertainties in characteristic soil properties,” in *Proceedings of the ASCE Specialty Conference on Uncertainty in the Geologic Environment: From Theory to Practice*, 2006.
 - [24] I. K. Lee, W. White, and O. G. Ingles, *Geotechnical Engineering*, Pitman, London, UK, 1983.
 - [25] P. Lumb, “The variability of natural soils,” *Canadian Geotechnical Journal*, vol. 3, no. 2, pp. 74–97, 1966.
 - [26] P. Lumb, “Application of statistics in soil mechanics,” in *Soil Mechanics: New Horizons*, I. K. Lee, Ed., chapter 3, American Elsevier, 2nd edition, 1974.

- [27] J. Christian and G. Baecher, “Unresolved problems in geotechnical risk and reliability,” in *Proceedings of the ASCE Geotechnical Risk Assessment and Management Conference (GeoRisk '11)*, pp. 50–63, American Society of Civil Engineers, Atlanta, Ga, USA, 2011.
- [28] G. A. Fenton and D. V. Griffiths, *Risk Assessment in Geotechnical Engineering*, John Wiley & Sons, New York, NY, USA, 2008.
- [29] J. R. Hess, G. L. Sills, R. Costa, and S. Shewbridge, “California’s levees at risk,” *Geo-Strata—Geo Institute of ASCE*, vol. 7, no. 6, pp. 24–28, 2006.
- [30] USGS, “National mapviewer,” 2010, <http://viewer.nationalmap.gov/viewer/>.
- [31] E. J. Helley and D. S. Harwood, *Geologic Map of the Late Cenozoic Deposits of the Sacramento Valley and Northern Sierran Foothills California*, Miscellaneous Field Studies Map MF-1790, U.S. Geological Survey, 1985.
- [32] J. F. Mount, *California Rivers and Streams: The Conflict Between Fluvial Process and Land Use*, University of California Press, Berkeley, Calif, USA, 1995.
- [33] P. Julien, *River Mechanics*, Cambridge University Press, Cambridge, UK, 1st edition, 2002.
- [34] C. R. Thorne, R. D. Hey, and M. D. Newson, *Applied Fluvial Geomorphology for River Engineering and Management*, John Wiley & Sons, New York, NY, USA, 1997.
- [35] L. B. Leopold, M. G. Wolman, and J. P. Miller, *Fluvial Processes in Geomorphology*, W. H. Freeman, Hampshire, UK, 1964.
- [36] USGS, “National water information system: web interface,” 2011, <http://nwis.waterdata.usgs.gov/nwis>.
- [37] URS, “Geotechnical investigation data for West Sacramento, American River, Marysville, Sutter, and RD784,” Personal Communication with Mr. Richard Millet, Vice President, Program Manager DWR Geo-Levee, URS Corporation, 2010.
- [38] T. Lunne, P. K. Robertson, and J. J. M. Powell, *Cone Penetration Testing in Geotechnical Practice*, Blackie Academic & Professional, New York, NY, USA, 1997.
- [39] P. K. Robertson and R. G. Campanella, “Interpretation of cone penetration tests. Part I: sand,” *Canadian Geotechnical Journal*, vol. 20, no. 4, pp. 718–733, 1983.
- [40] R. S. Olsen and J. K. Mitchell, “CPT stress normalization and prediction of soil classification,” in *Proceedings of the International Symposium on Cone Penetration Testing (CPT '95)*, Linkoping, Sweden, 1995.
- [41] ASTM, 2011. ASTM Standard D2487-11, “Standard practice for classification of soils for engineering purposes (unified soil classification system),” Tech. Rep., ASTM International, West Conshohocken, Pa, USA, 2003, <http://www.astm.org/>.

Research Article

The Influence of Infill Wall Topology and Seismic Characteristics on the Response and Damage Distribution in Frame Structures

Nikos Nanos and David Begg

School of Civil Engineering and Surveying, University of Portsmouth, Portsmouth PO1 3AH, UK

Correspondence should be addressed to Nikos Nanos; nikos.nanos@port.ac.uk

Received 9 August 2013; Revised 5 November 2013; Accepted 6 November 2013

Academic Editor: Anaxagoras Elenas

Copyright © 2013 N. Nanos and D. Begg. This is an open access article distributed under the Creative Commons Attribution License, which permits unrestricted use, distribution, and reproduction in any medium, provided the original work is properly cited.

This paper identifies the effects of infill wall existence and arrangement in the seismic response of frame structures utilising the global structural damage index after Park/Ang (GDI_{PA}) and the maximum interstorey drift ratio (MISDR) to express structural seismic response. Five different infill wall topologies of a 10-storey frame structure have been selected and analysed presenting an improved damage distribution model for infill wall bearing frames, hence promoting the use of nonstructural elements as a means of improving frame structural seismic behaviour and highlighting important aspects of structural response, demonstrating the suitability of such element implementation beyond their intended architectural scope.

1. Introduction

In their theory regarding the seismic behaviour of masonry infilled frames Paulay and Priestley [1] called for alteration, the existence of such infill elements bring, to the structural system: resulting in improved overall lateral load capacity. More contemporary work [2] has utilised the bracing of moment resisting steel frames as a means of improving the existing seismic response characteristics with great benefit. On the other hand, from site surveys and results of analytical and experimental analysis, it is widely acknowledged that infill walls contribute to the modal response of the structure.

Identifying these possible, positive effects the Federal Emergency Management Agency (FEMA) prepared FEMA 273 [3] in the NEHRP Guidelines for the Seismic Rehabilitation of Buildings provisions, dictating that concrete frames with infill walls must be constructed in such a way as to ensure infill element and frame interact under design loads. The reasons behind such contribution usually being related to the effect of infill walls on the overall building structural rigidity, the structure's natural period, and damping coefficient. Similarly, in steel frame structures, a lot of effort has been spent on research into the contribution of infill walls on seismic characteristics; leading to the identification of

several important properties of infill walls in terms of their contribution to overall seismic behaviour.

In this paper the numerical relationship between infill wall existence in a frame structure and the overall structural response in case of seismic loading is investigated. The existence of infill walls in frame structures as well as their contribution to the seismic response has been a major point of study from various researchers in the past in an attempt to establish the relationship between the frame lateral load capacity and the existence of frame infill [4]. This fundamental research has further been enhanced with tests and observations of actual buildings during earthquakes.

With the advent of new and improved methods of recording, the significant role of infill on overall structure's seismic response has been established [5]. Klingner and Bertero [6] described the superiority of infilled frames over their bare frame counterparts with respect to energy dissipation and resistance to incremental collapse as well as the benefits of increased strength and energy absorption capacities. One can therefore see the potential advantages of infill wall inclusion in the design process that can possibly outweigh the detrimental effects of an increase in inertial forces due to their presence.

The above have been the point of further research in terms of infilled frames and their ability to improve structural response during seismic excitation over the years [7, 8]. More work has been carried out on the issue of partially infilled frames, where openings are present, in an effort to address the issue of seismic behaviour a more diverse population of structures [9, 10] showing the significance of infill wall presence in frame structures. One notable exception to the above has been identified in the case of partial-height infill walls that often cause columns to experience nonductile shear failures (short column effect) rather than respond in a ductile and predominately flexural manner as intended [11].

From the seminal work of Polyakov [12] that first used the equivalent diagonal strut analogy for replacing the infill wall a lot of ground has been covered with an array of researchers studying the effect of infill walls in the seismic response of frame structures. Smith and Coull [13] presented a design method for infilled frame based on the diagonal strut bracing frame criteria taking under consideration the three possible modes of failure of the infill element. These were the shear failure along the masonry; the diagonal cracking through masonry; and the infill corner crashing, all assuming that a frame must be designed on the basis of gravity loading. D'Ayala et al. [14] highlighted in his work the importance of proper modelling characteristics to ascertain the validity of the infill model damage propagation. Smith and Carter [15] examined multistorey infilled frames with respect to lateral loading and proposed the equivalent strut concept focusing on the composite behaviour of infilled frame and failure modes. The factors affecting the effective width of diagonal compression strut were determined and the relevant design curves to estimate equivalent strut width, cracking and crushing strength of the infill element were given.

The above details of infill wall modelling are not explicitly covered in this work by the use of overall structural damage indices instead of examining the particular infill wall damage development. This enables the researchers to qualitatively address the infill wall contribution as well in an effectively more general form.

Regarding the type of infill wall material several different suggestions have been investigated in the past, each one with its own merits and limitations. Bruneau and Bhagwagar [16] studied the effects of steel and other ductile materials as well as steel plates, while Di Sarno and Elnashai [2] focused on frame bracing, all showing improvement in the overall structural response. Of the aforementioned the most easily applicable and readily available material is masonry infill. It can therefore be considered as a rather interesting solution for frame structure's seismic rehabilitation despite the apparent shortcomings in terms of additional weight added to the structure.

The extent of infill wall application as well as its individual frame coverage has been a point of extensive research in the past with restrained or partially restrained infill wall frames showing improved seismic characteristics [17]. Nevertheless, the difficulty to achieve this kind of restrain in frames that has not been designed for this purpose renders this a solution with limited practical use for structural rehabilitation. Most recently Tasnimi and Mohebkhah [18] once more

demonstrated the beneficial contribution of both solid and nonsolid infill walls in individual frames' seismic response, while specific numerical models to study the above have been proposed [19]. This kind of in depth analysis would be out of the scope of this paper that concentrates on the overall structural characteristics of steel moment resisting frame structures and it would be of little consequence when the importance is shifted to a macro, building-wise scale.

2. Proposed Methodology

2.1. Overview. Having established the beneficial effects of infill walls in the seismic response of frame structures the importance of identifying the actual structural behaviour and damage distribution of a building becomes evident in assessing the actual contribution of the different infill wall topologies. Therefore, greater effort must be spent in the integration of the existing research into a generalized framework that will allow researchers and other interested parties to assess and quantify not only the effects of the existence of infill walls in a frame structure but also account for the different possible topologies and their subsequent effects.

It is the intention of this research not only to provide a study on the effect of different infill wall topologies for a specific structure but also act as a methodology that can be implemented for the identification of the best possible infill wall arrangement. Essentially, an optimisation tool that can be utilised in both new and retrofitted structures to assess the effectiveness of different wall arrangements according to possible structural and architectural constraints. Such an implementation can effectively yield the particular characteristics of seismic behaviour for different infill wall topologies and allow for a thorough overview of all available solutions before resulting in a more detailed study of the structural system. This is the main reason behind the suitability of a solution that remains essentially agnostic of the microscale seismic effects, on an element basis, but rather concentrates on the overall damage distribution and seismic behaviour. Either being based on global or regional damage indices instead of detailed calculations on a structural element basis. This research was based on addressing the issue of the overall seismic behaviour in a way that will account for the differences in alternative infill wall topologies and provide the seismic response characteristics of a frame structure.

The main objective of this paper is to provide a framework rather than a specific study of the infill wall contribution in seismic structural response. Due to the above and because the methodology presented is intended to act as a research tool for the identification of the intervention guidelines for potential seismic rehabilitation the whole process was built upon the merit of generalization. It has therefore been ensured that the proposed assessment methodology can, according to the research and implementation needs and with the necessary modifications, address the overall structural seismic response for a variety of structural types; infill elements; and seismic conditions.

This paper identifies and quantifies the effects of solid, industrialized, clay infill wall existence and arrangement in the seismic response of frame structures highlighting their potential seismic design significance. To achieve the above, several artificial accelerograms compatible with the Greek Antiseismic Code [20] have been composed and a nonlinear dynamic analysis has been carried out to provide the structural response for the given seismic excitations. The global structure damage index after Park/Ang (GDI_{PA}) and the maximum interstorey drift ratio (MISDR) have been selected as some of the most widely utilized structural seismic response parameters in contemporary state of art. Furthermore, their storey level equivalents (LDI_{PA} and LISDR) assess the more regionalized seismic behaviour.

For the structure under investigation, the creation of a simple analytical model of a typical commercial steel frame 10 storey building and the application of 4 different infill wall layouts resulting in 5 different structure types were realised. All structural elements and connections were designed in such way as to be in compliance with the relevant recent Euro codes for steel and antiseismic structures for steel moment resisting frame buildings. By utilising the EC3 [21] and EC8 [22] codes, respectively, to effectively represent a typical contemporary steel structure.

The use of spectrum compatible artificial accelerograms was selected to enable the production of a wide range of response data that share a common ancestry and allowed for executing a range of comparative studies between them, something not possible if naturally occurring ground motions were utilized. In light of the above, a set of 225 EC8 spectrum compatible accelerograms conforming to the Greek national annex requirements as described in the Greek antiseismic code have been created to assess the behaviour of the aforementioned models in a wide range of seismic excitations in their operating environment and a series of nonlinear dynamic analyses have been executed to record this behaviour.

2.2. Synthetic Accelerograms. The seismic excitations used for the dynamic analyses in this study are based on artificial accelerograms created to be compatible with the design spectra of the current Greek antiseismic code. The reason for choosing this approach rather than relying on natural accelerograms was dictated by the need to have a sufficiently large database for statistical reasons. For the creation of the aforementioned artificial accelerograms the program SIMQKE [23] has been utilized. With the use of a differentiated choice of seismic parameters 225 artificial accelerograms have been created all compatible to EC8 response spectra [22] in reference with the Greek seismic characteristics, as those are described in the relevant antiseismic codes of practice.

The aforementioned parameters were the peak ground acceleration (PGA), the total duration (T_D) of the seismic event (with T_D values of 20 s, 30 s, and 40 s), and the design spectra acceleration (α) for all three Greek seismic regions (nominal α equal to 0.16 g, 0.24 g, and 0.36 g) which have been used with 5 pseudorandom generator allocated numbers each to approximate the inherent variability of

the seismic phenomenon without any reduction factors. All generated spectra were calculated based on the assumption of category B subsoil, deep deposits of medium dense sand, or overconsolidated clay at least 70 m thick, as described in EC8 [22] and incorporated in the Greek Antiseismic Code [20] to represent the most common Greek subsoil type.

For all recorded nonlinear analyses, the maximum interstorey drift ratio (MISDR) and the global structural damage index after Park/Ang (GDI_{PA}) [24] have been evaluated as widely accepted direct methods of postseismic structural damage evaluation, based on the simplicity and straightforwardness of their calculation. Furthermore, for the specific needs of this project the level damage index after Park/Ang (LDI_{PA}) and the local maximum interstorey drift ratio (LISDR) have also been used to express the relevant values on a level basis to demonstrate the distribution characteristics recorded.

2.3. Damage Indices. As explained previously, attention is focused on damage indicators that consolidate all member damage into one single value that can be easily and accurately used for the statistical exploration of the interrelation with the also single-value seismic parameters in question. Thus, in the GDI model after Park/Ang [24] the global damage is obtained as a weighed average of the local damage at the ends of each element. The local damage index is given in the following equation:

$$\text{DI}_L = \frac{\theta_m - \theta_r}{\theta_u - \theta_r} + \frac{\beta}{M_y \theta} E_T, \quad (1)$$

where DI_L is the local damage index; θ_m the maximum rotation attained during the load history; θ_u the ultimate rotation capacity of the section; θ_r the recoverable rotation at unloading; β a strength degrading parameter; M_y the yield moment of the section; and E_T the dissipated hysteretic energy. The Park/Ang damage index is a linear combination of the maximum ductility and the hysteretic energy dissipation demand imposed by the earthquake on the structure. The global DI after Park/Ang is presented in the following equation:

$$\text{GDI}_{\text{PA}} = \frac{\sum_{i=1}^n \text{DI}_L E_i}{\sum_{i=1}^n E_i}, \quad (2)$$

where GDI_{PA} is the global damage index after Park/Ang; DI_L the local damage index after Park/Ang; E_i the energy dissipated at location i ; and n the number of locations at which the local damage is computed. In the same context the localised form of GDI_{PA} has been evaluated, as the sum of the recorded DI_L concentrated in each respective level, providing a local damage index relevant to each separate level as shown in the following equation:

$$\text{LDI}_{\text{PA}} = \frac{\sum_{i=1}^n \text{DI}_{LL} E_{iL}}{\sum_{i=1}^n E_{iL}}, \quad (3)$$

where LDI_{PA} is the level structural damage index after Park/Ang; DI_{LL} the local damage index after Park/Ang for a

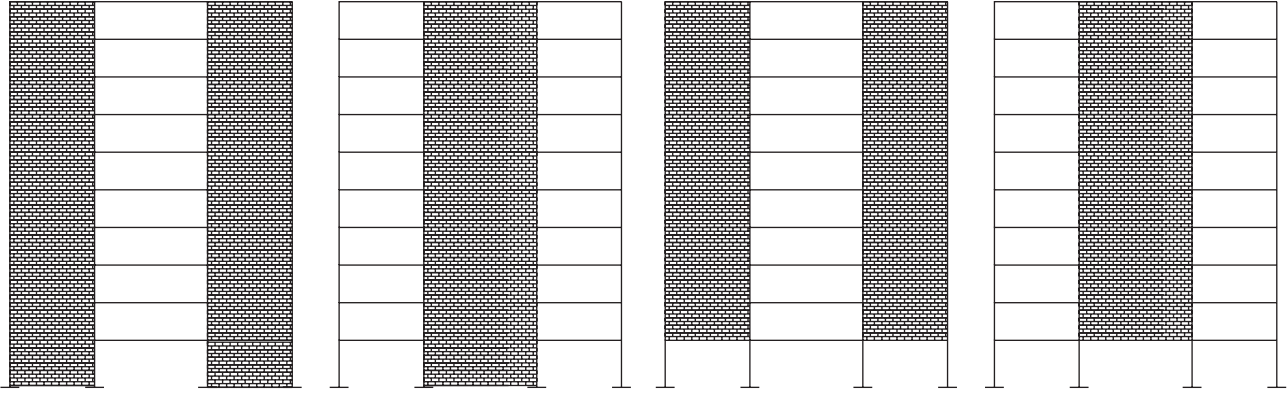


FIGURE 1: Bare frame structure (Frame 0).

particular level; E_{iL} the energy dissipated at location i of the level in question; and n the number of locations at which the local damage is computed.

The maximum interstorey drift ratio (MISDR) is believed to accurately depict the recorded postseismic level of structural and architectural damage of a structure alike. The correlation of MISDR with the above has repeatedly been proven both experimentally as well as from postearthquake site surveys in areas where catastrophic seismic events took place [25] and is widely recognized as an effective tool of damage representation. Furthermore, MISDR is simple in its calculation, as the maximum observed value throughout the recorded individual interstorey drift ratio of each level (LISDR) is given in the following equation:

$$\text{LISDR}_i = \frac{u_i - u_{i-1}}{h_i} 100, \quad (4)$$

where LISDR _{i} is the level interstorey drift ratio; u_i is the recorded drift of floor i ; u_{i-1} is the recorded drift of floor $i - 1$ and h_i representing the height of floor i and MISDR is the maximum recorded value amongst the total amount of storeys.

3. Numerical Example

The geometry, layout, and the structural elements profiles of the 5 different 10 storey building structural models for Frame 0 (bare frame), Frame 1 (2 outer bays bearing infill walls), Frame 2 (central bay bearing infill wall), Frame 3 (same as Frame 1 but with no infill wall present at ground level), and Frame 4 (same as Frame 2 but with no infill wall present at ground level) are given in more detail in Figure 1. Structural detailing was completed by implementing the requirements of both EC3 [21] and the current Greek antiseismic code [20] for steel antiseismic structures. The slabs' thickness has been designed to be 20 cm. The whole design was based on the assumption of a building of importance category 2 (common buildings), low ductility requirements, and type B subsoil (deep deposits of medium dense sand or overconsolidated clay at least 70 m thick) belonging to a seismic zone I ($a = 0.16$ g) according to the Greek antiseismic code. In addition, live, snow, and wind loads have also been taken into

account as well as the eccentricity of structural element from verticality as per the nominal values pertaining to the relevant construction codes for the design of the structural frame in order to represent a typical steel frame structure. The numerical values of loads, safety factors, and load combinations have been chosen in accordance with Eurocode 1 and 3 and the Greek antiseismic code requirements. The load values used for structural design constitute an imposed load of 5 kN/m², a snow load of 0.075 kN/m² for the roof, wind action according to EC1, and concrete slab self-weight assumed to come from a C20/25 concrete slab with a depth of 200 mm, while the infill walls were considered as loads coming from a single nonload bearing infill element of 140 mm thickness. The frame design parameters as well as element dimensions are presented in Figure 2 and the material utilised was S355.

Next, the creation of the alternative patterns of infill walls to be studied has been realized in such a way as to provide a diverse yet comparable arrangement of infill walls. Namely, Frame 1 that constitutes infill wall present in the two 9 m wide corner frames and Frame 2 that only furnished infill walls in the middle 12 m frames both having no infill walls at ground elevation bays.

With the completion of all involved frames' design procedure the implementation of nonlinear dynamic analysis utilizing the 225 spectrum compatible accelerograms followed. The analysis was facilitated with the use of IDARC2D [26] computer program. The results allowed the researchers to effectively evaluate the structural seismic response of all frames on an overall and storey level basis with the extraction of GDI_{PA}, MISDR and LDI_{PA}, and LISDR values, respectively. This study uses the nominal parameter for the involved steel elements to avoid any bias in the results. Furthermore, the evaluation of the Newmark- β method of numerical integration, followed by Newton/Raphson's method for root approximation for every time step, has been carried out as part of IDARC2D analysis operation. A bilinear elastoplastic model with 5% offset yield strength has been selected to represent the steel elements' behaviour.

The steel material has been modeled as a von Mises material with isotropic hardening. The steel used is S355 according to EN 1993-1-1 [21]. Plastic strains were included with the bilinear elastic-plastic stress-strain curve with 5%

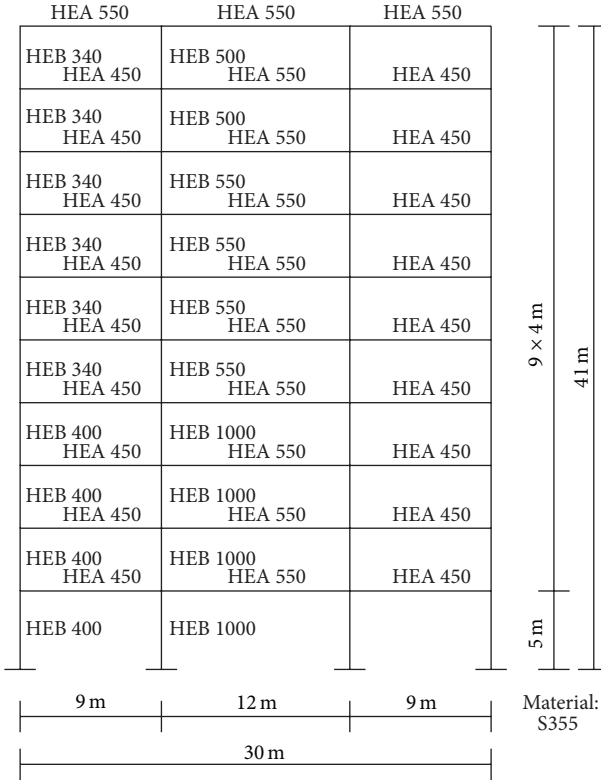


FIGURE 2: Alternative infill wall arrangements (Frames 1 to 4).

linear strain hardening used to simulate the steel material as per Figure 3, while the ultimate deformation (curvature) for members was specified as the lowest of either the maximum strain at fracture divided by the neutral axis or the maximum plastic moment and a postyield hardening capacity of 0.05.

The infill elements have been incorporated in the model in the form of diagonal compression struts in the respective subframes. Finally, the smooth hysteretic model that was also used for the infill panels includes the effects of stiffness degradation, strength deterioration, and pinching. The development of the present hysteretic model is based on the nonlinear Bouc-Wen model [26]. For reasons of nonlinear dynamic analysis execution the stress-strain model selected for the infill wall element in compression is presented in Figure 4 and constitutes a parabolic part up to the maximum permissible stress f'_m and is then reduced at a lower point where it remains constant.

The infill wall element's diagonal struts are considered inactive when in tension, but the combined action of the two diagonals provides the necessary resistance from both directions. The relationship between the horizontal force-displacement system of the diagonal strut system is shown in Figure 5(a), while a mild hysteretic Bouc-Wen behaviour model shown in Figure 5(b) has been utilized.

For the calculation of the hysteretic response of the infill wall sections the Saneinejad and Hobbs [27] allowable compression diagonal strut element calculation (5) has been

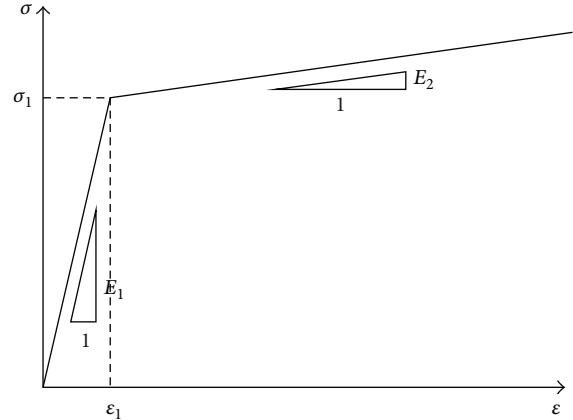


FIGURE 3: Structural steel stress-strain diagram.

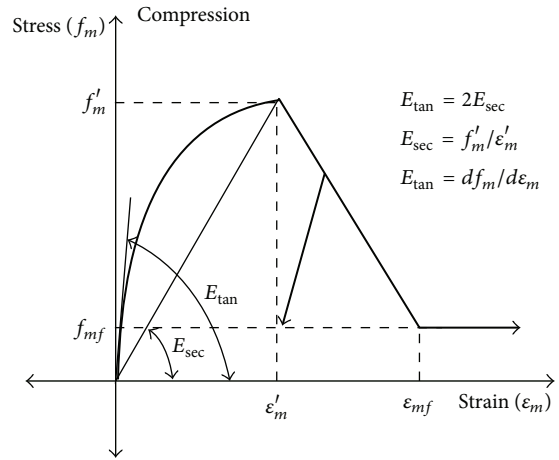


FIGURE 4: Infill wall element stress-strain diagram.

utilised for the permissible compression f_a with values of $f_c = 0.6 * \varphi * f_m$ and $\varphi = 0.65$:

$$f_a = f_c \left[1 - \left(\frac{I_{eff}}{40t} \right)^2 \right]. \quad (5)$$

The structural response of the building for the artificial accelerograms under investigation was based on the extraction of the overall structural damage index after Park and Ang as well as the maximum interstorey drift ratio in lieu of their ability to consolidate all recorded damages in one arithmetic value. The above selection was made in order to cover both the structural damage due to deformation (MISDR) and also the effects of the combination of deformation and hysteretic energy absorption.

4. Results and Discussion

4.1. General Remarks. As previously stated, the main objective of this research is the quantification of the overall seismic response characteristics. In this regard, the focus of interest has been the underlying effect of infill walls in frame structures rather than the response of the infill walls

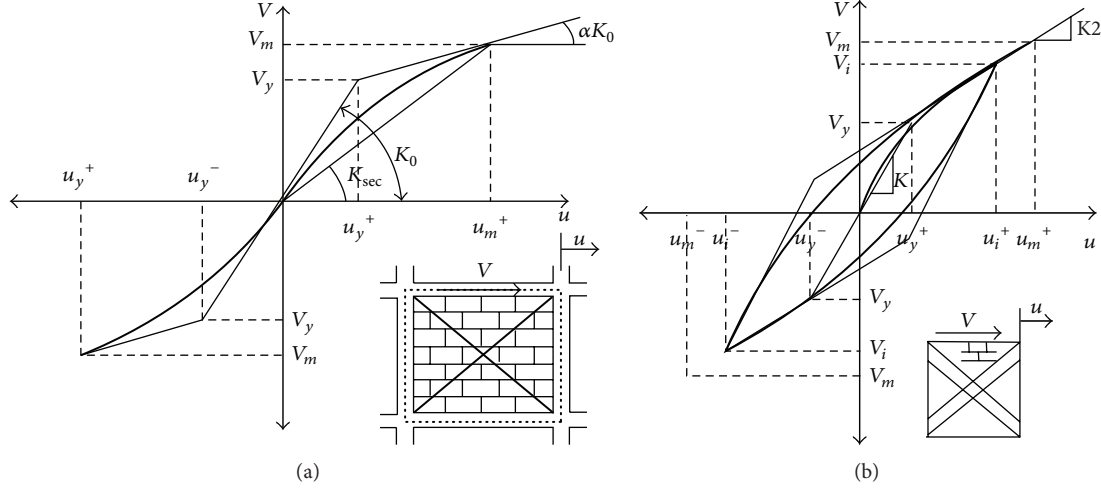


FIGURE 5: (a) presents the relationship between horizontal force and displacement in infill wall elements. (b) presents the Bouc-Wen model for the mild hysteretic behaviour of infill wall elements.

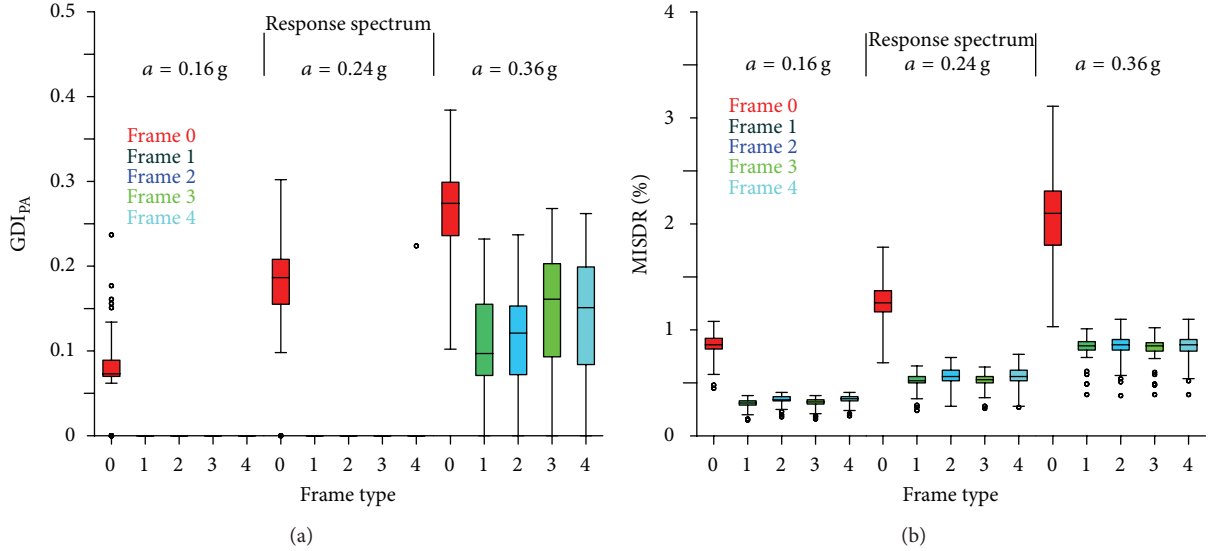


FIGURE 6: (a) GDI_{PA} values range over response spectra characteristics. (b) MISDR values range over response spectra characteristics.

themselves. Therefore, the selection of result indicators has been carried out in such a way as to better facilitate the description of the overall damage distribution and seismic behaviour rather than the microscale seismic effects.

All 4 selected indicators have been separately studied in an attempt to better classify the effects of infill wall inclusion and topology in the seismic behaviour and damage distribution of frame structure as a result from the recorded ISDR and DI_{PA} values, respectively. As such, the two different types of structural behaviour indicators have been selected to demonstrate the recorded damage and behaviour in both the overall and local domain.

4.2. Overall Damage Indices. The nonlinear dynamic analysis result data, from the 255 selected spectrum compatible artificial accelerogram induced events, suggested an overall

reduction of the recorded average GDI_{PA} and MISDR values in the order of 78% and 60%, respectively, for infill wall bearing frames as presented in Table 1. An additional reduction of 40% in the maximum GDI_{PA} values as well as a 62% and 74% in the minimum and maximum MISDR values has been similarly established between the bare frame and its infill wall bearing counterparts. All aforementioned results indicate the overall beneficial effects the incorporation of infill elements can have in a frame structure in terms of seismic behaviour and structural damage.

To avoid any result obfuscation a clustered approach towards GDI_{PA} and MISDR value, in terms of the different seismic characteristics, has been selected to identify the importance of seismic response spectrum and total duration parameters chosen during the artificial accelerogram creation. Figure 6 gives an overview of the recorded GDI_{PA} and MISDR values in respect to the selected seismic response

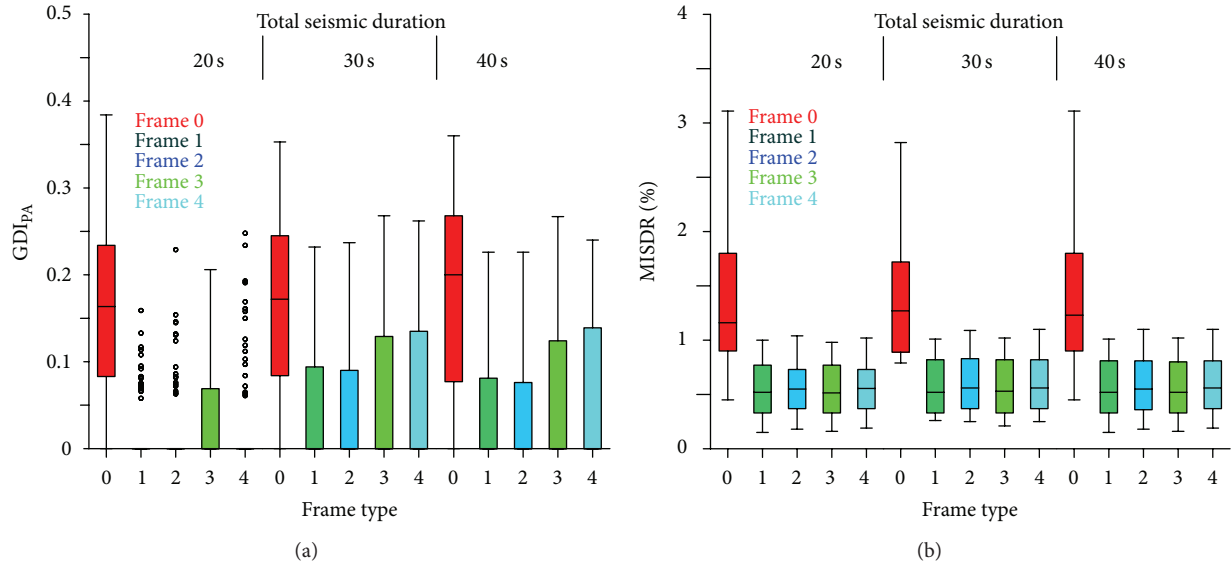


FIGURE 7: (a) GDI_{PA} values range over total duration of seismic events. (b) MISDR values range over total duration of seismic events.

TABLE 1: Overall and reduction values of damage and behaviour indices for all frames.

(a)				
	Frame	Min.	Max.	Average
GDI _{PA}	0	0.000	0.304	0.188
	1	0.000	0.162	0.035
	2	0.000	0.175	0.037
	3	0.000	0.197	0.049
	4	0.000	0.191	0.047
MISDR (%)	0	0.45	4.11	1.41
	1	0.15	1.01	0.55
	2	0.18	1.10	0.59
	3	0.16	1.02	0.55
	4	0.19	1.10	0.59
(b)				
	Percentage reduction against frame 0 (%)			
	Frame	Min.	Max.	Average
GDI _{PA}	1	N/A	47	81
	2	N/A	42	80
	3	N/A	35	74
	4	N/A	37	75
MISDR (%)	1	67	75	61
	2	60	73	58
	3	64	75	61
	4	58	73	58

spectrum. The outlier data factors (>2.5 standard deviations) have been separately indicated as small circles. Therefore, a quick overview of the minimum and maximum values (whiskers) as well as the lower and upper quartiles (box) and

the median (straight line marking in the box) values can be realised. The recorded data suggests the uniform reduction in terms of MISDR throughout the different seismic response spectra selected, while GDI_{PA} values present an effective 100% reduction in both low and medium seismic region artificial accelerograms.

Similar work has been carried out for the different total duration clusters selected for the creation of the artificial accelerograms presented in Figure 7 in terms of GDI_{PA} and MISDR values, respectively. In this case a uniform reduction of the recorded values can be observed indicating a reduced participation of the overall seismic duration in the reduction characteristics of the overall indices studied.

4.3. Level Damage Indices. Similar procedure has been followed in terms of behavioural and damage indicators in the local domain. In this case the interstorey drift ratio (ISDR) along with the relevant level structural damage index after Park/Ang (LDI_{PA}) for each one of the 255 response spectrum compatible seismic accelerograms utilised.

With the incorporation of a stratified postprocess analysis, in terms of seismic signal's response spectrum compatibility characteristics, the results reveal an effective 100% reduction in GDI_{PA} values recorded for virtually all low and medium seismicity response spectrum originating cases (with $\alpha = 0.16$ g and 0.24 g values). In lieu of data spread in the aforementioned cases the decision to concentrate this study in the identification of structural damage distribution characteristics in the high seismicity region has been made. In this respect the detailed examination of only the cases results relevant to the high seismic response spectrum artificial accelerograms ($\alpha = 0.36$ g) has been carried out. On the other hand, the structures' seismic behaviour has been examined taking under consideration the full range of results. Figure 8 presents the distribution characteristics of structural damage

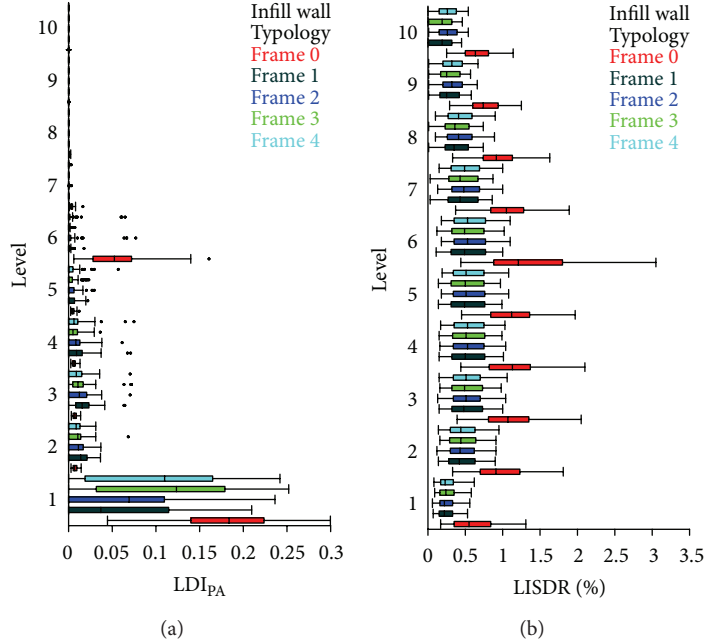


FIGURE 8: (a) Structural damage distribution characteristics (LDI_{PA}) for $a = 0.36$ g response spectrum compatible artificial accelerograms (75 cases). (b) Structural behaviour distribution characteristics (LISDR) for all available data (225 cases).

TABLE 2: Contribution of sixth level damage index in GDI_{PA} and reduction values over Frame 0.

6th level	Frame typology					Reduction against Frame 0 (%)			
	0	1	2	3	4	1	2	3	4
Average	0.20	0.01	0.05	0.00	0.03	95.0	75.0	100	85.0
3rd quartile	0.21	0.01	0.01	0.00	0.01	95.2	95.2	100	95.2
Maximum	0.30	0.04	0.15	0.02	0.12	86.7	50.0	93.3	60.0

and behaviour as recorded through the LDI_{PA} and LISDR indices, respectively, for each of the 10 levels comprising the structure under investigation. In this case, the outlier data factors (>2.5 standard deviations) have been separately indicated and not included for the determination of extreme values to avoid result obfuscation of the recorded min. and max. points due to these extreme contributors.

As outlined before, in terms of structural response the results have been divided into two distinct characteristics, structural damage and structural behaviour. Result data suggest the promotion of structural damage concentration in the first and sixth level for the bare frame structure (Frame 0) expressed through the respective LDI_{PA} distribution creating potentially dangerous conditions for the manifestation of localised damages that lead to the creation of an unfavourable structural damage mechanism. Furthermore, due to the particular structural and seismic characteristics of the analytical models examined, there is a seemingly large influence of the 6th elevation in both structural behaviour and damage distribution where infill wall elements seem to address by distrusting structural damage in a series of levels ranging, predominantly, from first to sixth elevation rather than

concentrate damage on the 1st and 6th elevations as is the case with the bare frame (Frame 0). Data presented in Table 2 suggests a quantifiable improvement of structural damage distribution characteristics of infill wall bearing frames against their bare frame counterpart with a significant reduction in the recorded sixth level average LDI_{PA} values of 95%, 75%, 100%, and 85% for Frame 1, Frame 2, Frame 3, and Frame 4, respectively.

Furthermore, a comparison of the first to sixth level's LDI_{PA} versus the structures' GDI_{PA} distribution ratio reveals the overall structural damage distribution uniformity demonstrated by Frames 1 and 2. Data suggests that infill frames presented and more evenly distributed damage characteristics with a 57:13:16:10:03:01 and 61:10:12:08:03:05 LDI_{PA} versus GDI_{PA} percentage ratio for Frames 1 and 2, respectively, against the 69:03:03:02:02:20 ratio recorded in their bare frame counterpart.

In terms of structural behaviour as expressed through interstorey drift ratio (LISDR) for each individual level Figure 9 presents the relevant values for seismic excitations compatible to $a = 0.16$ g, 0.24 g, and 0.36 g in Figures 9(a), 9(b), and 9(c), respectively. In this respect the particular

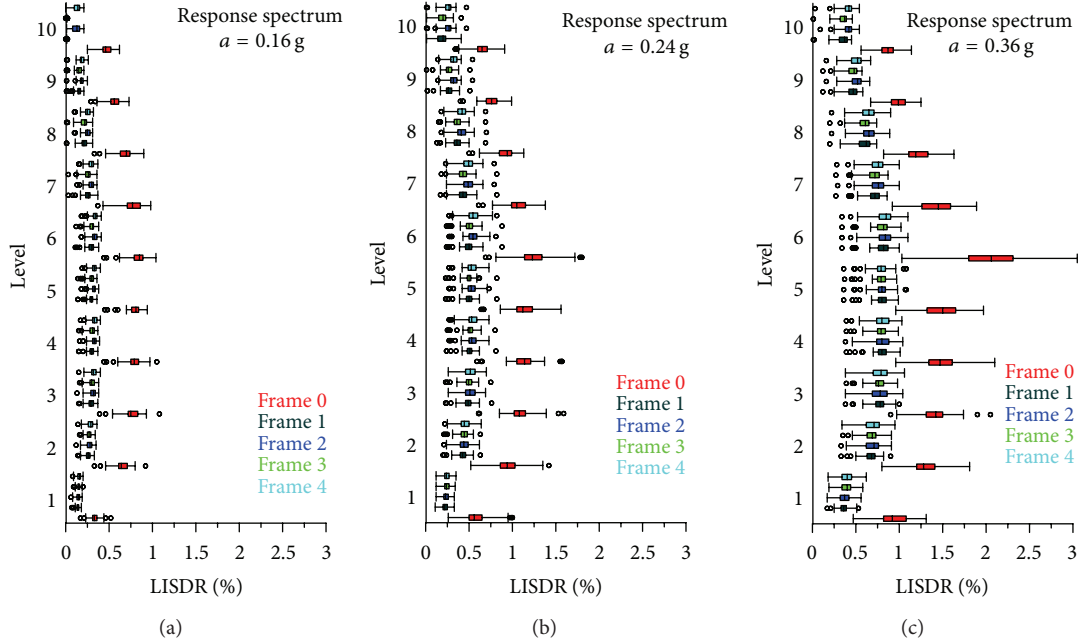


FIGURE 9: (a) All frame typologies recorded LISDR values for $a = 0.16$ g. (b) All frame typologies recorded LISDR values for $a = 0.24$ g. (c) All frame typologies recorded LISDR values for $a = 0.36$ g.

TABLE 3: Average recorded LISDR value reduction (%).

Frame	Response spectrum	Level									
		1	2	3	4	5	6	7	8	9	10
1	0.16 g	59	60	61	62	63	66	67	70	75	98
	0.24 g	62	55	56	56	57	61	60	61	66	74
	0.36 g	61	48	46	46	48	62	50	51	54	60
2	0.16 g	57	58	58	59	60	61	62	64	68	75
	0.24 g	60	53	53	53	53	57	55	56	58	60
	0.36 g	60	47	45	46	47	60	48	47	49	53
3	0.16 g	55	59	61	62	63	65	67	70	75	98
	0.24 g	59	54	55	55	56	60	60	61	65	73
	0.36 g	57	47	46	47	48	62	51	51	54	60
4	0.16 g	54	56	58	58	59	60	62	64	68	74
	0.24 g	58	52	53	53	53	57	55	55	58	60
	0.36 g	57	46	45	46	47	60	48	47	49	53

differences between the alternative infill walls' topologies can be reviewed as per the recorded seismic response influence at different levels of seismic excitation dictated through the selection of their respective response spectrum.

The reduction in the recorded LISDR values for all infill wall frame typologies against the bare frame has been summarized in Table 3 as observed on a level to level basis.

Figure 10 highlights the similarities in structural behaviour presented between frame typologies with comparable area of infill wall patterns irrespective of the existence or not of infill walls in the first elevation (ground floor) frames. It is therefore concluded that little difference can be attributed in the first elevation infill walls and those differences register in the reduction values of the ground floor only, in respect to the structures seismic behaviour in terms of observed inter storey drift ratio.

In light of the above and in terms of seismic behaviour, the study of the effect of infill walls' alternative typologies measured through the reduction of the average recorded LISDR values against the bare frame can be deemed appropriate to be carried out utilizing Frames 1 and 2. Figure 11 presents the LISDR reduction for Frames 1 and 2 in terms of percentage of the bare frame (Frame 0) LISDR values across the three different response spectra selected. The results indicate the tendency of infill wall presence towards the cancellation of the increased sixth level drift of the bare frame demonstrating the beneficial effect of their incorporation. Furthermore, the progressive convergence of the reduction values between the different frames in different strength seismic excitations can be deemed as an indication of the overall influence of infill walls against the specific typologies studied. Therefore, the tendency for the infill wall bearing frames to act in a similar

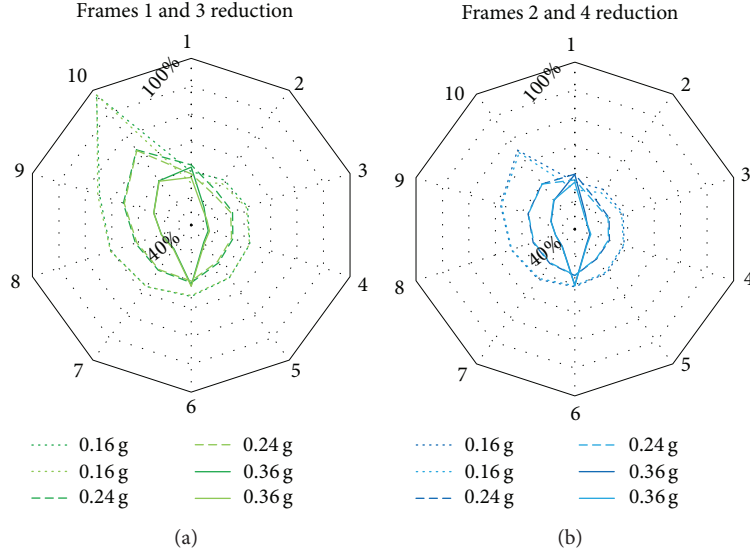


FIGURE 10: (a) Level reduction values for infill wall bearing Frames 1 and 3 over Frame 0. (b) Level reduction values for infill wall bearing Frames 2 and 4 over Frame 0.

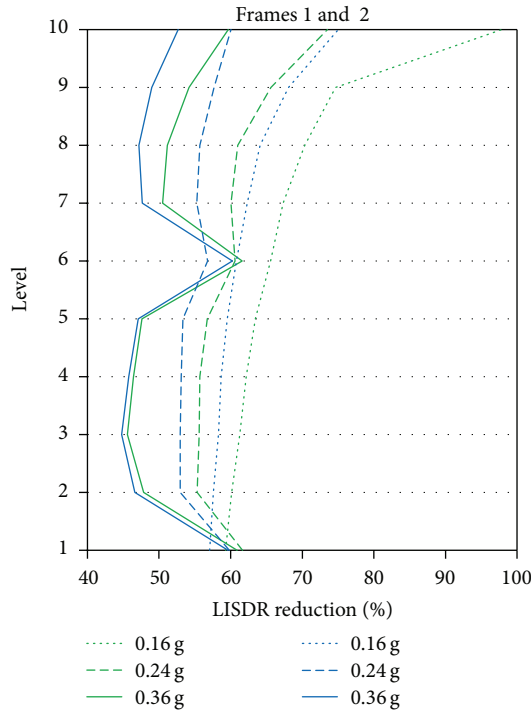


FIGURE 11: Level average reduction values recorded for Frames 1 and 2 against Frame 0.

manner in increasing seismic load, with little respect to the particular infill wall topology conditions, advocates an additional point for consideration by further demonstrating the suitability of infill wall incorporation in the structural system of either new designs or cases of structural rehabilitation.

Table 4 summarises the recorded reductions in the average values of LISDR between the bare frame and its infill

TABLE 4: Average LISDR reduction (%) recorded over the whole structure.

LISDR reduction (%)	Response spectrum (a)		
	0.16 g	0.24 g	0.36 g
Frame			
1	68	61	54
2	62	56	51
3	68	60	54
4	61	55	50

walled counterparts for each of the respective response spectrum compatible seismic excitation groups. In this respect, the progressively smaller influence of infill walls in the structural seismic behaviour is indicated by a 61% to 68% reduction of the average LISDR result values for seismic events corresponding to a response spectrum with $a = 0.16\text{ g}$. Similarly, a reduction of 55% to 61% and 50% to 54% has been recorded for seismic events corresponding to a response spectrum of $a = 0.24\text{ g}$ and 0.36 g , respectively.

Once more, the distinctively greater improvement which is seismic response of Frames 1 and 3 over Frames 2 and 4 is suggested by the results, indicated by the greater LISDR reduction values observed. It therefore consolidates the relevant findings over the infill wall topology influence on the recorded structural response under seismic excitation. Moreover, the converging nature of the reduction values indicates the diminishing effect of these differences in infill wall topologies as progressing towards stronger seismic excitations.

4.4. Results Summary. A closer look at the outcomes of this work suggests an overall reduction of the recorded average GDI_{PA} and MISDR values in the order of 78% and 60%,

respectively, between infill and noninfill bearing frames. Additionally, a reduction of 40% in the maximum GDI_{PA} , as well as a 62% and 74% in the minimum and maximum MISDR, values has been similarly established between the bare frame and its infill wall containing steel structure counterparts.

The data suggests a uniform reduction in terms of MISDR throughout the different seismic response spectra selected. On the other hand, GDI_{PA} values present an effective 100% reduction in both low and medium seismic region artificial accelerograms ($a = 0.16\text{ g}$ and 0.24 g), while measurable improvement has been recorded in the high seismicity region response spectrum compatible accelerograms ($a = 0.36\text{ g}$). The above indicates the strong influence of the overall response spectra seismic characteristics in the effectiveness of infill walls as seismic behaviour altering elements. On the other hand, a uniform reduction of the recorded ISDR and DI_{PA} values observed hints towards the reduced participation of the overall seismic duration in the seismic response characteristic alteration of infill walls effectiveness. Therefore, indicating that total duration characteristics present a less significant seismic feature, with only a small contribution to the overall structural seismic response behaviour.

In terms of structural response on a storey level, represented by the recorded LISDR and LDI_{PA} values, the results indicated the difference of influence between the structural damage distribution and structural behaviour characteristics. This becomes evident by the quantifiable improvement of structural damage distribution characteristics, of infill wall bearing frames against their bare frame counterparts. This has been demonstrated with the observed significant reduction in the recorded sixth level average LDI_{PA} values of 95%, 75%, 100%, and 85% for Frames 1, 2, 3, and 4, respectively. In this regard, the results suggest the alteration of the predominant damage concentration in the first and sixth level for the bare frame structure (Frame 0) with a more distributed allocation of the recorded structural damage in a series of levels. In more detail, a comparison of first to sixth level's LDI_{PA} versus GDI_{PA} distribution ratio revealed the overall structural damage distribution uniformity that is demonstrated by Frames 1 and 2 with a 57:13:16:10:03:01 and 61:10:12:08:03:05 LDI_{PA} versus GDI_{PA} percentage damage distribution ratio against the 69:03:03:02:02:20 recorded for Frame 0. This effectively illustrates a strong case in favour of the beneficial effects of infill wall existence in the overall seismic behaviour of frame structures. Similarly for seismic behaviour, as expressed through the interstorey drift (ISDR) characteristics of magnitude and distribution, significant improvements were recorded in all cases examined for all frames under consideration. Most prominently, Frame 1 and 3 topologies recorded better results and bigger influence in the improvement of the overall structural behaviour. Furthermore, LISDR results indicate a converging trend between the improvement values of the 4 infill wall topologies for increasing seismic excitation characteristics but remain far superior over the bare frame counterpart. In this respect LISDR reduction values of 61% to 68%, 55% to 61%, and 50% to 54% were recorded for seismic events corresponding to

a response spectrum of $a = 0.16\text{ g}$, 0.24 g , and 0.36 g between infill wall and bare frame structures.

5. Conclusions

This paper investigated the influence of alternative infill wall topologies in terms of a frame structure's seismic behaviour and damage distribution characteristics. The work was carried out with the utilization of a set of 225 Greek anti-seismic code spectrum compatible artificial accelerograms and the execution of nonlinear dynamic analyses for all individual cases to obtain the relevant structural response data. Structural damage results were quantified with the help of the global structure damage index (GDI) after Park/Ang (GDI_{PA}) and the maximum interstorey drift ratio (MISDR), respectively. Their level-wise counterparts were utilised to identify the structural behaviour in the forms of level damage index after Park/Ang (LDI_{PA}) and the level interstorey drift ratio (LISDR).

Based on the results presented, a significant reduction in both GDI_{PA} and MISDR indices for all examined selected infill wall topologies was recorded, vividly demonstrating the improvement in terms of structural damage and seismic behaviour, respectively. The data suggests that a significant reduction in the observed interstorey drift ratio is achieved with the incorporation of any infill wall typology without significant impact in the individual LISDR distribution characteristics for any of the investigated infill wall typologies. In terms of the LDI_{PA} recorded values, representing the recorded structural damage on each individual level, a significant reduction can be observed followed by a differentiation in damage distribution. The most notable contributions of infill walls in terms of structural damage besides the significant reduction in GDI_{PA} values observed were the improvement of the damage distribution characteristics where the first and sixth level damage concentration mode recorded for the bare frame has greatly improved from the first to sixth level structural distribution mode. Thus, by avoiding damage concentration and promoting a structurally beneficial spread of the damage into different elevations effectively improved the overall structural damage response in both magnitude (DIPA) as well as its distribution characteristics.

Care shall be taken to avoid generalizations that would not take into account the localized impact of infill elements to the frame structure due to stress localization, especially in the case of weak frame structures. In this regard, due diligence needs to be spent to avoid introducing plan irregularities that might introduce inelastic deformation demands that could concentrate in the part of the building which has more sparse infills. As a matter of further work to be carried out the estimation of the reduction of the drift demands as a function of different structures (e.g., buildings with different number of stories, designed for different ductility classes), of diverse types of infill, and of "density" or area of walls in the bays of the frame could be carried out in the future.

In this work the use of nonstructural elements as means of improving frame structural seismic behaviour has been investigated and important aspects of structural response

have been highlighted demonstrating the suitability of such element implementation beyond their intended architectural scope provided that consideration was spent to take into account all possible stress conditions that such an intervention might give rise to. This work gave rise to elements of the suitability of infill walls in the structural rehabilitation of frame structures in all infill typologies while demonstrated the lesser improvement recorded when the infill element layout creates a soft storey effect. Furthermore, by testing different infill wall topologies this work advocated the improved seismic response characteristics against similar bare frame structures in terms of structural damage and behaviour, while the nature of infill wall topology specifics, based on possible architectural constraints and design requirements, does not significantly negate these effects. It is therefore the conclusion of this research that infill walls can play an important role in frame buildings seismic behaviour both with their inclusion in the original design or when utilized as a seismic retrofit to improve a structure's characteristics.

References

- [1] T. Paulay and M. J. N. Priestley, *Seismic Design of Reinforced Concrete and Masonry Buildings*, John Wiley & Sons, Hoboken, NJ, USA, 1992.
- [2] L. Di Sarno and A. S. Elnashai, "Bracing systems for seismic retrofitting of steel frames," *Journal of Constructional Steel Research*, vol. 65, no. 2, pp. 452–465, 2009.
- [3] ATC-33, "NEHRP guidelines for the seismic rehabilitation of buildings," Tech. Rep. FEMA 273, Federal Emergency Management Agency, Washington, DC, USA, 1997.
- [4] R. H. Wood, "The stability of tall buildings," *ICE Proceedings*, vol. 11, no. 1, pp. 69–102, 1958.
- [5] M. Wakabayashi, "Behaviour of systems," in *Proceedings of the 6th World Conference on Earthquake Engineering (WCEE '77)*, pp. 65–76, New Delhi, India, 1977.
- [6] R. E. Klingner and V. V. Bertero, "Earthquake resistance of infilled frames," *Journal of The Surveying and Mapping Division*, vol. 104, no. 6, pp. 973–989, 1978.
- [7] J. L. Dawe, A. B. Schriver, and C. Sofocleous, "Masonry infilled steel frames subjected to dynamic load," *Canadian Journal of Civil Engineering*, vol. 16, no. 6, pp. 877–885, 1989.
- [8] Y. Yamazaki, S. Okamoto, T. Kaminosono, and M. Teshigawara, "Seismic tests on a five storey full scale reinforced masonry building," in *Proceedings of the 5th North American Masonry Conference (NAMC '90)*, vol. 1, no. 2, pp. 69–80, University of Illinois at Urbana-Champaign, Champaign, Ill, USA, 1990.
- [9] S. Albanesi, T. Albanesi, and F. Carboni, "The influence of infill walls in RC frame seismic response," in *High Performance Structures and Materials II*, C. A. Brebbia and W. P. De Wilde, Eds., pp. 621–630, WIT Press, Southampton, UK, 2004.
- [10] G. Mondal and S. K. Jain, "Lateral stiffness of masonry infilled reinforced concrete (RC) frames with central opening," *Earthquake Spectra*, vol. 24, no. 3, pp. 701–723, 2008.
- [11] R. Zarnic and S. Gostic, "Masonry infilled frames as an effective structural subassemblage," in *Proceedings of the International Workshop on Seismic Design Methodologies for the Next Generation of Codes*, pp. 335–346, August Aimé Balkema, Bled, Slovenia, 1997.
- [12] S. V. Polyakov, *Masonry in Framed Buildings: An Investigation Into the Strength and Stiffness of Masonry Infilling*, Gosudarstvennoe Izdatel'stvo Literatury Po stroitel'stvu iarkhitektury, Moscow, Russia, English translation by G. L. Cairns, National Lending Library for Science and Technology, Yorkshire, Boston, UK, 1956.
- [13] B. S. Smith and A. Coull, *Tall Building Structures: Analysis and Design*, John Wiley & Sons, Hoboken, NJ, USA, 1991.
- [14] D. D'Ayala, J. Worth, and O. Riddle, "Realistic shear capacity assessment of infill frames: comparison of two numerical procedures," *Engineering Structures*, vol. 31, no. 8, pp. 1745–1761, 2009.
- [15] B. S. Smith and C. Carter, "A method of analysis for infilled frames," *ICE Proceedings*, vol. 44, no. 1, pp. 31–48, 1969.
- [16] M. Bruneau and T. Bhagwagar, "Seismic retrofit of flexible steel frames using thin infill panels," *Engineering Structures*, vol. 24, no. 4, pp. 443–453, 2002.
- [17] G. Sun, R. He, G. Qiang, and Y. Fang, "Cyclic behavior of partially-restrained steel frame with RC infill walls," *Journal of Constructional Steel Research*, vol. 67, no. 12, pp. 1821–1834, 2011.
- [18] A. A. Tasnimi and A. Mohebkhah, "Investigation on the behavior of brick-infilled steel frames with openings, experimental and analytical approaches," *Engineering Structures*, vol. 33, no. 3, pp. 968–980, 2011.
- [19] A. Mohebkhah, A. A. Tasnimi, and H. A. Moghadam, "Non-linear analysis of masonry-infilled steel frames with openings using discrete element method," *Journal of Constructional Steel Research*, vol. 64, no. 12, pp. 1463–1472, 2008.
- [20] OASP, "Greek antiseismic code," Greek Ministry of Environment and Public Works, Athens, Greece, 2003, (Greek).
- [21] CEN, "EN 1993: Eurocode 3—design of steel structures," European Committee for Standardization, Brussels, Belgium, 1993.
- [22] CEN, "EN 1998: Eurocode 8—earthquake resistance design of structures," European Committee for Standardization, Brussels, Belgium, 2004.
- [23] D. A. Gasparini and E. H. Vanmarcke, "SIMQKE, a program for artificial motion generation," User's manual and documentation, Publication no. R76-4, Department of Civil Engineering, MIT, Cambridge, Mass, USA, 1976.
- [24] Y.-J. Park and A. H.-S. Ang, "Mechanistic seismic damage model for reinforced concrete," *Journal of Structural Engineering*, vol. 111, no. 4, pp. 722–739, 1985.
- [25] S. K. V. Gunturi and H. C. Shah, "Building specific damage estimation," in *Proceedings of the 10th World Conference On Earthquake Engineering (WCEE '92)*, pp. 6001–6006, Madrid, Spain, 1992.
- [26] A. M. Reinhorn, H. Roh, M. Sivaslan et al., "IDARC 2D version 7.0: a program for the inelastic damage analysis of structures," Tech. Rep. MCEER-09-0006, State University of New York, Buffalo, NY, USA, 2009.
- [27] A. Saneinejad and B. Hobbs, "Inelastic design of infilled frames," *Journal of Structural Engineering*, vol. 121, no. 4, pp. 634–650, 1995.

Research Article

Simultaneous Identification of Moving Vehicles and Bridge Damages Considering Road Rough Surface

Qingxia Zhang,^{1,2,3} Łukasz Jankowski,² and Zhongdong Duan^{3,4}

¹ College of Civil and Architecture Engineering, Dalian Nationalities University, Dalian 116650, China

² Smart-Tech Centre, Institute of Fundamental Technological Research, Polish Academy of Sciences, 02-106 Warsaw, Poland

³ School of Civil Engineering, Harbin Institute of Technology, Harbin 150090, China

⁴ Harbin Institute of Technology Shenzhen Graduate School, Shenzhen 5180553, China

Correspondence should be addressed to Qingxia Zhang; zhangqingxia.hit@hotmail.com

Received 9 August 2013; Revised 19 October 2013; Accepted 3 November 2013

Academic Editor: Nawawi Chouw

Copyright © 2013 Qingxia Zhang et al. This is an open access article distributed under the Creative Commons Attribution License, which permits unrestricted use, distribution, and reproduction in any medium, provided the original work is properly cited.

A method for the simultaneous identification of moving vehicles and the damages of the supporting structure from measured responses is presented. A two-axle vehicle model with two degrees of freedom (DOF) is adopted. The extent of the damage and the vehicle parameters were chosen as the optimisation variables, which allow ill conditioning to be avoided and decrease the number of sensors required. The identification is performed by minimising the distance between the measured responses and the computed responses to given optimisation variables. The virtual distortion method (VDM) was used, such that the response of the damaged structure can be computed from comparison with the intact structure subjected to the same vehicle excitation and to the response-coupled virtual distortions. These are related to the optimisation variables by the system impulse response matrix and are expressed by a linear system, which allowed both types of optimisation variables to be treated in a unified way. The numerical cost is reduced by using a moving influence matrix. The adjoint variable method is used for fast sensitivity analysis. A three-span bridge numerical example is presented, where the identification was verified with 5% root mean square (RMS) measurement, and model, error whilst also considering the surface roughness of the road.

1. Introduction

In structural health monitoring, accurate load and damage identification are indispensable to the maintenance of structural integrity, as well as providing the evidence for forensic engineering. Particularly, moving loads or moving vehicle parameter identification is important not only for prediction and analysis of the dynamic responses of bridges, but also in traffic studies, in design code calibration, for traffic control, and so forth. In recent decades, many investigations have been performed on either load identification or damage identification. However, in practice, both unknown system damage and unknown (moving) excitations usually coexist and together influence the system response in a coupled way. Therefore, their simultaneous identification is worthy of further exploration.

As opposed to local, high-frequency ultrasonic scanning, this paper considers only global or low-frequency damage

identification methods which are based on the structural vibrations. These methods are mainly categorised into two groups: frequency domain methods or time domain methods. In the frequency domain, damage is detected, located, and identified through measured changes in the related modal parameters or dynamic signature [1] such as natural frequency and mode shape. However, the modal parameters are obtained from the responses to a certain kind of excitation and these methods are limited to time-invariant systems. Under the action of a moving vehicle, a coupled bridge-vehicle system is time variant, and the system parameters are changing as the vehicles move [2]. The vibration caused by traffic is a nonstationary process that strengthens with decreasing span [3]. In this case, the analysis is most often performed in the time domain by the direct comparison of the simulated and measured responses [4]. However, this usually requires a known moving load or other such vehicle

parameters. Sieniawska et al. [5] identify parameters of a linear structure from its responses to a moving load using a static substitution of the equation of motion, where the moving load is a known constant magnitude. Chang et al. [3, 6] present, and experimentally verify, a methodology for damage identification in bridges using a pseudostatic formulation based on coupling vibration with a moving vehicle, where the moving force is provided as a vector or calculated using the measured acceleration responses of the axles. Ling and Haldar [7] propose a linear system identification approach with unknown input, but they require a known dynamic response of all the degrees of freedoms; this is hard to perform on real-life, complex structures.

Moving load identification has been studied extensively in the past two decades [8]. Techniques of indirect identification from measured responses have been investigated and can be performed more easily and at lower cost compared to methods requiring direct measurements of moving loads. Chan et al. and Law et al. have proposed four methods for indirect identification: the time-domain method (TDM) [9], the frequency-time domain method (FTDM) [10], interpretive method I (IM-I) [11], and interpretive method II (IM-II) [12]. All of them require, *a priori*, known model parameters for the bridge. Each method has its merits and limitations, which are compared elsewhere [13]. Load identification is an inverse problem, and numerical ill-conditioning seems to be the main factor that influences the accuracy of the identification results. The accuracy can be improved by some regularisation methods, such as Tikhonov regularisation [14]. However, the determination of the optimal value of the regularisation parameter is numerically costly and requires lengthy computation. Pinkaew and Asnachinda [15, 16] point out that the regularisation parameter turns out to be sensitive to properties of both the vehicle and bridge and is difficult to be precisely assigned: they propose, and experimentally verify, an iterative regularisation method called the updated static component (USC) technique to decrease the sensitivity of the regularisation parameter. Moving forces are usually treated as unknown quantities to be identified. This requires a number of sensors equal to or exceeding the number of unknown moving forces to obtain a unique solution. Jiang et al. [17] present a moving vehicle parameter identification method based on genetic algorithms, where each moving vehicle is modelled as a two-DOF system that comprises mass, spring stiffness, and damping. Zhang et al. [18] provide an approach of identifying moving vehicle parameters based on VDM using a dynamic influence matrix. In general, the identification of moving forces or vehicle(s) requires a known, well-defined, bridge model to establish the relationship between load and response.

For unknown coexistent load and structural damage, it is generally difficult to decouple the related identification problems and solve any one of them independently. Since the two factors have essentially different natures, Zhang et al. [19] present a method to identify load and damage simultaneously using Chebyshev polynomials to parameterise the unknown force, and thus all parameters related to the damage and excitation can be updated simultaneously in each iteration. Zhang et al. [20] present, and experimentally verify, a method for

the simultaneous identification of nonmoving excitations and damage, which uses a VDM [21] to model structural damage and thus improve the identification efficiency thereof. In case of unknown moving loads, the vehicle-bridge system is a coupled time-varying system. Zhu and Law [22] present a two-step iteration procedure to simultaneously identify the moving loads and the damage caused to an Euler-Bernoulli simply supported beam; the number of the sensors is one less than the number of the beam elements.

Zhang et al. [23] present a method for the simultaneous identification of structural damage and moving masses; moving masses and damage extents are used as its optimisation variables, which avoids the ill-conditioning problem present in traditional moving force identification and decreases the number of sensors required; damage is modelled using virtual distortions, and a dynamic influence matrix is introduced to reduce numerical analysis cost. This paper simulates the vehicle using a two-axle, two-DOF, vehicle model, and the related parameters including mass, rotary inertia, spring stiffness, and damping are treated as unknowns together with the structural damage induced. The damaged bridge is assumed to be modelled by the decay of its mechanical properties and is often represented as a decreasing stiffness [24]. Based on VDM, the response of the damaged structure is modelled by the intact structure subjected to the same vehicle excitation and to the response-coupled virtual distortions. Through the related system impulse response matrix (*dynamic influence matrix* in the terminology of VDM), the moving loads and virtual distortions are connected with the optimisation variables in a linear system. In this way, the optimisation variables related to the vehicle parameter, and to the damage, are treated in a unified way. Then, they can be optimised using any standard optimisation algorithm. The numerical cost is reduced by using the moving dynamic influence matrix. Moreover, rapid sensitivity analysis is performed using the adjoint variable method.

Sections 2 and 3 discuss the equation of motion of the system and simulation of the system dynamic response by moving vehicle and virtual distortions; Section 4 discusses the inverse identification problem. Section 5 verifies the proposed approach using a numerical example of a three-span frame structure considering road surface roughness. The approach and the results are discussed in Section 6.

2. Dynamic Analysis of a Coupled Vehicle-Beam System

2.1. Equation of Motion for a Moving Vehicle on a Bridge. A popular two-axle, two-DOF, vehicle model [3] was adopted; see Figure 1, where u^v and θ^v , respectively, denote the bounce and pitching motions of the vehicle. Exactly speaking, u^v is the vertical displacement of the vehicle, which is measured vertically upwards from its vertical static equilibrium position before the vehicle reached the bridge and θ_i^v are its rotary displacement relative to the static position. Denoted by m and J , respectively, are the vehicle mass and the rotary inertia; denoted by k and c , respectively, are the spring constant and damping coefficient of the vehicle.

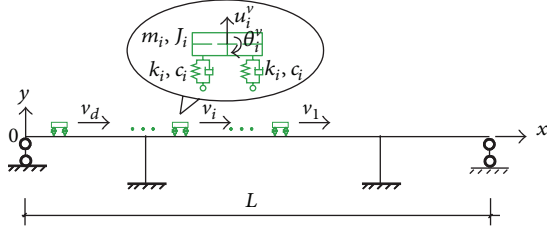
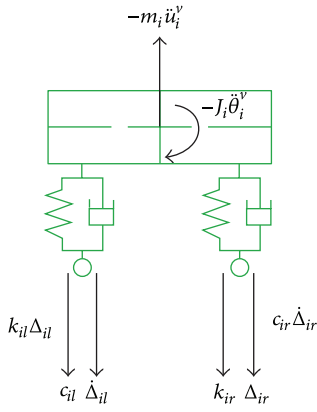


FIGURE 1: A coupled vehicle-bridge system.

FIGURE 2: Forces of the i th moving vehicle.

For the i th moving vehicle on the bridge, the additional elongation of the left and right spring except the elongation caused by the weight is respectively denoted by Δ_{il} and Δ_{ir} , then

$$\begin{aligned}\Delta_{il} &= u_i^v + \theta_{i1} e_{il} - x_{il} - r_{il}; \\ \Delta_{ir} &= u_i^v - \theta_{i1} e_{ir} - x_{ir} - r_{ir},\end{aligned}\quad (1)$$

where e_{il} , e_{ir} denote, respectively, the distance from the left and right axle to the vehicle's centre of mass; x_{il} , x_{ir} , respectively, denote the vertical displacements of the bridge at the current position of the vehicle's left and right axle; r_{il} , r_{ir} denote the roadway surface roughness at the current respective position, which is also measured vertically upwards with reference to the deck level.

The forces of the i th moving vehicle are shown in Figure 2, which includes the inertial forces. Based on the dynamic balance, the equation of motion of the i th moving vehicle can be formulated as

$$\begin{aligned}\mathbf{m}_i^v \ddot{Y}_i^v(t) + c_i \mathbf{e}_{ik} \dot{Y}_i^v(t) + k_i \mathbf{e}_{ik} Y_i^v(t) \\ = k_i S_i (x_i(t) + r_i(t)) + c_i S_i (\dot{x}_i(t) + \dot{r}_i(t)),\end{aligned}\quad (2)$$

where $\mathbf{m}_i^v = [m_i \ 0]^\top$, $Y_i^v(t) = [u_i^v(t) \ \theta_i^v(t)]^\top$, $r_i(t) = [r_{il}(t) \ r_{ir}(t)]^\top$, $S_i = [1 \ -1]^\top$, $x_i(t) = [x_{il}(t) \ x_{ir}(t)]^\top$, $\mathbf{e}_{ik} = \begin{bmatrix} 2 & e_{il}-e_{ir} \\ e_{il}-e_{ir} & e_{il}^2+e_{ir}^2 \end{bmatrix}$.

In this study, the random roughness of the road surface $r(x)$ is simulated by a zero-mean, real-value, stationary Gaussian process as described in the following [17, 25]:

$$r(x) = \sum_{k=1}^{N_T} \alpha_k \cos(2\pi n_k x + \varphi_k), \quad (3)$$

where α_k is the amplitude of the cosine wave, n_k is the spatial frequency (in cycle/m), φ_k is a random phase angle with uniform probability distribution in the interval $[0, 2\pi]$, x is the position measured from the left end of the bridge, and N_T is the total number of the cosine waves which are used to construct the roughness. Parameter α_k is computed by

$$\alpha_k^2 = 4G_d(n_k) \Delta n, \quad (4)$$

where $G_d(n_k)$ is the power spectral density function of the road surface and related to the ground flatness coefficient $G_d(n_0)$ in the form as [26]

$$\begin{aligned}G_d(n_k) &= G_d(n_0) \left(\frac{n_k}{n_0} \right)^{-2}, \\ n_k &= n_l + k \Delta n,\end{aligned}\quad (5)$$

$$\Delta n = \frac{n_u - n_l}{N_T},$$

where $G_d(n_0)$ depends on the classification of road surface condition. n_l and n_u , are respectively, lower and upper cut-off spatial frequencies, and the power spectral density function $G_d(n_k)$ is defined within the interval of $[n_l, n_u]$. For the vehicle velocity between 70 km/h and 120 km/h on expressway, the power spectral density is most meaningful in the frequency interval of $[0.0221 \text{ m}^{-1}, 1.4142 \text{ m}^{-1}]$.

2.2. Equation of Motion for a Bridge under Moving Vehicles. The bridge is idealized as a beam, which suffers the traffic excitations. Denoted by $p_{il}(t)$ and $p_{ir}(t)$, respectively, are the interaction forces of the i th moving vehicle at its left and right wheel, and through the dynamic balance analysis, they can be expressed using the additional elongation of the spring and the gravity of the vehicle,

$$\begin{aligned}p_{il}(t) &= k_i \Delta_{il}(t) + c_i \dot{\Delta}_{il}(t) + \frac{m_i g e_{ir}}{e_{il} + e_{ir}}, \\ p_{ir}(t) &= k_i \Delta_{ir}(t) + c_i \dot{\Delta}_{ir}(t) + \frac{m_i g e_{il}}{e_{il} + e_{ir}}.\end{aligned}\quad (6)$$

The equation of motion for the bridge can be formulated as follows:

$$\mathbf{M} \ddot{\mathbf{u}}^b(t) + \mathbf{C} \dot{\mathbf{u}}^b(t) + \mathbf{K} \mathbf{u}^b(t) = \sum_{i=1}^{n_m} \mathbf{b}_i(t) \mathbf{p}_i(t), \quad (7)$$

where \mathbf{M} , \mathbf{C} , and \mathbf{K} are, respectively, the mass, stiffness, and damping matrices of the bridge, \mathbf{u}^b represents the displacement vector, and $\mathbf{p}_i(t) = [p_{il}(t) \ p_{ir}(t)]^\top$, $\mathbf{b}_i(t) =$

$[b_{il}(t) \ b_{ir}(t)]$, $b_{il}(t)$, $b_{ir}(t)$, are respectively, the time-varying load distribution vector in global coordinates with regard to the left and right wheels. Thus, $b_{il}(t)$, $b_{ir}(t)$ can be formulated using the shape function of the beam element in finite element (FE) analysis, and their elements are zeroed when the corresponding wheel is off the bridge during the sampling time.

2.3. Dynamic Response of the Coupled Vehicle-Bridge System. In the equation of motion for the moving vehicle and bridge ((2) and (7)), it can be seen that the system is coupled: the vibration of the bridge influenced the vibration of the moving vehicle (2), and the vehicle in return interactively influenced the vibration of the bridge (7). The equation of motion for the coupled system can be expressed as follows:

$$\begin{aligned}
& \left[\begin{array}{c} \mathbf{M} \\ \mathbf{m}_1^v \\ \ddots \\ \mathbf{m}_{n_m}^v \end{array} \right] \left[\begin{array}{c} \ddot{\mathbf{u}}^b(t) \\ \ddot{Y}_1^v(t) \\ \vdots \\ \ddot{Y}_{n_m}^v(t) \end{array} \right] \\
& + \left[\begin{array}{cccc} \mathbf{K} + \Delta\mathbf{K}(t) & -b_1(t) S_1^T k_1 & \cdots & -b_{n_m}(t) S_{n_m}^T k_d \\ -S_1 b_1^T(t) k_1 & k_1 \mathbf{e}_{1k} & & \\ \vdots & & \ddots & \\ -S_{n_m} b_{n_m}^T(t) k_{n_m} & & & k_{n_m} \mathbf{e}_{n_m k} \end{array} \right] \\
& \times \left[\begin{array}{c} \mathbf{u}^b(t) \\ Y_1^v(t) \\ \vdots \\ Y_{n_m}^v(t) \end{array} \right] \\
& + \left[\begin{array}{cccc} \mathbf{C} + \Delta\mathbf{C}(t) & -b_1(t) S_1^T c_1 & \cdots & -b_{n_m}(t) S_{n_m}^T c_d \\ -S_1 b_1^T(t) c_1 & c_1 \mathbf{e}_{1k} & & \\ \vdots & & \ddots & \\ -S_{n_m} b_{n_m}^T(t) c_{n_m} & & & c_{n_m} \mathbf{e}_{n_m k} \end{array} \right] \\
& \times \left[\begin{array}{c} \dot{\mathbf{u}}^b(t) \\ \dot{Y}_1^v(t) \\ \vdots \\ \dot{Y}_{n_m}^v(t) \end{array} \right] \\
= & \left[\begin{array}{c} \sum_i b_i (m_i e_i g - k_i r_i + c_i \dot{r}_i) \\ k_1 S_1 r_1 + c_1 S_1 \dot{r}_1 \\ \vdots \\ k_{n_m} S_{n_m} r_{n_m} + c_{n_m} S_{n_m} \dot{r}_{n_m} \end{array} \right], \tag{8}
\end{aligned}$$

where $\Delta\mathbf{K}(t) = \sum_i k_i b_i(t) b_i^T(t)$, $\Delta\mathbf{C}(t) = \sum_i c_i b_i(t) b_i^T(t)$, $e_i = [e_{il}/(e_{il} + e_{ir}) \ e_{ir}/(e_{il} + e_{ir})]^T$.

Equation (8) shows that the system is time variant with the vehicle's motion, and this indicated that the vibration of the bridge caused by the traffic was nonstationary. Therefore, the performance of damage identification in this case may

have similar limitations to those pertaining to methods subjected to a stationary assumption, for example, modal based methods in the frequency domain. In contrast, time-domain analysis for identification is more accurate and appropriate. Then, the key procedure is the estimation of the system response to damage. However, if the response is computed in the traditional way by using the system motion equation, it will need to reassemble the varying system parameter matrix at each sampling time-step, which will be time-consuming, especially for bridges with complex structures. Aiming at solving this problem, the following section presents a fast reanalysis, VDM-based method.

3. Fast Reanalysis of the Damaged System

3.1. Dynamic Response of the Damaged Structure under Known Excitation. Denoted by μ_i the damage extent of the i th finite element, which is quantified by the ratio between its original stiffness matrix \mathbf{K}_i and the damaged stiffness matrix $\tilde{\mathbf{K}}_i$,

$$\tilde{\mathbf{K}}_i = \mu_i \mathbf{K}_i. \tag{9}$$

Then, the stiffness matrix of the damaged bridge can be expressed by

$$\tilde{\mathbf{K}} = \sum_i \mu_i \mathbf{K}_i. \tag{10}$$

Substitute (10) into the equation of motion of the damaged beam to obtain

$$\mathbf{M}\ddot{\mathbf{u}}^b(t) + \mathbf{C}\dot{\mathbf{u}}^b(t) + \sum_i \mu_i \mathbf{K}_i \mathbf{u}^b(t) = \sum_{i=1}^{n_m} \mathbf{b}_i(t) \mathbf{p}_i(t). \tag{11}$$

Compared with the intact structure, remove the modified part of the stiffness matrix on the right-hand side of (11); then the equation is transformed into the equation of motion of the *distorted structure* (in the terminology of VDM); that is, the intact structure was subjected to the same external excitation and to a certain response coupled pseudoload $\mathbf{p}^0(t)$,

$$\mathbf{M}\ddot{\mathbf{u}}^b(t) + \mathbf{C}\dot{\mathbf{u}}^b(t) + \mathbf{K}\mathbf{u}^b(t) = \sum_{i=1}^{n_m} \mathbf{b}_i(t) \mathbf{p}_i(t) + \mathbf{p}^0(t), \tag{12}$$

where the pseudo-load $\mathbf{p}^0(t)$ is related to the extent of the damage by

$$\mathbf{p}^0(t) = \sum_i (1 - \mu_i) \mathbf{K}_i \mathbf{u}(t). \tag{13}$$

In VDM, virtual distortion is more often adopted to simulate stiffness-degrading damage, which is related to the pseudo-load as follows:

$$\mathbf{p}_{e,i}^0(t) = \mathbf{K}_{e,i} \sum_j \kappa_{ij}^0(t) \varphi_{ij}, \tag{14}$$

where $\mathbf{p}_{e,i}^0$ is the local pseudo-load applied on the i th element expressed in the local DOFs, $\mathbf{K}_{e,i}$ is the stiffness matrix of

the i th element in its local coordinate, $\kappa_{ij}^0(t)\varphi_{ij}$ is the j th virtual distortion of the i th element, φ_{ij} is the j th nonzero eigenvector to the j th nonzero positive eigenvalue λ_{ij} of the stiffness matrix $\mathbf{K}_{e,i} = \sum_j \lambda_{ij} \varphi_{ij} \varphi_{ij}^T$, and φ_{ij} represents the j th local unit distortion, $\kappa_{ij}^0(t) = (1 - \mu_i) \varphi_{ij}^T \mathbf{u}_{e,i}(t)$ is the time-varying combination coefficient of the corresponding j th local unit distortion φ_{ij} . $\mathbf{u}_{e,i}(t)$ is the nodal displacement of the i th element in its local coordinate system, which shows that $\kappa_{ij}^0(t)$ is coupled with the system vibration.

Denoted by $\mathbf{p}_{e,i}$ is the local nodal load applied on the i th element; then it can be similarly expressed by

$$\mathbf{p}_{e,i}(t) = \mathbf{K}_{e,i} \sum_j \kappa_{ij}(t) \varphi_{ij}, \quad (15)$$

where $\kappa_{ij}(t)\varphi_{ij}$ is the j th actual distortion of the i th damaged element and the combination coefficient $\kappa_{ij}(t) = \varphi_{ij}^T \mathbf{u}_{e,i}(t)$ has the relation to the coefficient $\kappa_{ij}^0(t)$ as follows [23]:

$$\kappa_{ij}^0(t) = (1 - \mu_i) \kappa_{ij}(t). \quad (16)$$

Based on (12), by virtual distortions, the response of the damaged bridge under moving vehicles can be expressed by

$$\begin{aligned} y_\alpha(t) &= \sum_i \int_0^t D_{\alpha i}^m(t, \tau) p_i(\tau) d\tau \\ &\quad + \sum_{i,j} \int_0^t D_{\alpha ij}^\kappa(t - \tau) \kappa_{ij}^0(\tau) d\tau. \end{aligned} \quad (17)$$

Here, it assumed zero value initial conditions and $y_\alpha(t)$ was the response of the α th measurement, which is modelled as the sum of the linear responses of the intact structure to a known excitation $p_i(t)$ and to certain virtual distortions. $D_{\alpha i}^m(t, \tau)$ denoted the impulse response of the intact structure at time t to unit impulsive excitation applied at time τ at the respective locations of the excitation $p_i(t)$. It is worth noticing that the excitation location is changing with the vehicles. $D_{\alpha ij}^\kappa(t)$ denotes the impulse response (in the scope of the VDM, it is called the *dynamic influence matrix*) to an impulse unit distortion φ_{ij} of the i th element which is equivalent to a local impulsive load $\mathbf{K}_{e,i}\varphi_{ij}$.

Similarly to (17), the distortion response $\kappa_{ij}(t)$ of the damaged structure can be formulated as

$$\begin{aligned} \kappa_{ij}(t) &= \sum_k \int_0^t D_{ijk}^{km}(t, \tau) p_k(\tau) d\tau \\ &\quad + \sum_{k,l} \int_0^t D_{ijkl}^{\kappa k}(t - \tau) \kappa_{kl}^0(\tau) d\tau, \end{aligned} \quad (18)$$

where $D_{ijk}^{km}(t, \tau)$ is the j th distortion of the i th damaged element at time t to unit impulsive excitation applied at time τ at the respective location of the excitation $p_k(t)$, and $D_{ijkl}^{\kappa k}(t)$ is the j th distortion of the i th damaged element to an impulse unit distortion φ_{kl} of the k th damaged element.

Substitute (16) into (18) to obtain

$$\begin{aligned} (1 - \mu_i) \sum_k \int_0^t D_{ijk}^{km}(t, \tau) p_k(\tau) d\tau \\ = \kappa_{ij}^0(t) - (1 - \mu_i) \sum_{k,l} \int_0^t D_{ijkl}^{\kappa k}(t - \tau) \kappa_{kl}^0(\tau) d\tau. \end{aligned} \quad (19)$$

If combined, all the damaged elements i and the distortions j form a system of Volterra integral equations of the second kind, which is always well posed and thus uniquely solvable (Kress 1989 [27]). Then, the response $y_\alpha(t)$ can be computed by (17) with the obtained virtual distortions.

3.2. Response of the Damaged Structure under Moving Vehicles. In practice, the interaction between the moving vehicle and the bridge, (see (6)), is time varying and coupled with the system vibration, which is usually hard to measure in advance for monitoring and identification of the extent of damage in a bridge. While the vehicle parameters, such as mass, stiffness, and damping, can be obtained more easily through traffic count statistics on the bridge, in this case, the gain of the moving excitation, besides the virtual distortion, is the key procedure, by which the response of the damaged structure in (17) is computed. Equation (6) shows that the interaction was related to the vibration of the moving vehicle; that is, $u_i^v(t)$, $\theta_i^v(t)$, and the vertical response of the bridge $x_i(t)$ at the contact location of the vehicle wheels, as well as their corresponding vibration velocity: the solutions are discussed in the following paragraphs.

For the response $x_i(t)$, it can be formulated in a manner similar to

$$\begin{aligned} x_i(t) &= \sum_\beta \int_0^t D_{i\beta}^{mm}(t, \tau) p_\beta(\tau) d\tau \\ &\quad + \sum_{j,k} \int_0^t D_{ijk}^{mk}(t - \tau) \kappa_{jk}^0(\tau) d\tau, \end{aligned} \quad (20)$$

where $\beta = 2l + l_w - 2$ is the number of the contact point of the l_w th wheel ($l_w = 1, 2$) of the l th moving vehicle. $D_{i\beta}^{mm}(t, \tau)$ is the impulse response at the location of contact point β to unit moving impulsive excitation applied at time τ at the location of $p_\beta(\tau)$ and to an impulse unit distortion φ_{jk} of the j th damaged element. It is worth noticing that position of $x_i(t)$ changes with vehicle move. Matrix $\mathbf{D}_{i\beta}^{mm}$ consisting of $D_{i\beta}^{mm}(t, \tau)$ is thus called *moving dynamic influence matrix*. $D_{ijk}^{mk}(t)$ is the impulse response corresponding to an impulse unit distortion φ_{jk} of the j th damaged element.

Similarly to (20), the velocity response of the bridge $\dot{x}_i(t)$ can be expressed as follows:

$$\begin{aligned} \dot{x}_i(t) &= \sum_\beta \int_0^t \dot{D}_{i\beta}^{mm}(t, \tau) p_\beta(\tau) d\tau \\ &\quad + \sum_{j,k} \int_0^t \dot{D}_{ijk}^{mk}(t - \tau) \kappa_{jk}^0(\tau) d\tau, \end{aligned} \quad (21)$$

where $\dot{D}_{i\beta}^{mm}(t, \tau)$ and $\dot{D}_{ijk}^{mk}(t)$ are the respective velocity impulse responses.

Using the equation of motion of the moving vehicle (2), the dynamic response of the moving vehicle can be expressed by the convolution integral between the impulse response and the excitation (the right-hand side of (2))

$$\begin{aligned} \mathbf{Y}_i^v(t) = & \int_0^t \mathbf{H}_i^v(t-\tau) \mathbf{s}_i(k_i(\mathbf{x}_i(\tau) + \mathbf{r}_i(\tau)) \\ & + c_i(\dot{\mathbf{x}}_i(\tau) + \dot{\mathbf{r}}_i(\tau))) d\tau, \end{aligned} \quad (22)$$

where $\mathbf{H}_i^v(t) = \begin{bmatrix} \mathbf{h}_{uu,i}(t) & \mathbf{h}_{u\theta,i}(t) \\ \mathbf{h}_{\theta u,i}(t) & \mathbf{h}_{\theta\theta,i}(t) \end{bmatrix}$ consists of the impulse response with respect to each DOF of the vehicle. For example, $\mathbf{h}_{u\theta,i}(t)$ is the impulse response along the vertical direction to unit impulsive excitation along the rotational direction: the velocity of the vehicle vibration $\mathbf{Y}_i^v(t)$ is formulated as

$$\begin{aligned} \dot{\mathbf{Y}}_i^v(t) = & \int_0^t \dot{\mathbf{H}}_i^v(t-\tau) \mathbf{s}_i \\ & \times (k_i(\mathbf{x}_i(\tau) + \mathbf{r}_i(\tau)) + c_i(\dot{\mathbf{x}}_i(\tau) + \dot{\mathbf{r}}_i(\tau))) d\tau, \end{aligned} \quad (23)$$

where matrix $\dot{\mathbf{H}}_i^v(t)$ consists of the corresponding velocity impulse response.

Then, given damage extents and the moving vehicle parameters, the moving excitation $p_i(t)$, and virtual distortions $\kappa_{ij}^0(t)$, can be computed by solving the combined equations (6), (19), (20), (21), (22), and (23), where the relevant impulse matrices of the intact bridge and of the vehicles are required. Then, substitute excitation $p_i(t)$ and virtual distortions $\kappa_{ij}^0(t)$ into (17); the responses of the damaged structure can be rapidly computed.

3.3. Discretization. In applications, the responses are usually measured or obtained by numerical simulation and are thus discrete. Collect the dynamic responses $y_\alpha(t)$ for all the time steps and arrange them in a certain sequence, and the discrete matrix form of (17) becomes

$$\mathbf{y} = \mathbf{D}^m \mathbf{p} + \mathbf{D}^\kappa \boldsymbol{\kappa}^0, \quad (24)$$

where vectors \mathbf{y} , \mathbf{p} , $\boldsymbol{\kappa}^0$, respectively, consist of the discrete responses (of all the considered sensors), discrete excitations, discrete virtual distortions (of all the damaged elements) for all time steps, and thus they are of respective lengths $n_a n_t$, $2n_m n_t$, and $n_d n_t$, where n_t denotes the measured time step, and n_a denotes the number of sensors, and n_d denotes the considered number of virtual distortions. Matrices \mathbf{D}^m and \mathbf{D}^κ are block matrices and, respectively, consist of the corresponding discrete integral operators in (17) with lower-triangular $n_t \times n_t$ blocks. Thereinto, the submatrix of \mathbf{D}^κ is Toeplitz matrix.

Similarly, the discrete response \mathbf{x} , $\dot{\mathbf{x}}$ and the discrete distortions $\boldsymbol{\kappa}$ depend on the discrete excitation \mathbf{p} and discrete virtual distortions $\boldsymbol{\kappa}^0$ in the following way:

$$\begin{bmatrix} \mathbf{x} \\ \dot{\mathbf{x}} \\ \boldsymbol{\kappa} \end{bmatrix} = \begin{bmatrix} \mathbf{D}^{mm} & \mathbf{D}^{mk} \\ \dot{\mathbf{D}}^{mm} & \dot{\mathbf{D}}^{mk} \\ \mathbf{D}^{km} & \mathbf{D}^{\kappa\kappa} \end{bmatrix} \begin{bmatrix} \mathbf{p} \\ \boldsymbol{\kappa}^0 \end{bmatrix}, \quad (25)$$

which is an aggregated discrete version of (20), (21), and (18).

The discrete version of vehicle vibration in (22) and (23) is as follows:

$$\begin{aligned} \mathbf{Y}^v &= \mathbf{H}^v \mathbf{S} (\mathbf{k}(\mathbf{x} + \mathbf{r}) + \mathbf{c}(\dot{\mathbf{x}} + \dot{\mathbf{r}})), \\ \dot{\mathbf{Y}}^v &= \dot{\mathbf{H}}^v \mathbf{S} (\mathbf{k}(\mathbf{x} + \mathbf{r}) + \mathbf{c}(\dot{\mathbf{x}} + \dot{\mathbf{r}})), \end{aligned} \quad (26)$$

where $\mathbf{H}^v = \sum_{i=1}^{n_m} \mathbf{I}_i \otimes \mathbf{H}_i^v$, $\mathbf{S} = \sum_{i=1}^{n_m} \mathbf{I}_i \otimes \bar{\mathbf{S}}_i$, $\bar{\mathbf{S}}_i = \mathbf{S}_i \otimes \mathbf{I}_{n_t \times n_t}$, $\mathbf{k} = \sum_{i=1}^{n_m} k_i \hat{\mathbf{I}}_i$, $\mathbf{c} = \sum_{i=1}^{n_m} c_i \hat{\mathbf{I}}_i$, $\hat{\mathbf{I}}_i = \mathbf{I}_i \otimes \mathbf{I}_{2n_t, 2n_t}$, $\mathbf{I}_{2n_t, 2n_t}$ is a unit matrix with dimension $2n_t$. \mathbf{I}_i is a square matrix with dimension n_m , of which only element $\mathbf{I}_i(i, i)$ has value 1, and all other elements have zero values.

Equation (27) shows the expression of discrete excitation \mathbf{p} :

$$\mathbf{p} = \mathbf{k} \mathbf{S}^T \mathbf{Y}^v + \mathbf{c} \mathbf{S}^T \dot{\mathbf{Y}}^v - \mathbf{k}(\mathbf{x} + \mathbf{r}) - \mathbf{c}(\dot{\mathbf{x}} + \dot{\mathbf{r}}) + \mathbf{m} \bar{\mathbf{e}}, \quad (27)$$

where $\mathbf{m} = \sum_{i=1}^{n_m} m_i \hat{\mathbf{I}}_i$, and \mathbf{g} is the vector of Earth's gravities g . $\bar{\mathbf{e}} = [e_1^T, \dots, e_{n_m}^T]^T \otimes \mathbf{I}_{n_t \times 1}$, $\mathbf{e}_i = [e_{ir}/(e_{ir} + e_{il}) \ e_{il}/(e_{ir} + e_{il})]^T$.

Further, the discrete version of (16) is as follows:

$$\boldsymbol{\kappa}^0 = (\mathbf{I} - \boldsymbol{\mu}) \boldsymbol{\kappa}, \quad (28)$$

where $\boldsymbol{\mu}$ is a block diagonal matrix of respective dimensions with diagonal blocks $\mu_i \mathbf{I}_{2n_t, 2n_t}$.

Finally, the previous discrete equations (25), (26), and (27) are combined and generate the following large linear system:

$$\begin{aligned} & \left[\mathbf{I} - \begin{bmatrix} \mathbf{0} & \mathbf{H}_c^v \mathbf{S} \Theta_1 & \mathbf{0} \\ \mathbf{D}_{all}^{mm} \Theta_2 & -\mathbf{D}_{all}^{mm} \Theta_1 & \mathbf{D}_{all}^{mk} (\mathbf{I} - \boldsymbol{\mu}) \\ \mathbf{D}_{km} \Theta_2 & -\mathbf{D}_{km} \Theta_1 & \mathbf{D}_{\kappa\kappa} (\mathbf{I} - \boldsymbol{\mu}) \end{bmatrix} \right] \\ & \times \begin{bmatrix} \mathbf{Y}_{all} \\ \mathbf{x}_{all} \\ \boldsymbol{\kappa} \end{bmatrix} \\ & = \begin{bmatrix} \mathbf{0} \\ \mathbf{D}_{all}^{mm} \\ \mathbf{D}_{km} \end{bmatrix} \bar{\mathbf{e}} + \begin{bmatrix} \mathbf{H}_c^v \mathbf{S} \\ -\mathbf{D}_{all}^{mm} \\ -\mathbf{D}_{km} \end{bmatrix} \Theta_1 \mathbf{r}_{all} dy, \end{aligned} \quad (29)$$

where $\mathbf{H}_c^v = [(\mathbf{H}^v)^T \ (\dot{\mathbf{H}}^v)^T]^T$, $\Theta_1 = [\mathbf{k} \ \mathbf{c}]$, $\mathbf{Y}_{all} = [(\mathbf{Y}^v)^T \ (\dot{\mathbf{Y}}^v)^T]^T$, $\mathbf{D}_{all}^{mm} = [(\mathbf{D}^{mm})^T \ (\dot{\mathbf{D}}^{mm})^T]^T$, $\mathbf{D}_{all}^{mk} = [(\mathbf{D}^{mk})^T \ (\dot{\mathbf{D}}^{mk})^T]$, $\Theta_2 = [\mathbf{k} \mathbf{S}^T \ \mathbf{c} \mathbf{S}^T]$, $\mathbf{x}_{all} = [\mathbf{x}^T \ \dot{\mathbf{x}}^T]^T$, $\mathbf{r}_{all} = [\mathbf{r}^T \ \dot{\mathbf{r}}^T]^T$.

The block matrices in (29) store all the necessary information about the dynamics of the systems and are independent of the damage. Thus, given the values of the moving vehicle parameters m_i , v_i , c_i and the extent of the damage μ_i , the

system (29) can be quickly assembled and then solved to obtain the moving excitations and virtual distortions, which can then be used in (24) to compute the response of the damaged structure to the moving vehicles.

However, in application there are different vehicles passing over any given bridge, and it was necessary to set up the corresponding impulse frequency matrix of the vehicle(s), \mathbf{H}_c^v in (29), repeatedly. Based on the reanalysis concept of VDM, the problem can be improved. Denote \tilde{m}_i , \tilde{J}_i , \tilde{k}_i , \tilde{c}_i as the initial vehicle system parameters of the i th moving vehicle, and denote μ_i^m , μ_i^J , μ_i^k , μ_i^c , respectively, as the ratios between the actual, and initial, values; that is,

$$\begin{aligned} m_i &= \mu_i^m \tilde{m}_i, & J_i &= \mu_i^J \tilde{J}_i, \\ k_i &= \mu_i^k \tilde{k}_i, & c_i &= \mu_i^c \tilde{c}_i. \end{aligned} \quad (30)$$

Substitute (30) into (2), and shift the modified counterpart compared to the initial vehicle value to obtain

$$\begin{aligned} \tilde{\mathbf{m}}_i^v \ddot{\mathbf{Y}}_i^v(t) &+ \tilde{c}_i \mathbf{e}_{ik} \dot{\mathbf{Y}}_i^v(t) + \tilde{k}_i \mathbf{e}_{ik} Y_i^v(t) \\ &= \mu_i^k \tilde{k}_i S_i(x_i(t) + r_i(t)) + \mu_i^c \tilde{c}_i S_i(\dot{x}_i(t) + \dot{r}_i(t)) \\ &\quad + (\mathbf{I} - \mu_i^{mJ}) \tilde{\mathbf{m}}_i^v \ddot{\mathbf{Y}}_i^v(t) + (1 - \mu_i^c) \tilde{c}_i \mathbf{e}_{ki} \dot{\mathbf{Y}}_i^v(t) \\ &\quad + (1 - \mu_i^k) \tilde{k}_i \mathbf{e}_{ki} Y_i^v(t), \end{aligned} \quad (31)$$

where $\mu_i^{mJ} = \text{diag}[\mu_i^m \mu_i^J]$.

Then, through the use of the impulse response matrix of the initial vehicle system $\tilde{\mathbf{H}}^v$, the vibration of the vehicle can be reformulated as follows:

$$\begin{aligned} \mathbf{Y}^v &= \tilde{\mathbf{H}}^v \mathbf{S}(\mu^k \tilde{\mathbf{k}}(\mathbf{x} + \mathbf{r}) + \mu^c \tilde{\mathbf{c}}(\dot{\mathbf{x}} + \dot{\mathbf{r}})) \\ &\quad + \tilde{\mathbf{H}}^v (\mathbf{I} - \mu^{mJ}) \tilde{\mathbf{m}}_{mJ} \ddot{\mathbf{Y}}^v \\ &\quad + \tilde{\mathbf{H}}^v \mathbf{S}_e ((\mathbf{I} - \mu^k) \tilde{\mathbf{k}} \mathbf{Y}^v + (\mathbf{I} - \mu^c) \tilde{\mathbf{c}} \dot{\mathbf{Y}}^v), \end{aligned} \quad (32)$$

where matrices $\tilde{\mathbf{k}}$, $\tilde{\mathbf{c}}$, $\tilde{\mathbf{m}}$ have a similar form to matrices \mathbf{k} , \mathbf{c} , \mathbf{m} , as did μ^k , μ^c , and μ^m . $\tilde{\mathbf{m}}_{mJ} = \sum_{i=1}^{n_m} \mathbf{I}_i \otimes \tilde{\mathbf{m}}_i^v$, $\tilde{\mathbf{m}}_i^v = \tilde{\mathbf{m}}_i^v \otimes \mathbf{I}_{n_t n_t}$, $\mathbf{S}_e = \sum_{i=1}^{n_m} \mathbf{I}_i \otimes \mathbf{S}_{ei}$, $\mathbf{S}_{ei} = \mathbf{e}_{ik} \otimes \mathbf{I}_{n_t n_t}$, $\mu^{mJ} = \sum_{i=1}^{n_m} \mathbf{I}_i \otimes \mu_i^{mJ}$.

Meanwhile, if $\tilde{\mathbf{H}}^v$, in (32), is replaced by $\tilde{\mathbf{H}}^v$, it yields the expression for $\dot{\mathbf{Y}}^v$ and using the reformulated expression for the vehicle vibration \mathbf{Y}^v and $\dot{\mathbf{Y}}^v$, (29) becomes

$$\begin{aligned} \left[\mathbf{I} - \left[\begin{array}{cc} \tilde{\mathbf{H}}_{all} \mathbf{I}_2 \mathbf{S}_{em} (\mathbf{I} - \mu^{kcm}) & \tilde{\mathbf{H}}^v \mathbf{S} \Theta_1 \mu^{kc} \\ \mathbf{D}_{all}^{mm} \Theta_2 \mu^{kcm} & -\mathbf{D}_{all}^{mm} \Theta_1 \mu^{kc} \mathbf{D}_{all}^{mk} (\mathbf{I} - \mu) \\ \mathbf{D}_{km} \Theta_2 \mu^{kcm} & -\mathbf{D}_{km} \Theta_1 \mu^{kc} \mathbf{D}_{kk} (\mathbf{I} - \mu) \end{array} \right] \right] \\ \times \begin{bmatrix} \mathbf{Y}^v_{all} \\ \mathbf{x}_{all} \\ \boldsymbol{\kappa} \end{bmatrix} = \begin{bmatrix} 0 \\ \mathbf{D}_{all}^{mm} \\ \mathbf{D}_{km} \end{bmatrix} \mu^m \tilde{\mathbf{m}} \bar{\mathbf{g}} + \begin{bmatrix} \tilde{\mathbf{H}}^v \mathbf{S} \\ -\mathbf{D}_{all}^{mm} \\ -\mathbf{D}_{km} \end{bmatrix} \Theta_1 \mu^{kc} \mathbf{r}_{all}, \end{aligned} \quad (33)$$

where $\tilde{\mathbf{H}}_{all}^{mm} = \text{diag}[\tilde{\mathbf{H}}^v \tilde{\mathbf{H}}^v]$, $\mathbf{S}_{em} = \text{diag}[\mathbf{S}_e \tilde{\mathbf{k}} \mathbf{S}_e \tilde{\mathbf{m}}_{mJ}]$, $\mu^{kcm} = \text{diag}[\mu^k \mu^c \mu^{mJ}]$, $\mu^{kc} = \text{diag}[\mu^k \mu^c]$, $\mathbf{I}_2 = \text{one}(2) \otimes \mathbf{I}_{2n_m n_t}$.

Equation (33), like (29), is a large linear system with full rank, and its solution is well conditioned. There, the block matrices, such as the related *influence matrix* or initial system matrices, are generated by the FE model, which is noiseless and only needs to compute once for each set of moving vehicle and damage parameters. Therefore, it provides a fast reanalysis approach to the estimation of the dynamic responses and the moving excitation, which makes the optimisation of the structural damage identification and vehicle parameters feasible.

4. Identification of Moving Vehicles and Damages

The analysis in Section 2.3 shows that the coupled vehicle-bridge system is time variant, and the response is nonstationary. Time-domain analysis is the proper identification of unknown structural systems and moving vehicles.

4.1. Objective Function and the Optimization Variables. Equation (24) shows that the dynamic response of the damaged bridge was a function of the moving excitation and virtual distortions, which were in a one-to-one correspondence to the moving vehicle parameters and structural damage. Thus, here the inverse problem of identification of unknown vehicle and damage extent was stated as an optimisation problem involving the minimisation of the normalised mean-square distance between the measured structural response \mathbf{y}^M and the computed response \mathbf{y} . The optimisation variables are the modifying factors of vehicle parameters μ_i^m , μ_i^J , μ_i^k , μ_i^c , and damage extent μ_i which takes advantage of two aspects: on one hand, the magnitudes of the adopted optimisation variables were much less than the magnitudes between the vehicle parameters and bridge damage extents, for the latter can seriously impair the accuracy of many optimisation procedures: the damage extents μ_i belong to the interval $[0, 1]$, but the vehicle parameters might be as large as tens of tonnes, and so forth. Moreover, this makes the direct adoption of (33) to obtain the moving excitation and dynamic response of the damaged bridge to given optimisation variables with the prerequisite of the initial system matrices which only are computed once.

Therefore, the initial vehicle parameters were firstly computed using the measured responses of the damaged structure while assuming that the bridge was intact and was under the action of moving excitations which equal the weight forces of the vehicles with initial mass \tilde{m}_i , for which the corresponding responses equal the measured responses, therefore giving rise to the following expression:

$$\mathbf{y}^M = \mathbf{D}^m \tilde{\mathbf{m}} \mathbf{g}, \quad (34)$$

where \mathbf{y}^M and \mathbf{g} are known, and matrix \mathbf{D}^m can be constructed using the intact bridge system, matrix vector $\tilde{\mathbf{m}}$ consisting of \tilde{m}_i is the unknown to be solved. For the number of the required sensors is bigger than the number of vehicles, (34) is an overdetermined system and the initial mass \tilde{m}_i can be computed via the least-square method.

Then, the rest of the initial parameters for the vehicles are determined by their empirical relationships to the vehicles' masses. Given the initial parameters, the optimisation variables can be represented by the following dimensionless variables μ_i^* ($i = 1, \dots, 4n_m + n_e$), n_e is the number of the potential damaged elements. Denote $i = 4(j-1) + j_m$, there is

$$\mu_i^* = \begin{cases} \mu_j^m & \text{if } j \leq n_m, j_m = 1 \\ \mu_j^j & \text{if } j \leq n_m, j_m = 2 \\ \mu_j^k & \text{if } j \leq n_m, j_m = 3 \\ \mu_j^c & \text{if } j \leq n_m, j_m = 4 \\ \mu_{i-4n_m} & \text{if } j > n_m. \end{cases} \quad (35)$$

All the optimization variables μ_i^* are of the same magnitude and have the natural initial value of 1 for the optimization. The objective function is thus built as

$$\begin{aligned} \text{minimize} \quad & f(\mu_1^*, \dots, \mu_{4n_m+n_e}^*) = \frac{1}{2} \frac{\|\mathbf{y}^M - \mathbf{y}\|^2}{\|\mathbf{y}^M\|^2} \\ \text{subject to} \quad & \mu_i^* \geq 0, \quad i = 1, \dots, 4n_m + n_e, \end{aligned} \quad (36)$$

where \mathbf{y} is the computed response of the structure to the given optimization variables by (35), (33), (27), and (28).

4.2. Sensitivity Analysis. For the optimization of the objective function (36), it can be performed quickly using the gradient-based algorithms provided that the gradient can be computed at a reasonable cost. The formulation based on (24), (27), (28), and (33) allows the discrete adjoint method to be used, which is quicker by one order of magnitude compared with the standard differentiation method [28].

Denote $\mathbf{D} = [\mathbf{D}^{mm} \quad \mathbf{D}^\kappa]$, $\Lambda = [\mathbf{P}^T \quad (\kappa^0)^T]^T$; then the first derivative of (36) with respect to the variable μ_i^* is stated as

$$f_i = -\frac{(\mathbf{y}^M - \mathbf{y})^T}{\|\mathbf{y}^M\|^2} \mathbf{D} \Lambda_i. \quad (37)$$

Here and below, the subscript i in each variable stands for its first derivative to the variable μ_i^* .

In order to obtain the expression of Λ_i , (27) is firstly reformulated as follows:

$$\mathbf{p} = \Gamma_1 \mathbf{z}_1 + \mathbf{w}, \quad (38)$$

where $\Gamma_1 = [\mathbf{kS}^T \quad \mathbf{cS}^T \quad -\mathbf{k} \quad -\mathbf{c}]$, $\mathbf{z}_1 = [(\mathbf{Y}^v)^T \quad (\dot{\mathbf{Y}}^v)^T \quad \mathbf{x}^T \quad \dot{\mathbf{x}}^T]^T$, $\mathbf{w} = -\mathbf{kr} - \mathbf{cr} + \bar{\mathbf{m}}\mathbf{g}$. Then

$$\mathbf{p}_i = \Gamma_1 \mathbf{z}_{1i} + \Gamma_{1i} \mathbf{z}_1 + \mathbf{w}_i. \quad (39)$$

Equation (28) is differentiated to obtain

$$(\kappa^0)_i = \Gamma_2 \kappa_i + \Gamma_{2i} \kappa, \quad (40)$$

where $\Gamma_2 = \mathbf{I} - \boldsymbol{\mu}$.

The combination of (39) and (40) generates the following expression:

$$\Lambda_i = \Gamma \mathbf{z}_i + \Omega_i, \quad (41)$$

where $\mathbf{z} = [(\mathbf{Y}^v)^T \quad \mathbf{x}^T \quad \boldsymbol{\kappa}^T]^T$, $\Gamma = \text{diag}[\Gamma_1 \quad \Gamma_2]$, $\Omega_i = [\Gamma_{1i} \mathbf{z}_1] [(\Gamma_{1i} \mathbf{z}_1 + \mathbf{w}_i)^T \quad (\Gamma_{2i} \boldsymbol{\kappa})^T]^T$.

Vector \mathbf{z} represents the parameters in (33) required to be solved. By reformulating (33) as the form $\mathbf{Az} = \mathbf{b}$, the first derivative \mathbf{z}_i satisfies the following relationship:

$$\mathbf{Az}_i = \mathbf{b}_i - \mathbf{A}_i \mathbf{z}. \quad (42)$$

Substitute (41) into (37); there is

$$f_i = -\frac{(\mathbf{y}^M - \mathbf{y})^T}{\|\mathbf{y}^M\|^2} \mathbf{D} \Gamma \mathbf{z}_i - \frac{(\mathbf{y}^M - \mathbf{y})^T}{\|\mathbf{y}^M\|^2} \mathbf{D} \Omega_i \quad (43)$$

which includes the first derivatives \mathbf{z}_i . The discrete adjoint method adds the scalar product of the adjoint vector λ with (42) to (43), to obtain

$$\begin{aligned} f_i = & \lambda^T (\mathbf{b}_i - \mathbf{A}_i \mathbf{z}) - \frac{(\mathbf{y}^M - \mathbf{y})^T}{\|\mathbf{y}^M\|^2} \mathbf{D} \Omega_i \\ & + \left(\lambda^T \mathbf{A} - \frac{(\mathbf{y}^M - \mathbf{y})^T}{\|\mathbf{y}^M\|^2} \mathbf{D} \Gamma \right) \mathbf{z}_i. \end{aligned} \quad (44)$$

In this way, the gradient of the objective function can be expressed as

$$f_i = \lambda^T (\mathbf{b}_i - \mathbf{A}_i \mathbf{z}) - \frac{(\mathbf{y}^M - \mathbf{y})^T}{\|\mathbf{y}^M\|^2} \mathbf{D} \Omega_i, \quad (45)$$

where the adjoint vector λ is computed only at the cost of a single solution of the adjoint equation

$$\mathbf{A}^T \lambda = \Gamma^T \mathbf{D}^T \frac{(\mathbf{y}^M - \mathbf{y})}{\|\mathbf{y}^M\|^2}. \quad (46)$$

4.3. Remarks. If a small number of time steps are used, then the system matrix in (33) can be computed and used directly. However, for offline identification, in the case of a dense time discretization or a longer sampling time, the system can become prohibitively large and computationally hardly manageable. To reduce the numerical costs, the system matrix, which is a block matrix composed of lower triangular matrices, can be rearranged into a lower triangular block form; then the system can be solved by a specialized linear solver, like block forward substitution [29]. Due to the fact that all the data in the system (33) are computed based on the ideal FEM model and are away from any measurement noise pollution, the unknown vectors can be computed stepwise precisely.

If the bridge is undamaged, the virtual distortions in (24) vanish; that is, the value of damage extent equals one in related Equations, and the proposed method can be also used for identification of moving vehicles only.

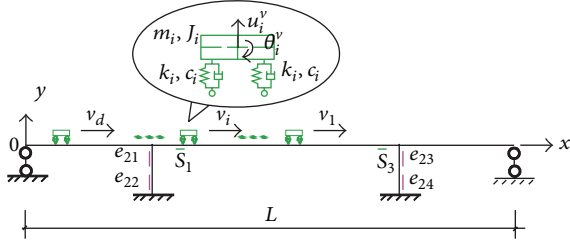


FIGURE 3: The vehicle-bridge coupled system.

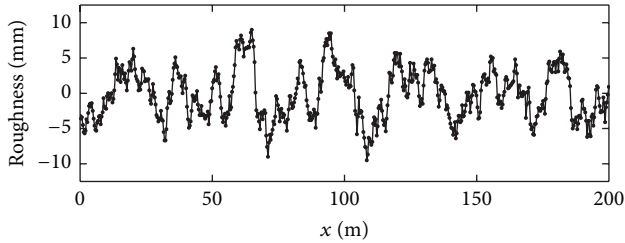


FIGURE 4: The road surface roughness.

5. Numerical Example

A multispan frame was used to illustrate and verify the proposed methods for simultaneous identification of moving vehicles and damage. Measurement error and model error were taken into account to test the robustness of the method.

5.1. Structural and Moving Vehicles. The frame, shown in Figure 3, is made of steel with Young's modulus 2.15×10^{11} Pa, and a density of 7.8×10^3 kg/m³. It has a uniform mass distribution of 15.3×10^3 kg/m³. The beam is 200 m long with a simplified rectangular cross-section of $b \times h = 0.89$ m \times 2.21 m, so that the inertial moment of the area is 0.8 m⁴; each of the two side spans is 50 m. Each pier is 20 m high with inertial moment of 0.16 m⁴.

The road surface condition is considered to be good, and the roughness coefficient $G_d(n_0)$ is 16×10^{-6} m³. According to the vehicle velocity, $n_l = 0.0221$ m⁻¹, $n_u = 1.4142$ m⁻¹; then the length of the shortest effective pavement is $1/n_l = 45.25$ m, so the effective pavement can be the whole length of the bridge. In this way, $\Delta n = 1/L = 0.01$ m⁻¹, $N_T = \text{fix}((n_u - n_l)/\Delta n) = 278$. Figure 4 shows the simulated road surface roughness via (3).

Two moving vehicles passed through the bridge from opposite direction, with respective constant velocities $v_1 = 34$ m/s, $v_2 = -30$ m/s. A two-axle, two-DOF, vehicle model was adopted. The vehicle masses were $m_1 = 61.2 \times 10^3$ kg, $m_2 = 53 \times 10^3$ kg. The other vehicle parameters such as the rotary inertia, stiffness, and damping are provided by multiplying the vehicle mass by a certain coefficient according to the literature [30]. The rest of the parameters of the two vehicles were defined, respectively, as $k = 396$ m N/m, $c = 1.4$ m N · s/m; the rotary inertia $J = 9$ m kg · m². The distance between the centre of mass and either of the two axles was 3 m. Denoted by $x_{1,0} = -3$ m, $x_{2,0} = 204$ m,

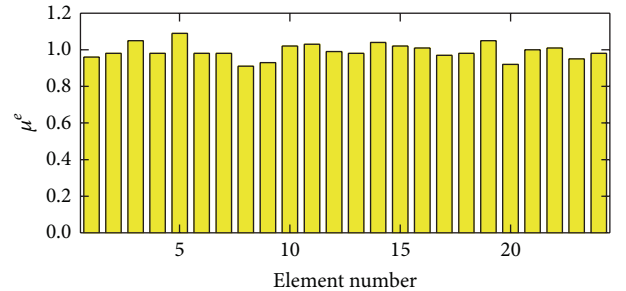


FIGURE 5: Stiffness reduction levels of the elements.

respectively, were the initial centroidal points of each vehicle's mass.

Two sensors are employed: S_1 at the location of 65.2 m and S_2 at the location 145.2 m as shown in Figure 3. The sensors are placed at bottom surface of the beam.

5.2. Identification Cases. For the identification purpose, the beam is divided into 20 elements, and each of the piers is divided into two elements. Measurements are simulated with an uncorrelated Gaussian noise. Besides the measurement error, the influence of the model error is tested by using a different finite element (FE) model of the structure; that is, the theoretical FE model of the intact structure is modified as the actual intact structure.

Two following identification cases are discussed.

Case 1. Measurement error is simulated at 5% RMS level. No model error is assumed. Assume that two pier elements (Nos. 21 and 23) are damaged with the damage extents $\mu_{21} = 0.4$ and $\mu_{23} = 0.7$.

Case 2. As in Case 1, but the model error is additionally simulated. It considers the modification of the stiffness of all the elements. More precisely, uncorrelated Gaussian modifications with mean -2% and standard deviation 5% are used; see Figure 5, for the stiffness modifications. Then, the actual damage extents are slightly different from that listed in case 1, which include the model error besides the real damage.

In both of the two cases, it was assumed that the damage location was limited to the four pier elements. Two moving vehicles were identified simultaneously as being causally linked to the extent of the damage. Four stiffness modification coefficients were used in the optimisation, besides the eight variables related to the masses, rotary moments, stiffness, and damping of the two vehicles. In this way, the damage extent and its location, as well as vehicle parameters, were treated as unknowns and thus identified. Meanwhile, the dynamic interaction of the coupled vehicle-bridge system was established.

5.3. Moving Vehicle and the Damage Identification. Responses of the two sensors are used for vehicle and damage identification. In each case, the dynamic responses are calculated using the discrete FE model and the Newmark integration

TABLE 1: The first eight natural frequencies of the original and damaged bridge model (Hz).

	ω_1	ω_2	ω_3	ω_4	ω_5	ω_6	ω_7	ω_8
Original model	5.023	5.707	14.432	17.279	20.6	35.324	53.397	59.437
Damaged model	4.552	5.526	13.958	17.054	20.56	35.036	52.782	58.606

TABLE 2: Identified parameters of moving vehicles in Case 1.

	m_1 (kg)	J_1 (kg·m ²)	k_1 (N/m)	c_1 (N·s/m)	m_2 (kg)	J_2 (kg·m ²)	k_2 (N/m)	c_2 (N·s/m)
Actual value	6.12×10^4	5.51×10^5	2.42×10^7	8.57×10^4	5.30×10^4	4.77×10^5	2.10×10^7	7.42×10^4
Trial value	7.00×10^4	4.20×10^5	3.50×10^7	7.00×10^4	6.33×10^4	3.80×10^5	3.16×10^7	6.33×10^4
Identified μ	0.88	1.33	0.7	1.32	0.84	1.38	0.67	1.24
Identified value	6.18×10^4	5.58×10^5	2.44×10^7	9.25×10^4	5.35×10^4	5.23×10^5	2.12×10^7	7.84×10^4
Identified error (%)	0.97	1.39	0.59	8.01	0.86	9.62	0.79	5.59

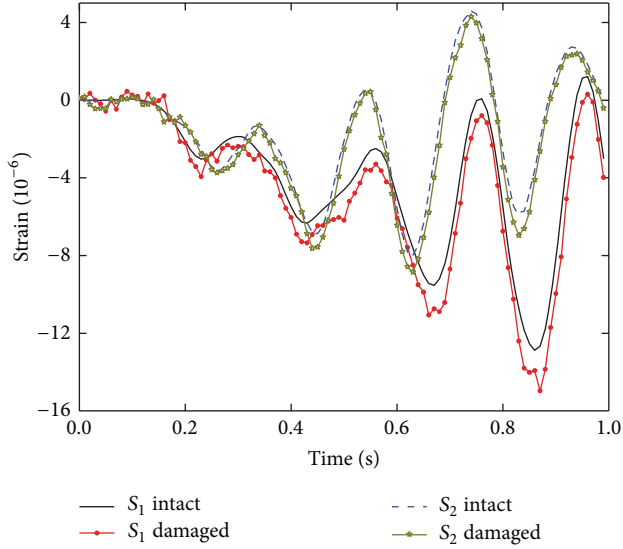


FIGURE 6: Simulated strain responses of the damaged and the intact structure in Case 1 with measurement noise at 5% RMS level.

method with the parameters $\alpha = 0.25$ and $\beta = 0.5$. The first two damping ratios are 0.01 and 0.015. The integration time step equals 0.01 s (100 Hz sampling frequency). A total of 100 time steps is used; hence, the measured time is 1 s. The simulated responses with measurement noise in Case 1 are shown in Figure 6. Table 1 shows the natural frequencies of the original and damaged bridge model.

The damage was limited to the two piers, that is, to the four pier elements. Together with two known vehicles (eight modification coefficients), there were twelve variables to be optimised by minimising the objective function (36). Responses from two sensors were used for this purpose. The initial trial mass values were estimated using (34). Then, the other initial vehicle parameters were provided based on their masses.

The identification results for the two vehicle parameters are listed, respectively, in Table 2 (Case 1) and Table 3 (Case 2).

The identified extents of the structural damages in the two cases are listed, respectively, in Table 4 (Case 1) and Table 5 (Case 2).

The parameter identification results were assessed by their relative accuracy, while the damage identification results were more naturally assessed in terms of their absolute accuracy. It showed that, even with all the simulated errors, the parameters of the two vehicles and four potential damage identifiers could be identified acceptably. Since only two damages were actually assumed, the optimisation allowed their number and location (limited to the four considered pier elements) to be identified as well.

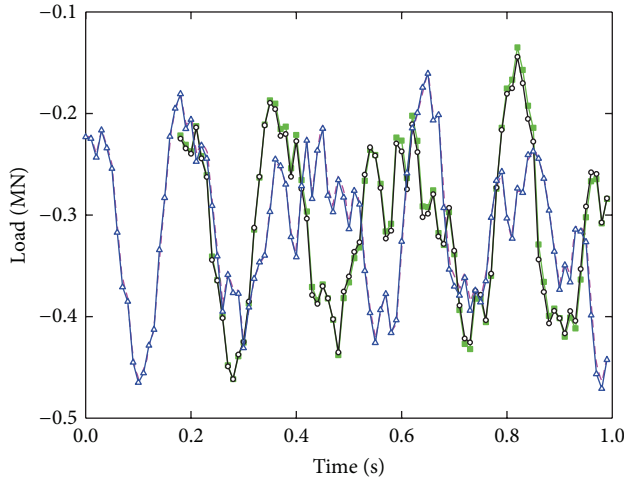
With the identified vehicles and structural damage, the moving loads can be computed meanwhile by using (27). Figure 7 shows the estimated results which have reasonable accuracy. The relative error was 2.6% even under both 5% RMS measurement noise and model error in Case 2.

6. Conclusion

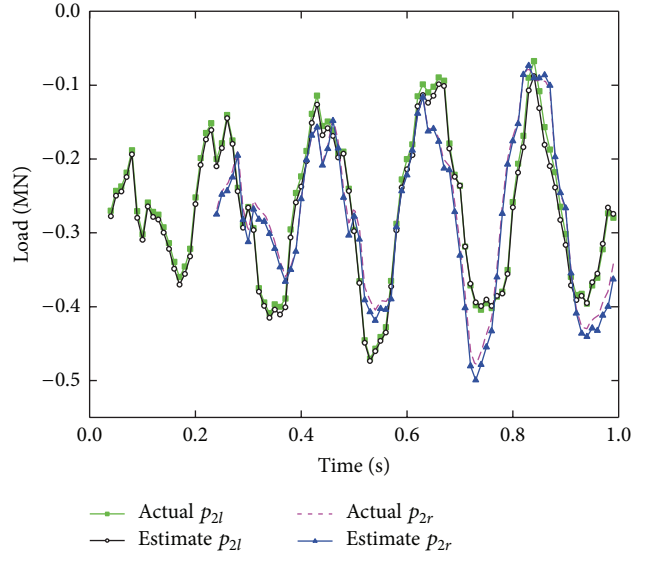
This paper presented an effective method for the simultaneous identification of moving vehicles and structural damage based on a virtual distortion method. The vehicle parameters and the structural damage were treated as optimisation variables. Through the use of a moving dynamic influence matrix, the response of the damaged system to given optimisation variables could be computed quickly without the need of a numerical simulation and the repeated assembly of the time-variant system parameter matrix at each time-step. This reduced the numerical cost significantly. The adjoint method was adopted for the fast sensitivity analysis of the objective function. A numerical example of a three-span beam was presented to verify the proposed method, where two vehicles (eight variables) and two damaged piers (four damage instances) were identified using only two sensors. Even with both the pollution of 5% RMS measurement error

TABLE 3: Identified parameters of moving vehicles in Case 2.

	m_1 (kg)	J_1 ($\text{kg}\cdot\text{m}^2$)	k_1 (N/m)	c_1 (N·s/m)	m_2 (kg)	J_2 ($\text{kg}\cdot\text{m}^2$)	k_2 (N/m)	c_2 (N·s/m)
Actual value	6.12×10^4	5.51×10^5	2.42×10^7	8.57×10^4	5.30×10^4	4.77×10^5	2.10×10^7	7.42×10^4
Trial value	6.96×10^4	4.18×10^5	3.48×10^7	6.96×10^4	6.38×10^4	3.83×10^5	3.19×10^7	6.38×10^4
Identified μ	0.89	1.3	0.7	1.35	0.85	1.37	0.67	1.26
Identified value	6.16×10^4	5.44×10^5	2.44×10^7	9.41×10^4	5.45×10^4	5.23×10^5	2.14×10^7	8.02×10^4
Identified error (%)	0.7	1.29	0.79	9.79	2.82	9.66	2.05	8.07



(a) Moving loads of vehicle 1



(b) Moving loads of vehicle 2

FIGURE 7: Identified moving loads.

TABLE 4: Identified extents of the damages in Case 1.

	μ_{21}	μ_{22}	μ_{23}	μ_{24}
Actual value	0.400	1.000	0.700	1.000
Identified value	0.454	0.930	0.709	0.965
Identified error (%)	13.50	7.00	1.29	3.5

TABLE 5: Identified extents of the damages in Case 2.

	μ_{21}	μ_{22}	μ_{23}	μ_{24}
Actual value	0.398	1.004	0.666	0.977
Identified value	0.453	0.908	0.755	0.990
Identified error (%)	13.82	9.56	13.36	1.33

and a certain model error, the maximum identification error was 13.82%. Moreover, the moving excitation effects were estimated accurately.

Acknowledgments

The authors gratefully acknowledge the support of National Science Foundation of China (NSFC) (51108066, 51108067), of the Fundamental Research Funds for the Central Universities (China) (DC13010316), of the Dr. Start-up fund of Dalian

Nationalities University (20116207), and of the Project of Housing and Urban-Rural Development (K2201243, 2013-k2-7). Financial support of Structural Funds in the Operational Programme-Innovative Economy (IE OP) financed from the European Regional Development Fund-Project “Modern material technologies in aerospace industry” (POIG.0101.02-00-015/08) is gratefully acknowledged.

References

- [1] S. W. Doebling, C. R. Farrar, M. B. Prime, and D. W. Shevitz, “Damage identification and health monitoring of structural and mechanical system from changes in their characteristics: a literature review,” Tech. Rep., Los Alamos National Laboratory, Los Alamos, NM, USA, 1996.
- [2] J. Li, M. Su, and L. Fan, “Natural frequency of railway girder bridges under vehicle loads,” *Journal of Bridge Engineering*, vol. 8, no. 4, pp. 199–203, 2003.
- [3] K. -C. Chang, C. -W. Kim, and M. Kawatani, “Feasibility investigation for a bridge damage identification method through moving vehicle laboratory experiment,” *Structure and Infrastructure Engineering*, 2013.
- [4] L. Majumder and C. S. Manohar, “Nonlinear reduced models for beam damage detection using data on moving oscillator-beam interactions,” *Computers and Structures*, vol. 82, no. 2–3, pp. 301–314, 2004.

- [5] R. Sieniawska, P. Śniady, and S. Zukowski, "Identification of the structure parameters applying a moving load," *Journal of Sound and Vibration*, vol. 319, no. 1-2, pp. 355–365, 2009.
- [6] C.-W. Kim and M. Kawatani, "Pseudo-static approach for damage identification of bridges based on coupling vibration with a moving vehicle," *Structure and Infrastructure Engineering*, vol. 4, no. 5, pp. 371–379, 2008.
- [7] X. Ling and A. Haldar, "Element level system identification with unknown input with Rayleigh damping," *Journal of Engineering Mechanics*, vol. 130, no. 8, pp. 877–885, 2004.
- [8] L. Yu and T. H. T. Chan, "Recent research on identification of moving loads on bridges," *Journal of Sound and Vibration*, vol. 305, no. 1-2, pp. 3–21, 2007.
- [9] S. S. Law, T. H. T. Chan, and Q. H. Zeng, "Moving force identification: a time domain method," *Journal of Sound and Vibration*, vol. 201, no. 1, pp. 1–22, 1997.
- [10] S. S. Law, T. H. T. Chan, and Q. H. Zeng, "Moving force identification—a frequency and time domains analysis," *Journal of Dynamic Systems, Measurement and Control*, vol. 121, no. 3, pp. 394–401, 1999.
- [11] T. Chan and C. O'Connor, "Wheel loads from highway bridge strains: field studies," *Journal of Structural Engineering*, vol. 116, no. 7, pp. 1751–1771, 1990.
- [12] S. S. Law, T. H. T. Chan, and Q. H. Zeng, "Moving force identification: a time domain method," *Journal of Sound and Vibration*, vol. 201, no. 1, pp. 1–22, 1997.
- [13] T. H. T. Chan, L. Yu, S. S. Law, and T. H. Yung, "Moving force identification studies, II: comparative studies," *Journal of Sound and Vibration*, vol. 247, no. 1, pp. 77–95, 2001.
- [14] X. Q. Zhu and S. S. Law, "Moving load identification on multi-span continuous bridges with elastic bearings," *Mechanical Systems and Signal Processing*, vol. 20, no. 7, pp. 1759–1782, 2006.
- [15] T. Pinkaew, "Identification of vehicle axle loads from bridge responses using updated static component technique," *Engineering Structures*, vol. 28, no. 11, pp. 1599–1608, 2006.
- [16] T. Pinkaew and P. Asnachinda, "Experimental study on the identification of dynamic axle loads of moving vehicles from the bending moments of bridges," *Engineering Structures*, vol. 29, no. 9, pp. 2282–2293, 2007.
- [17] R. J. Jiang, F. T. K. Au, and Y. K. Cheung, "Identification of vehicles moving on continuous bridges with rough surface," *Journal of Sound and Vibration*, vol. 274, no. 3–5, pp. 1045–1063, 2004.
- [18] Q. Zhang, Z. Duan, and Ł. Jankowski, "Moving mass identification of vehicle-bridge coupled system based on virtual distortion method," *Chinese Journal of Theoretical and Applied Mechanics*, vol. 43, no. 3, pp. 598–610, 2011.
- [19] K. Zhang, H. Li, Z. Duan, and S. S. Law, "A probabilistic damage identification approach for structures with uncertainties under unknown input," *Mechanical Systems and Signal Processing*, vol. 25, no. 4, pp. 1126–1145, 2011.
- [20] Q. Zhang, Ł. Jankowski, and Z. Duan, "Simultaneous identification of excitation time histories and parametrized structural damages," *Mechanical Systems and Signal Processing*, vol. 33, pp. 56–68, 2012.
- [21] J. Holnicki-Szulc, Ed., *Smart Technologies for Safety Engineering*, John Wiley & Sons, Chichester, UK, 2008.
- [22] X. Q. Zhu and S. S. Law, "Damage detection in simply supported concrete bridge structure under moving vehicular loads," *Journal of Vibration and Acoustics*, vol. 129, no. 1, pp. 58–65, 2007.
- [23] Q. Zhang, Ł. Jankowski, and Z. Duan, "Simultaneous identification of moving masses and structural damage," *Structural and Multidisciplinary Optimization*, vol. 42, no. 6, pp. 907–922, 2010.
- [24] M. Dilena and A. Morassi, "Dynamic testing of a damaged bridge," *Mechanical Systems and Signal Processing*, vol. 25, no. 5, pp. 1485–1507, 2011.
- [25] H. Honda, Y. Kajikawa, and T. Kobori, "Spectra of road surface roughness on bridges," *Journal of the Structural Division*, vol. 108, no. 9, pp. 1956–1966, 1982.
- [26] GB/T7031-2005/ ISO, 8608. (Mechanical Vibration-Road surface profiles-Reporting of measured data. GB/T7031-2005/ ISO, 8608, 1995, (Chinese).
- [27] R. Kress, "Linear integral equations," in *Applied Mathematical Sciences*, vol. 82, Springer, New York, NY, USA, 1989.
- [28] D. I. Papadimitriou and K. C. Giannakoglou, "Aerodynamic shape optimization using first and second order adjoint and direct approaches," *Archives of Computational Methods in Engineering*, vol. 15, no. 4, pp. 447–488, 2008.
- [29] T. Uhl, "The inverse identification problem and its technical application," *Archive of Applied Mechanics*, vol. 77, no. 5, pp. 325–337, 2007.
- [30] G.-G. Sheng, C.-X. Li, and B. Zhao, "Dynamic analysis of a simply-supported beam subjected to moving vehicles," *Engineering Mechanics*, vol. 23, no. 12, pp. 99–158, 2006.

Research Article

Factor of Safety Reduction Factors for Accounting for Progressive Failure for Earthen Levees with Underlying Thin Layers of Sensitive Soils

Adam J. Llobbestael, Adda Athanasopoulos-Zekkos, and Josh Colley

Department of Civil and Environmental Engineering, University of Michigan, 2350 Hayward Street, 1354 GG Brown Laboratory, Ann Arbor, MI 48109, USA

Correspondence should be addressed to Adam J. Llobbestael; ajimlobb@umich.edu

Received 7 August 2013; Accepted 13 October 2013

Academic Editor: Anaxagoras Elenas

Copyright © 2013 Adam J. Llobbestael et al. This is an open access article distributed under the Creative Commons Attribution License, which permits unrestricted use, distribution, and reproduction in any medium, provided the original work is properly cited.

The effects of progressive failure on flood embankments with underlying thin layers of soft, sensitive soils are investigated. Finite element analysis allows for investigation of strain-softening effects and progressive failure in soft and sensitive soils. However, limit equilibrium methods for slope stability analysis, widely used in industry, cannot capture these effects and may result in unconservative factors of safety. A parametric analysis was conducted to investigate the effect of thin layers of soft sensitive soils on the stability of flood embankments. A flood embankment was modeled using both the limit equilibrium method and the finite element method. The foundation profile was altered to determine the extent to which varying soft and sensitive soils affected the stability of the embankment, with respect to progressive failure. The results from the two methods were compared to determine reduction factors that can be applied towards factors of safety computed using limit equilibrium methods, in order to capture progressive failure.

1. Introduction

The design and construction of levee systems are often challenging tasks due to the complex nature of the geologic conditions that typically comprise the site of a levee or flood embankment. This complex geology is the result of the processes of deposition and erosion that take place along coasts and riverbanks. The failure of the 17th Street Drainage Canal in New Orleans, during Hurricane Katrina, illustrates the potentially dangerous effects of thin layers of soft and sensitive material beneath a levee [1, 2], which are often found in such geologic environments. The additional load placed on a levee during a storm surge or high-water event has the potential to initiate progressive failure through the layer of soft, sensitive material, causing the levee to fail.

The importance of strain-softening soils and the role they play in progressive failure and delayed collapse of earthen embankments has long been established [3–5]. The potential for progressive failure to occur arises when strain-softening soils are present. As the levee is loaded with a

rising water level on the water side, shear strains develop beneath the levee in a nonuniform fashion. The peak shear strength throughout the developing sliding surface is not simultaneously mobilized because the shear stresses that develop within sensitive soils are highly strain dependent. This critical mechanism however cannot be captured by limit equilibrium analysis methods, which are widely used in industry for their ease and simplicity but assume that the stress-strain characteristics of soils forming the slope are nonbrittle [6, 7]. The use of peak strengths, therefore, to model sensitive soils results in an overestimation of the available shear strength and thus an overestimation of the slope stability factor of safety, defined as the ratio of available shear strength to the shear strength at slope failure. The alternative approach, using residual shear strengths in design, has proven to result in an underestimation of the factor of safety [8].

The purpose of this study is to determine the extent to which progressive failure in thin layers of soft sensitive soils underlying levees affects the stability of the levee. Parametric

analyses were conducted in which a levee, founded upon medium stiff clay with an embedded thin layer of soft, sensitive clay, was modeled using both limit equilibrium analysis and finite element analysis. The strength parameters of the thin layer of sensitive soil, as well as the thickness of the layer and the location of the layer beneath the levee, were varied to assess the influence of each parameter on levee stability. The results of the two analysis types were compared to derive reduction factors that can be applied toward limit equilibrium analysis factors of safety, in order to capture progressive failure effects.

The potential effects of progressive failure in sensitive soils have been studied and presented in the literature over the past several decades. Bjerrum [9] addressed progressive failure as a potential factor contributing to the vane shear overestimation of undrained shear strength of clay, which then led to embankment failures. Chirapuntu and Duncan [10] suggested that progressive failure may occur if an embankment is stiffer and stronger than its foundation and presented shear strength reduction factors to account for this. Specifically, the potential for progressive failure through thin layers of soft sensitive soil has been recognized [11]. Up until this point, most of the literature focusing on the effects of progressive failure was primarily qualitative and did not offer guidelines as to how to incorporate them into the design process. More recently, Filz et al. [12] studied the effect of progressive failure through thin layers in the context of lined waste impoundments and showed that accounting for progressive failure is critical in the design of such facilities. They proposed shear strength reduction factors for use in limit equilibrium analysis of lined landfills in order to account for progressive failure.

The issue of incorporating strain softening into geomechanics finite element analyses has been addressed by researchers as early as 1972 [13]. One approach to capturing progressive failure in finite-element analysis is to incorporate true strain-softening constitutive models such as those developed by Duncan and Chang [14], Pietruszczak and Mroz [15], Yoshida et al. [16], and Yoshida et al. [17]. These models capture the contraction of the yield surface and reduce the soil strength parameters in accordance with plastic theory. These models are theoretically robust; however they are complex and pose several challenges with regard to their mathematical formulation. Such models suffer from problems such as mesh dependency and difficulty in monitoring convergence as pointed out by numerous researchers such as de Borst et al. [18], Potts and Zdravkovic [19], Zhou and Randolph [20], Wu and Wang [21], and Galavi and Schweiger [22]. Also, these models require a large number of input parameters and therefore extensive calibration. These issues often combine to hinder such constitutive models from being used in practical applications where strain softening is applicable.

An alternative approach followed by Lo and Lee [23] employed an incremental stress release method to approximately capture strain softening in finite element analysis of slopes. In their approach, the strength of individual elements is iteratively reduced based on the strains developed. The stress is then transferred from the overstressed elements to the surrounding elements. Although this method

is approximate, it is relatively simple to implement in terms of the parameters required and the results agree well with field observations. This approach was furthered at the Soil Mechanics Section of Imperial College, London, using the Imperial College Finite Element Program (ICFEP) [24]. The model used for the analysis is a nonlinear strain-softening/hardening model that incorporates a Mohr-Coulomb yield criterion. The model accounts for softening by varying the angle of shearing resistance and cohesion with the calculated deviatoric plastic strain invariant. In this manner, undrained strength is reduced with increasing plastic strain. The model is presented in detail in Potts and Zdravkovic [25]. The approach has been used to analyze numerous documented slope failures (Chingford Embankment, Carsington Dam, Eppingham Dam, Abberton Reservoir, etc.) and hypothetical embankment sections where progressive failure was thought to play a role [24, 26–30]. The results showed good agreement with the field observations and confirmed the validity of the approach. Other authors have followed the approach set out by Dounias et al. [24] and implemented it in “user defined models” in programs such as Plaxis (Gens and Alonso [31]), GeoStudio (Hughes et al. [32], Kelln et al. [33], and Kelln et al. [34]), and TOCHNOG (Troncone [35]). These additional analyses also showed good agreement with field observations further verifying the validity of the approach and confirming the critical effect of progressive failure. This approach has been used extensively and confidence in this approach has grown to the point where it has also been used to predict the likelihood of progressive failure in future projects. For example, this approach was used in a 700 m tall escarpment underwater in the Gulf of Mexico [36] and in the heightening of the Abberton Reservoir embankment [30]. This approach has advantages over true strain-softening models since it is easier to implement and has been shown to achieve a level of accuracy suitable for practical applications.

Some additional recent advances by other researchers include Wu and Wang [21] and Galavi and Schweiger [37] who demonstrated the ability of “nonlocal” approaches as a way of overcoming mesh dependence. Zhou and Randolph [20] investigated large displacement finite element (LDFE) analysis as a way to overcome mesh dependence when modeling cylindrical and spherical penetrometers in strain-softening clays. They made use of remeshing and interpolation technique with small strain (RITSS) implemented in AFENA. Zabala and Alonso [38] successfully modeled progressive failure of the Aznalcóllar Dam using the material point method.

2. Slope Stability Analysis

In order to determine the effects of progressive failure on the stability of a levee with an underlying thin layer of soft sensitive material, slope stability analyses were performed on a series of levee-foundation profiles with each profile being analyzed using both the limit equilibrium analysis method and the finite element analysis method. The profile used in the study is a generic, symmetric levee cross-section constructed on a soft soil foundation. The levee consists of stiff clay with

TABLE 1: Material parameters used in limit equilibrium analyses.

Material	Soil model	γ_{sat} (kN/m ³)	γ_{unsat} (kN/m ³)	Undrained shear strength (kPa)
Embankment	Undrained ($\varphi = 0$)	18.1	16.5	43.1
Foundation clay	Undrained ($\varphi = 0$)	17.6	15.7	Varied: 35.9–47.8 ^a
Thin layer material	Undrained ($\varphi = 0$)	18.1	16.5	Varied: 14.4–19.1 ^a

^aThese strengths were varied throughout the parametric analysis. See Table 3 and Figures 3 and 4 for strengths used within range.

TABLE 2: Material parameters used in finite element analyses.

Material	Soil model	E_{ref} (kPa)	c_{ref} (kPa)	φ (°)	k_h (m/day)	k_v (m/day)
Embankment	Mohr-Coulomb	2215	43.1	0	0.008	0.002
Foundation clay	Mohr-Coulomb	2299	Varied: 35.9–47.8	0	0.08	0.02
Thin layer material	Mohr-Coulomb ^a	Varied ^b	Varied ^b	0	0.08	0.02

^aA stepwise strength reduction scheme was used in conjunction with the Mohr-Coulomb model to capture strain-softening behavior. See the description of this method in Section 2.2.

^bThese strengths were varied throughout the parametric analysis. See Table 3 and Figures 3 and 4 for strengths used within range.

Unit weights used in finite element modeling are equal to those used in limit equilibrium modeling. Refer to Table 1 for values.

a height of 7.6 meters, 3:1 (H : V) slopes, and a 6.1 meter crest width. The foundation soil consists of medium stiff clay, in which a thin layer of soft, sensitive clay is embedded. The depth, at which the thin layer occurs, and the thickness of the layer are two of the parameters varied in the parametric analysis. An example profile from the study is presented in Figure 1. The analyses were conducted using undrained material properties to investigate the short-term behavior of the system under loading by an increase in water level due to a storm surge. For each profile, the factor of safety against slope instability was calculated with the levee under high-water conditions (i.e., water elevation on one side at the levee crest and on the other side at the ground surface and the phreatic surface varying linearly between the toe and the crest as shown in Figure 1).

The limit equilibrium analysis was performed without accounting for the possibility of progressive failure through the thin layer of sensitive soil, that is, assigning peak strength to all soil materials in the embankment foundation. In the finite element analysis an approximate method to capture progressive failure effects was used. Sections 2.1 and 2.2 present the details of the limit equilibrium analyses and the finite element analyses, respectively. Finally, a strain-softening soil model was used in finite difference analysis to perform analysis for validating the simplified finite element approach, as described in Section 6.

2.1. Limit Equilibrium Analysis Modeling. Limit equilibrium analysis (LEA) was performed using the Morgenstern-Price method as implemented in the computer program SLOPE/W [39]. The embankment soil, the thin layer of sensitive clay, and the foundation material above the thin layer were modeled as undrained using a Tresca yield condition ($\varphi_u = 0$). The thin layer of sensitive clay was modeled using the peak undrained shear strength of the material. Preliminary analysis was performed to determine the geometry of the failure surface and showed that the critical failure surface was approximately circular through the upper foundation material and linear along the sensitive clay layer, consistent

with field observations of slope stability failures in New Orleans [2]. This observation was also later confirmed with the finite element analyses. Because a portion of the critical failure surface is expected to progress along the thin layer of sensitive clay, the foundation material underlying the thin layer was modeled as impenetrable. The material properties used to model the soils in the limit equilibrium analyses are presented in Table 1. The range of strengths used for the thin layer material is presented in Section 3.

2.2. Finite Element Analysis Modeling. Finite element analysis (FEA) was performed using the finite element code Plaxis 2D [40]. The levee and foundation materials were modeled as undrained with elastoplastic models. The thin layer of sensitive soil was also modeled as elastoplastic, but an approximated strain-softening approach, described later in this section, was used to capture the effects of progressive rupture. Table 2 summarizes the material properties used to model the soils in the finite element analyses.

Initial stress states were generated using the K_o procedure. Plastic analysis of the levee profile was conducted using staged construction, with the levee being placed in five lifts of equal thickness, followed by an incremental increase in the water level on one side of the levee. The water level remained at the ground surface on the opposite side of the levee throughout the staged construction process. Static pore pressures within the profile were calculated using the phreatic level.

At the expense of some accuracy relative to other strain-softening methods, an approximate method was used in this parametric analysis which is simpler to implement. The approximate method used here avoids several of the mathematical implications of true strain-softening models and requires less input parameters. The method consists of using incremental elasto-plastic models, discussed below, and therefore avoids a negative tangent modulus in the constitutive model which prevents violation of the stability criterion and the mesh sensitivity associated with localization and strain softening. The method is similar to those presented by

Lo and Lee [23] and Potts et al. [26] in its approach at tracking plastic strains and reducing shear strength accordingly.

In order to capture the strain-softening behavior of the sensitive material comprising the thin layer embedded in the foundation, a stepwise strength reduction scheme was employed. The thin layer of sensitive soil was divided into several smaller regions (clusters) to allow for local assignment of strength parameters, as shown in Figure 2. These clusters do not represent elements of the mesh but rather regions in which soil is assigned a single set of shear strength and stiffness parameters.

To capture the strain dependence of the thin layer soil strength, the strain development within the layer was tracked through the staged construction process. The calculation process was paused at the conclusion of each incremental loading in order to investigate the strains developed and accordingly reassign strength parameters to the thin layer regions. Depending on the strains within each cluster, a new strength was assigned which better reflects the “new” peak shear strength and the calculation was allowed to proceed to the next incremental loading. This can essentially be thought of as incrementally replacing the soil in small areas with weaker soil. This captured the effect of progressive rupture in the factor of safety calculation, discussed below, since different levels of shear strength were mobilized along the failure surface.

It is important to emphasize that the assigned clusters do not significantly affect or constrain the formation of the shear surface and potential failure surface. This was assured by comparing shear surfaces with and without the clusters. No differences were observed between the two approaches with respect to the formation of the sliding surface.

Following the strain-based strength reduction process, once the model was allowed to reach equilibrium, factors of safety against levee instability were determined using a phi-c reduction methodology employed by PLAXIS, in which the soil strength parameters are successively reduced along the failure surface until failure occurs.

3. Parametric Analysis

To investigate the effects of various parameters on the performance of flood embankments founded on soils with potential for progressive failure, an embankment was modeled with varying foundation conditions. A list of parameters was identified which potentially affect the degree to which progressive failure occurs. The parameters investigated in this study were (1) depth of the thin layer of sensitive material, (2) peak and residual shear strengths of the thin layer material, (3) thickness of the thin layer, (4) undrained shear strength of the foundation material, and (5) embankment height. This is not intended to be an all-inclusive list of parameters that may affect progressive failure but rather a list of what the authors believe are the most critical parameters. Furthermore, some of the parameters were investigated more extensively than others. A large range of thin layer depths and thin layer strength parameters were investigated, while only two thin

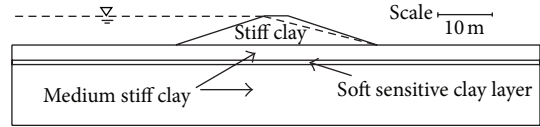


FIGURE 1: Levee profile used in analyses.

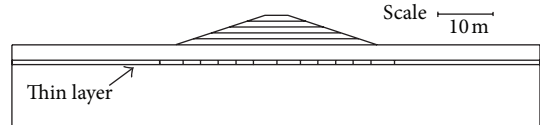


FIGURE 2: Finite element model geometry showing the thin layer separated into regions.

layer thicknesses, two foundation material strengths, and three embankment heights were examined.

Three main groups of analyses were performed in the parametric analysis and are presented in tabular form in Table 3.

The first group of analyses was performed for an embankment with a foundation material having an undrained shear strength of 47.8 kPa and an embedded thin layer of sensitive material with a thickness of 0.6 meters. The depth of the thin layer was varied from 1.8 to 10.1 meters, and the stress-strain characteristics of the soil material forming the thin layer were varied as shown in Figures 3(a) and 4(b).

The stress-strain relationship for curve 1(a) is based on the strain-softening parameters for Onsøy Clay presented by Randolph and Andersen [41] and is characteristic of moderately sensitive clays. The remaining stress-strain curves are synthetic and were created by scaling the original relationship (curve 1(a)) to suit the needs of the parametric analysis. The second group of analyses was performed for an embankment with a foundation material having undrained shear strength of 47.8 kPa and an embedded thin layer of sensitive material with a thickness of 0.9 meters. The depth of the thin layer was varied from 2.4 to 15.2 meters, and the stress-strain characteristics of the soil material forming the thin layer were varied as shown in Figures 3(a) and 3(b). The third group of analyses was performed for an embankment with a foundation material having undrained shear strength of 35.9 kPa and embedded thin layer depths of both 0.6 and 0.9 meters. The depth of the thin layer was varied from 5.2 to 10.1 meters, and the stress-strain characteristics of the soil material forming the thin layer were varied as shown in Figure 4. The change in thin layer depth range and thin layer strength parameters between groups 1 and 2 and group 3 was necessary to ensure that enough shear strain was mobilized within the thin layer to induce strain softening and thereby progressive failure.

4. Analyses Results

Each group of analyses was performed using both limit equilibrium analysis (LEA) and finite element analysis (FEA) with the strain-softening approximation. Figure 5 presents

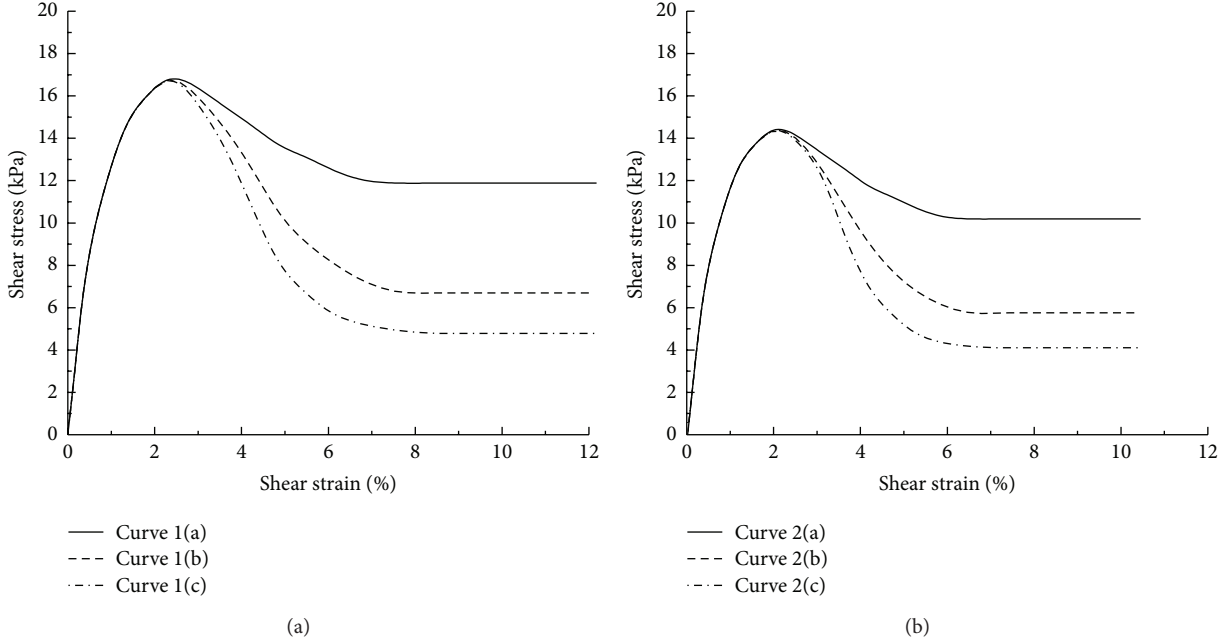


FIGURE 3: Shear stress-shear strain curves for thin layer material (curves 1 and 2).

TABLE 3: Parameter combinations investigated in the present study.

Analysis group	Foundation material strength (kPa)	Thin layer thickness (m)	Thin layer depth range (m)	Thin layer curve number
Group 1	47.8	0.6	1.8–10.1	1(a)
			2.4–10.1	1(b)
			1.8–10.1	1(c)
			1.8–10.1	2(a)
			2.4–10.1	2(b)
			1.8–10.1	2(c)
Group 2	47.8	0.9	2.4–12.2	1(a)
			2.4–15.2	1(b)
			2.4–12.2	1(c)
			2.4–12.2	2(a)
			2.4–10.1	2(b)
Group 3	35.9	0.6	5.2–10.1	3(a)
			5.2–10.1	3(b)
			5.2–10.1	3(c)
		0.9	5.2–10.1	3(b)
			5.2–10.1	3(c)

the finite element factors of safety plotted against the limit equilibrium factors of safety.

As seen in Figure 5, the vast majority of the data points plot below the 1:1 line, indicating that the progressive failure indeed significantly reduces the stability of the embankment. The results from the three analyses groups, for each analysis method (i.e., LEA and FEA), were then compared to determine to what extent each parameter affects the stability of the slope with regard to progressive failure for each analysis type. For each combination of parameters, the resulting factors

of safety against slope instability from the limit equilibrium analysis (FS_{LE}) and the finite element analysis (FS_{FE}) were compared.

Figures 6(a)–6(e) show plots of the FS_{FE}/FS_{LE} versus sensitivity (defined as the ratio of peak strength to residual strength) for various combinations of foundation soil shear strength, thin layer depth, thin layer thickness, and thin layer peak shear strength. Figures 7(a)–7(f) show plots of FS_{FE}/FS_{LE} versus thin layer depth for various combinations of foundation soil shear strength, thin layer thickness, thin layer

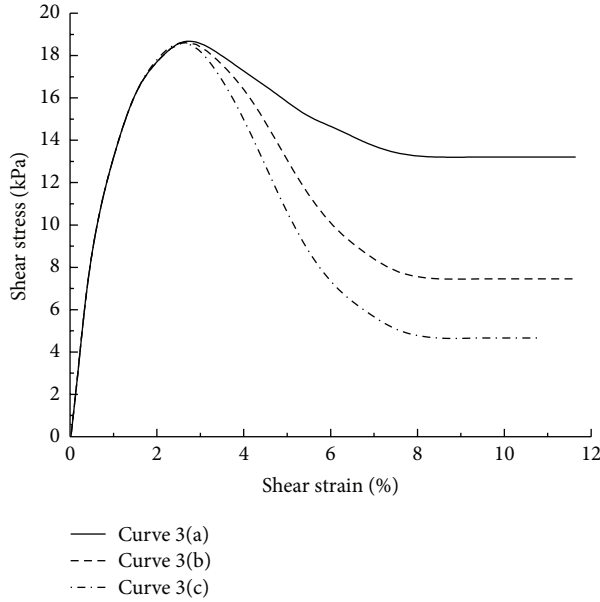


FIGURE 4: Shear stress-shear strain curves for thin layer material (curve 3).

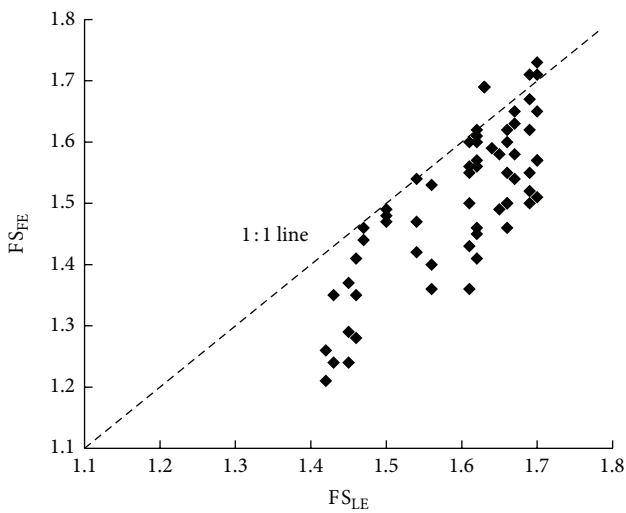


FIGURE 5: Summary plot of parametric analysis data points.

peak shear strengths, and thin layer sensitivity. From these figures, the relative effect on the potential for progressive failure of each of the parameters investigated can be observed.

4.1. Effect of Thin Layer Sensitivity and Shear Strength. The analyses performed in this study indicate that the peak shear strength and sensitivity are the most influential parameters with regard to progressive failure. It is difficult to discern the effects of the two parameters separately and some of their effects appear to be a function of their combination. Figures 6(a)–6(e) show that, in general, as the sensitivity of the thin layer increases, the extent to which progressive failure influences the embankment stability increases. As the peak

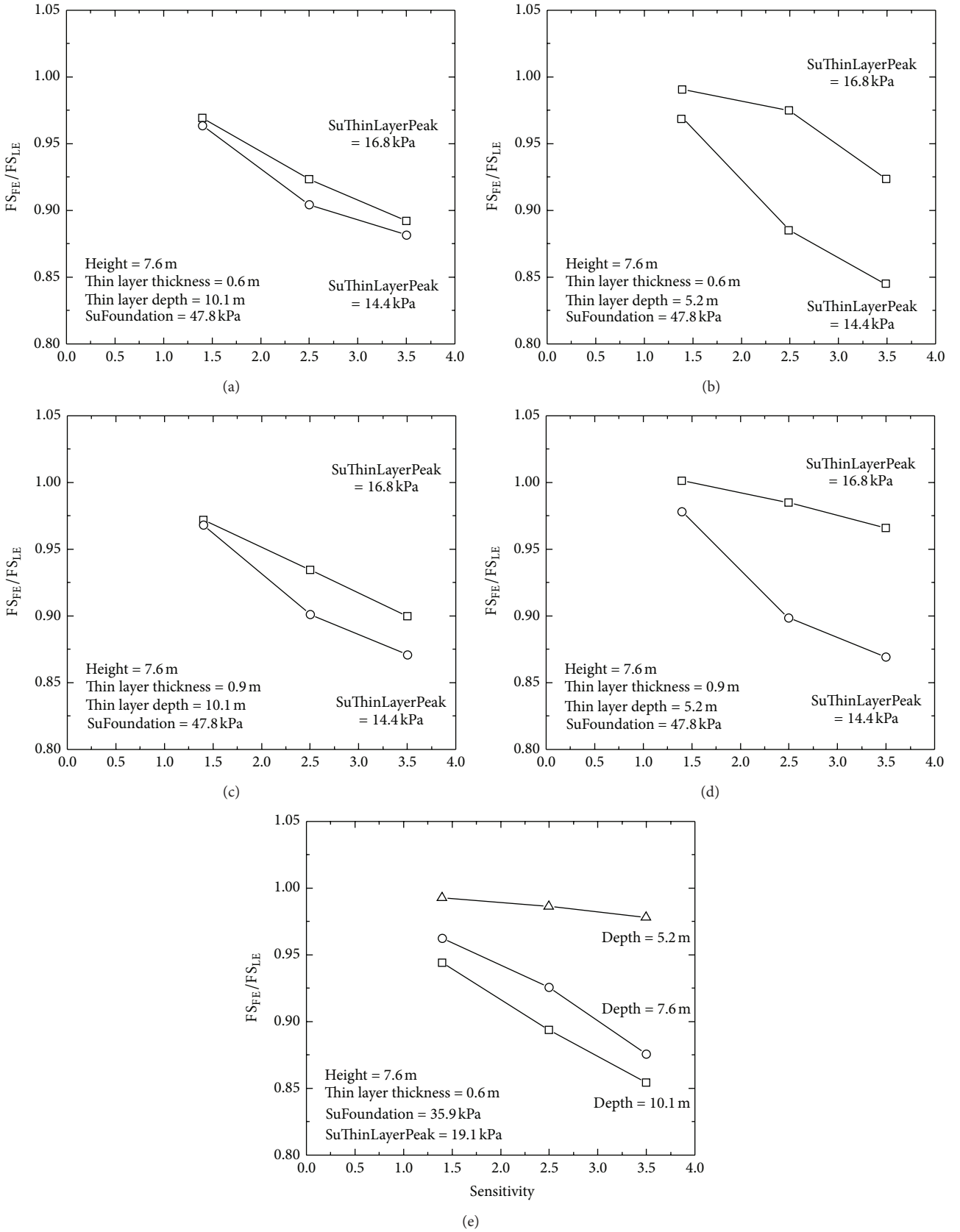
strength of the thin layer decreases, the impact of progressive failure on slope stability increases.

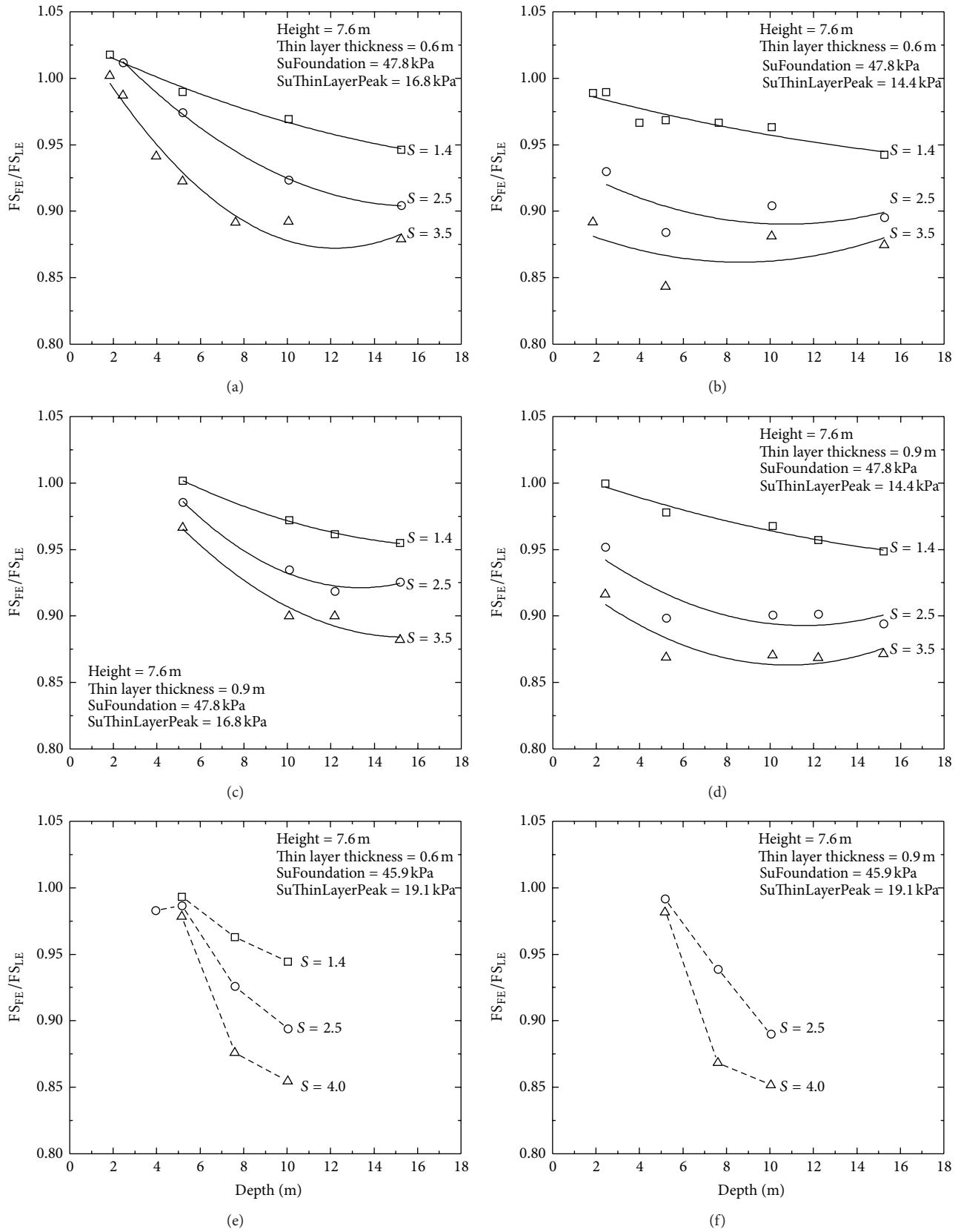
4.2. Effect of Thin Layer Depth. It can be readily seen that the depth of the thin layer plays a significant role in the occurrence of progressive failure for the profiles investigated in this study. Comparison of Figure 6(a) with Figure 6(b) and Figure 6(c) with Figure 6(d) shows that as thin layer depth increases the impact of thin layer peak shear strength on progressive failure decreases. Figure 6(e) and Figures 7(a)–7(f) show that as the thin layer depth increases, the ratio of finite element factor of safety to limit equilibrium factor of safety decreases, suggesting that progressive failure has a greater effect for deeper thin layers. This trend continues to a certain thin layer depth, after which the effect of progressive failure diminishes with an increase in thin layer depth. The effect of thin layer depth observed in this study is logical, since as the depth increases, the driving force increases. The resisting force also increases, due to the extended failure surface, but, due to the presence of the embankment, does not entirely compensate for the increased driving force until a certain depth, after which an increase in thin layer depth causes a decrease in progressive failure. It would be expected that for large thin layer depths (beyond those investigated here), progressive failure through the thin layer would play no role, since a more critical failure through the overlying material would develop.

4.3. Effect of Thin Layer Thickness. Comparison of Figure 6(a) with Figure 6(c) and Figure 6(b) with Figure 6(d) shows that the thin layer thickness has a negligible impact on progressive failure. For layers with a thickness that is thin relative to the depth beneath the embankment, it is logical that the thickness would have little impact on progressive failure, since the failure surface through the sensitive material is primarily linear. This however is only true over this narrow range of thin layer thicknesses. It has been shown that for thicker layers of soft and sensitive soils beneath embankments (on the order of 3 meters and greater) the thickness of the layer is a key parameter with respect to the degree to which progressive failure affects the stability of the embankment [42].

4.4. Effect of Foundation Soil Shear Strength. Although not studied in extensive detail, the effect of foundation soil shear strength can be evaluated by comparing Figures 7(a)–7(d) with Figures 7(e)–7(f). The foundation soil shear strength was reduced to produce Figures 7(e) and 7(f) and so in order to allow for the mobilization of adequate shear strains for the initiation of progressive failure, the thin layer peak strength was increased. It appears that as foundation soil shear strength decreases the influence of progressive failure on slope stability increases. Also, progressive failure appears to have significantly less effect at shallower depths for the cases with the lower foundation material strength.

4.5. Effect of Embankment Height. To investigate the effect of embankment height the embankment properties were held constant while the height was varied. The external water

FIGURE 6: Plots of FS_{FE}/FS_{LE} versus thin layer sensitivity.

FIGURE 7: Plots of FS_{FE}/FS_{LE} versus thin layer depth for various sensitivities (S).

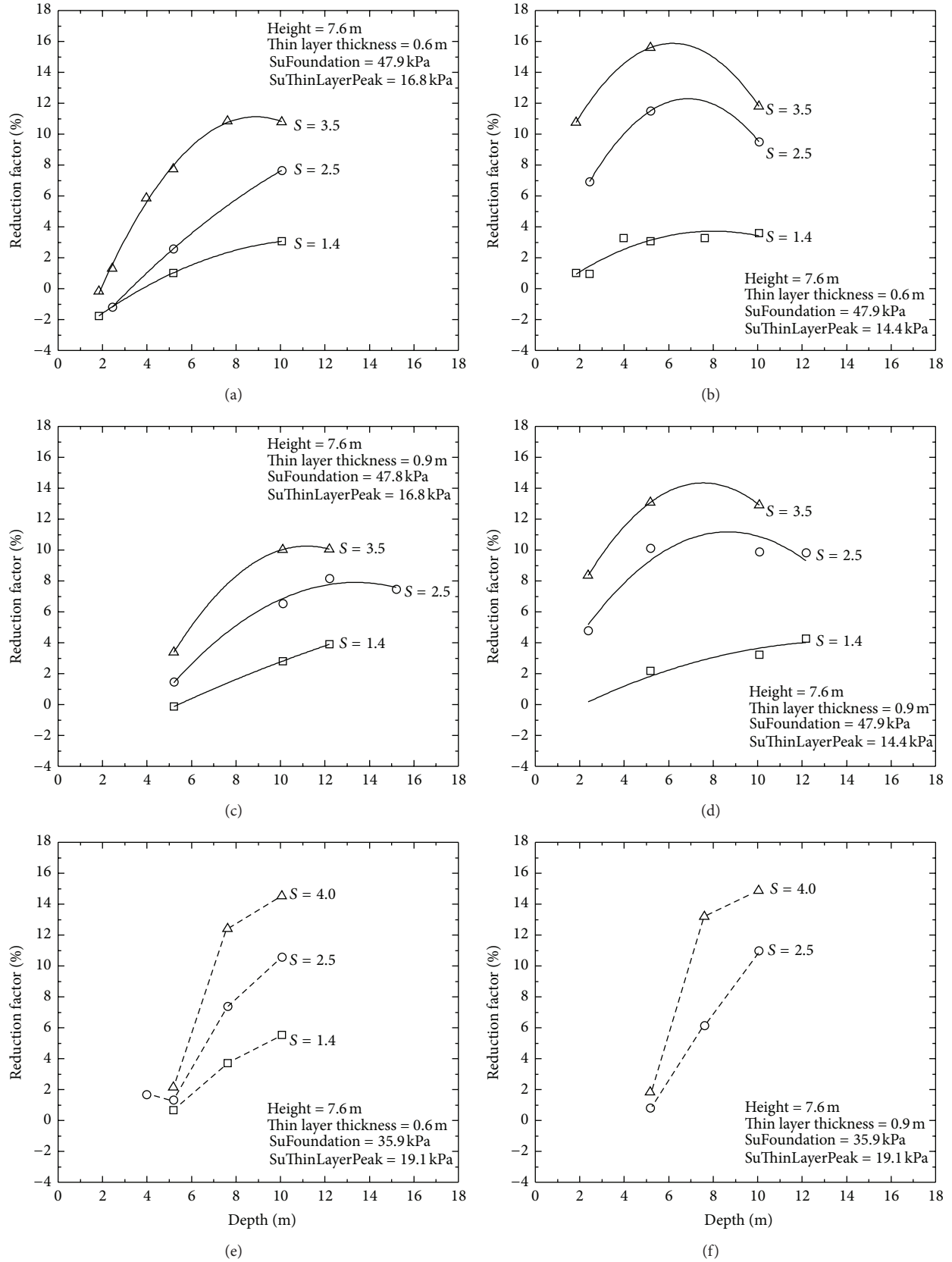


FIGURE 8: Plots of reduction factor versus thin layer depth.

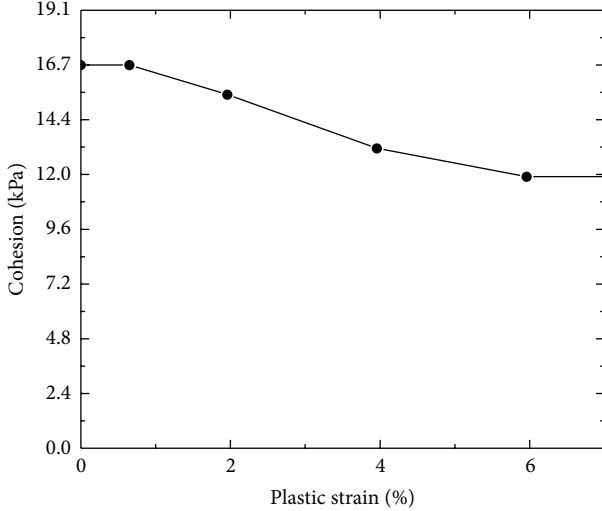


FIGURE 9: Variation of thin layer cohesion with plastic strain for FLAC analysis.

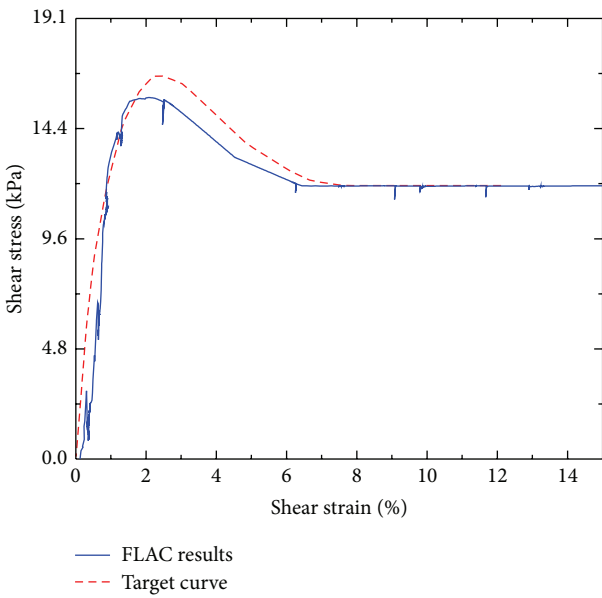


FIGURE 10: Computed and target stress-strain values within the thin layer material for the FLAC comparison analysis.

level at which strain softening occurred was recorded and the factors of safety were calculated using the finite element method, with approximate modeling of strain softening, and the limit equilibrium method. Table 4 shows the results of this study.

The numerical analysis showed that regardless of embankment height the mechanism of failure is still the same (i.e., progressive failure initiating within the thin layer beneath the toe of the downstream face and running along the thin layer). The effect of embankment height on the influence of progressive failure is, somewhat intuitively, that as embankment height increases the external load at which progressive failure occurs decreases.

TABLE 4: Analyses Results for different embankment heights.

Slope height (ft)	Water level at progressive failure (ft)	FS _{FE}	FS _{LE}	FS _{FE} /FS _{LE}
25	No progressive failure	1.82	1.67	1.09
30	20	1.48	1.51	0.98
35	10	1.25	1.34	0.93

As seen in Figures 6 and 7 some of the FS_{FE}/FS_{LE} ratios are slightly greater than 1.0. This should not be interpreted as the effects of progressive failure *increasing* the factor of safety against slope stability. Rather, it is an indication of the range of error that arises when comparing the two methods when the factors of safety are essentially equal. This occurs for cases when progressive failure either barely initiates or does not initiate at all (for shallow thin layer depths and relatively strong thin layer parameters).

5. Factor of Safety Reduction Factors

The percent decrease in the limit equilibrium factor of safety required to match the finite element (with approximate strain softening) factor of safety was designated as the necessary reduction factor to account for progressive failure effects when using limit equilibrium analysis. The behavior and trends of the reduction factor, based on the combination of parameters, were studied and the resulting observations and correlations are presented in the following section. The reduction factor (RF) is defined as

$$RF = \frac{FS_{LE} - FS_{FE}}{FS_{LE}} \cdot 100\%. \quad (1)$$

Figures 8(a)–8(f) show plots of RF against thin layer depth for a combination of embankment and soil properties. The plots can be used to determine the necessary reduction in factor of safety (from limit equilibrium analysis) to account for strain softening, for properties matching those for a specific plot. A negative reduction factor should be neglected, since including strain softening should not lead to an increase in factor of safety. Instead it should be assumed that in those cases the role of strain softening is negligible and the factor of safety from limit equilibrium analysis does not need to be modified.

6. Strain-Softening Model Validation

In order to validate the stepwise reduction method used to account for strain softening in the parametric analysis, a comparison analysis was conducted using the finite difference software FLAC 2D [43]. The sensitive thin layer material was modeled using a built-in strain softening model which is a Mohr-Coulomb formulation that accounts for strain softening by varying the model strength parameters as a function of plastic strain. The comparison analysis was conducted for a 25-foot levee with a 2-foot thick thin layer located at 17 feet below the levee. The thin layer had a peak strength of 16.75 kPa and a sensitivity of 1.4. All material

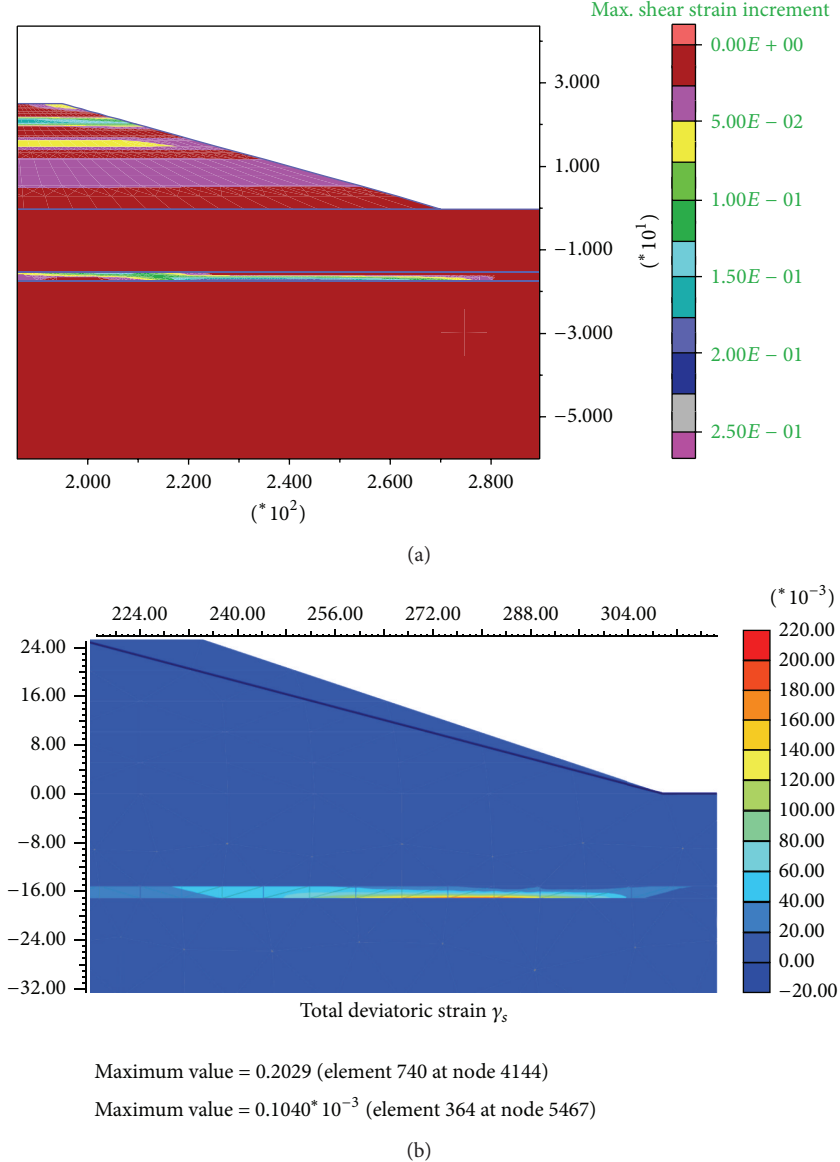


FIGURE 11: Shear strain contours at high water level in (a) FLAC and (b) PLAXIS.

properties and staged construction sequences were the same as for the analyses conducted in PLAXIS, except for the thin layer model, for which the cohesion was defined as a function of plastic strain, as shown in Figure 9.

The results of the FLAC analysis, using the built-in strain-softening model, were used to validate the stepwise strength reduction technique used in the PLAXIS analyses. Figure 10 presents the stress strain curve from the FLAC analysis calculated within the thin layer, at the location of maximum shear strain. The target stress strain curve for the thin layer material is also plotted for comparison, and it can be seen that the FLAC analysis accurately captures the strain-softening behavior of the sensitive material. Figures 11(a) and 11(b) present the shear strain contours at the high water level in FLAC and PLAXIS, respectively. The shear strains from the

two analyses have very similar extents within the thin layer and have maximum values at roughly the same locations. Also, the magnitudes of the strains for the two analyses are very close, with the FLAC analysis having a maximum value of approximately 22.5% and the PLAXIS analysis having a maximum value of approximately 20.3%.

7. Concluding Remarks and Recommendations

A parametric analysis was conducted to investigate the effect of thin layers of soft, sensitive soils on the stability of flood embankments and to propose factor of safety reduction factors that can be applied to factors of safety computed using limit equilibrium analysis. The results of the parametric analysis emphasize the importance of accounting for progressive

failure in thin layers of soft sensitive soils and the inadequacy of limit equilibrium methods with respect to accounting for progressive failure. From the parametric analysis presented here, it can be concluded that progressive failure can have a significant effect on the stability of flood embankments with underlying thin layers of sensitive material. A host of parameters (i.e., thin layer depth, thin layer thickness, thin layer peak and residual shear strength, foundation soil shear strength, and embankment height) have been shown to contribute to the development and likelihood of progressive failure. However, the parameters that mostly affect the reduction factors recommended herein are the depth of the sensitive, soft layer and the peak shear strength and sensitivity of the sensitive, soft layer. The reduction factors shown in Figure 8 are recommended when performing limit equilibrium slope stability analysis of embankments with geometries and soil properties similar to the ones included in this study.

Additional analysis is needed to investigate the effect of soil type of the levee foundation materials surrounding the sensitive soft layer, as well as the effect of inclined layering, to be able to provide similar recommendations for a wider range of levees.

Acknowledgments

This material is based in part on work supported by the National Science Foundation under Grant no. CMMI-1030159 and the authors are grateful for their support. Any opinions, findings, and conclusions or recommendations expressed here are those of the authors and do not necessarily reflect the views of the National Science Foundation. The authors would also like to express their thanks to the Horace Rackham School of Graduate Studies at the University of Michigan for their support provided by the Rackham Merit Fellowship for Mr. Lobbestael.

References

- [1] J. D. Rogers, G. P. Boutwell, D. W. Schmitz et al., "Geologic conditions underlying the 2005 17th Street Canal levee failure in New Orleans," *ASCE Journal of Geotechnical and Geoenvironmental Engineering*, vol. 134, no. 5, pp. 583–601, 2008.
- [2] R. B. Seed, R. G. Bea, A. Athanasopoulos-Zekkos et al., "New orleans and hurricane katrina. III: the 17th Street drainage canal," *Journal of Geotechnical and Geoenvironmental Engineering*, vol. 134, no. 5, pp. 740–761, 2008.
- [3] K. Terzaghi and R. B. Peck, *Soil Mechanics in Engineering Practice*, John Wiley & Sons, New York, NY, USA, 1948.
- [4] A. W. Skempton, "Long term stability of clay slopes," *Geotechnique*, vol. 14, no. 2, pp. 77–101, 1964.
- [5] R. B. Peck, "Stability of natural slopes," *Journal of Soil Mechanics and Foundations Division*, vol. 93, pp. 403–436, 1967.
- [6] J. M. Duncan and S. G. Wright, "The accuracy of equilibrium methods of slope stability analysis," *Engineering Geology*, vol. 16, no. 1-2, pp. 5–17, 1980.
- [7] J. M. Duncan, "State of the art: limit equilibrium and finite-element analysis of slopes," *Journal of Geotechnical and Geoenvironmental Engineering*, vol. 122, no. 7, pp. 577–596, 1996.
- [8] A. W. Skempton, "Slope stability of cuttings in Brown London Clay," in *Proceedings of the 9th International Conference on Soil Mechanics and Foundation Engineering*, vol. 3, pp. 261–270, 1977.
- [9] L. Bjerrum, "Embankments on soft ground," in *Proceedings of the Specialty Conference on Earth and Earth Supported Structures*, vol. 2 of ASCE, pp. 1–54, 1972.
- [10] S. Chirapuntu and J. M. Duncan, "The role of fill strength in the stability of embankments on soft clay foundations," Final Report Contract S-76-6, University of California at Berkeley, Berkeley, Calif, USA, 1976.
- [11] G. A. Leonards, "Investigation of failures," *Journal of the Geotechnical Engineering Division*, vol. 108, no. 2, pp. 187–246, 1982.
- [12] G. M. Filz, J. J. B. Esterhuizen, and J. Michael Duncan, "Progressive failure of lined waste impoundments," *Journal of Geotechnical and Geoenvironmental Engineering*, vol. 127, no. 10, pp. 841–848, 2001.
- [13] K. Höeg, "Finite element analysis of strain-softening clay," *Journal of the Soil Mechanics and Foundations Division*, vol. 98, no. 1, pp. 43–58, 1972.
- [14] J. M. Duncan and C. Y. Chang, "Nonlinear analysis of stress and strain in soils," *Journal of Soil Mechanics and Foundations Division*, vol. 96, no. 5, pp. 1629–1653, 1970.
- [15] S. Pietruszczak and Z. Mroz, "Finite element analysis of deformation of strain-softening materials," *International Journal for Numerical Methods in Engineering*, vol. 17, no. 3, pp. 327–334, 1981.
- [16] N. Yoshida, N. R. Morgenstern, and D. H. Chan, "A failure criterion for stiff soils and rocks exhibiting softening," *Canadian Geotechnical Journal*, vol. 27, no. 2, pp. 195–202, 1990.
- [17] N. Yoshida, N. R. Morgenstern, and D. H. Chan, "Finite-element analysis of softening effects in fissured, overconsolidated clays and mudstones," *Canadian Geotechnical Journal*, vol. 28, no. 1, pp. 51–61, 1991.
- [18] R. de Borst, L. J. Sluys, H.-B. Muhlhaus, and J. Pamin, "Fundamental issues in finite element analyses of localization of deformation," *Engineering Computations*, vol. 10, no. 2, pp. 99–121, 1993.
- [19] D. M. Potts and L. Zdravkovic, *Finite Element Analysis in Geotechnical Engineering: Application*, Thomas Telford, London, UK, 2001.
- [20] H. Zhou and M. F. Randolph, "Computational techniques and shear band development for cylindrical and spherical penetrometers in strain-softening clay," *International Journal of Geomechanics*, vol. 7, no. 4, pp. 287–295, 2007.
- [21] S. Wu and X. Wang, "Mesh dependence and nonlocal regularization of one-dimensional strain softening plasticity," *Journal of Engineering Mechanics*, vol. 136, no. 11, pp. 1354–1365, 2010.
- [22] V. Galavi and H. F. Schweiger, "Nonlocal multilaminate model for strain softening analysis," *International Journal of Geomechanics*, vol. 10, no. 1, pp. 30–44, 2010.
- [23] K. Y. Lo and C. F. Lee, "Stress analysis and slope stability in strain-softening materials," *Geotechnique*, vol. 23, no. 1, pp. 1–11, 1973.
- [24] G. T. Dounias, D. M. Potts, and P. R. Vaughan, "Finite element analysis of progressive failure: two case studies," *Computers and Geotechnics*, vol. 6, no. 2, pp. 155–175, 1988.
- [25] D. M. Potts and L. Zdravkovic, *Finite Element Analysis in Geotechnical Engineering: Theory*, Thomas Telford, London, UK, 1999.

- [26] D. M. Potts, G. T. Dounias, and P. R. Vaughan, "Finite element analysis of progressive failure of Carsington embankment," *Geotechnique*, vol. 40, no. 1, pp. 79–101, 1990.
- [27] G. T. Dounias, D. M. Potts, and P. R. Vaughan, "Analysis of progressive failure and cracking in old British dams," *Geotechnique*, vol. 46, no. 4, pp. 621–640, 1996.
- [28] D. M. Potts, N. Kovacevic, and P. R. Vaughan, "Delayed collapse of cut slopes in stiff clay," *Geotechnique*, vol. 47, no. 5, pp. 953–982, 1997.
- [29] N. Kovacevic, K. G. Higgins, D. M. Potts, and P. R. Vaughan, "Undrained behaviour of brecciated Upper Lias Clay at empingham dam," *Geotechnique*, vol. 57, no. 2, pp. 181–195, 2007.
- [30] N. Kovacevic, D. W. Hight, D. M. Potts, and I. C. Carter, "Finite-element analysis of the failure and reconstruction of the main dam embankment at Abberton Reservoir, Essex, UK," *Geotechnique*, vol. 63, no. 9, pp. 753–767, 2012.
- [31] A. Gens and E. E. Alonso, "Aznalcóllar dam failure—part 2: stability conditions and failure mechanism," *Geotechnique*, vol. 56, no. 3, pp. 185–201, 2006.
- [32] D. Hughes, V. Sivakumar, D. Glynn, and G. Clarke, "A case study: delayed failure of a deep cutting in lodgement till," *Geotechnical Engineering*, vol. 160, no. 4, pp. 193–202, 2007.
- [33] C. Kelln, J. Sharma, and D. Hughes, "A finite element solution scheme for an elastic-viscoplastic soil model," *Computers and Geotechnics*, vol. 35, no. 4, pp. 524–536, 2008.
- [34] C. Kelln, J. Sharma, D. Hughes, and J. Graham, "An improved elastic-viscoplastic soil model," *Canadian Geotechnical Journal*, vol. 45, no. 10, pp. 1356–1376, 2008.
- [35] A. Troncone, "Numerical analysis of a landslide in soils with strain-softening behaviour," *Geotechnique*, vol. 55, no. 8, pp. 585–596, 2005.
- [36] N. Kovacevic, R. J. Jardine, D. M. Potts, C. E. Clukey, J. R. Brand, and D. R. Spikula, "A numerical simulation of underwater slope failures generated by salt diapirism combined with active sedimentation," *Geotechnique*, vol. 62, no. 9, pp. 777–786, 2012.
- [37] V. Galavi and H. F. Schweiger, "Nonlocal multilaminate model for strain softening analysis," *International Journal of Geomechanics*, vol. 10, no. 1, pp. 30–44, 2010.
- [38] F. Zabala and E. E. Alonso, "Progressive failure of aznalcó llar dam using the material point method," *Geotechnique*, vol. 61, no. 9, pp. 795–808, 2011.
- [39] GEO-SLOPE International, *Stability Modeling with SLOPE/W*, 2007, Calgary, Alberta, Canada, 2008.
- [40] R. Brinkgreve and W. Broere, "PLAXIS 2D Version 9 finite element code for soil and rock analyses," The Netherlands, 2008.
- [41] M. F. Randolph and K. H. Andersen, "Numerical analysis of T-bar penetration in soft clay," *International Journal of Geomechanics*, vol. 6, no. 6, pp. 411–420, 2006.
- [42] A. Llobbestael and A. Athanasopoulos-Zekkos, "A parametric analysis of the effects of progressive failure on embankments founded on soft sensitive soils," in *Proceedings of the Geo-Frontiers: Advances in Geotechnical Engineering*, pp. 3669–3678, Dallas, Tex, USA, March 2011.
- [43] Itasca Consulting Group, *FLAC—Fast Lagrangian Analysis of Continua, Version 7.0 User's Guide*, Itasca, Minneapolis, Minn, USA, 2011.

Research Article

Qualitative Behaviour of Elastic-Plastic Solutions for a Class of Damage Mechanics Models Near Bimaterial Interfaces: A Simple Analytical Example

Sergei Alexandrov¹ and Yusof Mustafa²

¹ A.Yu. Ishlinskii Institute for Problems in Mechanics, Russian Academy of Sciences, 101-1 Prospect Vernadskogo, Moscow 119526, Russia

² Faculty of Mechanical Engineering, Universiti Teknologi Malaysia, 81310 Skudai, Johor, Malaysia

Correspondence should be addressed to Sergei Alexandrov; sergei_alexandrov@spartak.ru

Received 8 August 2013; Revised 22 November 2013; Accepted 24 November 2013

Academic Editor: Yuri Petryna

Copyright © 2013 S. Alexandrov and Y. Mustafa. This is an open access article distributed under the Creative Commons Attribution License, which permits unrestricted use, distribution, and reproduction in any medium, provided the original work is properly cited.

The paper presents an exact analytic solution for a class of elastic-plastic models with damage evolution. The boundary value problem consists of a planar deformation comprising the simultaneous shearing and expansion of a hollow cylindrical specimen of material and involves a bimaterial interface at which the materials stick to each other. With no loss of generality for understanding the qualitative behaviour of the solution near the bimaterial interface, an extreme case when the hard material is rigid is considered. The solution is reduced to a transcendental equation for the value of the equivalent plastic strain at the bimaterial interface. This equation predicts that the equivalent plastic strain attains a maximum under certain conditions. The existence of the solution of the boundary value problem depends on the value of the damage parameter at fracture, which is a material constant. In particular, if this value is larger than the value of the damage parameter at the bimaterial interface corresponding to the maximum possible value of the equivalent strain at this interface, then no solution exists. Experimental data available in the literature are used to assess whether Lemaitre's model is applicable.

1. Introduction

The ductile damage evolution equations of continuum mechanics can be conveniently divided into three groups: (i) uncoupled models, (ii) partly coupled models, and (iii) coupled models. In the case of the models of group (i) the damage evolution equation is solved having found the solution for the system of equations of plasticity theory. A recent review of models of this group is provided in [1]. The models of group (iii) include the fully coupled system of equations of plasticity theory and the damage evolution equation. In particular, the material is plastically compressible. A recent review of models of this group is provided in [2]. In the present paper, a wide class of models of group (ii) for elastic-plastic materials is adopted. These models containing one scalar measure of damage are based on the pressure-independent yield criterion and the associated flow rule for plastic strain rates. The evolution of the damage parameter is controlled

by an additional equation. Such models are presented, for example, in [3–7]. The yield criterion and elastic moduli depend on the damage parameter. Many structures and machine parts are composed of two or more different materials and, therefore, contain bimaterial interfaces. Solution behaviour in the vicinity of such interfaces may reveal some qualitative features that provide an assessment of the model adopted to find the solution. For example, using a rigid perfectly plastic material model, it has been shown in [8] that the velocity field is singular in the vicinity of some bimaterial interfaces. This singularity in the velocity field is not compatible with the class of damage evolution models reviewed in [9]. In order to assess the mathematical model, it is possible to study any boundary value problem, even if its practical application is not feasible. It is more important to find the exact solution of the problem without relaxing the boundary conditions and field equations. Such a boundary value problem has been proposed and solved for a rigid

plastic linear hardening material model in [10]. Then, this boundary value problem has been successfully used in [11, 12] to study various qualitative features of solutions for several material models. However, all of these solutions are for rigid plastic materials with no damage evolution. In the present paper, the same boundary value problem is combined with a class of elastic-plastic models with damage evolution at small strains. The solution is reduced to a transcendental equation for the value of the equivalent plastic strain at the bimaterial interface. The solution to this equation predicts that this value attains a maximum under certain conditions. The existence of the solution of the boundary value problem depends on the value of the damage parameter at fracture, which is supposed to be a constitutive parameter. In particular, if the value of the damage parameter at the bimaterial interface corresponding to the maximum possible value of the equivalent plastic strain at this interface is smaller than the damage parameter at fracture, then no solution exists. The model proposed by Lemaître [3] is studied in some detail. In particular, experimental data provided in [13] are used to assess whether the model for this specific set of constitutive parameters is applicable (in the sense that the solution exists).

2. Statement of the Problem

Consider an infinite elastic-plastic circular cylinder of internal radius r_0 and external radius R_0 subject to the action of tangential stresses uniformly distributed over its external radius. It is assumed that a rigid rod of radius r_0 is inserted into the hole of the cylinder. The rod is motionless and fixed to the cylinder. Due to this system of loading and constraints, the cylinder is twisted. It is convenient to introduce a cylindrical polar coordinate system (r, θ, z) with its z -axis coinciding with the axis of symmetry of the cylinder. The boundary conditions are

$$u_\theta = 0 \quad (1)$$

for $r = r_0$ and

$$u_\theta = \omega R_0 \quad (2)$$

for $r = R_0$. Here u_θ is the circumferential displacement and ω is the angular displacement of the external surface of the cylinder.

A typical dependence of the shear yield stress, k , on the equivalent plastic strain, ξ_{eq}^p , and damage parameter, D , is [3, 4, 7]

$$k = k_0 \left[1 + f(\xi_{\text{eq}}^p) \right] (1 - D). \quad (3)$$

Here k_0 is the initial shear yield stress when $\xi_{\text{eq}}^p = 0$ and $D = 0$. The function $f(\xi_{\text{eq}}^p)$ satisfies the conditions $f(0) = 0$ and $df/d\xi_{\text{eq}}^p > 0$ for any ξ_{eq}^p . The equivalent plastic strain is defined by the equation

$$\frac{d\xi_{\text{eq}}^p}{dt} = \xi_{\text{eq}}^p. \quad (4)$$

Here t is the time and d/dt is the convected derivative. The equivalent plastic strain rate, ξ_{eq}^p , is defined by

$$\xi_{\text{eq}}^p = \sqrt{\frac{2}{3} \xi_{ij}^p \xi_{ij}^p}, \quad (5)$$

where ξ_{ij}^p are the plastic strain rate components. The yield criterion is

$$\tau_{ij} \tau_{ij} = 2k^2, \quad (6)$$

where τ_{ij} are the deviatoric components of the stress tensor. The flow rule associated with (6) is

$$\xi_{ij}^p = \lambda \tau_{ij}, \quad (7)$$

where λ is a scalar factor of proportionality. The elastic strains, ε_{ij}^e , obey Hooke's law. The total strains are

$$\varepsilon_{ij} = \varepsilon_{ij}^e + \varepsilon_{ij}^p. \quad (8)$$

In the case of isotropic models with a single scalar measure of damage typical damage evolution equations are [3, 4, 7]

$$\frac{dD}{dt} = F \left(\frac{\sigma}{\sqrt{3k}}, D \right) \xi_{\text{eq}}^p \quad \text{if } \xi_{\text{eq}}^p \geq \varepsilon_0, \quad (9)$$

$$\frac{dD}{dt} = 0 \quad \text{if } \xi_{\text{eq}}^p < \varepsilon_0,$$

$$\frac{dD}{dt} = F \left(\frac{\sigma}{\sqrt{3k}}, D \right) (\xi_{\text{eq}}^p)^{1/M} \xi_{\text{eq}}^p \quad \text{if } \xi_{\text{eq}}^p \geq \varepsilon_0, \quad (10)$$

$$\frac{dD}{dt} = 0 \quad \text{if } \xi_{\text{eq}}^p < \varepsilon_0.$$

Here σ is the hydrostatic stress, ε_0 is the threshold equivalent plastic strain for the initiation of damage, M is constant, and F is a given function of its arguments. The fracture criterion is

$$D = D_c, \quad (11)$$

where D_c is a material constant whose value for metallic materials lies in the range $0.2 < D_c < 0.8$ [7]. Equations (3) to (11) along with Hooke's law represent a typical isotropic elastic-plastic material model with damage evolution at small strains. These equations should be supplemented with the equilibrium equations.

3. Solution

In this section, an exact solution of the equations of the previous section is derived in the cylindrical coordinates assuming that the solution is independent of θ and z . It is then demonstrated that the solution is compatible with the boundary conditions (1) and (2). Suppose that all components of the stress tensor vanish except for the shear component $\tau_{r\theta}$. The yield criterion (6) is satisfied if

$$\tau_{r\theta} = k. \quad (12)$$

The only nontrivial equilibrium equation is

$$\frac{\partial \tau_{r\theta}}{\partial r} + \frac{2\tau_{r\theta}}{r} = 0. \quad (13)$$

Denote the radius of the elastic-plastic boundary by R , $r_0 \leq R \leq R_0$. The material just on the elastic side of the boundary must be on the point of yielding. Therefore, $\tau_{r\theta} = k = k_0$ at $r = R$. Integrating (13) with the use of this condition gives

$$\frac{\tau_{r\theta}}{k_0} = \left(\frac{R}{r}\right)^2. \quad (14)$$

It follows from Hooke's law that

$$2G\varepsilon_{r\theta}^e = \tau_{r\theta}, \quad (15)$$

where G is the modulus of shear.

Consider the elastic region, $R \leq r \leq R_0$. In this region, $\varepsilon_{ij}^e = \varepsilon_{ij}$ and $G = G_0$, where G_0 is the shear modulus of undamaged material. Therefore, substituting (14) into (15) yields

$$\varepsilon_{r\theta} = \frac{k_0}{2G_0} \left(\frac{R}{r}\right)^2. \quad (16)$$

In the plastic region, $r_0 \leq r \leq R$, combining (12) and (14) gives

$$\frac{k}{k_0} = \left(\frac{R}{r}\right)^2. \quad (17)$$

A typical assumption is that $G = G_0(1 - D)$ [3, 4, 7]. Then, substituting (12) into (15) results in

$$\varepsilon_{r\theta}^e = \frac{k}{2G_0(1 - D)}. \quad (18)$$

Since the only nonzero stress component is $\tau_{r\theta}$, it follows from (7) that the only nonzero plastic strain rate component is $\xi_{r\theta}^p$. Then, (5) reduces to

$$\xi_{eq}^p = \frac{2}{\sqrt{3}} \xi_{r\theta}^p. \quad (19)$$

It has been taken into account here that $\tau_{r\theta} > 0$, as follows from (12). Since strains are small, $\xi_{eq}^p = \partial \varepsilon_{eq}^p / \partial t$ and $\xi_{r\theta}^p = \partial \varepsilon_{r\theta}^p / \partial t$. Therefore, integrating (19) with respect to t gives

$$\varepsilon_{eq}^p = \frac{2}{\sqrt{3}} \varepsilon_{r\theta}^p. \quad (20)$$

The total shear strain in the plastic region is found from (8), (18), and (20) as

$$\varepsilon_{r\theta} = \frac{k}{2G_0(1 - D)} + \frac{\sqrt{3}}{2} \varepsilon_{eq}^p. \quad (21)$$

Since $\sigma = 0$, (9) becomes

$$\begin{aligned} \frac{dD}{dt} &= F_1(D) \xi_{eq}^p && \text{if } \varepsilon_{eq}^p \geq \varepsilon_0, \\ \frac{dD}{dt} &= 0 && \text{if } \varepsilon_{eq}^p < \varepsilon_0, \end{aligned} \quad (22)$$

where $F_1(D) = F(0, D)$. Assuming that $D = 0$ at the initial instant, (22) can be integrated to give

$$\begin{aligned} \Omega(D) &= \varepsilon_{eq}^p - \varepsilon_0 && \text{if } \varepsilon_{eq}^p \geq \varepsilon_0 \\ D &= 0 && \text{if } \varepsilon_{eq}^p < \varepsilon_0. \end{aligned} \quad (23)$$

Here

$$\Omega(D) = \int_0^D \frac{dx}{F_1(x)}, \quad (24)$$

where x is a dummy variable of integration. It follows from (3), (17), and (23) that

$$\left(\frac{R}{r}\right)^2 = [1 + f(\varepsilon_{eq}^p)] [1 - \Omega^{-1}(\varepsilon_{eq}^p - \varepsilon_0)], \quad (25)$$

where Ω^{-1} is the function inverse to Ω . It has been assumed here that $\varepsilon_{eq}^p \geq \varepsilon_0$. Substituting (3) into (21) yields

$$\varepsilon_{r\theta} = \frac{k_0 [1 + f(\varepsilon_{eq}^p)]}{2G_0} + \frac{\sqrt{3}}{2} \varepsilon_{eq}^p. \quad (26)$$

For the problem under consideration, the total shear strain is defined by

$$\varepsilon_{r\theta} = \frac{1}{2} \left(\frac{\partial u_\theta}{\partial r} - \frac{u_\theta}{r} \right) = \frac{r}{2} \frac{\partial (u_\theta/r)}{\partial r}. \quad (27)$$

Combining (26) and (27) gives

$$r \frac{\partial (u_\theta/r)}{\partial r} = \frac{k_0 [1 + f(\varepsilon_{eq}^p)]}{G_0} + \sqrt{3} \varepsilon_{eq}^p. \quad (28)$$

It is convenient to introduce new independent variables as

$$\rho = \frac{R}{r}, \quad s = \frac{R}{R_0}. \quad (29)$$

Then,

$$\frac{\partial}{\partial r} = -\frac{\rho^2}{R} \frac{\partial}{\partial \rho}, \quad \frac{\partial}{\partial t} = \frac{\dot{R}}{R} \left(\rho \frac{\partial}{\partial \rho} + s \frac{\partial}{\partial s} \right), \quad (30)$$

where $\dot{R} \equiv dR/dt$. Using (29), (30), (25) and (28) transforms to

$$\rho^2 = [1 + f(\varepsilon_{eq}^p)] [1 - \Omega^{-1}(\varepsilon_{eq}^p - \varepsilon_0)] \equiv \Lambda(\varepsilon_{eq}^p), \quad (31)$$

$$-\frac{\rho \partial (u_\theta/r)}{\partial \rho} = \frac{k_0 [1 + f(\varepsilon_{eq}^p)]}{G_0} + \sqrt{3} \varepsilon_{eq}^p \equiv \Phi(\varepsilon_{eq}^p), \quad (32)$$

respectively. Eliminating ρ between (31) and (32) leads to

$$\frac{\partial (u_\theta/r)}{\partial \varepsilon_{eq}^p} = -\frac{\Phi(\varepsilon_{eq}^p) \Lambda'(\varepsilon_{eq}^p)}{2\Lambda(\varepsilon_{eq}^p)}, \quad (33)$$

where $\Lambda'(\varepsilon_{\text{eq}}^p) \equiv d\Lambda(\varepsilon_{\text{eq}}^p)/d\varepsilon_{\text{eq}}^p$. Let u_R be the value of u_θ at $r = R$. Since $\varepsilon_{\text{eq}}^p = 0$ at $r = R$, the solution to (33) is

$$\frac{u_\theta}{r} = -\frac{1}{2} \int_0^{\varepsilon_{\text{eq}}^p} \frac{\Phi(x) \Lambda'(x)}{\Lambda(x)} dx + \frac{u_R}{R}. \quad (34)$$

The value of u_R should be found using the solution in the elastic region. Substituting (27) into (16) and using (29) and (30) give

$$\frac{\partial(u_\theta/r)}{\partial\rho} = -\rho \frac{k_0}{G_0}. \quad (35)$$

The solution of this equation satisfying the boundary condition (2) is

$$\frac{u_\theta}{r} = \frac{k_0}{2G_0} (s^2 - \rho^2) + \omega. \quad (36)$$

It follows from (29) that $\rho = 1$ if $r = R$. Therefore, the value of u_R is determined from (36) as

$$\frac{u_R}{R} = \frac{k_0}{2G_0} (s^2 - 1) + \omega. \quad (37)$$

Substituting (37) into (34) gives

$$\frac{u_\theta}{r} = -\frac{1}{2} \int_0^{\varepsilon_{\text{eq}}^p} \frac{\Phi(x) \Lambda'(x)}{\Lambda(x)} dx + \frac{k_0}{2G_0} (s^2 - 1) + \omega. \quad (38)$$

Let ε_s be the value of $\varepsilon_{\text{eq}}^p$ at $r = r_0$. Then, combining (38) and the boundary condition (1) results in

$$\int_0^{\varepsilon_s} \frac{\Phi(\varepsilon_{\text{eq}}^p) \Lambda'(\varepsilon_{\text{eq}}^p)}{\Lambda(\varepsilon_{\text{eq}}^p)} d\varepsilon_{\text{eq}}^p = \frac{k_0}{G_0} (s^2 - 1) + 2\omega. \quad (39)$$

It follows from (29) that $\rho = R/r_0$ at $r = r_0$, and, therefore, $\rho = sR_0/r_0$ at $r = r_0$. Then, (31) shows that $s^2 R_0^2/r_0^2 = \Lambda(\varepsilon_s)$. Using this equation to eliminate s in (39) yields

$$\int_0^{\varepsilon_s} \frac{\Phi(\varepsilon_{\text{eq}}^p) \Lambda'(\varepsilon_{\text{eq}}^p)}{\Lambda(\varepsilon_{\text{eq}}^p)} d\varepsilon_{\text{eq}}^p - \frac{k_0}{G_0} \left[\frac{r_0^2}{R_0^2} \Lambda(\varepsilon_s) - 1 \right] = 2\omega. \quad (40)$$

It follows from (23) that the value of D at $r = r_0$ is given by

$$D_s = \Omega^{-1}(\varepsilon_s - \varepsilon_0). \quad (41)$$

It has been assumed here that $\varepsilon_s \geq \varepsilon_0$.

4. Fracture Initiation and Nonexistence of the Solution

Equation (40) determines ε_s as a function of ω . It follows from this equation that

$$2 \frac{d\omega}{d\varepsilon_s} = \left[\frac{\Phi(\varepsilon_s)}{\Lambda(\varepsilon_s)} - \frac{k_0}{G_0} \frac{r_0^2}{R_0^2} \right] \Lambda'(\varepsilon_s). \quad (42)$$

The right hand side of this equation vanishes if

$$\frac{\Phi(\varepsilon_s)}{\Lambda(\varepsilon_s)} = \frac{k_0}{G_0} \frac{r_0^2}{R_0^2} \quad (43)$$

or

$$\Lambda'(\varepsilon_s) = 0. \quad (44)$$

Using (31) and (32), the left hand side of (43) can be represented in the form

$$\frac{\Phi(\varepsilon_s)}{\Lambda(\varepsilon_s)} = \frac{k_0}{G_0} \frac{(A + \sqrt{3}\varepsilon_s G_0/k_0)}{A [1 - \Omega^{-1}(\varepsilon_s - \varepsilon_0)]}, \quad (45)$$

where $A = 1 + f(\varepsilon_s)$. Consider the coefficient of k_0/G_0 in (45). It follows from the definition for the function $\Omega(D)$ that $\Omega^{-1}(\varepsilon_s - \varepsilon_0)$ is equal to the value of D at $r = r_0$. Therefore, $0 < 1 - \Omega^{-1}(\varepsilon_s - \varepsilon_0) < 1$ and the denominator of the coefficient of k_0/G_0 in (45) is smaller than A . On the other hand, it is evident that its numerator is larger than A . Therefore, the coefficient is larger than 1. However, the coefficient of k_0/G_0 in (43) is smaller than 1. Hence (43) has no solution. Let ε_m be the solution to (44). The corresponding values of $\omega = \omega_m$ and $D_s = D_m$ are determined from (40) and (41) at $\varepsilon_s = \varepsilon_m$. Expanding the left hand side of (42) in a series in the vicinity of $\varepsilon_s = \varepsilon_m$ gives $d\omega/d\varepsilon_s = \beta(\varepsilon_s - \varepsilon_m)$ to leading order. Here β is constant. Integrating this equation with the use of the condition $\varepsilon_s = \varepsilon_m$ at $\omega = \omega_m$ results in $2(\omega - \omega_m) = \beta(\varepsilon_s - \varepsilon_m)^2$ to leading order. This solution can be rewritten in the form $\varepsilon_s = \varepsilon_m - \sqrt{2\beta^{-1}(\omega - \omega_m)}$. It is evident from this expression that ε_s cannot exceed the value of ε_m . Thus if (43) has a solution, then the solution given in the previous section does not exist for $\omega \geq \omega_m$. On the other hand, according to the fracture criterion (II), the initiation of fracture at the bimaterial interface occurs if $D_s = D_c$. The corresponding value of $\varepsilon_s = \varepsilon_c$ is determined from (41) as $\varepsilon_c = \Omega(D_c) + \varepsilon_0$. Hence the solution to the boundary value problem of the previous section, including the fracture criterion, exists if and only if

$$\varepsilon_c \leq \varepsilon_m \quad (\text{or } D_c \leq D_m). \quad (46)$$

In particular, the solution predicts the initiation of fracture at the bimaterial interface at $\varepsilon_s = \varepsilon_c$. It will be shown in the next section that the inequality (46) is not satisfied for some specific damage evolution laws and constitutive parameters used in applications.

5. Illustrative Example

In the case under consideration the damage evolution model [3, 4] is obtained if $F_1(D) = \alpha$ where α is constant. Therefore, evaluating the integral in (24) gives

$$\Omega(D) = \frac{D}{\alpha}. \quad (47)$$

Then, it follows from (23) that

$$\Omega^{-1}(\varepsilon_{\text{eq}}^p - \varepsilon_0) = \alpha(\varepsilon_{\text{eq}}^p - \varepsilon_0). \quad (48)$$

The equation of the strain hardening curve for the steel tested in [13], is

$$f(\varepsilon_{\text{eq}}^p) = 2.78(\varepsilon_{\text{eq}}^p)^{0.32}. \quad (49)$$

Using experimental data provided in [13] it is possible to find that

$$D_c = 0.24, \quad \varepsilon_0 = 0.023, \quad \alpha = 0.6. \quad (50)$$

Substituting (48)–(50) into (31) gives $\Lambda(\varepsilon_{\text{eq}}^p) = [1 + 2.78(\varepsilon_{\text{eq}}^p)^{0.32}][1 - 0.6(\varepsilon_{\text{eq}}^p - 0.023)]$. Hence, (44) becomes $0.89\varepsilon_m^{-0.68}[1 - 0.6(\varepsilon_m - 0.023)] - 0.6(1 + 2.78\varepsilon_m^{0.32}) = 0$. Its solution is $\varepsilon_m = 0.29$. Substituting this value of $\varepsilon_{\text{eq}}^p = \varepsilon_m$ into (41) with the use of (48) gives $D_m = 0.16$. This means that the solution to the boundary value problem without using the fracture criterion breaks down when $D_s = 0.16$. On the other hand, the fracture criterion (11) is not satisfied as follows from (50). Therefore, it is necessary to conclude that the damage evolution model adopted is not compatible with the constitutive parameters recommended in [13].

6. Conclusions

An exact analytic solution for an elastic-plastic model coupled with a damage evolution equation has been found. Special attention has been devoted to the qualitative behavior of the solution in the vicinity of the bimaterial interface. Even though the boundary value problem solved is not feasible for practical applications, the main result obtained is useful for assessing damage evolution models by mathematical methods. In particular, it has been shown that the boundary value problem may have no solution because the equation relating the equivalent plastic strain at the bimaterial interface and one of the boundary conditions has no solution. This conclusion is not valid if the initiation of fracture occurs at a lower value of this strain. Therefore, having specific damage evolution equation and constitutive parameters, it is possible to verify that the model is compatible with conditions at bimaterial interfaces where shear straining prevails. As an example, the constitutive equations proposed in [13] have been used, and it has been demonstrated that the aforementioned equation has no solution. This means that some boundary value problems may have no solution for this model.

Even though (9) has been considered explicitly, it is evident that (10) can be treated in a similar manner. It is just necessary to replace (23) with

$$\begin{aligned} \Omega(D) &= E_{\text{eq}}^p - E_0 && \text{if } \varepsilon_{\text{eq}}^p \geq \varepsilon_0, \\ D &= 0 && \text{if } \varepsilon_{\text{eq}}^p < \varepsilon_0, \end{aligned} \quad (51)$$

where $E_{\text{eq}}^p = m^{-1}(\varepsilon_{\text{eq}}^p)^m$, $E_0 = m^{-1}\varepsilon_0^m$, and $m = 1 + M^{-1}$.

Conflict of Interests

The authors declare that there is no conflict of interests regarding the publication of this paper.

Acknowledgment

The research described in this paper has been supported by the Grants RFBR-11-01-00987 and NSH-3842.2012.1.

References

- [1] Y. J. Liu, Q. Sun, X. L. Fan, and T. Suo, "A stress-invariant based multi-parameters ductile progressive fracture model," *Materials Science and Engineering A*, vol. 576, pp. 337–346, 2013.
- [2] L. A. B. Cunha and G. J. Creus, "Mechanical response of porous materials: the Gurson model," in *Plasticity of Pressure-Sensitive Materials*, H. Altenbach and A. Öchsner, Eds., pp. 349–376, Springer, Berlin, Germany, 2014.
- [3] J. Lemaitre, "A continuous damage mechanics model for ductile fracture," *Transactions of ASME Journal of Engineering Materials and Technology*, vol. 107, no. 1, pp. 83–89, 1985.
- [4] J. Lemaitre, "Formulation and identification of damage kinetic constitutive equations," in *Continuum Damage Mechanics: Theory and Applications*, D. Krajcinovic and J. Lemaitre, Eds., pp. 37–89, Springer, Wien, Austria, 1987.
- [5] S. Chandrakanth and P. C. Pandey, "A new ductile damage evolution model," *International Journal of Fracture*, vol. 60, no. 4, pp. R73–R76, 1993.
- [6] P. Hartley, F. R. Hall, J. M. Chiou, and I. Pillinger, "Elastic-plastic finite-element modelling of metal forming with damage evolution," in *Advanced Methods in Materials Processing Defects*, M. Predeleanu and P. Gilormini, Eds., pp. 135–142, Elsevier, Amsterdam, The Netherlands, 1997.
- [7] S. Murakami, *Continuum Damage Mechanics*, Springer, Dordrecht, The Netherlands, 2012.
- [8] S. Alexandrov and O. Richmond, "Singular plastic flow fields near surfaces of maximum friction stress," *International Journal of Non-Linear Mechanics*, vol. 36, no. 1, pp. 1–11, 2001.
- [9] A. G. Atkins, "Fracture in forming," *Journal of Materials Processing Technology*, vol. 56, no. 1–4, pp. 609–618, 1996.
- [10] I. F. Collins, "Boundary value problems in plane strain plasticity," in *Mechanics of Solids*, H. G. Hopkins and M. J. Sewell, Eds., pp. 135–184, Pergamon Press, Oxford, UK, 1982.
- [11] S. Alexandrov and O. Richmond, "Couette flows of rigid/plastic solids: analytical examples of the interaction of constitutive and frictional laws," *International Journal of Mechanical Sciences*, vol. 43, no. 3, pp. 653–665, 2001.
- [12] S. Alexandrov and G. Mishuris, "Viscoplasticity with a saturation stress: distinguishing features of the model," *Archive of Applied Mechanics*, vol. 77, no. 1, pp. 35–47, 2007.
- [13] J. Lemaitre, "Coupled elasto-plasticity and damage constitutive equations," *Computer Methods in Applied Mechanics and Engineering*, vol. 51, no. 1–3, pp. 31–49, 1985.

Research Article

Earthquake Damage Assessment for RC Structures Based on Fuzzy Sets

Haoxiang He, Maolin Cong, and Yongwei Lv

Beijing Key Lab of Earthquake Engineering and Structural Retrofit, Beijing University of Technology, Beijing 100124, China

Correspondence should be addressed to Haoxiang He; hhx7856@163.com

Received 3 August 2013; Revised 25 October 2013; Accepted 28 October 2013

Academic Editor: Anaxagoras Elenas

Copyright © 2013 Haoxiang He et al. This is an open access article distributed under the Creative Commons Attribution License, which permits unrestricted use, distribution, and reproduction in any medium, provided the original work is properly cited.

A global damage index based on multiple linear force-deformation curves in pushover analysis is presented to evaluate the integrated damage of reinforced concrete structure. The modified coefficient is provided considering the cyclic load and hysteresis energy. The number of inelastic cycles and the coefficient of hysteresis energy concentration are also introduced as damage indices. Hence, multiple damage indices about displacement and energy for performance-based design are considered. The relation of multiple damage indices or factors and the fuzzy damage set is presented by comprehensive fuzzy evaluation; hence, a performance-based multiple fuzzy seismic damage-assessment method for reinforced concrete frame structures is established. The method can be accomplished based on pushover analysis, code spectrum, and capacity spectrum method. The fuzzy seismic damage-assessment method is verified through nonlinear analysis four different structures and the corresponding results and assessment conclusions are accurate.

1. Introduction

The reinforced concrete structure will inevitably be damaged and enter elastoplasticity deformation stage when it is subjected to strong ground motion. In order to determine the appropriate and economical selective intervention or rehabilitation strategy for an existing structure, it is necessary to assess accurately the actual resistance and the potential failure modes. It is also essential to carry out the damage assessment for a new designed building in order to verify that the performance and capacity meet the target specification of the seismic design guideline. Based on broad categories for advanced seismic design approaches, performance-based seismic design (PBSD) is at the forefront of earthquake engineering research [1–3]. One of the primary aspects of PBSD is the realistic characterization of seismic structural damage and its direct incorporation in the design or performance evaluation methodology. The damage assessment based on PBSD is to ensure that the structures achieve the expected targets for different performance requirements.

Structural ductility, storey drift, element and connection rotation, dissipated energy, and fatigue of the structure are the parameters considered for traditional damage assessment

[4]. Based on the fundamental parameters, various local and global damage indices have been proposed to evaluate reinforced concrete structures. Research on the global damage indices is essential because the integral damage assessment should be accurate and involve the damage properties of local elements. However, the global damage indices presented until now have the disadvantages such as limited convergence and not considering cumulative damage. In addition, many damage indices are obtained from pushover analysis and capacity spectrum method whose purpose is to evaluate structural performance under earthquake by overprinting seismic response spectrum curve and structural capacity curve [5]. A significant amount of research has shown that capacity spectrum method can simplify computation, consider the nonlinear performance of the structural elements and finally obtain effective results. Because capacity spectrum method has major simplifications, such as a multi-degree of freedom system being transformed into a single-degree of freedom system, nonlinear time-history analysis being replaced by pushover method, and accumulated dissipative effect not sufficiently considered, thus the evaluation is inexact in some cases, especially for irregular or complex structures. Hence, it is necessary to present a comprehensive

method to combine multiple damage parameters and obtain more accurate results.

Moreover, the uncertainty always affects the modeling and evaluation of real physical phenomena with different intensity, the damage of structures in earthquake is a vague concept because there exists not explicit classification criterion to evaluate different damaged members and the structure with different damaged information. The values from different damage-assessment methods are also different and even distinct. Hence, the seismic damage assessment and the decision problem are very complex for large and complex structure, which needs the integration based on multiclass information, and the combination of different information is a valid method to reduce the deviation and the uncertainty. In the past decades several alternative mathematical approaches to deal with uncertainty have been developed and the main categories methods include fuzzy set theory, artificial neural networks, interval analysis, and convex modeling.

In classical set theory, the membership of elements in a set is assessed in binary terms according to a bivalent condition; that is, an element either belongs or does not belong to the set. By contrast, fuzzy set theory permits the gradual assessment of the membership of elements in a set [6]. This is described with the aid of a membership function valued in the real unit interval $[0, 1]$. Fuzzy sets generalize classical sets, since the indicator functions of classical sets are special cases of the membership functions of fuzzy sets, if the latter only takes value 0 or 1. The fuzzy logic and the fuzzy set provide a powerful tool to solve the uncertainty problem and describe the fuzzy characteristics of the target. Especially, fuzzy logic is fit for describing and processing the uncertain information from multiple sources. In recent years, the methods such as the fuzzy logic system, artificial neural networks, and other soft computing methods develop rapidly, which provides a solid theoretical basis for information fusion and system assessment.

In this paper, the multiple damage indices on displacement and energy for reinforced concrete structures are discussed and applied based on performance-based seismic design and the comprehensive evaluation method is proposed by applying fuzzy set theory. The relationship between the multiple damage factors and the fuzzy damage set is established and an effective and accurate seismic damage-assessment method is presented.

2. Damage-Assessment Index Based on Displacement and Energy

2.1. Damage Index Based on Capacity Curve. The vulnerability of many existing structures may be due to structural weaknesses and low ductility. Common weaknesses in the structural system are due to incomplete load path; strength and stiffness discontinuities, vertical, horizontal and mass irregularities; weak column and strong beam, and eccentricities. Low ductility detailing is characterized as insufficient shear reinforcement, inadequate confinement, and insufficient anchorage length of the beam-reinforcement bars.

The state of damage of a component, a story, or the whole structure may be represented by an index. The damage

index is used as an indicator to describe the state of the lateral load-carrying capacity and the reserve capacity of existing structures. Thus, the study on damage index and its availability is necessary.

Some damage indices are calculated for each component of the building (local damage index). The component damage indices may be integrated using a weighting procedure to provide the global damage index for the structure. These damage indices have been formulated using response parameters of the structure that are obtained through analytical evaluation of structural response. There are several techniques and approaches for damage analysis of structures, such as pushover analysis, nonlinear time history analysis, and vulnerability analysis. The typical response-based damage indices include ductility ratio, interstory drift, slope ratio, maximum drift, flexural damage ratio, low cycle fatigue, final softening index and Park-Ang index. The damage indices such as interstory drift and maximum drift, are fundamental and essential for representing the displacement or deformation.

Though various local and global damage indices were presented, the most acceptable damage index is the Park-Ang damage index combining both ductility and cumulative hysteretic energy demand [7, 8]:

$$D_{PA} = \frac{\delta_m}{\delta_u} + \frac{\beta}{\delta_u F_y} \int dE_h, \quad (1)$$

where δ_m is the maximum experienced deformation, δ_u is the ultimate deformation of the element, F_y is the yield strength of the element, $\int dE_h$ is the hysteretic energy absorbed by the element during the response history, and β is the model constant, parameter, which was suggested to be 0.1 for nominal strength deterioration.

The Park-Ang damage index also has deficiencies even though many modified method were proposed [9–12]. A perfect damage index typically normalizes the damage on a scale of 0 to 1, where zero represents undamaged state while unity represents the collapse state of the building. The maximum of the Park-Ang damage index is over 1 and nearly close to 2 in some cases. In addition, the Park-Ang damage index is not directly suitable for nonlinear static pushover analysis or normal capacity spectrum method because the cumulative damage does not occur in this case.

Based on pushover analysis, a stiffness damage index of the global frame was presented by Ghobarah et al. [4]:

$$D_k = 1 - \frac{k_F}{k_I}, \quad (2)$$

where k_I is the initial slope of the base shear-top deflection relationship resulting from the pushover analysis of the frame before subjecting it to the earthquake ground motion and k_F is the initial slope of the same relationship but after subjecting the frame to the earthquake time history. The values of these damage indices range from zero to one depending on the amount of damage experienced.

Although the stiffness damage index has some advantages such as being concise and using pushover analysis twice

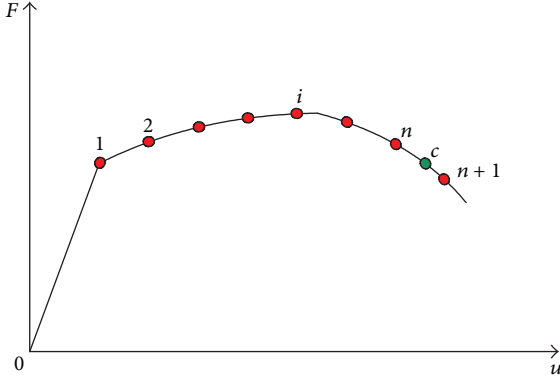


FIGURE 1: Multiple linear force-deformation curve.

without any other dynamic analysis, the limitation is also obvious. The damage evaluation is not accurate for moderate damage and collapse stage and the value may exceed 1 and the index is not obtained taking into account cumulative effect. In general, a new and comprehensive damage index needs to be proposed by combining the stiffness damage index and Park-Ang damage index.

Referring to (2), a similar stiffness damage index is proposed as

$$D_c = 1 - \frac{k_c}{k_0}, \quad (3)$$

where k_0 is the initial stiffness of elastic stage and k_c is the current stiffness.

It is worth noticing that the damage index in (2) and (3) can also be transferred as the index presented by Dipasquale and Cakmak [5].

$$D_c = 1 - \frac{T_0^2}{T_c^2}, \quad (4)$$

where T_0^2 is the initial fundamental period and T_c^2 is the current fundamental period. The equation above is suitable especially for damage assessment based on time-history analysis because the instantaneous fundamental period can be acquired conveniently.

According to (3), the relationship of current force F_c , the current displacement u_c and the damage index are as follows

$$F_c = k_0 (1 - D_c) u_c. \quad (5)$$

Based on the form of (5) The typical skeleton curve or capacity curve of reinforced concrete structure behaves nonlinear or multiple linear, as shown Figure 1, and the current force between the i th point and the $i + 1$ th point can be expressed as

$$F_c = k_0 u_1 + k_1 (u_2 - u_1) + k_2 (u_3 - u_2) + \dots + k_{n-1} (u_n - u_{n-1}) + k_n (u_c - u_n), \quad (6)$$

where $k_i = (F_{i+1} - F_i)/(u_{i+1} - u_i)$.

A general global damage index for capacity curve or skeleton curve is obtained by substituting to (6) in (5) with the following result

$$D_c = 1 - \frac{\sum_{i=0}^{n-1} k_i (u_{i+1} - u_i) + k_n (u_c - u_n)}{k_0 u_c}. \quad (7)$$

Compared to (2), the general global damage index presented in this paper has some advantages as follows: (a) the damage index varies from 0 to 1, rigorously, and has definite mechanical significance. (b) The damage index is calculated based on only one capacity curve that is, only one pushover analysis is carried out (c) the damage index is suitable for the capacity curve and the damage index of any displacement or any force can be obtained.

2.2. Damage-Index Adjustment Considering Hysteretic Energy. During strong earthquakes, the deformation capacity of structures is reduced due to the cumulative damage caused by cyclic load. However, as the deficiency of pushover analysis, the cumulative damage is not embodied sufficiently and the corresponding modified coefficient is essential. A research on equivalent (reduced) ductility factors has been proposed by Fajfar and the cumulative damage effect is taken into account [13].

The total structure can be simplified as an equivalent single-degree-of-freedom ideal elastoplastic system and the following relations are found or defined: $F_y = m\omega^2\delta_y$, $\mu_u = \delta_u/\delta_y$, and $\mu_m = \delta_m/\delta_y$, where F_y is the yield strength of the system, m is the mass, ω is the natural frequency, δ_y is the yield displacement, and μ_u is the normal ductility. δ_m is the monotonic displacement or current displacement and μ_m is the monotonic ductility factor.

The parameter γ , which is a function of dissipated hysteretic energy, maximum displacement, and the natural frequency of the structural system, is introduced as follows:

$$\gamma = \frac{\sqrt{E_H/m}}{\omega\delta_m} = \frac{1}{\mu_u} \sqrt{\frac{E_H}{m}}, \quad (8)$$

where E_h is the total hysteretic energy. The transformation can be obtained as

$$\frac{E_H}{F_y\delta_y} = \gamma^2 \mu_m^2. \quad (9)$$

Substituting to (8) in (1), the Park-Ang damage index is rewritten as

$$D_{PA} = (1 + \beta\gamma^2\mu_u) \frac{\mu_u}{\mu_m}. \quad (10)$$

Thus, the relationship between displacement ductility factor on cumulative damage in earthquake and the displacement ductility factor in monotonic load is as follows:

$$\frac{\mu_u}{\mu_m} = \frac{D_{PA}}{(1 + \beta\gamma^2\mu_u)}. \quad (11)$$

For normal structure, the ratio μ_u/μ_m ranges from 0.65 to 0.85. The result of (11) can also be applied to (7) in order to

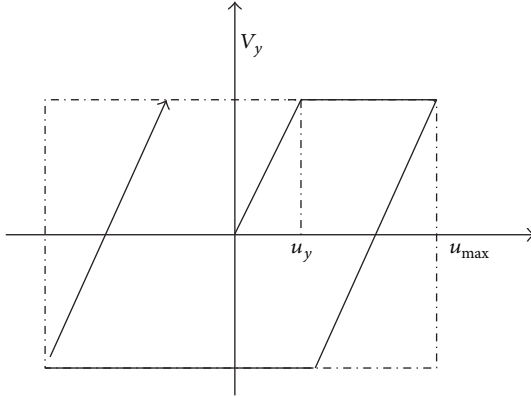


FIGURE 2: Idealized force-deformation behavior.

compute the damage index considering dissipated hysteretic energy. For the capacity point which means the crossover point of the capacity curve and the ductility spectrum curve, the corresponding displacement ductility is viewed as μ_u , but the damage status in pushover analysis is related to the monotonic ductility μ_m , so the displacement on the capacity point is advised to be amplified according to (11) in order to represent the actual damage.

2.3. Number of Inelastic Cycles. From another point of view, the cyclic demand spectrum for use in preliminary seismic assessment and design is necessary and Kunnath proposed a method based on estimating the number of equivalent cycles at a specified ductility [14]. The methodology is determined using well established relationships between seismic input energy and dissipated hysteretic energy.

If symmetric behavior is assumed, a commonly used idealization of the non-linear behavior is the elastic perfectly-plastic behavior shown in Figure 2. Assuming V_y is the yield force, u_y is the yield displacements and u_{\max} is the peak displacements. The energy dissipated by the yielding element per cycle is

$$E_c = 4V_y u_{\max} \left(1 - \frac{1}{\mu_c}\right) = 4\alpha_h V_y u_{\max}, \quad (12)$$

where $\mu_c = u_{\max}/u_y$, is the cyclic displacement ductility factor and α_h is an energy shape factor that depends on both the ductility and the shape of the hysteresis loops. For a non-degrading system subjected to N_f full cycles at the same ductility, the total energy dissipated is the product of N_f and E_c , and the following expression between the number of inelastic cycles and dissipated hysteretic energy can be derived:

$$N_f = \frac{E_h}{(4\alpha_h \mu_c V_y u_y)}. \quad (13)$$

Considering the dynamic characteristics and seismic design parameter, the number of inelastic cycles can also be rewritten as

$$N_f = \left(\frac{r_{hI} E_I}{m}\right) \frac{\pi^2}{\alpha_h \mu_c} \left(\frac{R_\mu}{TS_a}\right)^2 = \left(\frac{r_{hI} \nu_e^2}{2}\right) \frac{\pi^2}{\alpha_h \mu_c} \left(\frac{R_\mu}{TS_a}\right)^2, \quad (14)$$

where $r_{hI} = 1.13(\mu_c - 1)^{0.82}/\mu_c$ is the ratio of hysteresis energy to the total input energy E_I , R_μ is the force-reduction factor and the following expression is used

$$R_\mu = \begin{cases} \frac{(\mu_c - 1)T}{T_0} + 1, & T \leq T_0, \\ \mu_c, & T > T_0, \end{cases} \quad (15)$$

$$T_0 = 0.65T_g(\mu_c)^{0.3},$$

where T is fundamental period and T_g is the characteristic period.

S_a is the design spectral acceleration; ν_e is the equivalent input energy velocity, which is equal to the Fourier amplitude spectrum of the ground acceleration, and the typical expression is

$$\nu_e = \begin{cases} \nu_e^* \left(\frac{2T}{T_g} - \left[\frac{T}{T_g} \right]^2 \right), & T \leq T_g, \\ \nu_e^* \left[\frac{T}{T_g} \right]^{-\lambda}, & T > T_g, \end{cases} \quad (16)$$

$$\nu_e^* = \frac{\ddot{x}_{g \max}}{4\dot{x}_{g \max}} \sqrt{\frac{\lambda + 0.5}{2\lambda + 2} t_d T_g} = 0.22\pi \sqrt{\frac{t_d}{T_g}},$$

where ν_e^* is the peak amplification factor for the input energy spectrum, t_d is the duration for the strong motion phase of the ground motion, and λ is a parameter that characterizes the spectral shape of the input energy spectrum for periods longer than the predominant period of the ground motion.

It is demonstrated that the force-deformation characteristics of the system, the ductility-based force-reduction factor R_μ , and the ground motion characteristics play a significant role in the cyclic demand imposed on a structure during severe earthquakes.

2.4. Coefficient of Hysterisis Energy Concentration. The new and effective global damage indices are described as above. Furthermore, the deformation and hysteresis energy of the special weak stories is important because the structural weakest-part would suffer from severe damages due to its inability to withstand the different types of loads (lateral, vertical and moments) produced by the ground motion [15, 16]. The failure of the weak story can reduce the structural performance though other floors are merely in moderate damage stage. For irregular structures and complex structures, the damage assessment on weak floors is necessary besides the normal analysis carried out.

The coefficient of story yield shear is defined as $\xi_y = V_y/V_e$, where V_y is the yield shear force of a story in the

TABLE 1: Statistical values for story yield shear and hysteresis energy concentration.

Structure	Parameter		
	a_n	b_n	c_n
5-story	-8.50	6.50	3.00
12-story	-10.0	7.02	4.00
20-story	-12.0	8.06	5.00

structure, and V_e is the elastic shear force of the story, that is, the shear force for the same deformation if the structure is elastic. The coefficients of story yield shear in each story are equivalent for a regular structure; otherwise the values diverge. The story belongs to a weak story if the coefficient of story yield shear exceeds the threshold value.

The input energy of a multidegree-of-freedom system sustained to an earthquake depends on the structural mass and initial stiffness, in spite of the yield strength value. The story yield first almost is the story that the elastic displacement is the largest and the inelastic interstory drift is also greater than others. The hysteresis energy of the weak story is also greater than that of other stories.

Based on a large number of nonlinear time-history analyses considering various ground motions, fundamental periods, coefficients of story yield shear, and different number of weak stories, the fitting equation of the coefficient of story yield shear and the coefficient of hysteresis energy concentration is as follows:

$$\eta_n = -a_n \xi_y^2 + b_n \xi_y + c_n, \quad (17)$$

where n is the story number of structure and a_n , b_n , and c_n are the parameters varying with n . The statistical values for the structures with different stories are given in Table 1.

The coefficient of story yield shear in each story used to be over 0.3 even if the normal structures are subjected to severe earthquake. Thus the coefficient of hysteresis energy concentration generally decrease when the coefficient of story yield shear increases. Hence, the energy distribution can be obtained through calculating the coefficient of hysteresis energy and measuring the damage-degree by energy is achieved.

2.5. Damage Grade and Damage Target. According to the discussion above and the damage indices presented, the global damage index and corresponding adjustment are viewed as an accurate damage-evaluation approach and the number of inelastic cycles can fully embody the integral hysteresis. These two damage indices represent the integral damage states in a reinforced concrete structure. On the other hand, the maximum interstory drift and the coefficient of hysteresis energy concentration can represent the local damage details. Hence, all the four damage indices are advised to be combined and used in damage assessment generally.

Taking into account the damage degree description in Table 2 and the empirical values from nonlinear analysis, the damage degree and the limit values for different damage indices are listed in Table 3.

3. Damage-Assessment Based on Fuzzy Set

3.1. Damage Assessment Model Based on Fuzzy Set. In many practical cases, the structural damage is a fuzzy and vague state because there are no obvious and clear grading marks in the actual status; furthermore, the results of damage assessment based on different damage indices disagree in special cases [17]. These problems may occur when data in Table 3 is used without identification and consideration. Thus, this is more scientific and objective for structural damage according to fuzzy set theory by introducing the concept of fuzzy subset and fuzzy membership [18–21]. In classical set theory, the membership of elements in a set is assessed in binary terms according to a bivalent condition; that is, an element either belongs or does not belong to the set. By contrast, fuzzy set theory permits the gradual assessment of the membership of elements in a set; this is described with the aid of a membership function valued in the real unit interval $[0, 1]$. Fuzzy sets generalize classical sets, since the indicator functions of classical sets are special cases of the membership functions of fuzzy sets, if the latter only take the value 0 or 1. The fuzzy decision fusion method realizes the integration fusion by using fuzzy transform principle and maximum membership principle and considering the various factors relevant to the evaluation objects. In the evaluation process, the factors constitute the factor set as $U = \{U_1, U_2, \dots, U_m\}$ according to different extent and the decision is expressed as the decision set as $V = \{V_1, V_2, \dots, V_n\}$.

First, the single factor decision is made for the single factor u_i ($i = 1, 2, \dots, m$) in the factor set U , then the membership degree r_{ij} in the decision degree v_j ($j = 1, 2, \dots, n$) is determined according to u_i . Thus, the single factor decision set for the factor u_i is obtained as $r_i = \{r_{i1}, r_{i2}, \dots, r_{in}\}$, which is the fuzzy subset of the decision set. Hence, considering all the m factors, the general fuzzy decision matrix is constructed as

$$R = \begin{Bmatrix} r_1 \\ \vdots \\ r_m \end{Bmatrix} = \begin{bmatrix} r_{11} & \cdots & r_{1n} \\ \vdots & \ddots & \vdots \\ r_{m1} & \cdots & r_{mn} \end{bmatrix}, \quad (18)$$

where R is the fuzzy relationship between factor domain and decision domain and r_{ij} is the membership degree. Multi-factor decision should consider the weighted grade for each factor in the fusion process. The fuzzy subset $A = \{a_1, a_2, \dots, a_m\}$ is the weighted set in factor domain U , where a_i ($a_i \leq a_i \leq 1$) is the weight value of the single factor u_i in the total decision. When A and R are determined, the fusion is carried out by fuzzy transformation $B = A \circ R$, B is equivalent fuzzy subset in the evaluation set V , the element b_j ($j = 1, 2, \dots, n$) is the fusion result for grade v_j , and \circ is the fuzzy synthesis operator.

The membership function is the normal distribution function $\mu(x) = e^{-(x-k)/t^2}$, where the parameters k and t could be determined according to the following principles: (1) the membership value is 1 when the factor is equal to the mean value, (2) the membership value of the top and bottom limitations in the universe of a fuzzy set can be adjusted to

TABLE 2: Damage-degree description.

Damage degree	Global appearance	Column	Beam
Slight	Sporadic occurrence of cracking	Very fine cracks (less than 0.1 mm)	Very fine cracks (less than 0.1 mm)
Minor	Minor cracks; partial crushing of concrete in columns	Visible cracks (0.1 to 0.2 mm)	Visible shear cracks (near support) or tension cracks (at bottom) (0.1 to 0.2 mm)
Moderate	Extensive large cracks; spalling of concrete in weaker elements	Major portion of outer layer of concrete is spalled but core is intact except for hairline cracks (0.2 to 0.5 mm)	Major portion of outer layer of concrete is spalled but core is intact except for hairline cracks (0.2 to 0.5 mm)
Severe	Extensive crashing of concrete; disclosure of buckled reinforcement	Diagonal/torsional cracks in concrete core (0.5 to 3 mm), opening of tie bars, and buckling of longitudinal bars	Reinforcement and concrete bond is broken, there are cracks in the core concrete (0.5 to 3 mm), and shear tie bar have failed
Collapse	Partial or total collapse of building	Crushing of core concrete at joints and relative movement with respect to slab and other columns (cracks > 3 mm)	Crushing of concrete at supports and excessive deflection

TABLE 3: Damage degree and the limit value for different damage indices.

Seismic fortification level	Frequent earthquake	Moderate earthquake	Rare earthquake		
Damage degree	Intact	Minor damage	Moderate damage	Severe damage	Collapse
Global damage index	0~0.10	0.10~0.30	0.30~0.65	0.65~0.85	0.85~1.0
Number of inelastic cycles	—	—	10~20	4~10	0~4
Maximum interstory drift	0~1/450	1/450~1/300	1/300~1/150	1/150~1/50	>1/50
Coefficient of hysteresis energy concentration	1.0~2.073 + 0.046n	2.073 + 0.046n~2.854 + 0.084n	2.854 + 0.084n~3.346 + 0.113n	3.346 + 0.113n~3.554 + 0.132n	>3.554 + 0.132n

1, and (3) the membership value on the boundary in the universe of a fuzzy set is 0.5.

3.2. Damage Assessment Based on Fuzzy Set. Considering various damage indices for reinforced concrete structures, the damage assessment should use one or multilevel fuzzy fusion. According to the importance and the accuracy of each index, the factor fuzzy vector can be determined by the expert experience or analytic hierarchy process, and the membership function is Gaussian model.

Taking a reinforced concrete structure as an example, the global damage index, the number of inelastic cycles, the maximum interstory drift, and the coefficient of hysteresis energy concentration are the main parameters that accurately reflect the structural damage information and they are easy to obtain. Therefore, these parameters are selected in for fuzzy decision.

The weighted values for the parameters can be determined according to the experts grading method or the analytic hierarchy process (AHP). The AHP is a theory of measurement through pairwise comparisons and relies on the judgments of experts to derive priority scales [22].

Considering the importance and calculation accuracy of the grade index about damage state in the factor domain and the result from AHP, the weight value matrix of the damage index is $A = [0.4, 0.25, 0.2, 0.15]$. The structural damage grade is divided into 5 grades: intact, minor damage, moderate damage, severe damage, and collapse. The damage assessment and grade index are shown in Table 1.

After the fuzzy damage subset is determined, the membership value for the specific damage status in each damage grade can be calculated. In order to meet the requirements of performance-based design, the quantitative description of damage degree is needed. To highlight the dominance hierarchy, the general fuzzy damage index for decision-making is suggested as

$$GFD = \frac{\sum_{i=1}^4 b_i^k Da_i}{\sum_{i=1}^4 b_i^k}, \quad (19)$$

where b_i is the membership value of the i -level damage, Da_i is the median value in the i -level damage and K is the comprehensive adjustment index, where it is recommended that k is taken as 2.

TABLE 4: The results of performance indexes of example structures.

Parameter	Global damage index	Maximum interstory drift	Number of inelastic cycles	Coefficient of hysteresis energy concentration	Equivalent yield displacement (m)	Equivalent ductility factor	Equivalent period (s)
Frame 1	0.783	0.019	10.564	4.201	0.183	2.743	0.411
Frame 2	0.762	0.025	3.338	5.334	0.205	2.126	1.968
Frame 3	0.861	0.043	2.278	4.616	0.229	1.741	1.191
Frame 4	0.726	0.017	6.073	4.238	0.131	2.774	0.752

3.3. *Damage-Assessment Procedure.* In summary, the procedure of damage assessment based on fuzzy set is as follows:

- (1) Determine the decision set as $V = \{V_1, V_2, \dots, V_n\}$ in order to describe the different damage grade and the get the equivalent fuzzy subset B in the evaluation set V .
- (2) Select the factor domain as $U = \{U_1, U_2, \dots, U_m\}$; then the damage factors are determined. The corresponding fuzzy subset $A = \{a_1, a_2, \dots, a_m\}$ is also established.
- (3) The nonlinear response is obtained by pushover analysis and capacity spectrum method and the damage indices are calculated.
- (4) The membership function is calculated and the fuzzy relationship matrix is obtained.
- (5) The equivalent fuzzy subset in the evaluation set V is calculated by $B = A \otimes R$.
- (6) Compute the general fuzzy damage index (GFD) and determine the damage degree of the structure.

4. Case Studies

In order to verify the damage-assessment method based on fuzzy set, four three-dimensional reinforced concrete frames sustained to strong earthquake are selected to be analyzed by pushover analysis and nonlinear dynamic time history analysis using the three-dimensional nonlinear program CANNY [23]. These 4 structures are as follows: 5-story regular frame, 15-story regular frame, 9-story eccentric frame and 4-story partially symmetric frame, as shown in Figure 3. The concrete compressive strength of the columns is 4×10^7 KN/m 2 , the compressive strength of the beams is 3×10^7 KN/m 2 , the yield strength of the main steel bars is 2.35×10^8 KN/m 2 , the reinforcement ratio of the columns and the beams are 2.2% and 1.8%, respectively. According to the corresponding design demand, the dead loads and live loads in all the structures are 1.0 KN/m 2 and 2.0 KN/m 2 respectively, and the loads are transformed as node force in the finite element models. The seismic fortification intensity is 8 and the field type is medium soil.

The lateral load distribution of pushover analysis is adopted as the forms based on the stiffness distribution of each story. The capacity curves of the frames are obtained based on the capacity spectrum method. For the capacity

spectrum method, an equivalent single-degree-of-freedom (ESDOF) system is a simplistic representation of the actual MDOF model, based on properties of the real structure; a bilinear idealization of the pushover curve can be obtained based on the principle of equality of energy.

For the time-history analysis, each group of waves has two orthogonal horizontal components and one vertical component, the three peak accelerations of each group are adjusted into 4.0 m/s^2 , 3.4 m/s^2 and 2.6 m/s^2 , respectively, and the duration is 15 seconds.

Taking Frame 1 and Frame 3 as an example, the capacity curves and demand curves are shown in Figures 4 and 5 and the global damage curves are in Figures 6 and 7 shown respectively. In the figures, the global damage index on the capacity point is adjusted according to (11). The performance indices are calculated based on (7), (11), (14), and (17). The results are listed in Table 4. Damage assessment based on fuzzy set is carried out and the membership function is established according to the method previously described and specified index in Table 3. For example, the membership function of the global damage index is shown in Figure 8.

For frame 1, the fuzzy relation matrix is calculated according to (17) and, combined with the weight value matrix, the fuzzy damage vector is

$$\begin{aligned}
 B_1 &= A \cdot R_1 = [0.4, 0.25, 0.20, 0.15] \\
 &\times \begin{bmatrix} 0 & 0 & 0.116 & 0.926 & 0.236 \\ 0 & 0 & 0.472 & 0.551 & 0.015 \\ 0 & 0 & 0 & 0.618 & 0.447 \\ 0 & 0 & 0.081 & 0.565 & 0.451 \end{bmatrix} \\
 &= [0, 0, 0.177, 0.716, 0.255].
 \end{aligned} \tag{20}$$

Frame 1 is identified as the structure with severe damage according to the fuzzy damage vector, then collapse and finally moderate damage. The first story is weak story according to the results on interstory drift. Equation (4) is applied as the average damage index for frame 1 in seismic time-history analysis, the value is 0.776, and the damage degree and locations are similar to the results of capacity spectrum analysis. The general fuzzy damage index (GFD) is 0.755 and the final assessment value quantized the damage status accurately.

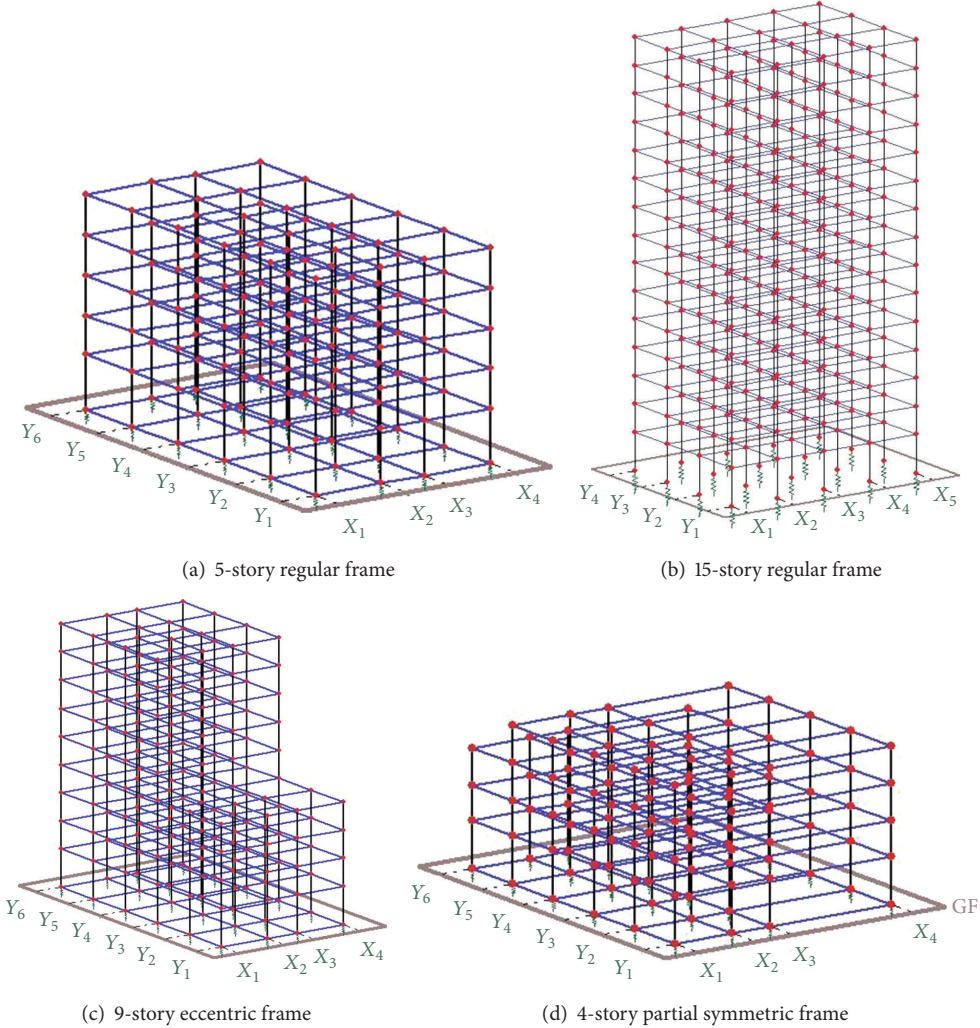


FIGURE 3: Side elevation of the reinforced concrete frames.

For frame 3, the fuzzy damage vector is

$$\begin{aligned}
 B_3 &= A \cdot R_3 = [0.4, 0.25, 0.20, 0.15] \\
 &\times \begin{bmatrix} 0 & 0 & 0.034 & 0.425 & 0.552 \\ 0 & 0 & 0.011 & 0.172 & 0.761 \\ 0 & 0 & 0 & 0 & 1.000 \\ 0 & 0 & 0 & 0 & 1.000 \end{bmatrix} \\
 &= [0, 0, 0.016, 0.213, 0.761].
 \end{aligned} \tag{21}$$

Frame 3 is identified as the structure collapse after earthquake. The top story and the story with irregular stiffness are weak stories according to the results on the interstory drift. The average damage index according to (4) for seismic time-history analysis is 0.856. The general fuzzy damage index (GFD) is 0.858 and the final assessment value is similar to the damage information from the time-history analysis for strong earthquakes.

The important performance results and the fuzzy damage vectors of all the four frames are shown in Table 3 and Figure 9. It is evident that the end deformation of the beam

and column in frame 2 and frame 3 is obvious, the weak stories are in failure, and the whole performance is deficient and will collapse in strong earthquakes, so the maintenance and retrofitting should be carried out. The damage of frame 1 and frame 4 are both severe but the structures still have the capacity and the performance requirements are met. It is obvious that the seismic damage-assessment method based on fuzzy sets is accurate and effective.

5. Conclusion

The damage index is the necessary basis of damage assessment for reinforced concrete structures. Both the global damage index which represents the integrated performance and the local damage index which highlight the damage details are discussed and presented. The response parameters based on displacement and hysteresis energy are all vital especially for the structures subject to earthquake, and the analysis method is suitable for performance-based seismic design and assessment. Though some damage indices such as Park-Ang damage index, are comprehensive and acceptable for normal

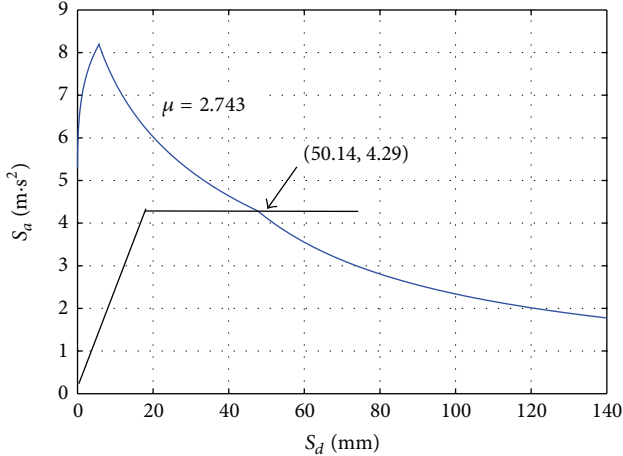


FIGURE 4: Capacity spectrum curve of frame 1.

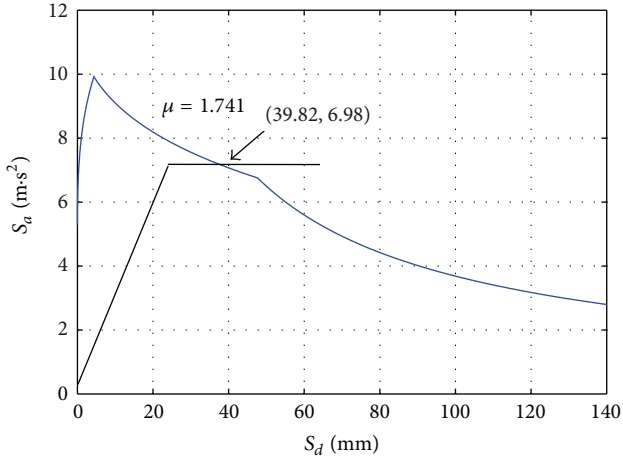


FIGURE 5: Capacity spectrum curve of frame 3.

damage assessment, it is unfortunate that these indices do not converge to unity and are unsuitable for pushover analysis if used directly. A global damage index based on multiple linear force-deformation curves in pushover analysis is presented to evaluate the integrate damage of reinforced concrete structure. The modified coefficient is provided considering the cyclic load and hysteresis energy. The number of inelastic cycles is introduced for the consideration of cyclic loads and hysteresis energy. The coefficient of hysteresis energy concentration is presented as a damage index which reflects the property and failure of the weak story. Thus, the global damage index, the number of inelastic cycles, the maximum interstory drift, and the coefficient of hysteresis energy concentration are all used as the damage indices of damage assessment.

In order to harmonize the different effects and weights, and reduce the uncertainty in the damage assessment, the fuzzy set theory is introduced, and the factor domain, the decision set, the fuzzy subset and the membership function are presented. The relation between the multiple damage

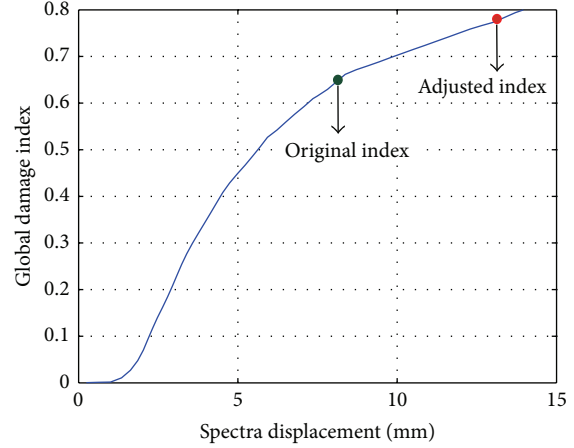


FIGURE 6: Curves of global damage index of frame 1.

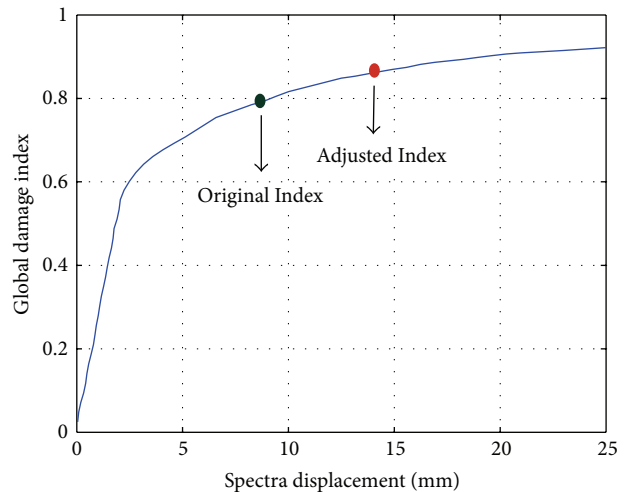


FIGURE 7: Curves of global damage index of frame 3.

indices or factors and the fuzzy damage set is established by comprehensive fuzzy evaluation based on fuzzy mathematics. The fuzzy seismic damage-assessment method is verified through nonlinear analysis for four different structures and the corresponding results and assessment conclusions are accurate, especially when compared with the responses from nonlinear time-history analysis.

The performance-based fuzzy seismic damage-assessment method presented in this paper can be improved and developed in some aspects such as determining the weight values by analytic hierarchy process (AHP) method and considering the multiple dimensional ground motion and the torsional effect in the irregular structures. Furthermore, the performance-based assessment including the foundation and the nonstructural components can also be established based on fuzzy evaluation system.

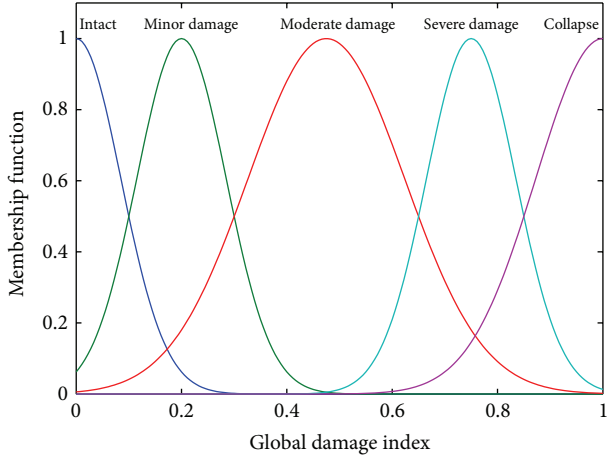


FIGURE 8: Membership grade of the global damage index.

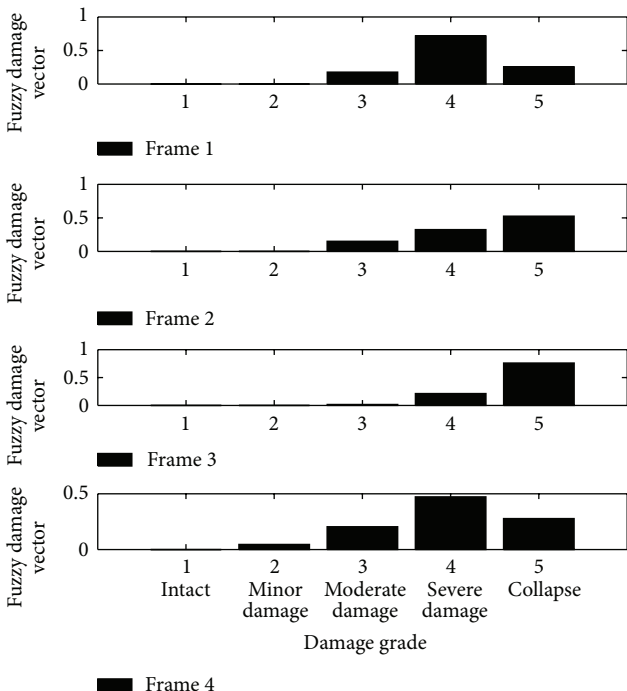


FIGURE 9: Damage grade for different frames.

Acknowledgments

This work is partially supported by Natural Science Foundation of China under Grant nos. 51008009 and 50878010, Foundation of the Ministry of Education of China for Outstanding Young Teachers in University under Grant no. 20111103120022, and Foundation of Beijing Key Lab of Earthquake Engineering and Structural Retrofit under Grant no. 2013TS02.

References

- [1] SEAOC, *Vision 2000: Performance Based Seismic Engineering of Buildings*. Sacramento (CA, USA), Structural Engineers Association of California, 1995.
- [2] A. Ghobarah, "Performance-based design in earthquake engineering: state of development," *Engineering Structures*, vol. 23, no. 8, pp. 878–884, 2001.
- [3] M. J. N. Priestley, G. M. Calvi, and M. J. Kowalsky, *Displacement Based Seismic Design of Structures*, IUSS Press, Pavia, Italy, 2007.
- [4] A. Ghobarah, H. Abou-Elfath, and A. Biddah, "Response based damage assessment of structures," *Earthquake Engineering & Structural Dynamics*, vol. 28, no. 1, pp. 29–104, 1999.
- [5] E. Dipasquale and A. S. Cakmak, "On the relation between local and global damage indices," Technical Report NCEER-89-0034, State University of New York at Buffalo, 1989.
- [6] P. Fajfar, "Capacity spectrum method based on inelastic demand spectra," *Earthquake Engineering & Structural Dynamics*, vol. 28, no. 5, pp. 979–993, 1999.
- [7] L. A. Zadeh, "Fuzzy sets," *Information and Control*, vol. 8, no. 3, pp. 338–353, 1965.
- [8] Y. J. Park, A. H. S. Ang, and Y. K. Wen, "Seismic damage analysis and damage limiting design of R.C. buildings," Structural Research Serial Report UILU-ENG-84-2007, University of Illinois at Urbana-Champaign, Urbana, Ill, USA, 1984.
- [9] Y.-J. Park and A. H.-S. Ang, "Mechanistic seismic damage model for reinforced concrete," *Journal of Structural Engineering*, vol. 111, no. 4, pp. 722–739, 1985.
- [10] D. Datta and S. Ghosh, "Uniform hazard spectra based on Park-Ang damage index," *Journal of Earthquake and Tsunami*, vol. 2, no. 3, pp. 241–258, 2008.
- [11] S. Ghosh, D. Datta, and A. A. Katakdhond, "Estimation of the Park-Ang damage index for planar multi-storey frames using equivalent single-degree systems," *Engineering Structures*, vol. 33, no. 9, pp. 2509–2524, 2011.
- [12] A. Massumi and E. Moshtagh, "A new damage index for RC buildings based on variations of nonlinear fundamental period," *The Structural Design of Tall and Special Buildings*, vol. 22, no. 1, pp. 50–61, 2013.
- [13] P. Fajfar, "Consistent inelastic design spectra: hysteretic and input energy," *Earthquake Engineering & Structural Dynamics*, vol. 23, no. 3, pp. 523–537, 1994.
- [14] S. K. Kunnath and Y. H. Chai, "Cumulative damage-based inelastic cyclic demand spectrum," *Earthquake Engineering & Structural Dynamics*, vol. 33, no. 4, pp. 499–520, 2004.
- [15] L. Ye and S. Otani, "Maximum seismic displacement of inelastic systems based on energy concept," *Earthquake Engineering & Structural Dynamics*, vol. 28, no. 12, pp. 1483–1499, 1999.
- [16] C.-C. Chou and C.-M. Uang, "A procedure for evaluating seismic energy demand of framed structures," *Earthquake Engineering & Structural Dynamics*, vol. 32, no. 2, pp. 229–244, 2003.
- [17] Y. S. Petryna and W. B. Krätsig, "Compliance-based structural damage measure and its sensitivity to uncertainties," *Computers and Structures*, vol. 83, no. 14, pp. 1113–1133, 2005.
- [18] M. Sugeno, *Industrial Applications of Fuzzy Control*, Elsevier Science, New York, NY, USA, 1985.
- [19] E. Cox, *The Fuzzy Systems Handbook*, Academic Press, New York, NY, USA, 2nd edition, 1999.
- [20] H. Y. Guo, "Structural damage detection using information fusion technique," *Mechanical Systems and Signal Processing*, vol. 20, no. 5, pp. 1173–1188, 2006.
- [21] I. Andreadis, I. Tsiftzis, and A. Elenas, "Intelligent seismic acceleration signal processing for damage classification in buildings," *IEEE Transactions on Instrumentation and Measurement*, vol. 56, no. 5, pp. 1555–1564, 2007.

- [22] N. Bhushan and K. Ria, *Strategic Decision Making: Applying the Analytic Hierarchy Process*, Springer, London, UK, 2004.
- [23] K. N. Li. CANNY99, *Three-Dimensional Nonlinear Dynamic Structural Analysis Computer Program Package*, CANNY Consultants PTE, Singapore, 1998.

Research Article

An Exact Approach for Structural Damage Assessment

Q. W. Yang

Department of Civil Engineering, Shaoxing University, Shaoxing 312000, China

Correspondence should be addressed to Q. W. Yang; yangqiuwei79@gmail.com

Received 10 August 2013; Accepted 28 October 2013

Academic Editor: Yuri Petryna

Copyright © 2013 Q. W. Yang. This is an open access article distributed under the Creative Commons Attribution License, which permits unrestricted use, distribution, and reproduction in any medium, provided the original work is properly cited.

An exact approach is proposed for damage identification in statically determinate structures. The contribution of this study is twofold. Firstly, a rigorous disassembly formulation of structural global flexibility matrix is presented based on the matrix spectral decomposition, which can provide an exact relationship between the modifications of structural stiffness parameters and the associated flexibility matrix. Secondly, the static minimum-rank flexibility change is derived to obtain the exact flexibility change before and after damage. The proposed method is economical in computation and is simple to implement. For the statically determinate structures, the proposed method can exactly compute the elemental perturbed stiffness parameter only using a few of incomplete static displacement data. The efficiency of the proposed method is demonstrated by two statically determinate structures.

1. Introduction

Detection, localization, and quantification of damage in a structure via techniques that examine changes in measured structural static/dynamic response have attracted much attention in recent years. The basic idea of this technique is that structural response parameters are functions of structural physical properties (mass, damping, and stiffness). Therefore, changes in the physical properties will cause changes in the response parameters. Recent surveys on the technical literature show that extensive efforts have been developed to find reliable and efficient numerical and experimental models to identify damage in structures [1–12].

One important group of damage identification methods is the perturbation-based techniques [13–35]. These methods start with the derivatives of the response parameters to changes in material and physical parameters. These sensitivity coefficients are then used to calculate changes in the parameters that would force the analysis response parameters to match those measured in test. The common advantage of these methods is that they can detect structural damage by directly using the incomplete modal parameters without any eigenvector expansion or model reduction [24, 25]. However, the efficiency of perturbation analysis methods is limited because these methods are complicated and may be only suitable for small modifications of structural parameters [35].

For the cases with relatively large modifications of structural parameters, the first-order perturbation may be inaccurate. It has been pointed out that when the change of structural parameter is more than 15%, the second-order perturbation should be taken into account [36]. As an alternative, some researches [33–35] have used the iteration scheme to tackle the large damage case. It is anticipated that the computational cost of these existing sensitivity methods will be very expensive for large damage case, since a higher-order approximation should be performed or an iteration scheme must be used to estimate the perturbation parameters more precisely.

To avoid the above shortcomings, an exact flexibility perturbation technique is developed in the paper for structural damage detection. The contribution of the present study is twofold. Firstly, a rigorous disassembly formulation of structural global flexibility matrix is presented based on the matrix spectral decomposition, which can provide an exact relationship between the modifications of structural stiffness parameters and the associated flexibility matrix. Secondly, a static minimum-rank formulation of structural flexibility change is presented to obtain the exact flexibility change before and after damage. The most significant advantage of the proposed method is that it is economical in computation and is simple to implement. Regardless of whether the damage is small or large, the proposed method can accurately

compute the elemental perturbed stiffness parameter only using a few of incomplete static displacements without any higher-order approximation or iteration. In the following theoretical development, it is assumed that structural damages only reduce the system stiffness matrix and structural refined FEM has been developed before damage occurrence.

2. Theoretical Development

2.1. The Disassembly Formulation of Structural Flexibility Matrix Based on Spectral Decomposition. The developed theory begins with the disassembly of the $(n \times n)$ global stiffness matrix K , which can be obtained by the elemental eigenparameter decomposition technique [16, 23] as

$$K = CPC^T, \quad (1)$$

where the $(n \times N)$ matrix C is defined as the stiffness connectivity matrix representation of the connectivity between DOFs and the $(N \times N)$ diagonal matrix P has the elemental stiffness parameters p_i ($i = 1 \sim N$) as its diagonal entries and n is the number of DOFs and N is the number of elemental stiffness parameters. The columns of matrix C physically embody the stiffness contribution to the global stiffness matrix in terms of the elemental stiffness parameters p_i . The diagonal entries p_i in the matrix P consist of the material and sectional properties of the element. The matrix C is independent of P and unchanged as damage occurs. A full description of the elemental eigenparameter decomposition technique can be seen in [16, 23]. According to (1), it is important to note that $N \geq n$ and the matrix C is of full rank ($\text{rank}(C_{n \times N}) = n$) because K is of full rank ($\text{rank}(K_{n \times n}) = n$). Assuming that α_i ($0 \leq \alpha_i \leq 1$) is the i th elemental stiffness perturbation parameter, the value of α_i is 0 if the i th element is undamaged and α_i is 1 or less than 1 if the corresponding element is completely or partially damaged. Then the global stiffness matrix of the damaged structure can be assembled as

$$K_d = CP_d C^T, \quad (2)$$

in which

$$P_d = \begin{bmatrix} p_1(1 - \alpha_1) & & & \\ & p_2(1 - \alpha_2) & & \\ & & \ddots & \\ & & & p_N(1 - \alpha_N) \end{bmatrix}. \quad (3)$$

The stiffness matrix perturbation ΔK can be expressed as

$$\begin{aligned} \Delta K &= K - K_d = C\Delta PC^T, \\ \Delta P &= \text{diag}(p_1\alpha_1, p_2\alpha_2, \dots, p_N\alpha_N). \end{aligned} \quad (4)$$

Now we turn our attention to investigating the disassembly formulation of structural global flexibility matrix. For the statically determinate structures, as will be shown in Section 3, $n = N$ is valid. Then the disassemblies of the $(n \times n)$ global flexibility matrices F and F_d , for the undamaged and damaged structure, can be given as

$$F = (C^{-1})^T P^{-1} C^{-1}, \quad (5)$$

$$F_d = (C^{-1})^T P_d^{-1} C^{-1}. \quad (6)$$

Apparently, (5) and (6) can be easily proved by $F \cdot K = F_d \cdot K_d = I_{n \times n}$. Letting

$$B = P^{-1}, \quad (7)$$

$$B_d = P_d^{-1}, \quad (8)$$

$$D = (C^{-1})^T, \quad (9)$$

then (5) and (6) can be rewritten as

$$F = DBD^T, \quad (10)$$

$$F_d = DB_d D^T. \quad (11)$$

From (10) and (11), it can be seen that the disassembly of the global flexibility matrix is similar in form to that of the stiffness matrix. Similarly, the matrix D is defined as the flexibility connectivity matrix and the diagonal entry b_i in B is defined as the i th flexibility parameter ($b_i = 1/p_i$). Subtracting (10) from (11), the flexibility matrix perturbation ΔF can be given as

$$\Delta F = D\Delta BD^T \quad (12)$$

in which the diagonal matrix ΔB is

$$\Delta B = B_d - B$$

$$= \begin{bmatrix} b_1 \left(\frac{1}{1 - \alpha_1} - 1 \right) & & & \\ & b_2 \left(\frac{1}{1 - \alpha_2} - 1 \right) & & \\ & & \ddots & \\ & & & b_N \left(\frac{1}{1 - \alpha_N} - 1 \right) \end{bmatrix}. \quad (13)$$

Define β_i to be the i th elemental perturbed flexibility parameter that satisfies

$$\beta_i = \frac{1}{1 - \alpha_i} - 1, \quad (14)$$

$$\Delta B = \text{diag}(b_1\beta_1, b_2\beta_2, \dots, b_N\beta_N). \quad (15)$$

From (14), the perturbed stiffness parameter α_i and the perturbed flexibility parameter β_i are related as follows:

$$\beta_i = \frac{\alpha_i}{1 - \alpha_i}, \quad (16)$$

or

$$\alpha_i = \frac{\beta_i}{1 + \beta_i}. \quad (17)$$

According to the above discussion, if the perturbed stiffness parameter α_i is given, we can obtain the exact ΔF by the course $\alpha_i \xrightarrow{(16)} \beta_i \xrightarrow{(12)} \Delta F$. Conversely, if ΔF is given, we can also obtain exact α_i by $\Delta F \xrightarrow{(12)} \beta_i \xrightarrow{(17)} \alpha_i$.

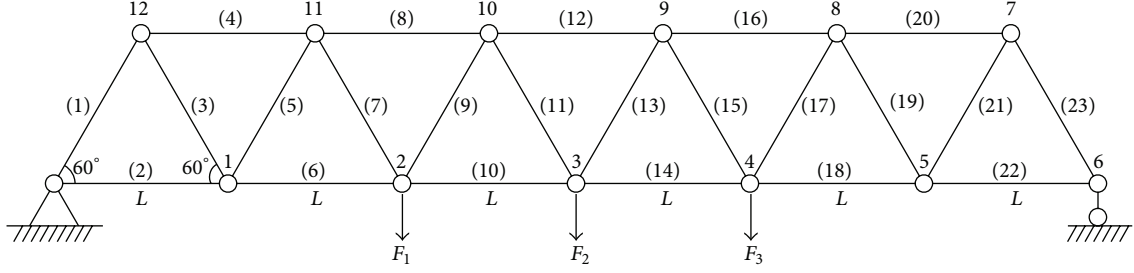


FIGURE 1: 23-bar truss structure with the static loads for Example 1.

2.2. The Static Minimum-Rank Formulation of Structural Flexibility Change. For the damage identification problem, ΔF can be firstly estimated by structural dynamic or static test, and then the stiffness perturbation parameters α_i ($i = 1 \sim N$) can be calculated by $\Delta F \xrightarrow{(12)} \beta_i \xrightarrow{(17)} \alpha_i$. To obtain the exact ΔF before and after damage, a static minimum-rank formulation of structural flexibility change is presented in this section by using a few of static displacement data. For an intact structure, the analytical static model can be expressed as

$$Ku_j = l_j, \quad (18)$$

where u_j is the displacement vector under the applied static load vector l_j and $j = 1, \dots, m$ as it is assumed that only m static load vectors are used. Rewriting (18), one has

$$u_j = Fl_j. \quad (19)$$

Similarly, the displacement vector u_{dj} for the damaged structure can be obtained by

$$u_{dj} = F_d l_j. \quad (20)$$

Therefore the change of the displacement vector Δu_j can be obtained as

$$\Delta u_j = \Delta F \cdot l_j. \quad (21)$$

For $j = 1 \sim m$, (21) can be written in matrix form as

$$\Delta F \cdot L = \Delta U, \quad (22)$$

where

$$\begin{aligned} \Delta U &= [\Delta u_1, \Delta u_2, \dots, \Delta u_m], \\ L &= [l_1, l_2, \dots, l_m]. \end{aligned} \quad (23)$$

Similar to the minimum-rank method [37, 38], the minimal rank solution of (22) for symmetric ΔF is given as

$$\Delta F = \Delta U (\Delta U^T L)^{-1} \Delta U^T. \quad (24)$$

2.3. Damage Detection. This section presents a step-by-step summary of the whole technique as follows.

TABLE 1: Load cases for Example 1.

Load case	Loads
1	$F_1 = 10 \text{ KN}; F_2 = 0; F_3 = 0$.
2	$F_1 = 10 \text{ KN}; F_2 = 10 \text{ KN}; F_3 = 0$.
3	$F_1 = 10 \text{ KN}; F_2 = 10 \text{ KN}; F_3 = 10 \text{ KN}$.

Step 1. Calculate ΔF by (24). In this step, the static displacement data of the damaged structure can be obtained by a static test on it, and the static parameters of the undamaged structure can be obtained by the analytical static model or through a static test on the intact structure.

Step 2. Compute the flexibility connectivity matrix D by (9) for the statically determinate structures.

Step 3. Compute the perturbed flexibility parameters β_i ($i = 1 \sim N$) by (12).

Step 4. Calculate the perturbed stiffness parameters α_i ($i = 1 \sim N$) using (17). Then structural damage can be assessed from these parameters.

3. Numerical Examples

To illustrate characteristics of the proposed damage detection algorithm, two statically determinate structures are presented. Example 1 is a 23-bar plane truss structure and Example 2 is a cantilever beam with 12 elements.

Example 1. A 23-bar truss structure (shown in Figure 1) is used in this example to verify the proposed method. The basic parameters of the structure are as follows: Young's modulus $E = 200 \text{ GPa}$, density $\rho = 7.8 \times 10^3 \text{ Kg/m}^3$, length of each bar $L = 1 \text{ m}$, and cross-sectional area $A = 0.004 \text{ m}^2$. It is noted that this example is a statically determinate structure ($N = n = 23$). Three load cases are shown in Table 1. The displacement data are contaminated with 3% random noise to simulate measurement error. Two damage scenarios were considered. The first one is a small damage case that elements 6, 12, and 17 are assumed to be damaged with stiffness losses of 15%, 15%, and 20%, respectively. The second scenario is a large damage case that elements 6, 12, and 17 have 60%, 70%, and 80% reductions in stiffness, respectively. Figure 2 shows the damage detection results for the small damage case and

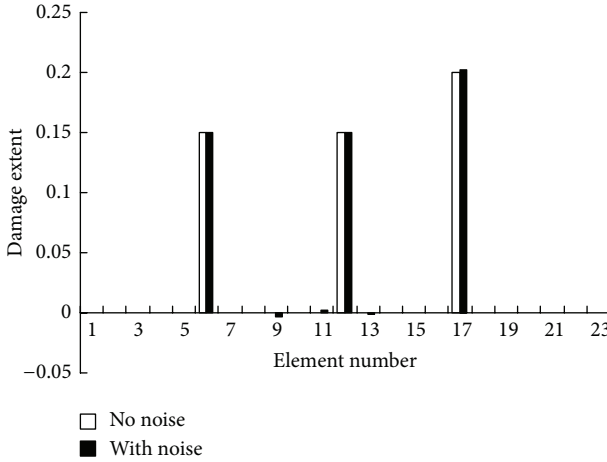


FIGURE 2: Damage detection results when elements 6, 12, and 17 are damaged with stiffness losses of 15%, 15%, and 20% (Example 1).

Figure 3 gives the identification results of the large damage case, respectively. For the small damage case, the calculated damage extents in Figure 2 without noise for elements 6, 12, and 17 are $\alpha_6 = 0.1500$, $\alpha_{12} = 0.1500$, and $\alpha_{17} = 0.2000$, which are exactly the assumed values (15%, 15%, and 20%). When 3% noise is introduced, the corresponding calculated damage extents are $\alpha_6 = 0.1499$, $\alpha_{12} = 0.1496$, and $\alpha_{17} = 0.2017$, which track the assumed values closely. For the large damage case, the calculated damage extents in Figure 3 without noise for elements 6, 12, and 17 are $\alpha_6 = 0.6000$, $\alpha_{12} = 0.7000$, and $\alpha_{17} = 0.8000$, which are exactly the assumed values (60%, 70%, and 80%). When 3% noise is introduced, the corresponding calculated damage extents are $\alpha_6 = 0.5897$, $\alpha_{12} = 0.7029$, and $\alpha_{17} = 0.7888$, which have 1.7%, 0.4%, and 1.4% relative errors as compared to the assumed values, respectively. From the above results, it is obvious that the stiffness perturbation parameter α_i can be computed exactly by the proposed method for the error-free case regardless of whether the damage is small or large. When noise is considered, the predicted damage extents only have slight deviation from the true values because of the error in the measured data.

One of the main disadvantages of the proposed method is that the static loading conditions should be the same for the undamaged and damaged structures. In practice, it is very difficult to reproduce the same loading conditions in both cases. In this example, in order to investigate the effect of changes in the loading conditions on the damage detection, random errors of up to 7% in the static data of the original system are introduced to simulate the loading condition change to a certain extent. And then the damage detection result for the large damage case is shown in Figure 4. It can be seen from Figure 4 that the prediction obtained is also reasonable.

Example 2. The second example is a cantilever beam as shown in Figure 5. The basic parameters of the structure are as follows: Young's modulus $E = 200$ GPa, density

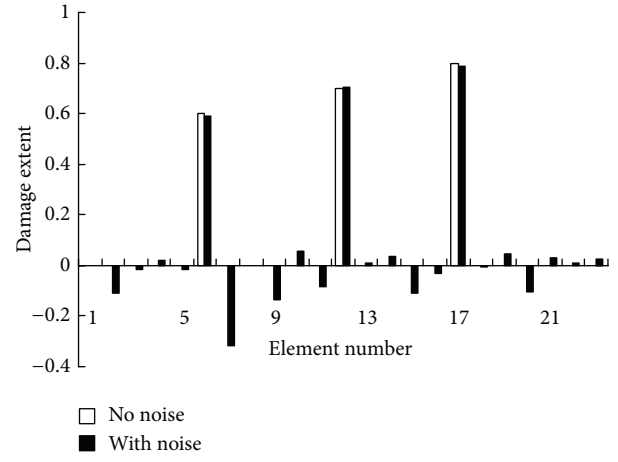


FIGURE 3: Damage detection results when elements 6, 12, and 17 are damaged with stiffness losses of 60%, 70%, and 80% (Example 1).

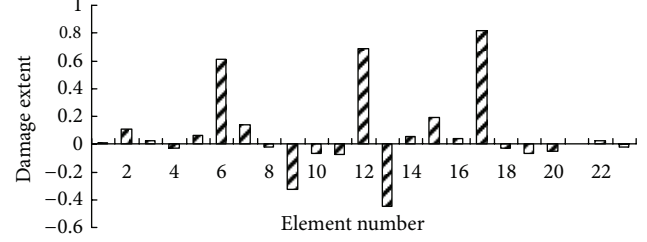


FIGURE 4: Damage detection results considering the loading condition change simulated by adding 7% noise in the static data of the original system (Example 1: large damage case).

TABLE 2: Load cases for Example 2.

Load case	Loads
1	$F_1 = 10$ KN; $F_2 = 0$; $F_3 = 0$; $F_4 = 0$.
2	$F_1 = 10$ KN; $F_2 = 10$ KN; $F_3 = 0$; $F_4 = 0$.
3	$F_1 = 10$ KN; $F_2 = 10$ KN; $F_3 = 10$ KN; $F_4 = 0$.
4	$F_1 = 10$ KN; $F_2 = 10$ KN; $F_3 = 10$ KN; $F_4 = 10$ KN.

$\rho = 7.8 \times 10^3$ Kg/m³, moment of inertia $I = 1.0416 \times 10^{-6}$ m⁴, and cross-sectional area $A = 0.0025$ m². The beam is modeled using 12 elements giving 24 DOFs (12 translational, 12 rotational) and the length of each element is $L = 0.1$ m. It is noted that this example is also a statically determinated structure ($N = n = 24$). Four load cases are shown in Table 2. As before, the displacement data are contaminated with 3% random noise to simulate measurement error. Furthermore, only the transnational DOFs are used in the calculation of ΔF since it is difficult to measure the rotational DOFs. Two damage scenarios were considered. The first one is a small damage case that elements 4 and 9 are assumed to be damaged with stiffness losses both of 15%. The second scenario is a large damage case that elements 4 and 9 have 70% and 80% reductions in stiffness, respectively. Figure 6 shows the damage detection results for the small damage case and Figure 7 gives the identification results of the large damage

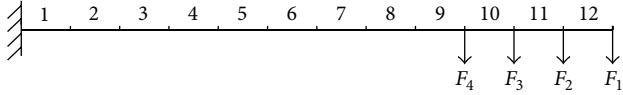


FIGURE 5: A cantilever beam with the static loads for Example 2.

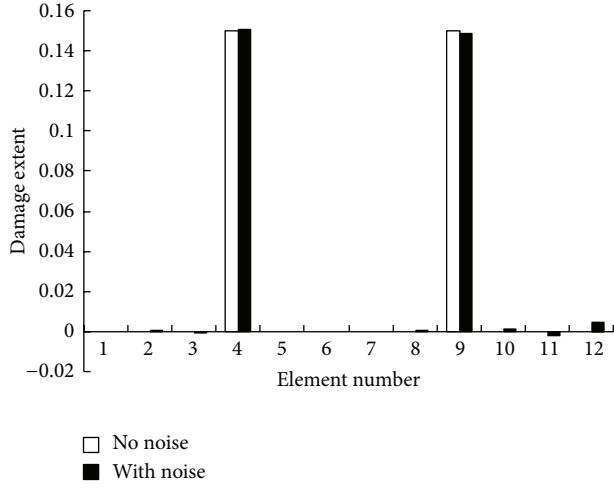


FIGURE 6: Damage detection results when elements 4 and 9 are damaged with stiffness losses both of 15% (Example 2).

case, respectively. For the small damage case, the calculated damage extents in Figure 6 without noise for elements 4 and 9 are $\alpha_4 = 0.1500$ and $\alpha_9 = 0.1500$, which are exactly the assumed values (15%, 15%). When 3% noise is introduced, the corresponding calculated damage extents are $\alpha_4 = 0.1505$ and $\alpha_9 = 0.1490$, which track the assumed values closely. For the large damage case, the calculated damage extents in Figure 7 without noise for elements 4 and 9 are $\alpha_4 = 0.7000$ and $\alpha_9 = 0.8000$, which are exactly the assumed values (70%, 80%). When 3% noise is introduced, the corresponding calculated damage extents are $\alpha_4 = 0.7008$ and $\alpha_9 = 0.7987$, respectively. It can be seen from Figures 6 and 7 that, only using the incomplete displacement data, precise results can be obtained by the proposed method for both small damage case and large damage case. It has been shown that the presented damage detection approach has remarkable advantage over the previous perturbation techniques in tackling the large damage case.

In many cases, the flexibility is estimated in an approximate way by using modal parameters [39, 40] as

$$\Delta F_m^d = \sum_{j=1}^m \frac{1}{\lambda_{dj}} \phi_{dj} \phi_{dj}^T - \sum_{j=1}^m \frac{1}{\lambda_j} \phi_j \phi_j^T, \quad (25)$$

where ΔF_m^d is the dynamic flexibility change using the first m modes, m is the number of measured modes in modal survey, ϕ_j and ϕ_{dj} are the eigenvectors of undamaged and damaged structures, and λ_j and λ_{dj} are the corresponding eigenvalues, respectively. Apparently, the modal truncation in the computation of dynamic flexibility change will have an adverse effect on the damage detection. In this study, the eigenvalue

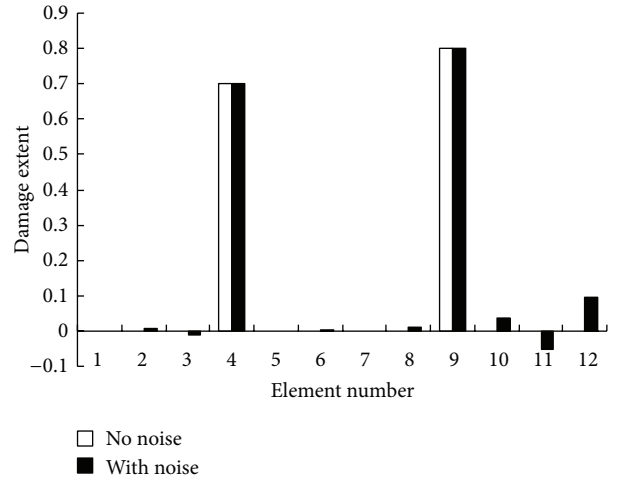


FIGURE 7: Damage detection results when elements 4 and 9 are damaged with stiffness losses of 70% and 80% (Example 2).

decomposition of dynamic flexibility change is used to reduce the effects of modal truncation and measurement noise on the damage detection. Performing an eigenvalue decomposition of ΔF_m^d one can write

$$\Delta F_m^d = U \Lambda U^T, \quad (26)$$

where $U = [u_1, u_2, \dots, u_n]$ is the eigenvector matrix consisting of the eigenvectors u_i ($i = 1 \sim n$) and Λ is the eigenvalue matrix whose diagonal entries are the eigenvalues of ΔF_m^d , that is, $\text{diag}(\Lambda) = (\sigma_1, \sigma_2, \dots, \sigma_n)^T$. In actual applications ΔF_m^d will have some negative eigenvalues. It is noted that ΔF_m^d obtained by a truncated set of modes using (26) is usually less than the exact change of structural flexibility. So one can have an intuitive guess that the negative eigenvalues of ΔF_m^d show the influence of the modal truncation in the computation of the dynamic flexibility change. Hence, all the negative eigenvalues should be set to zeros to reduce the errors caused by the modal truncation. On the other hand, when the damage is severe, the change in structural flexibility caused by the measurement noise is smaller than that caused by the damage. One can have another intuitive that the relatively smaller positive eigenvalues of ΔF_m^d can be seen as a product of the measurement errors and they will also be set to zero to reduce the influence of measurement errors. As a result, the filtered dynamic flexibility change can be obtained as

$$\Delta F_f^d = \sum_i^r (u_i \sigma_i u_i^T), \quad (27)$$

where r is the number of relatively larger entries in Λ , $\sigma_1, \sigma_2, \dots, \sigma_r$ are the relatively larger eigenvalues of ΔF_m^d , and u_1, u_2, \dots, u_r are the corresponding eigenvectors. In this example, only the first four modes are used to calculate the dynamic flexibility change by (26) and the modes are contaminated with 3% random noise to simulate measurement error.

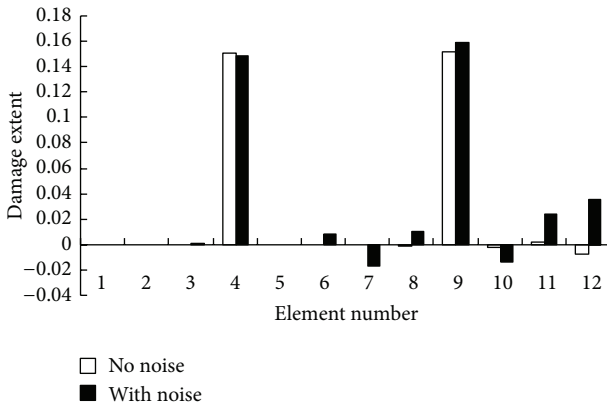


FIGURE 8: Damage detection results for the small damage case using the dynamic flexibility change (Example 2).

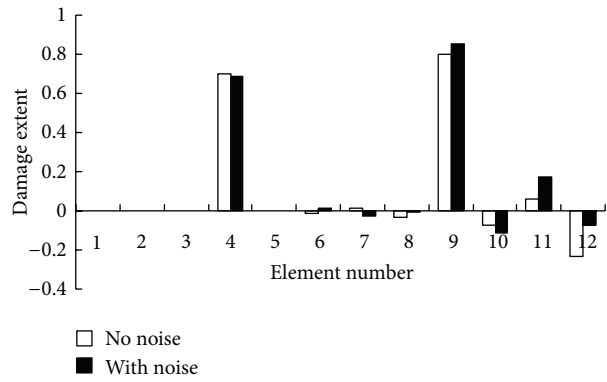


FIGURE 9: Damage detection results for the large damage case using the dynamic flexibility change (Example 2).

Figures 8 and 9 show the damage assessment results using the dynamic flexibility change for the small and large damage cases, respectively. It has been shown that the proposed method is applicable when the flexibility is estimated in an approximate way by using modal parameters.

4. Conclusions

An exact flexibility perturbation technique for damage identification in statically determinate structures has been developed in this study, which is based on matrix spectral decomposition and minimum-rank update theory. The most significant advantage of the proposed procedure is that it can obtain reliable extent of damage only by simple computation without any higher-order approximation or iteration, regardless of whether the damage is small or large. Two numerical examples are used to exercise this process and measurement noise is also simulated in damage detection. The results show the good efficiency and stability of the proposed method on the identification of damage on more than one element. It has been shown that the proposed procedure may be a promising method in structural damage identification. Future research on the technique can be carried out to tackle

the damage detection problem of the statically indeterminate structures, to compare the method with other damage assessment techniques, and to demonstrate the procedure using experimentally measured data.

Acknowledgments

This work is supported by National Natural Science Foundation of China (11202138) and Zhejiang Province Natural Science Foundation (Y1110949).

References

- [1] J. E. Mottershead and M. I. Friswell, "Model updating in structural dynamics: a survey," *Journal of Sound and Vibration*, vol. 167, no. 2, pp. 347–375, 1993.
- [2] M. I. Friswell and J. E. Mottershead, *Finite Element Model Updating in Structural Dynamics*, vol. 38 of *Solid Mechanics and Its Applications*, Kluwer Academic Publishers Group, Dordrecht, The Netherlands, 1995.
- [3] Y. Zou, L. Tong, and G. P. Steven, "Vibration-based model-dependent damage (delamination) identification and health monitoring for composite structures—a review," *Journal of Sound and Vibration*, vol. 230, no. 2, pp. 357–378, 2000.
- [4] F. K. Chang, *Structural Health Monitoring, Current Status and Perspectives*, Technomic Publishing, Lancaster, Pa, USA, 1997.
- [5] O. S. Salawu, "Detection of structural damage through changes in frequency: a review," *Engineering Structures*, vol. 19, no. 9, pp. 718–723, 1997.
- [6] S. V. Modak, T. K. Kundra, and B. C. Nakra, "Comparative study of model updating methods using simulated experimental data," *Computers and Structures*, vol. 80, no. 5-6, pp. 437–447, 2002.
- [7] A. Alvandi and C. Cremona, "Assessment of vibration-based damage identification techniques," *Journal of Sound and Vibration*, vol. 292, no. 1-2, pp. 179–202, 2006.
- [8] A. Prinaris, S. Alampalli, and M. Ettouney, "Review of remote sensing for condition assessment and damage identification after extreme loading conditions," in *Proceedings of the Structures Congress*, April 2008.
- [9] S. Kanev, F. Weber, and M. Verhaegen, "Experimental validation of a finite-element model updating procedure," *Journal of Sound and Vibration*, vol. 300, no. 1-2, pp. 394–413, 2007.
- [10] Q. W. Yang and J. K. Liu, "Structural damage identification based on residual force vector," *Journal of Sound and Vibration*, vol. 305, no. 1-2, pp. 298–307, 2007.
- [11] C. Rainieri, G. Fabbrocino, and E. Cosenza, "Integrated seismic early warning and structural health monitoring of critical civil infrastructures in seismically prone areas," *Structural Health Monitoring*, vol. 10, no. 3, pp. 291–308, 2011.
- [12] H.-F. Lam and T. Yin, "Dynamic reduction-based structural damage detection of transmission towers: practical issues and experimental verification," *Engineering Structures*, vol. 33, no. 5, pp. 1459–1478, 2011.
- [13] C. N. Wong, J. C. Chen, and W. M. To, "Perturbation method for structural damage detection of multi-storey buildings," in *Proceedings of the International Conference on Structural Dynamics, Vibration, Noise and Control*, 1995.
- [14] H. F. Lam, J. M. Ko, and C. W. Wong, "Localization of damaged structural connections based on experimental modal and

- sensitivity analysis," *Journal of Sound and Vibration*, vol. 210, no. 1, pp. 91–114, 1998.
- [15] J. V. A. Santos, C. M. Mota Soares, C. A. Mota Soares, and H. L. G. Pina, "A damage identification numerical model based on the sensitivity of orthogonal conditions," in *Advances in Computational Structural Mechanics*, B. H. V. Topping, Ed., pp. 215–222, Civil-Comp Press, Edinburgh, UK, 1998.
- [16] D. Wu and S. S. Law, "Eigen-parameter decomposition of element matrices for structural damage detection," *Engineering Structures*, vol. 29, no. 4, pp. 519–528, 2007.
- [17] L. Yu, L. Cheng, L. H. Yam, and Y. J. Yan, "Application of eigenvalue perturbation theory for detecting small structural damage using dynamic responses," *Composite Structures*, vol. 78, no. 3, pp. 402–409, 2007.
- [18] C. R. Ashokkumar and N. G. R. Iyengar, "Partial eigenvalue assignment for structural damage mitigation," *Journal of Sound and Vibration*, vol. 330, no. 1, pp. 9–16, 2011.
- [19] Z. Yang and L. W. Le Wang, "Structural damage detection by changes in natural frequencies," *Journal of Intelligent Material Systems and Structures*, vol. 21, no. 3, pp. 309–319, 2010.
- [20] H. Zhu, L. Li, and X.-Q. He, "Damage detection method for shear buildings using the changes in the first mode shape slopes," *Computers and Structures*, vol. 89, no. 9–10, pp. 733–743, 2011.
- [21] R. Perera and A. Ruiz, "A multistage FE updating procedure for damage identification in large-scale structures based on multiobjective evolutionary optimization," *Mechanical Systems and Signal Processing*, vol. 22, no. 4, pp. 970–991, 2008.
- [22] Q. W. Yang, "A mixed sensitivity method for structural damage detection," *Communications in Numerical Methods in Engineering*, vol. 25, no. 4, pp. 381–389, 2009.
- [23] Q. W. Yang and J. K. Liu, "Damage identification by the eigenparameter decomposition of structural flexibility change," *International Journal for Numerical Methods in Engineering*, vol. 78, no. 4, pp. 444–459, 2009.
- [24] B. Weber and P. Paultre, "Damage identification in a truss tower by regularized model updating," *Journal of Structural Engineering*, vol. 136, no. 3, pp. 307–316, 2010.
- [25] A. P. Adewuyi and Z. S. Wu, "Modal macro-strain flexibility methods for damage localization in flexural structures using long-gage FBG sensors," *Structural Control and Health Monitoring*, vol. 18, no. 3, pp. 341–360, 2011.
- [26] M. P. Limongelli, "Frequency response function interpolation for damage detection under changing environment," *Mechanical Systems and Signal Processing*, vol. 24, no. 8, pp. 2898–2913, 2010.
- [27] A. M. G. D. Lima, A. W. Faria, and D. A. Rade, "Sensitivity analysis of frequency response functions of composite sandwich plates containing viscoelastic layers," *Composite Structures*, vol. 92, no. 2, pp. 364–376, 2010.
- [28] W.-J. Yan and W.-X. Ren, "A direct algebraic method to calculate the sensitivity of element modal strain energy," *International Journal for Numerical Methods in Biomedical Engineering*, vol. 27, no. 5, pp. 694–710, 2011.
- [29] Z. R. Lu and S. S. Law, "Differentiating damage effects in a structural component from the time response," *Mechanical Systems and Signal Processing*, vol. 24, no. 8, pp. 2914–2928, 2010.
- [30] Z. R. Lu, M. Huang, and J. K. Liu, "State-space formulation for simultaneous identification of both damage and input force from response sensitivity," *Smart Structures and Systems*, vol. 8, no. 2, pp. 157–172, 2011.
- [31] C. N. Wong, H.-Z. Huang, J. Xiong, and H. L. Lan, "Generalized-order perturbation with explicit coefficient for damage detection of modular beam," *Archive of Applied Mechanics*, vol. 81, no. 4, pp. 451–472, 2011.
- [32] J. Li, B. Wu, Q. C. Zeng, and C. W. Lim, "A generalized flexibility matrix based approach for structural damage detection," *Journal of Sound and Vibration*, vol. 329, no. 22, pp. 4583–4587, 2010.
- [33] Z. Y. Shi, S. S. Law, and L. M. Zhang, "Damage localization by directly using incomplete mode shapes," *Journal of Engineering Mechanics*, vol. 126, no. 6, pp. 656–660, 2000.
- [34] C. N. Wong, W. D. Zhu, and G. Y. Xu, "On an iterative generalized-order perturbation method for multiple structural damage detection," *Journal of Sound and Vibration*, vol. 273, no. 1–2, pp. 363–386, 2004.
- [35] H.-P. Chen, "Efficient methods for determining modal parameters of dynamic structures with large modifications," *Journal of Sound and Vibration*, vol. 298, no. 1–2, pp. 462–470, 2006.
- [36] S. H. Chen, *Matrix Perturbation Theory in Structure Dynamics*, International Academic Publishers, 1993.
- [37] D. C. Zimmerman, "Statistical confidence using minimum rank perturbation theory," *Mechanical Systems and Signal Processing*, vol. 20, no. 5, pp. 1155–1172, 2006.
- [38] K. D'Souza and B. I. Epureanu, "Damage detection in nonlinear systems using system augmentation and generalized minimum rank perturbation theory," *Smart Materials and Structures*, vol. 14, no. 5, pp. 989–1000, 2005.
- [39] F. N. Catbas and A. E. Aktan, "Condition and damage assessment: issues and some promising indices," *Journal of Structural Engineering*, vol. 128, no. 8, pp. 1026–1036, 2002.
- [40] R. Perera, R. Marin, and A. Ruiz, "Static-dynamic multi-scale structural damage identification in a multi-objective framework," *Journal of Sound and Vibration*, vol. 332, no. 6, pp. 1484–1500, 2013.

Research Article

Study of the Residual Strength of an RC Shear Wall with Fractal Crack Taking into Account Interlocking Interface Phenomena

O. Panagouli and K. Iordanidou

Laboratory of Structural Analysis and Design, Department of Civil Engineering, University of Thessaly, Pedion Areos, 38334 Volos, Greece

Correspondence should be addressed to O. Panagouli; olpanag@uth.gr

Received 10 July 2013; Revised 25 September 2013; Accepted 2 October 2013

Academic Editor: Anaxagoras Elenas

Copyright © 2013 O. Panagouli and K. Iordanidou. This is an open access article distributed under the Creative Commons Attribution License, which permits unrestricted use, distribution, and reproduction in any medium, provided the original work is properly cited.

In the present paper, the postcracking strength of an RC shear wall element which follows the construction practices applied in Greece during the 70s is examined by taking into account the complex geometry of the crack of the wall and the mixed friction-plastification mechanisms that develop in the vicinity of the crack. Due to the significance of the crack geometry, a multiresolution analysis based on fractal geometry is performed, taking into account the size of the aggregates of concrete. The materials (steel and concrete) are assumed to have elastic-plastic behaviour. For concrete, both cracking and crushing are taken into account in an accurate manner. On the interfaces of the crack, unilateral contact and friction conditions are assumed to hold. For every structure corresponding to each resolution of the interface, a classical Euclidean problem is solved. The obtained results lead to interesting conclusions concerning the influence of the simulation of the geometry of the fractal crack on the mechanical interlock between the two faces of the crack, a factor which seems to be very important to the postcracking strength of the lightly reinforced shear wall studied here.

1. Introduction

Many RC structures are facing a number of challenges, that is, earthquakes, hurricanes, and so forth, which may threaten their safety and serviceability. Therefore, modern structures built in seismic prone areas are designed to have significant bending and shear strength and ductility. However, existing structures designed according to earlier versions of the seismic codes and constructed using low strength materials usually have inadequate shear strength. For that, shear cracks appear in the shear wall elements of these structures reducing their overall capacity.

Generally, cracks are of large interest in RC structures since their properties reflect not only the condition of concrete as material but also the condition of the entire system at structural level. Crack width is commonly used as a convenient indicator of damage to RC elements, but it should be noted that the distribution and the geometry of the cracks are also important in measuring the extent of damage

presented in the structure [1, 2] and in calculating the residual strength of it.

It is well known that the geometry of the interfaces of a crack is of fundamental importance to the study of friction, wear, and also strength evaluation. The recent research of fractured surfaces of various materials provides a deeper insight into the geometry of cracks. The corresponding research on metals [3] and on concrete and rocks [4–8] showed that the fractured surfaces hold fractal properties in a well-defined scale range. In the case of concrete the effects of aggregates sizes and the quality of concrete on the fractality of fractured surfaces were also investigated in [9–12], respectively. Therefore, an accurate description of the geometry of crack interfaces is of great importance for the simulation of contact. It is important to mention here that the actual contact between two real interfaces is realized only over a small fraction in a discrete number of areas. Consequently, the real contact area is only a fraction of the apparent area [13, 14], and the parameters of the actual

contact regions are strongly influenced by the roughness of the contacting surfaces.

The multiscale nature of the surface roughness suggests the use of fractal geometry. The fractal approach adopted here for the simulation of the geometry of the cracks formed in a shear wall uses computer generated self-affine curves for the modelling of the interface roughness, which is strongly dependent on the values of the structural parameters of these curves. The computer generated fractal interfaces, which are based on a given discrete set of interface data, are characterized by a precise value of the resolution δ of the interface. This fact permits the study of the interface roughness on iteratively generated rough profiles, making this approach suitable for engineering problems, since it permits the satisfactory study of the whole problem with reliable numerical calculations.

The aim of this paper is to study how the resolution of a fractal crack \mathcal{F} affects the strength of a reinforced concrete shear wall element. On the interface between the two cracked surfaces, unilateral contact and friction conditions are assumed to hold. The applied approach takes into account the nonlinear behaviour of the materials, including the limited strength of concrete under tension. The shear wall is submitted to shear loading. As a result of the applied approach, the contribution of the friction between the cracked surfaces is taken into account, as well as the additional strength coming from the mechanical interlock between the two faces of the crack. For every structure resulting for each resolution of the interface, a classical Euclidean problem is solved by using a variational formulation [15]. It must be mentioned here that the finest resolution of the interface is related to the size of the aggregates.

2. Fractal Representation of Rough Surfaces

The fractal nature of material damage has been a matter of a very intense research during the last three decades. The fractal nature of fractured surfaces in metals was shown more than 30 years ago by Mandelbrot et al. [3]. More specifically, it was shown that the fractured surfaces in metals develop a fractal structure over more than three orders of magnitude. In quasibrittle materials, observations have shown that fractured surfaces display self-affine scale properties in a certain range of scales which is in most cases very large and which greatly depends on the material microstructure. This is true for a large variety of quasibrittle materials such as rock, concrete, and ceramics [4–8, 16–18].

Fractal sets are characterized by noninteger dimensions [19]. The dimension of a fractal set in plane can vary from 0 to 2. Accordingly, by increasing the resolution of a fractal set, its length tends to 0 if its dimension is smaller than 1 (totally disconnected set) or tends to infinity if it is larger than 1. In these cases, the length is a nominal, useless quantity since it changes as the resolution increases. Conversely, the fractal dimension of a fractal set is a parameter of

great importance because of its scale-independent character.

Many methods which are based on experimental or numerical calculations, such as the Richardson method [19], have been developed for the estimation of the fractal dimension of a curve. According to this method, dividers, which are set to a prescribed opening δ , are used. Moving with these dividers along the curve so that each new step starts where the previous step leaves off, one obtains the number of steps $N(\delta)$. The curve is said to be of fractal nature if, by repeating this procedure for different values of δ , the relation

$$N(\delta) \sim \delta^{-D} \quad (1)$$

is obtained in some interval $\delta^* < \delta < \Delta^*$. The power D denotes the fractal dimension of the profile, which is in the range $1 < D < 2$. The relation between the fractal dimension D of this profile and the dimension of the corresponding surface is $D_s = D + 1$ [16].

In relation (1) there is an upper and a lower bound in the scaling range and, consequently, a transition from the fractal regime at the microscopic level to the Euclidean regime at largest scales. The upper bound is represented by the macroscopic size of the set, while the lower one is related to the size of the smallest measurable particles, that is, the aggregates in the case of concrete. Mandelbrot [20] first pointed out the transition from a fractal regime characterized by noninteger dimensions to the homogeneous one characterized by classical topological dimensions, a fact which points out the main difference between mathematical and physical fractals.

The idea of self-affinity is very popular in studying surface roughness because experimental studies have shown that, under repeated magnifications, the profiles of real surfaces are usually statistically self-affine to themselves [3, 21]. The self-affine fractals were used in a number of papers as a tool for the description of rough surfaces [22–28]. Typically, such a profile can be measured by taking height data y_i with respect to an arbitrary datum at N equidistant discrete points x_i . In the sequence, fractal interpolation functions $\mathcal{F}(x_i) = y_i$, $i = 0, 1, \dots, N$ are used for the passage from this discrete set of data $\{(x_i, y_i), i = 0, 1, 2, \dots, N\}$ to a continuous model. According to the theory of Barnsley [29], the sequence of functions $\mathcal{F}_{n+1}(x) = (T\mathcal{F}_n)(x) = c_i l_i^{-1}(x) + d_i \mathcal{F}_n(l_i^{-1}(x)) + g_i$ converges to a fractal curve \mathcal{F} as $n \rightarrow \infty$. The transformation l_i transforms $[x_0, x_N]$ to $[x_{i-1}, x_i]$, and it is defined by the relation $l_i(x) = a_i x + b_i$. The calculation of the parameters a_i, b_i, c_i , and g_i is based on the given set of data and the free parameters d_i .

Fractal interpolation functions give profiles which look quite attractive from the viewpoint of a graphic roughness simulation. In higher approximations, these profiles appear rougher as it is shown in the next section where the first to fifth approximations of a fractal interpolation function are presented. Moreover, the roughness of the profile is strongly affected by the free parameters d_i of the interpolation functions. As these parameters take larger values, the resulting profiles appear rougher with sharper peaks.

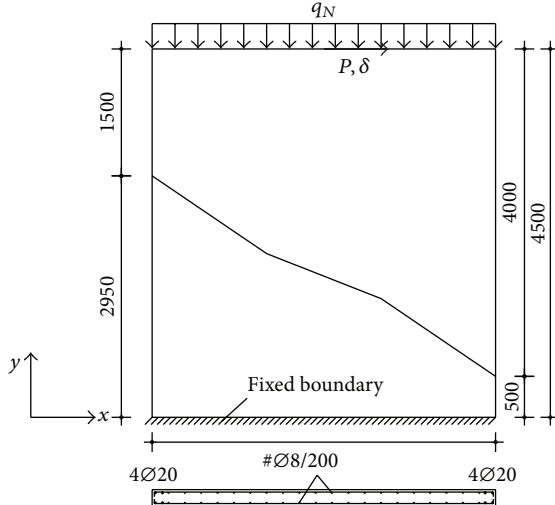


FIGURE 1: The considered shear wall.

Another model of self-affine profiles, which can be used for roughness description, is the multilevel hierarchical profile. This profile has a hierarchical structure and is constructed by using a certain iterative scheme presented in [24]. As in the case of the fractal interpolation functions, the surfaces produced by this scheme are characterized by a precise value of the resolution δ of the fractal curve. More specifically, in both cases, the iterative construction of the profiles permits us to analyse “prefractals” of arbitrary generation and, therefore, of arbitrary resolution δ_n .

It must be mentioned here that an important advantage of the fractal interpolation functions presented in [29] and of the multilevel hierarchical approach presented in [24] is that their fractal dimension can be obtained analytically and it depends strongly on their construction parameters. Thus, in the case of fractal interpolation functions which are used in this paper for the simulation of the geometry of the crack, the fractal dimension D is given by the relation

$$\sum_{i=1}^N |d_i| a_i^{D-1} = 1. \quad (2)$$

3. Description of the Considered Problem

In Figure 1, an RC shear wall element which follows the construction practices applied in Greece during the 70s is presented. More specifically, the wall is reinforced by a double steel mesh consisting of horizontal and vertical rebars having a diameter of 8 mm and a spacing of 200 mm. The quality of the steel mesh is assumed to be S220 (typical for buildings of that age). At the two ends of the wall, the amount of reinforcement is higher. Four 20 mm rebars of higher quality (S400) are used without specific provisions to increase the confinement. The thickness of the wall is 200 mm and the quality of concrete is assumed to be C16, typical for this kind of constructions. The wall is fixed on the lower horizontal boundary.

TABLE 1: Characteristics of the considered structures.

Iteration (n)	Resolution δ_n (m)	Interface length L_n (m)
1st	1.404	4.888
2nd	0.468	4.946
3rd	0.156	5.080
4th	0.052	5.373
5th	0.017	5.935

The considered shear wall is divided into two parts by a crack which has been formed due to shear failure of concrete. It is important to be mentioned here that, in low strength concretes, as in the case examined here, the fractured surfaces are rougher compared to the fractured surfaces developed in high strength concretes [12] because in the first case the cracks are developed in the contact zone between the aggregates and the cement paste, whereas in the second case the failure of the aggregates ensures a less rough interface. For the description of the roughness of the crack, the notion of fractals is used. More specifically, the crack is described by a fractal interpolation function which interpolates the set of data $\{(-1.0, 2.95), (0.4, 2.0), (1.8, 1.0), (3.2, 0.5)\}$. The free parameters of the function are taken to have the values $d_1 = d_2 = d_3 = 0.50$ in order for the interface to be rough (the fractal dimension of the interface results to be equal to 1.369).

The computer generated interfaces $\mathcal{F}_n, n = 1, 2, \dots$ are “prefractals” images of the fractal set characterized by a precise value of the resolution δ_n , which is related to the n th iteration of the fractal interpolation function and represents the characteristic linear size of the interface. As it is shown in Figure 2 where five iterations of a fractal interface are given, the linear size of the interface changes rapidly when higher iterations are taken into account. In Table 1, the characteristics of each resolution are presented. More specifically, in the second column, the resolution of the interface δ_n is given, whereas in the third column the total crack length L_n is presented.

The objective here is to estimate the capacity of the shear wall under an action similar to the one that has created the crack. For this reason, a horizontal displacement of 20 mm is applied on the upper side of the wall (see Figure 1). Moreover, a vertical distributed loading q_N is applied on the upper horizontal boundary, creating a compressive axial loading. The resultant of this loading is denoted by N . For N , six different values will be considered from 0 to 2.500 kN with a step of 500 kN.

For the modelling of the above problem it is assumed that the opposite sides of the fracture are perfectly matching surfaces in a distance of 0.1 mm and the finite element method is used. In order to avoid a much more complicated three-dimensional analysis, two-dimensional finite elements were employed; however, special consideration was given to the incorporation of the nonlinearities that govern the response of the wall. More specifically, the mass of concrete was modelled through quadrilateral and triangular plain stress elements. The finite element discretization density is similar for all the considered problems [30] in order for the discretization density not to affect the comparison between

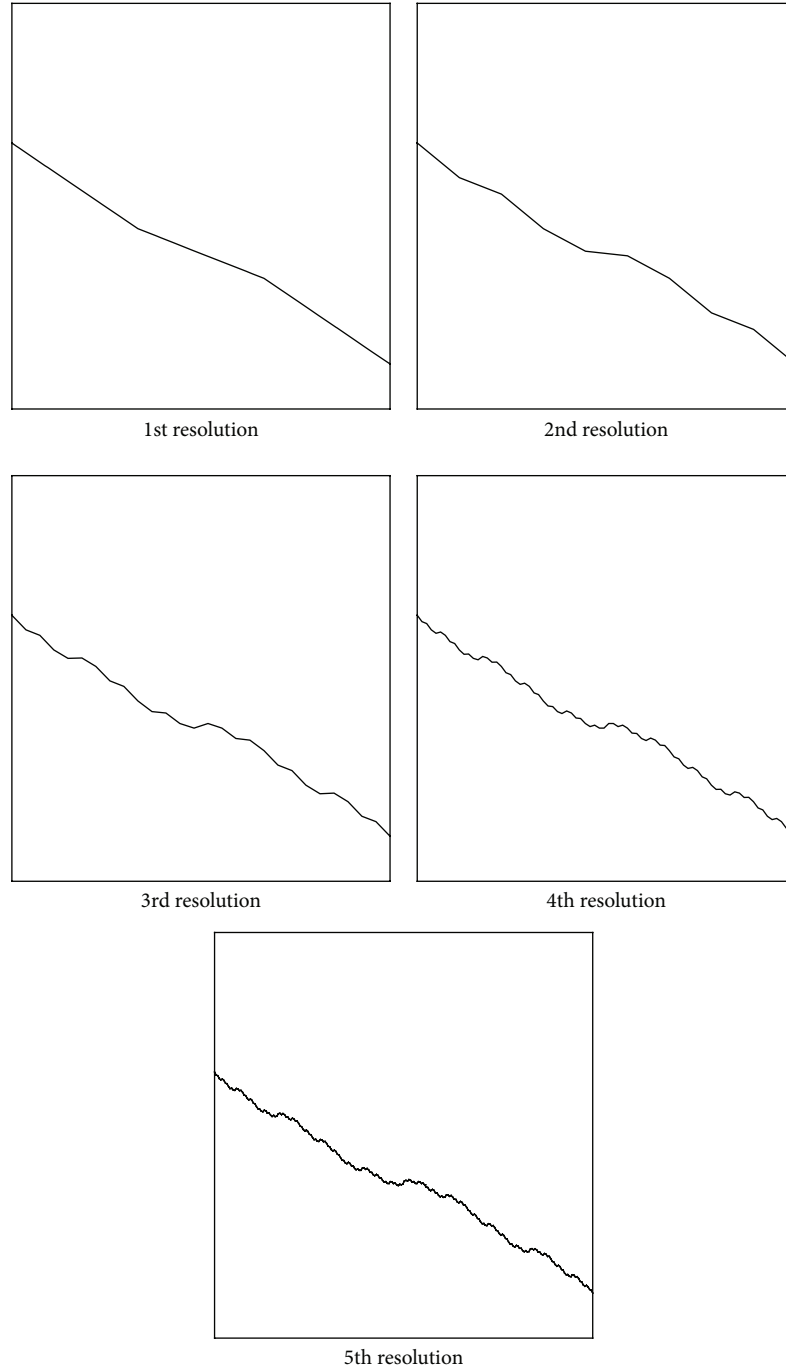


FIGURE 2: The first five resolutions of the fractal crack.

the results of the various analyses that were performed. The modulus of elasticity for the elements representing the mass of concrete was taken to be equal to $E = 21$ GPa and the Poisson's coefficient to be equal to $\nu = 0.16$. The material was assumed to follow the nonlinear law depicted in Figure 3(a). Under compression, the material behaves elastoplastically, until a total strain of 0.004. After this strain value crushing develops in concrete, leading its strength to zero. A more complicated behaviour is considered under tension. More specifically, after the exhaustion of the tension strength of

concrete, a softening branch follows, having a slope $k_s = 10$ GPa. Progressively the tension strength of concrete is also zeroed. The above unidirectional nonlinear law is complemented by an appropriate yield criterion (Tresca) which takes into account the two-dimensional stress fields that develop in the considered problem. For the simulation of cracking, a smeared crack algorithm is used, in which the cracks are evenly distributed over the area of each finite element [31].

The steel rebars were modelled through two-dimensional beam elements, which were connected to the same grid of

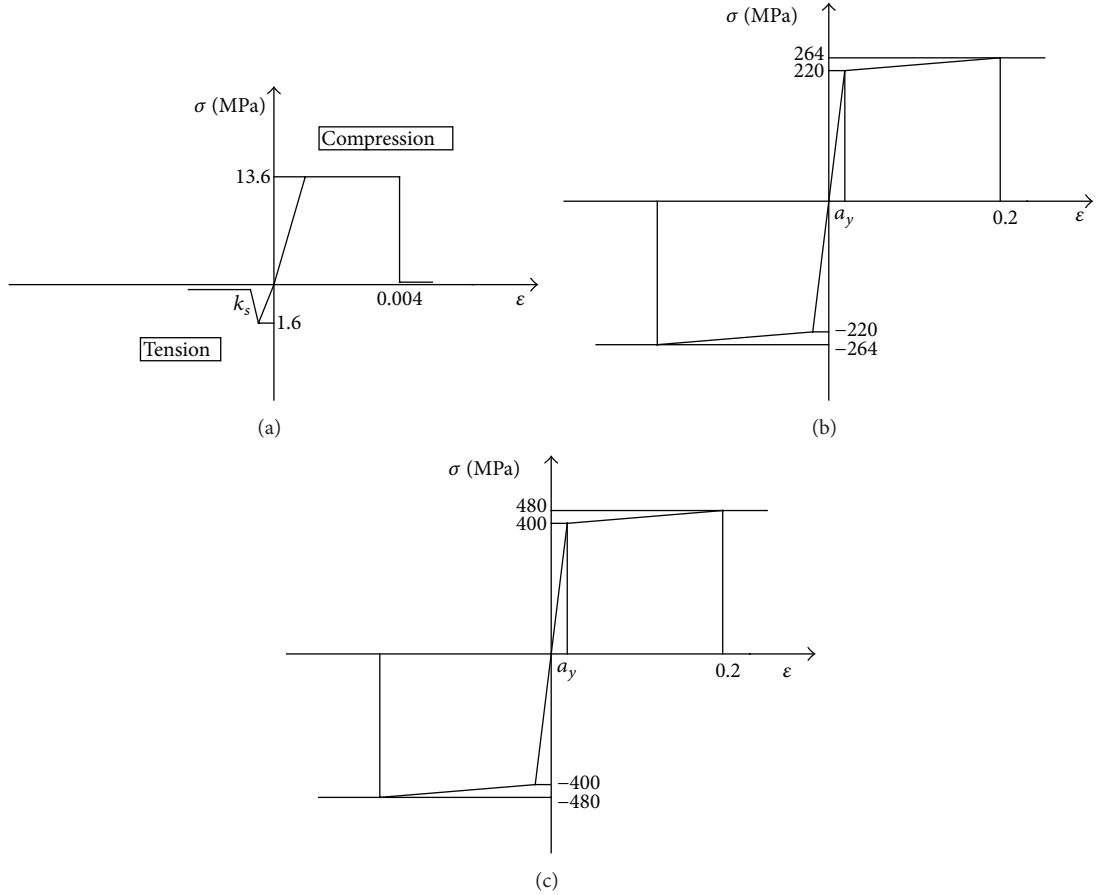


FIGURE 3: The adopted materials laws: (a) C16 concrete, (b) S220 steel, and (c) S400 steel.

nodes as the plain stress elements simulating the concrete. At each position, the properties that were given to the steel rebars take into account the reinforcement that exists in the whole depth of the wall. For example, the horizontal and vertical elements that simulate the steel mesh are assigned an area of 100.48 mm^2 that corresponds to the cross-sectional area of two 8 mm steel rebars. For simplicity, the edge reinforcements ($4\phi 20$) were simulated by a single row of beam elements that have an area of 1256 mm^2 (i.e., $4 \times 314 \text{ mm}^2$). For the steel rebars, a modulus of elasticity $E = 210 \text{ GPa}$ was assumed. Moreover, the nonlinear laws of Figures 3(b) and 3(c) which exhibit a hardening branch, after the yield stress of the material is attained, were considered for S220 and S400 steel qualities, respectively.

Figure 4 depicts the finite element discretizations for the structures that correspond to the third, fourth, and fifth iterations of the fractal crack. The grey lines in the finite element meshes correspond to the positions of the steel rebars. Special attention was given in the modelling so that the steel rebars retain their initial horizontal and vertical positions, that is, no eccentricity exists between the corresponding rows of beam finite elements due to the formation of the crack.

In this paper, only the finite element models corresponding to the 3rd, 4th, and 5th resolutions of the fractal crack

were considered, because 1st and 2nd resolutions do not have a meaning from the engineering point of view. On the other hand, the 5th resolution gives a good lower bound of δ because δ_5 is related to the size of the aggregates of concrete.

At the interfaces, unilateral contact and friction conditions were assumed to hold. The Coulomb's friction model was followed with a coefficient equal to 0.6. At each scale, a classical Euclidean problem is solved by using a variational formulation [15].

For every value of the vertical loading N , a solution is taken in terms of shear forces and horizontal displacements at the interface, for different values of the resolution of the cracked wall and for the case of the uncracked wall. The aim of this work is to study the behaviour of the shear wall, that is, the behaviour of concrete and the forces in the rods, as the vertical loading and the resolution of the interface change.

Two cases are considered:

- (i) In the first case, the wall is uncracked;
- (ii) In the second case, where a fractal crack \mathcal{F} has been developed in the wall, different resolutions are taken into account in order to examine how the resolution of a fractal interface \mathcal{F} affects the strength of the RC shear wall element.

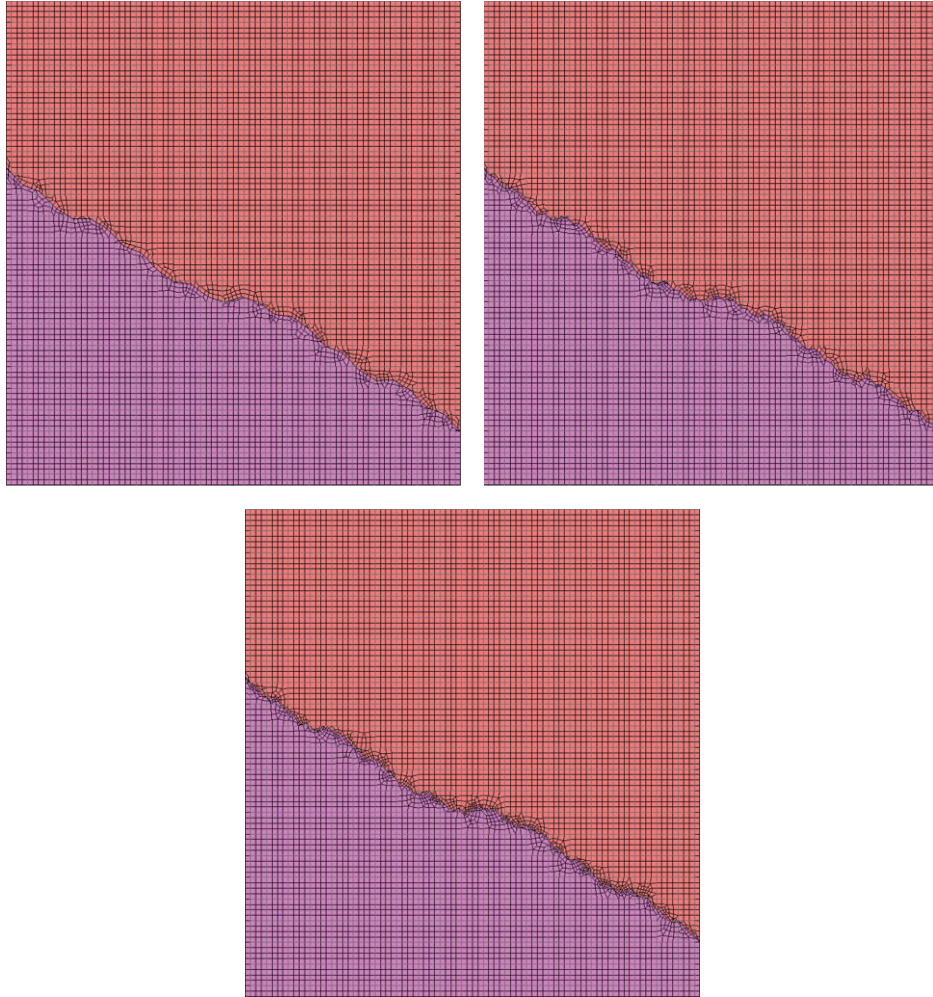


FIGURE 4: FE discretizations for third, fourth, and fifth resolutions of the fractal interface.

The solution of the above problems is obtained through the application of the Newton-Raphson iterative method. Due to the highly nonlinear nature of the problem, a very fine load incrementation was used. The maximum value of the horizontal displacement (20 mm) was applied in 2000 loading steps, while the total vertical loading was applied in the 1st load step and was assumed as being constant in the subsequent steps.

4. Numerical Results

Figure 5 presents the applied horizontal load versus the corresponding displacement (P - δ curves) for the different values of vertical loading N . Starting from the case of the uncracked wall, it must be mentioned that the value of the vertical loading plays a significant role. As the value of the vertical loading increases, the capacity of the wall to undertake horizontal loading increases as well. However, for higher load values (for $N = 2.000$ and 2.500 kN), strength degradations due to the exhaustion of the shear strength of concrete are noticed. In the sequel, the resistance of the wall

increases again as a result of the transfer of the loading from concrete to the horizontal steel rebars.

In cases of the cracked walls, the beneficial effect of the normal compressive loading is once more verified. This result holds for the 3rd, the 4th, and the 5th resolutions of the fractal crack but for small displacement values only. For larger displacement values, the three variants of the cracked wall behave differently. The 4th and the 5th resolutions appear to have a stable behaviour without strength degradations. However, it is noticed that, in the case of the 3rd resolution and for heavy axial loading, significant strength degradation takes place.

The above results can be more easily understood if we compare in the same diagram the curves obtained for the four different structures studied here (uncracked, 3rd resolution, 4th resolution, and 5th resolution) for specific load levels. In Figure 6, the P - δ curves for three cases of axial loading ($N = 0$, $N = 1500$ kN, and $N = 2.500$ kN) are presented. We observe that, for low values of the compressive axial loading, there is actually no difference between the uncracked and the cracked walls. In all cases, the horizontal loading is easily transferred and no signs of strength degradation are noticed

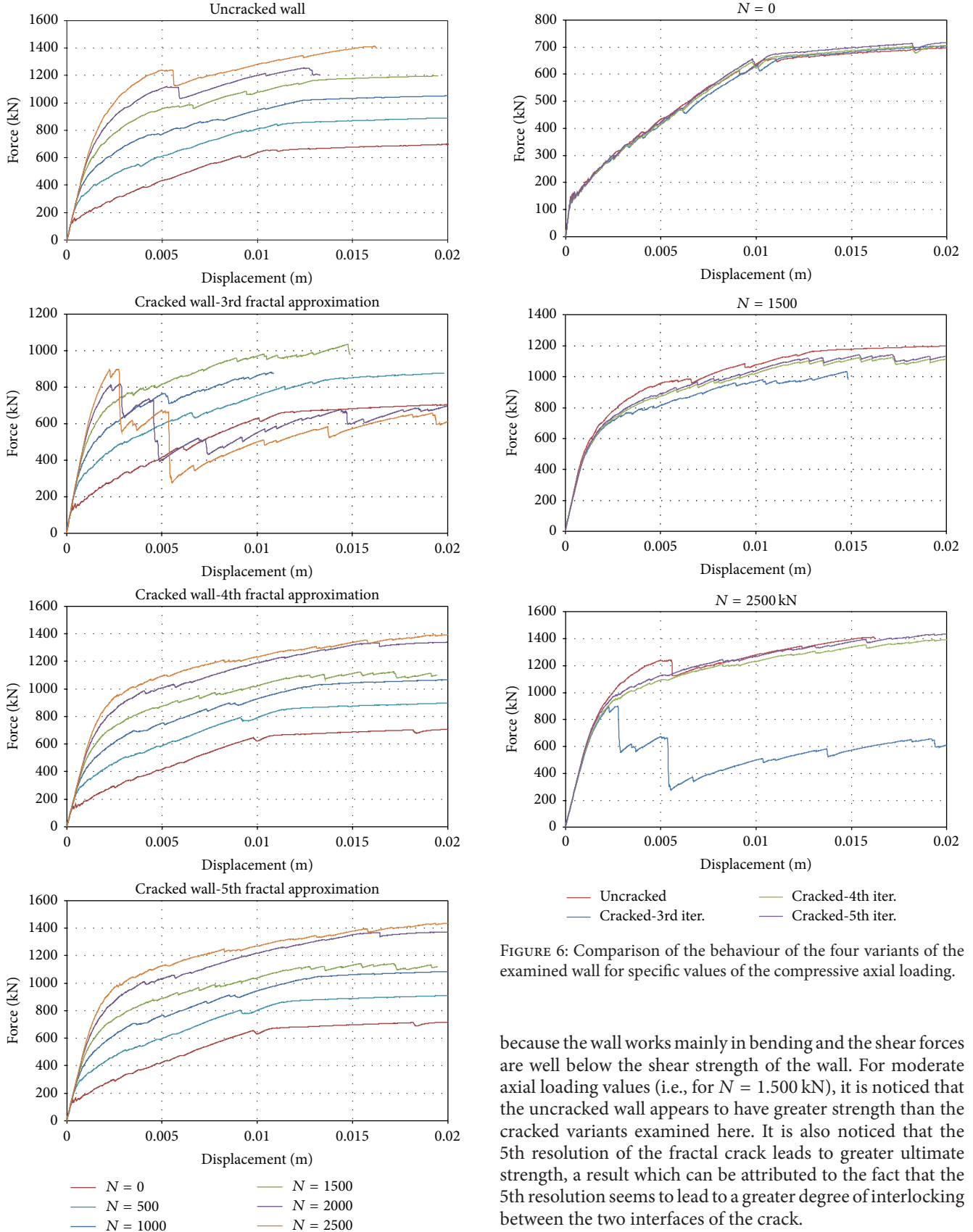


FIGURE 5: Load-displacement ($P-\delta$) curves for the cases of the uncracked and cracked walls.

FIGURE 6: Comparison of the behaviour of the four variants of the examined wall for specific values of the compressive axial loading.

because the wall works mainly in bending and the shear forces are well below the shear strength of the wall. For moderate axial loading values (i.e., for $N = 1.500$ kN), it is noticed that the uncracked wall appears to have greater strength than the cracked variants examined here. It is also noticed that the 5th resolution of the fractal crack leads to greater ultimate strength, a result which can be attributed to the fact that the 5th resolution seems to lead to a greater degree of interlocking between the two interfaces of the crack.

However, the most interesting case is the case where heavy axial loading ($N = 2.500$ kN) is applied to the wall. First, it can be noticed that the behaviour of the 4th and

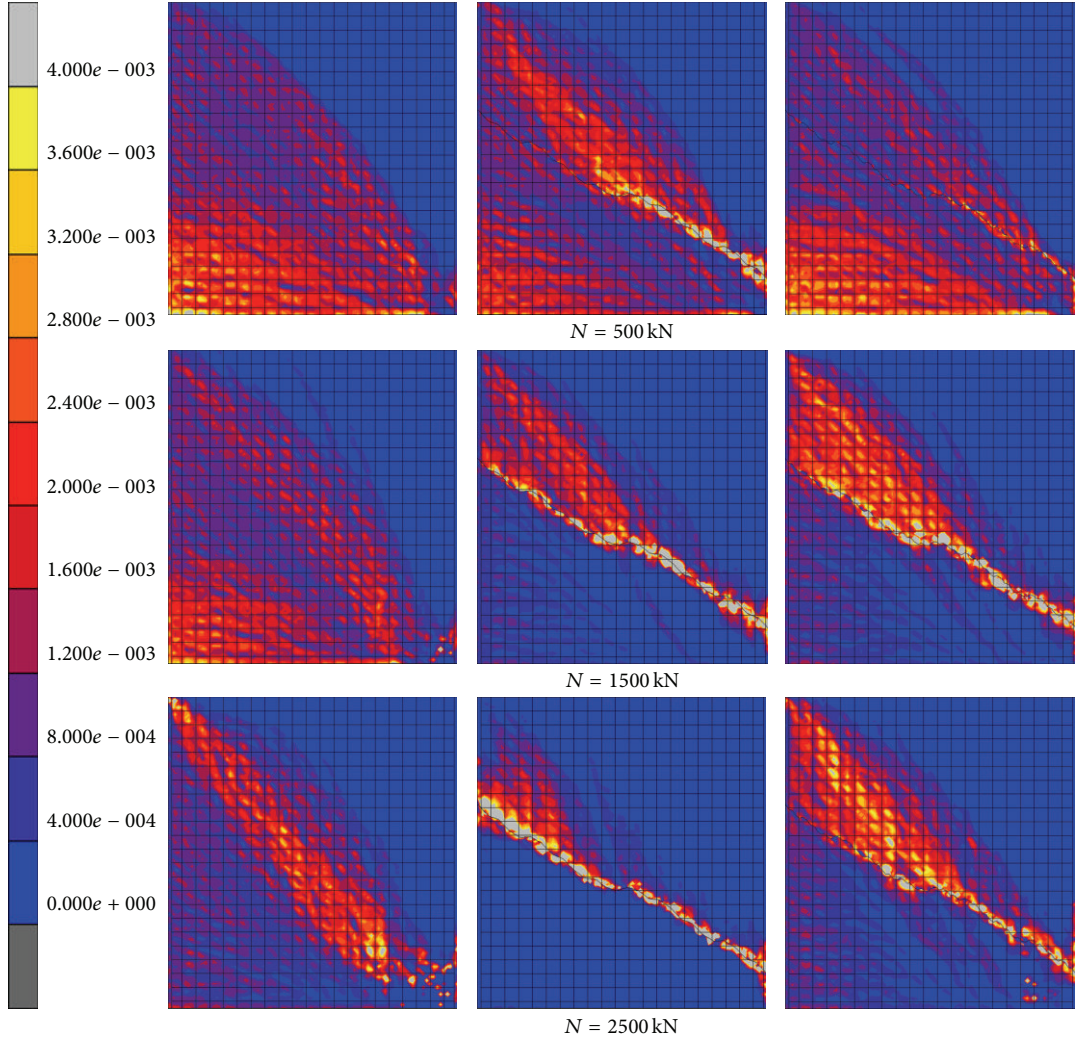


FIGURE 7: Cracking strains for various values of the vertical loading, for the cases of the uncracked wall (left column) and the cracked walls (3rd resolution: middle column and 4th resolution: right column).

the 5th resolutions of the crack leads to results that are close enough to those of the uncracked wall. There exist some differences between the uncracked and the cracked walls for horizontal displacements in the range of 2 mm–6 mm, where the uncracked wall exhibits greater resistance. However, when the horizontal displacement reaches the value of 6 mm, the uncracked wall appears to have strength degradation, and after this displacement value the results of the 4th and the 5th resolutions of the fractal crack are again very close to those of the initially uncracked wall.

Significantly different is the behaviour of the 3rd resolution of the fractal crack. Although in the first loading steps the results are close to those of the 4th and 5th resolutions, after a displacement value of 2.5 mm, significant strength degradation appears, having the form of successive vertical branches. Moreover, the ultimate strength of this wall is significantly lower than the other variants.

It is interesting to try to explain this significantly different behaviour that appears between the walls corresponding to the 3rd and the higher resolutions of the fractal crack. For this reason, all the parameters affecting the behaviour of the wall will be comparatively studied in the sequel.

Figure 7 depicts the cracking strains of concrete for specific values of the axial loading. All the depicted results correspond to the end of the analysis; that is, they have been obtained for an applied horizontal displacement of 20 mm. First of all, it can be noticed that, for low values of axial loading, the cracking patterns that have been developed in all the studied walls are rather similar. The larger cracking strain values (yellow and grey colours) have their nature in the bending deformation of the wall. For moderate axial loading, the cracking patterns are quite different. The uncracked wall presents a bending type cracking pattern. The cracked walls (3rd and 4th resolutions) seem to behave differently. Both of them exhibit significant cracking in the vicinity of the crack

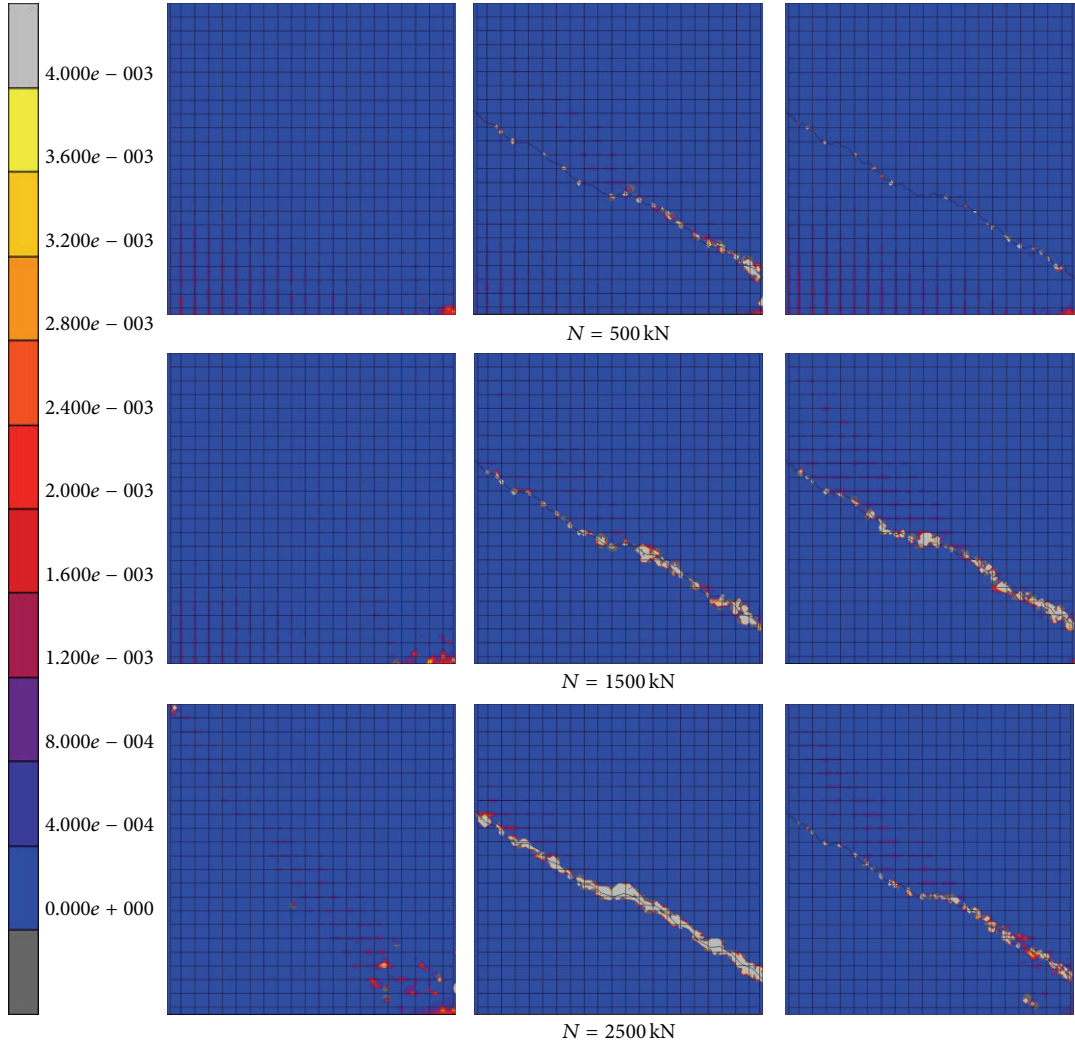


FIGURE 8: Plastic strains for various values of the vertical loading, for the cases of the uncracked wall (left column) and the cracked walls (3rd resolution: middle column and 4th resolution: right column).

(grey colours). Moreover, shear type cracking patterns are developed at the upper parts of the walls.

The above results alone cannot explain the significantly different responses that the two cracked variants of the wall exhibit. For this reason, the plastic strains of concrete obtained for the same applied horizontal displacement are examined. Figure 8 depicts the plastic concrete strains for the three different variants of the wall and for specific values of axial loading. The upper value of the presented scale corresponds actually to the crushing limit (grey values). Therefore, it can be considered that concrete stresses in these areas are actually zero. For the uncracked wall (left column of Figure 8) it can be noticed that the more heavily deformed region is the lower right corner. It is clear that in this case the wall exhibits a typical bending type deformation behaviour (cracking at the lower left region, crushing at the lower right corner).

On the other hand, the cracked walls seem to deform significantly in the vicinity of the crack. This phenomenon

is more pronounced in the case of the 3rd resolution of the fractured wall and especially in the case of heavy axial loading, where it can be noticed that the vicinity of the crack is in the crushed state; that is, the forces are transmitted solely by the steel mesh in this region. For the case of the 4th resolution, this phenomenon is rather limited; that is, it can be concluded that in this case the crack retains partially its ability to transfer shear and compressive forces through the contact and friction phenomena developed in the interface and through the mechanical interlocking that occurs between the two interface parts.

In the sequel, it is interesting to examine the deformations that have occurred at the steel mesh. Figure 9 displays the steel mesh for the cases studied above. The presented deformations which correspond to the last load step have been magnified by a factor of 10 so that the differences between the examined cases are visible. It is obvious that, for low vertical loading values, the deformations of the steel meshes are actually very similar. However, for moderate

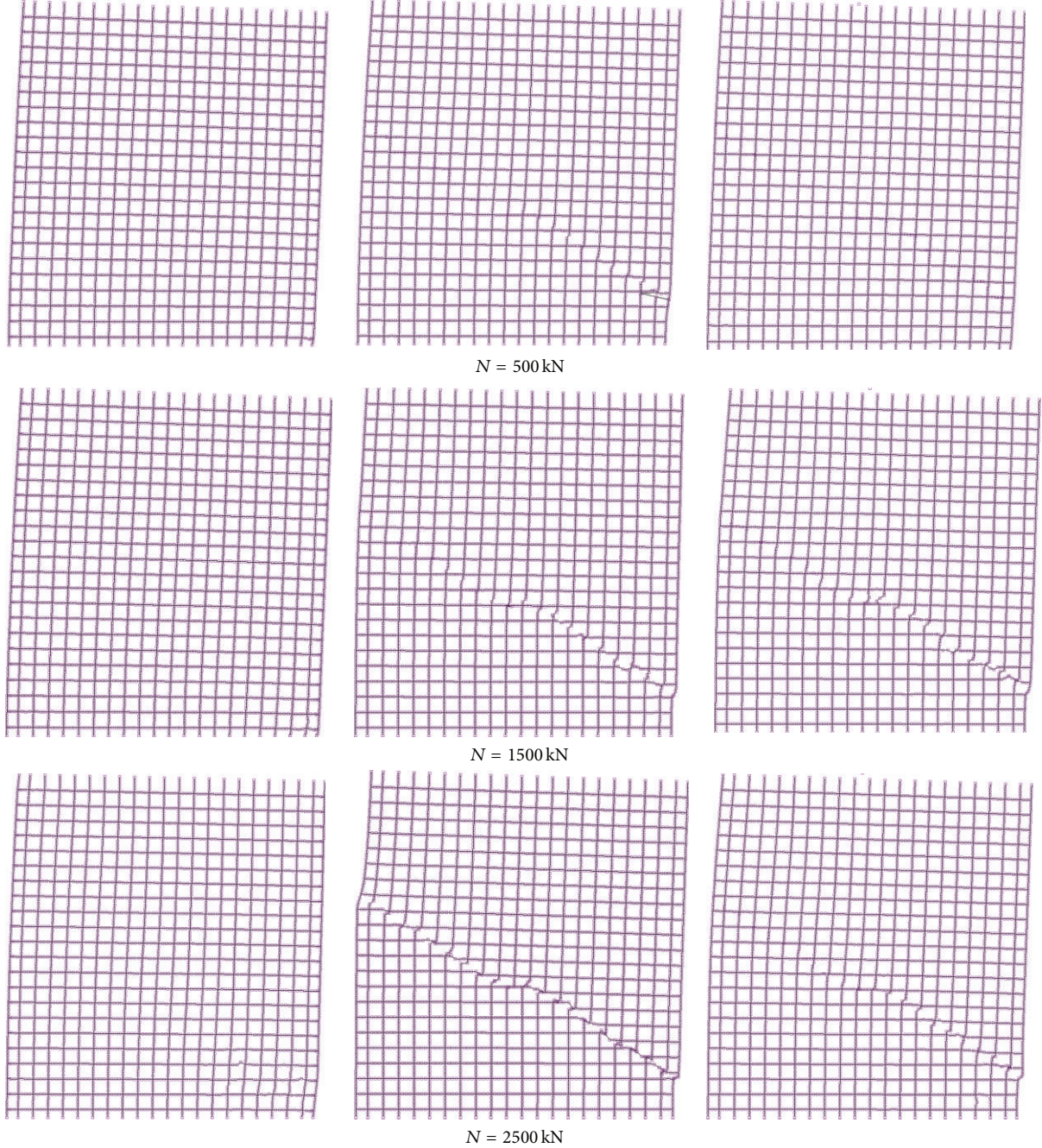


FIGURE 9: Deformation of the steel mesh for various values of the vertical loading, for the cases of the uncracked wall (left column) and the cracked walls (3rd resolution: middle column and 4th resolution: right column).

values of the vertical loading ($N = 1.500 \text{ kN}$), there exist some differences. The steel meshes of the cracked walls seem to be distorted in the vicinity of the right part of the formed crack. In this region, the vertical rebars above and below the crack present an offset which can be attributed to the inability of the interface to transfer shear forces. For the case of heavy vertical loading, the situation is much different. The wall corresponding to the 4th resolution of the fractal crack has a deformation similar to that of the case of moderate

loading. However, the steel mesh of the wall corresponding to the 3rd resolution of the fractal crack exhibits significant deformations along the crack. More specifically, the upper vertical rebars present a significant horizontal offset with respect to the lower ones. This horizontal offset is obvious even in the leftmost part of the wall. Moreover, the horizontal rebars of the upper part present a vertical offset with respect to the ones of the lower part. This deformation pattern of the steel mesh verifies the findings that were noticed in

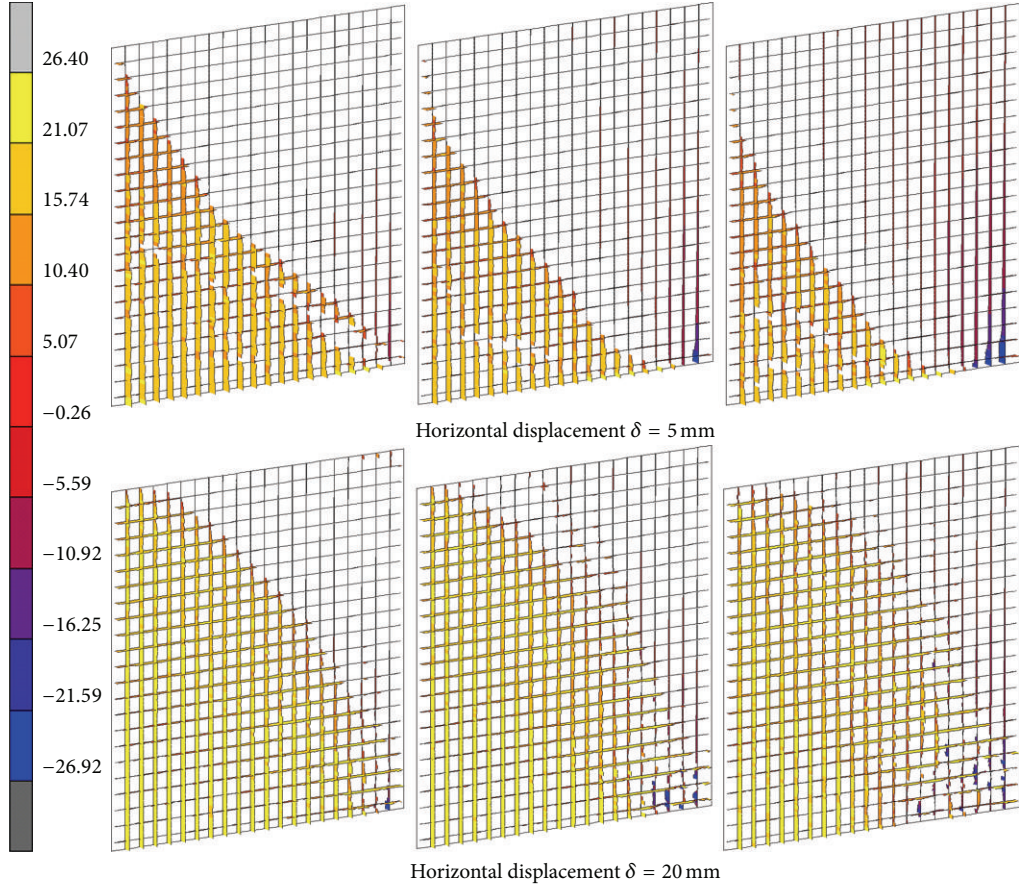


FIGURE 10: Forces developed in the steel mesh for various values of the vertical loading for the uncracked wall (left column: $N = 500$ kN, middle column: $N = 1500$ kN, and right column: $N = 2500$ kN).

Figure 8 concerning the excessive strains in the vicinity of the crack (which had values well above the crushing strain limit) resulting from the inability of concrete to transfer any loading in this case.

Now, the difference in the response between the 3rd and the 4th resolutions of the fractal crack for the case of heavy vertical loading will be explained. As it has already been noticed, higher vertical loading leads to higher values of the horizontal loading. The increased horizontal forces have to be transferred from the upper part of the cracked wall to its lower part. In this respect, three mechanisms are developed in order to facilitate the horizontal load transfer:

- (i) exploitation of the tensile strength of the horizontal rebars;
- (ii) development of friction on the part of the crack where contact forces occur;
- (iii) mechanical interlock between the two interfaces of the crack.

The first two mechanisms are almost similar in both cracked walls. However, it is obvious from Figure 6 that in higher resolutions fractal crack improves its capacity to transfer forces through the mechanical interlock mechanism.

According to the authors' opinion, this fact is the main reason for the difference in the response between the walls corresponding to the 3rd and the 4th resolutions of the fractal crack. For lower vertical load values the differences are rather limited; however, as the vertical loading increases, the response is completely different because the increased vertical forces are combined with the increased horizontal forces and "destroy" completely the vicinity of the interface.

Figures 10, 11, and 12 display the forces developed at the horizontal and vertical rebars of the steel mesh for the three variants of the wall examined here for displacements of 5 mm and 20 mm. The left column of each figure corresponds to lower values of the axial loading ($N = 500$ kN), the middle column to moderate loading values ($N = 1500$ kN), and the right column to heavy axial loading ($N = 2500$ kN).

For the case of the uncracked wall (Figure 10), it is noticed that, in the early horizontal loading steps ($\delta = 5$ mm), only the vertical rebars are significantly loaded. The rebars in the left side of the wall have tensile forces while the rebars in the right side develop compressive forces, as a result of the bending of the wall. For $\delta = 20$ mm, after the development of cracking in various parts of the initially uncracked wall, the horizontal rebars are also stressed, mainly in the areas where the corresponding cracks have

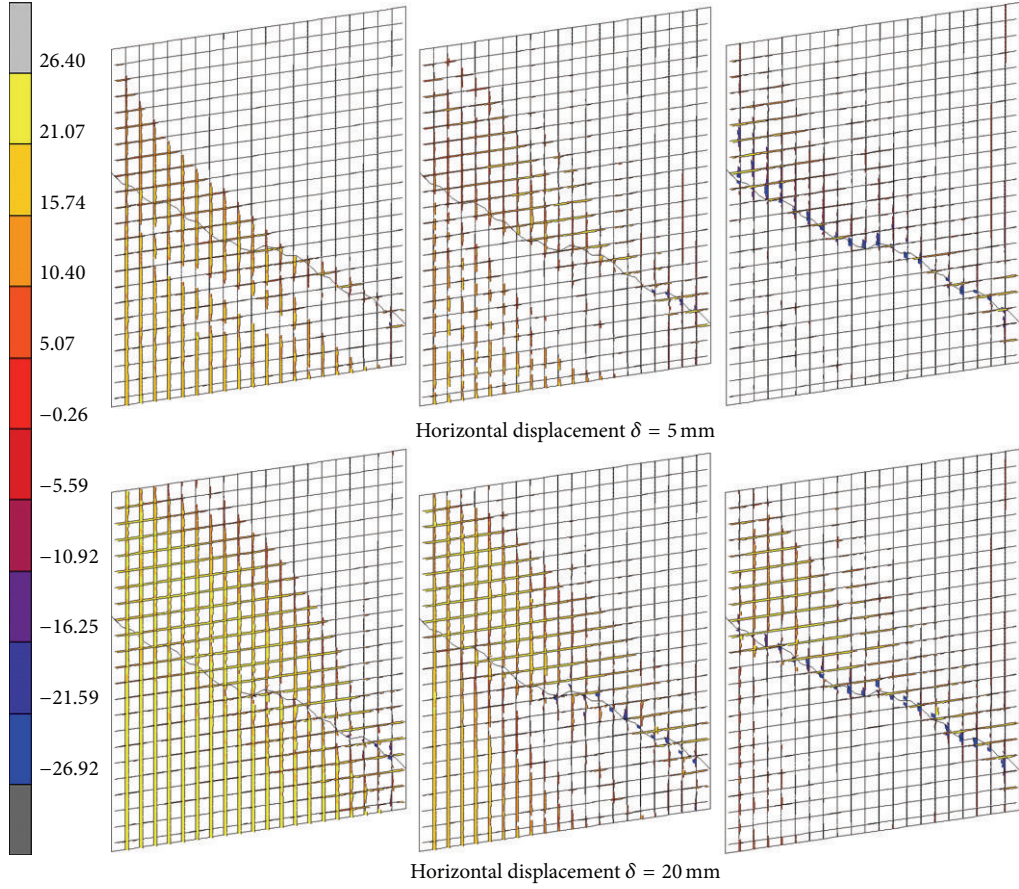


FIGURE 11: Forces developed in the steel mesh for various values of the vertical loading for the 3rd resolution of the crack (left column: $N = 500$ kN, middle column: $N = 1500$ kN, and right column: $N = 2500$ kN).

reduced or zeroed the ability of concrete to transfer shear forces.

For the case of the 3rd resolution of the crack (Figure 11), it is noticed that the vertical rebars are stressed only for small axial loading values. For moderate and heavy axial loading, the vertical rebars are partially stressed. It deserves to be noticed that the rebar stresses are negative in the vicinity of the crack, a fact which verifies that the concrete is unable to transfer even compressive loading. Moreover, it is noticed that the rebars of the right side of the wall do not develop compressive stresses any more, due to the fact that the magnitude of bending that develops in this case is significantly smaller than that in the case of the uncracked wall. The horizontal rebars are stressed only in specific areas, near the crack and in the regions where cracking strains have been developed. In any case, a closer look in the forces that have been developed in the rebars verifies the significantly decreased bending capacity of the specific wall.

The situation is rather different in the case of the 4th resolution of the fractal crack (Figure 12). It can easily be verified that, for small values of the axial loading, the picture of the forces of the vertical rebars is quite similar to that of the uncracked wall. The same holds also for the forces of the horizontal rebars. For moderate axial load values, the forces

of the vertical rebars appear to be discontinuities. At the right part of the crack, it can be noticed that in some rebars the forces are compressive, indicating once again the partial inability of concrete in this region to transfer compressive loading. The horizontal rebars are mainly stressed in the upper part of the cracked wall and in the vicinity of the crack. This result is absolutely compatible with the remarks given for the cracked areas in Figure 7.

5. Conclusions

In the paper, the finite element analysis of a typical shear wall element which follows the construction practices applied in Greece during the 70s was presented assuming that a certain crack has been developed as a result of an earthquake action. The crack was modelled following tools from the theory of fractals. Three different resolutions of the fractal crack were considered by taking into account the aggregate sizes of the concrete, and their results were compared to those of the initially uncracked wall. The main finding of the paper is that the cracked wall still has the capacity to sustain monotonic horizontal loading. For small axial loading values, this capacity is similar to that of the initially uncracked wall. However, for larger axial loading values where the

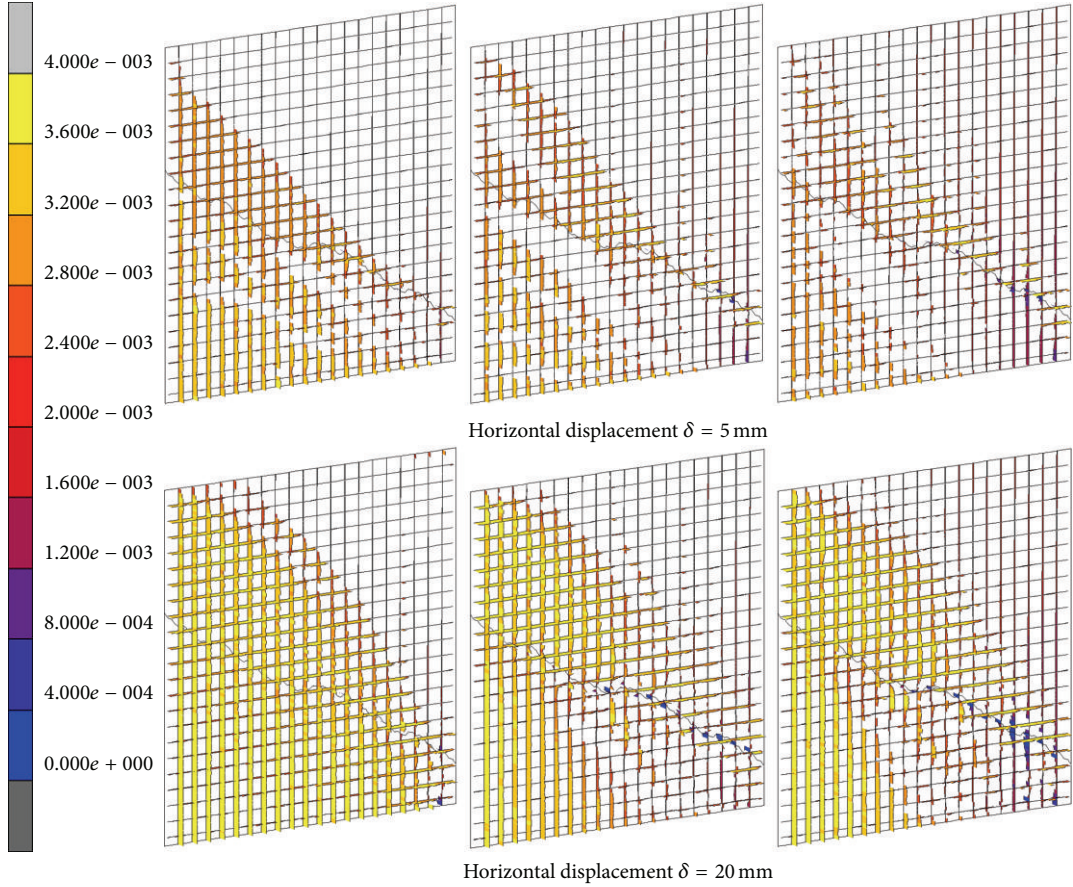


FIGURE 12: Forces developed in the steel mesh for various values of the vertical loading for the 4th resolution of the crack (left column: $N = 500$ kN, middle column: $N = 1500$ kN, and right column: $N = 2500$ kN).

demands increase, it seems that a more accurate simulation of the geometry of the fractal crack (i.e., considering higher values of the resolution of the interfaces) leads to better results. Using lower resolution values, the roughness of the interfaces is not taken into account, and therefore the mechanical interlock between the two faces of the crack is rather limited, leading the concrete in the vicinity of the crack to overstressing and gradually to a complete loss of its capacity to sustain any kind of forces. In this case the bending capacity of the wall is significantly limited.

References

- [1] H.-G. Sohn, Y.-M. Lim, K.-H. Yun, and G.-H. Kim, "Monitoring crack changes in concrete structures," *Computer-Aided Civil and Infrastructure Engineering*, vol. 20, no. 1, pp. 52–61, 2005.
- [2] T. C. Hutchinson and Z. Chen, "Image-based framework for concrete surface crack monitoring and quantification," *Advances in Civil Engineering*, vol. 2010, Article ID 215295, 2010.
- [3] B. B. Mandelbrot, D. E. Passoja, and A. J. Paullay, "Fractal character of fracture surfaces of metals," *Nature*, vol. 308, no. 5961, pp. 721–722, 1984.
- [4] V. E. Saouma, C. C. Barton, and N. A. Gamaleldin, "Fractal characterization of fracture surfaces in concrete," *Engineering Fracture Mechanics*, vol. 35, no. 1–3, pp. 47–53, 1990.
- [5] A. Majumdar and C. L. Tien, "Fractal characterization and simulation of rough surfaces," *Wear*, vol. 136, no. 2, pp. 313–327, 1990.
- [6] V. E. Saouma and C. C. Barton, "Fractals, fractures, and size effects in concrete," *Journal of Engineering Mechanics*, vol. 120, no. 4, pp. 835–854, 1994.
- [7] A. Carpinteri and B. Chiaia, "Multifractal nature of concrete fracture surfaces and size effects on nominal fracture energy," *Materials and Structures*, vol. 28, no. 8, pp. 435–443, 1995.
- [8] B. Chiaia, J. G. M. Van Mier, and A. Vervuurt, "Crack growth mechanisms in four different concretes: microscopic observations and fractal analysis," *Cement and Concrete Research*, vol. 28, no. 1, pp. 103–114, 1998.
- [9] H. Mihashi, N. Namura, and T. Umeoka, "Fracture mechanics parameters of cementitious composite materials and fractured surface properties," in *Europe-U.S. Workshop on Fracture and Damage in Quasibrittle Structures*, Prague, Czech Republic, 1994.
- [10] A. Carpinteri and P. Cornetti, "Size effects on concrete tensile fracture properties: an interpretation of the fractal approach based on the aggregate grading," *Journal of the Mechanical Behavior of Biomedical Materials*, vol. 13, no. 3–4, pp. 233–246, 2011.
- [11] H.-Q. Sun, J. Ding, J. Guo, and D.-L. Fu, "Fractal research on cracks of reinforced concrete beams with different aggregates

- sizes," *Advanced Materials Research*, vol. 250-253, pp. 1818–1822, 2011.
- [12] V. Mechtcherine, "Fracture mechanical behavior of concrete and the condition of its fracture surface," *Cement and Concrete Research*, vol. 39, no. 7, pp. 620–628, 2009.
- [13] M. Borri-Brunetto, A. Carpinteri, and B. Chiaia, "Scaling phenomena due to fractal contact in concrete and rock fractures," *International Journal of Fracture*, vol. 95, no. 1–4, pp. 221–238, 1999.
- [14] O. Panagouli and E. Mistakidis, "Dependence of contact area on the resolution of fractal interfaces in elastic and inelastic problems," *Engineering Computations*, vol. 28, no. 6, pp. 717–746, 2011.
- [15] E. Mistakidis and G. Stavroulakis, *Nonconvex Optimization in Mechanics. Algorithms, Heuristic and Engineering Applications by the FEM*, Kluwer, 1997.
- [16] A. Carpinteri, B. Chiaia, and S. Invernizzi, "Three-dimensional fractal analysis of concrete fracture at the meso-level," *Theoretical and Applied Fracture Mechanics*, vol. 31, no. 3, pp. 163–172, 1999.
- [17] G. Mourot, S. Morel, E. Bouchaud, and G. Valentin, "Anomalous scaling of mortar fracture surfaces," *Physical Review E*, vol. 71, no. 1, Article ID 016136, 2005.
- [18] A. Carpinteri, G. Lacidogna, and G. Niccolini, "Fractal analysis of damage detected in concrete structural elements under loading," *Chaos, Solitons & Fractals*, vol. 42, no. 4, pp. 2047–2056, 2009.
- [19] B. Mandelbrot, *The Fractal Geometry of Nature*, W.H. Freeman, 1982.
- [20] B. B. Mandelbrot, "Self-affine fractals and fractal dimension," *Physica Scripta*, vol. 32, no. 4, pp. 257–260, 1985.
- [21] K. J. Måløy, A. Hansen, E. L. Hinrichsen, and S. Roux, "Experimental measurements of the roughness of brittle cracks," *Physical Review Letters*, vol. 68, no. 2, pp. 213–215, 1992.
- [22] A. Majumdar and B. Bhushan, "Role of fractal geometry in roughness characterization and contact mechanics of surfaces," *Journal of Tribology*, vol. 112, no. 2, pp. 205–216, 1990.
- [23] P. D. Panagiotopoulos and O. K. Panagouli, "Fractal geometry in contact mechanics and numerical applications," in *CISM-Book on Scaling, Fractals and Fractional Calculus in Continuum Mechanics*, A. Carpintieri and F. Mainardi, Eds., pp. 109–171, Springer, 1997.
- [24] F. M. Borodich and D. A. Onishchenko, "Similarity and fractality in the modelling of roughness by a multilevel profile with hierarchical structure," *International Journal of Solids and Structures*, vol. 36, no. 17, pp. 2585–2612, 1999.
- [25] F. M. Borodich and A. B. Mosolov, "Fractal roughness in contact problems," *Journal of Applied Mathematics and Mechanics*, vol. 56, no. 5, pp. 681–690, 1992.
- [26] E. S. Mistakidis and O. K. Panagouli, "Strength evaluation of retrofit shear wall elements with interfaces of fractal geometry," *Engineering Structures*, vol. 24, no. 5, pp. 649–659, 2002.
- [27] E. S. Mistakidis and O. K. Panagouli, "Friction evolution as a result of roughness in fractal interfaces," *Engineering Computations*, vol. 20, no. 1–2, pp. 40–57, 2003.
- [28] C.-J. Chen, T.-Y. Lee, Y. M. Huang, and F.-J. Lai, "Extraction of characteristic points and its fractal reconstruction for terrain profile data," *Chaos, Solitons & Fractals*, vol. 39, no. 4, pp. 1732–1743, 2009.
- [29] M. Barnsley, *Fractals Everywhere*, Academic Press, 1988.
- [30] G.-D. Hu, P. D. Panagiotopoulos, P. Panagouli, O. Scherf, and P. Wriggers, "Adaptive finite element analysis of fractal interfaces in contact problems," *Computer Methods in Applied Mechanics and Engineering*, vol. 182, no. 1–2, pp. 17–37, 2000.
- [31] R. de Borst, J. J. C. Remmers, A. Needleman, and M.-A. Abellán, "Discrete vs smeared crack models for concrete fracture: bridging the gap," *International Journal for Numerical and Analytical Methods in Geomechanics*, vol. 28, no. 7–8, pp. 583–607, 2004.